PASSIVE DAMPING TREATMENTS FOR CONTROLLING VIBRATION IN ISOTROPIC AND ORTHOTROPIC STRUCTURAL MATERIALS

A thesis submitted in partial fulfillment of the requirements for the

Degree of

Doctor of Philosophy in Mechanical Engineering

in the University of Canterbury

by André Paul Verstappen

Department of Mechanical Engineering

University of Canterbury

2014

ABSTRACT

The structural vibration damping behaviour of plates and beams can be improved by the application of viscoelastic passive damping materials. Unconstrained layer damping treatments applied to metal plate systems were studied experimentally. Design and modelling of novel fibre reinforced constrained layer damping materials was performed, and implementation of these composite damping materials into laminated composite sandwich constructions commonly used as structural elements within large composite marine vessels was explored. These studies established effective methods for examining, designing and applying damping materials to metal and composite marine structures.

Two test fixtures were designed and constructed to facilitate testing of viscoelastic material damping properties to ISO 6721-3 and ASTM E756. Values of material damping made in accordance with ASTM E756 over a range of temperatures were compared to values produced by a Dynamic Mechanical Analyser (DMA). Glass transition temperatures and peak damping values were found to agree well, although results deviated significantly at temperatures above the glass transition temperature.

The relative influence of damping layer thickness, ambient temperature, edge conditions, plate dimensions and substrate material on the system damping performance of metal plates treated with an unconstrained viscoelastic layer was investigated experimentally. This investigation found that substrate material had the greatest influence on system damping performance, followed by damping layer thickness and plate size. Plate edge conditions were found to have little influence on the measured system damping performance. These results were dependent on the values of each variable used in the study.

Modal damping behaviour of a novel fibre reinforced composite constrained layer damping material was investigated using finite element analysis and experimental methods. The material consisted of two carbon fibre reinforced polymer (CFRP) layers surrounding a viscoelastic core. Opposing complex sinusoidal fibre patterns in the CFRP face sheets were used to achieve stress-coupling by way of orthotropic anisotopy about the core. A finite element model was developed in MATLAB to determine the modal damping, displacement, stress, and strain behaviour of these complex patterned fibre constrained layer damping (CPF-CLD) materials. This model was validated using experimental results produced by modal damping measurements on CPF-CLD beam test specimens. Studies of multiple fibre pattern arrangements found that fibre pattern properties and the resulting localised material property distributions influenced modal damping performance.

Inclusion of CPF-CLD materials in laminated composite sandwich geometries commonly used in marine hull and bulkhead constructions was studied experimentally. Composite

sandwich beam test specimens were fabricated using materials and techniques frequently used in industry. It was found that the greatest increases in modal damping performance were achieved when the CPF-CLD materials were applied to bulkhead geometries, and were inserted within the sandwich structure, rather than being attached to the surface.

ACKNOWLEDGMENTS

I would like to express my special appreciation and thanks to my supervisor Dr. John Pearse, my co-supervisor Dr. Stefanie Gutschmidt, and the members of the Acoustics Research Group. Your combined support, knowledge and encouragement has been invaluable throughout the course of my Ph.D. studies. I would also like to thank my industry mentor Mr. Mike Latimer for the resources and time he has generously provided during this project. My thanks go to Pyrotek Noise Control and the Ministry of Business, Innovation, and Employment for providing the funding which made this project possible.

To my parents Heather and Eric, and my younger sister Jennie. Your support, values, and constant encouragement have provided the foundation which allowed me to get to where I am now. Words are insufficient to express my gratitude. To my girlfriend Amanda, your unwavering support throughout the entirety of my Ph.D. studies has been a cornerstone of my life. You have given me the drive and outlook needed to reach the end of this journey. Your parents James and Diana, and sisters Sophie and Katie, were my surrogate family and their support and advice has been hugely appreciated.

Contents

List of Figures

List of Tables

Nomenclature

$\alpha_{_T}$	horizontal shift factor
β	aspect ratio
Δf	bandwidth at 3 dB below resonance peak
δ	phase angle between stress and strain response or tip deflection (according to context)
$\Delta_{\max}$	convergence criterion
$\eta, \tan\delta$	damping loss factor (loss factor)
$\eta_1, \eta_2, \eta_{12}, \eta_{23}$	directional loss factors
η_c	loss factor of damped beam at mode c
η_v	loss factor for isotropic viscoelastic layer
η_{to}	torsional loss factor
$\gamma_{12}, \gamma_{23}, \gamma_{31}$	directional shear strains
$\Gamma_{xy}, \Gamma_{yz}, \Gamma_{zx}$	strain field proportions
Λ	logarithmic decrement
λ	eigenvalue or wavelength (according to context)
λ_r^*	complex eigenvalue for mode r
λ_i	eigenvalue for mode i
μ	viscosity
ν	Poisson's ratio
ν_v	Poisson's ratio for isotropic viscoelastic layer

$\nu_{12}, \nu_{23}, \nu_{31}$	directional Poisson's ratios
ω	circular frequency
ω_D	damped natural frequency
ω_r	resonant frequency
ω_{mn}	modal frequency of mode (m, n)
$\overline{\theta}_{abs}$	average absolute waveform angle
ϕ	general displacement variable or waveform phase angle (according to context)
ρ	density
ρ_0	density at temperature T_0
ρ_c	density of composite material
ρ_d	density of damped beam
ρ_s	surface density
ρ_v	density of viscoelastic material
σ	stress
θ	angle
θ_{max}	maximum waveform angle
ε	strain
$\varepsilon_1, \varepsilon_2, \varepsilon_3$	directional extensional strains
φ	phase angle between input force and output response
ξ, η, ζ	isoparametric directions corresponding to x, y, z respectively
A	amplitude, constant, or variable designation (according to context)
a	length
b	width
b_T	vertical shift factor
c	viscous damping coefficient
C_1, C_2,..., C_n	empirical constants

C_1^g, C_2^g	empirical constants at T_g
D	flexural rigidity
E	elastic modulus
E^*	complex elastic modulus
E'	elastic storage modulus
E''	elastic loss modulus
E_1, E_2, E_3	directional elastic moduli
E_1^*, E_2^*, E_3^*	directional complex elastic moduli
E_1', E_2', E_3'	directional elastic storage moduli
E_f'	flexural elastic storage modulus
F	force
f	frequency
F_c	dimensional correction factor
f_c, f_n, f_r	resonant frequency at mode c, n, r respectively
f_d	damped oscillation frequency
G_v	shear modulus for isotropic viscoelastic layer
G_{12}, G_{23}, G_{31}	directional shear moduli
G_{12}^*, G_{23}^*	directional complex shear moduli
G_{12}', G_{23}'	directional shear storage moduli
G_{to}'	torsional shear storage modulus
H, h	thickness
h_p	element thickness
I	area moment of inertia, moment of inertia, or pseudo identity matrix (according to context)
i	$\sqrt{-1}$
i, j	integers
I_X	influence of variable X

J	determinant of the Jacobian matrix
k	stiffness wave number
k	wave number
k^*	complex stiffness
k_c	numerical factor for mode c
L, l	length
L_n	distance from beam end to closest mode n vibration node
m	mass
N_i	interpolation function of node i
p	uniformly distributed load
T	temperature
t	thickness or time (according to context)
T_0	reference temperature
T_g	glass transition temperature
T_s	reference temperature or structural reverberation time (according to context)
U_0	strain energy density
v_f	fibre volume fraction
v_m	matrix volume fraction
W	width
w, u, v	displacements in x, y, z directions respectively
W_ξ, W_η, W_ζ	Gauss quadrature weighting functions
x, y, z	Cartesian coordinates or displacements depending on context
$[\mathbf{\Gamma}]$	Jacobian matrix inverse
$[\mathbf{\Lambda}^*]$	complex eigenvalue matrix
$[\mathbf{\Phi}^*]$	complex eigenvector matrix
$[\mathbf{\Pi}]$	general element property matrix

$[\mathbf{B}]$	element strain matrix
$[\mathbf{E}^*]$	complex material constitutive matrix
$[\mathbf{K}^*]$	complex global stiffness matrix
$[\mathbf{k}^*]$	complex element stiffness matrix
$[\mathbf{M}]$	global mass matrix
$[\mathbf{m}]$	element mass matrix
$[\mathbf{N}]$	interpolation function matrix
$[\mathbf{Q}]$	stiffness matrix
$[\mathbf{S}]$	compliance matrix
$[\mathbf{T}]$	transformation matrix
$[J]$	Jacobian matrix
$\{\phi^*{}_r\}$	complex eigenvector for mode r
$\{\phi_i\}$	eigenvector for mode i
$\{\sigma\}$	stress vector
$\{\varepsilon\}$	strain vector
$\{\mathbf{a}\}$	displacement vector
$\{\mathbf{c}\}$	position vector
$\{\mathbf{F}\}$	force amplitude vector
$\{\mathbf{f}(t)\}$	forcing function vector

Chapter 1

Introduction and Background

1.1 Introduction

Controlling unwanted vibrations is an important aspect in the design of mechanical systems and structures which house sources of dynamic excitation. If not properly addressed, high vibration levels can propagate throughout a structure and result in undesirable conditions for occupants and equipment alike. This is particularly true in marine structures, which often house numerous and varied sources of vibration excitation. Vibration sources can include mechanical components such as engines, generators, drive-line equipment and ventilation services, as well as environmental sources such as wave slap. Each of these sources contribute to structural vibration within a vessel. There are several technologies available for reducing structural vibration, these include discrete dampers, isolation absorbers, active damping systems, and passive material treatments. The application of each of these technologies is highly dependent on the subject system and the required outcome. Passive material treatments are well suited to application over a large area of a structure or in key vibration transmission locations which are unsuitable for discrete or active dampers.

In the case of structure-borne noise, vibrations propagate from a source, such as rotating componentry, throughout a structure to areas where the vibration has a noticeable effect.

Panel geometries within a structure can be efficient sound radiators due to their large surface area and comparatively low flexural stiffness. Layered passive damping materials are an effective means of reducing excess vibration of such structural elements. Viscoelastic materials are well suited to this application as they convert mechanical deformation into heat through the straining and relaxation of their molecular structures [1]. When a viscoelastic damping treatment is applied as a coating to the surface of a structure it is designated an unconstrained layer damper and its damping properties are dominated by the extensional strains within the material [2]. Viscoelastic layers may also be embedded within a structure or applied as a coating with a bonded stiff upper layer. In these instances the treatment is designated a constrained layer damper and the damping properties are dominated by shear strains within the viscoelastic material.

Both metallic constructions and fibre reinforced polymer composites are used in marine structures. When applying or designing damping treatments for these constructions it is important to have a good knowledge the parameters which have the greatest effect on improving the system structural damping performance. Such knowledge enables judicious use of available damping materials and greater insight into effective design of new damping treatments. Each of these aspects are explored in this thesis.

The early chapters explore the state of the field of passive vibration damping using viscoelastic layers, measurement techniques for determining material damping properties, and the relative influence of several important parameters on system damping performance of metal panels with unconstrained layer damping treatments. The later chapters detail the development of a finite element model to analyse a new composite damping arrangement, and an experimental investigation into the implementation of this treatment in composite marine structural configurations.

1.2 Viscoelastic Damping

An effective method of reducing vibration is through the use of damping layers which are applied to a vibrating substrate. This was first studied in 1952 by Oberst and Frankenfeld [3] who investigated the effects of applying a layer of viscoelastic material to a flexible base structure as a means of achieving passive vibration control. Viscoelastic materials are well suited to this application as they convert mechanical deformation into heat through the straining and relaxation of their molecular structures. Early damping treatments involved materials that were trowelled or sprayed directly onto a base structure. Such damping treatments were referred to as unconstrained layer damping (ULD) treatments. Layered damping treatments were typically applied to load bearing structural elements (transmission paths for structural vibration) and areas prone to high sound radiation [2].

The primary damping mechanism in ULD treatments is through the extensional straining of the viscoelastic layer. Consequently, the effectiveness of unconstrained layer treatments is limited by the vibratory nature of the base structure. In 1959, Kerwin [4] investigated a new damping configuration where the applied viscoelastic layer was constrained by a stiff elastic upper layer. This constrained layer damping (CLD) treatment was found to produce greater damping performance than unconstrained layer treatments. It was determined that the primary damping mechanism of this configuration was through the shear straining of the viscoelastic layer induced by the upper constraining layer. Both ULD and CLD treatments were practical for treating metallic structural arrangements found in marine craft. More recent developments in laminated damping materials include a wide range of composite lay-ups, such as fibre reinforced viscoelastic layers [5] and honeycomb structures [6]. Layered composite structures provided an avenue of achieving greater structural damping performance through selection of their constituent materials. Constrained layer type ar-

rangements could also be created by interleaving viscoelastic materials into the lay-up of a composite laminate. The following review covers the chronological development of unconstrained layer damping treatments, constrained layer damping treatments, and composite treatments.

1.2.1 Unconstrained Layer Damping

Oberst and Frankenfeld's work [3] established a method for determining the damping performance of unconstrained layer damping treatments. Their work showed that when a two-layered beam, comprised of an elastic layer and a homogeneous viscoelastic layer, vibrates, its harmonic flexure is governed by the Euler-Bernoulli theory of bending. They also showed that the flexural rigidity of the beam can be regarded as being complex (due to the dynamic behaviour of the viscoelastic layer), with the normalised imaginary part being a measure of the damping performance of the system (flexural loss factor). Using the equation for flexural wave motion, it is possible to determine the decay rates of the wave motion at any given frequency and a simple relationship exists between the decay rate and the flexural loss factor. This was summarised in an equation linking the damping performance of a beam to the stiffness of the damping material, the damping material thickness and the loss factor of the damping material.

This model was used by Ross, Ungar and Kerwin [7], who explored the idea of an optimum thickness of applied damping material. Their research found that for thin layers (up to 1/5th the substrate thickness) of damping material, the damping was a linear function of thickness. In the vicinity of unity thickness ratio, the damping depended on the square of thickness, and at higher relative thicknesses it depended on a higher power. It was seen that there was an optimum damping layer thickness beyond which, additional damping material produced little additional performance. In their work they also produced a series of curves useful for evaluating and designing damping treatments. These were created with a rela-

tionship linking the loss factor of the damped beam with that of the damping material and the flexural stiffness ratios and thickness ratios of the substrate and damping treatment. In this same paper the authors also performed one of the first investigations of constrained layer damping treatments. This is discussed in a later section.

Practical investigations on the effectiveness of damping layers applied to plates were performed by Tarnóczy in 1970 [8]. Two excitation methods were used, the first involved excitation of the plate system with an electromagnetic transducer, the other involved point impulsive excitation achieved by striking the plate. The later method was found to be more suitable for determining the damping factor as a function of frequency. Another important discovery was made during the investigation. If the frame housing the plate was excited and the plate was not (i.e. structure-borne vibration) an equivalent damping performance with a 70% weight reduction was found possible by applying damping material only around the edge of the plate.

Baumgarten and Pearce [9] performed analyses on elastic beams with unconstrained damping layers using an energy method similar to Rayleigh's method. This was limited to the case of free vibration in the fundamental mode, of beams with no constraints. Their work also examined the case of unconstrained layer damping applied to both sides of an elastic beam. They found that in general, the thicker the coating applied, the greater the damping produced. However, it was also observed that in the case of coatings on one side only, there was an optimum thickness ratio beyond which additional viscoelastic material decreased damping performance due to the shift of the neutral axis. For small to moderate thickness ratios, they concluded that it was more effective to use a given amount of damping material on one side rather than divide it between the two sides. However, there was a thickness ratio beyond which it was more efficient to use two symmetric coatings rather than a single layer. Experimental results confirmed the theory they developed. They extended this work

to analyse the case of a non-homogeneous, damped plate composed of an elastic layer and an unconstrained viscoelastic layer [10]. This analysis was limited to the case of thin plates with no constraints, vibrating freely in the fundamental mode. Again, both single layer and two symmetric damping layer treatments were analysed. The theory developed allowed both the amount of damping produced by a given thickness of damping material and the natural frequency of the new composite structure to be accurately predicted for thin plates with coatings on one or both sides. The same conclusions regarding optimum thickness and application of symmetric damping layers were reached for plate damping. It was also found that if a plate and beam were composed of the same material and had the same coating to base thickness ratio, the damping of each would be the same order of magnitude. The value of the system loss factor would be the same only if the beam and plate had the same natural frequency or if the damping properties of the viscoelastic material did not vary with frequency.

The concept of using damping layers of non-uniform thickness and partially coated beams or plates was investigated by multiple authors in the late 1970s and early 1980s. The first comprehensive investigation into tapered damping layers was performed by Rao in 1978 [11]. In this work, Rao derived the equations of motion for a tapered damping layer applied to a beam under a variety of boundary conditions. The boundary conditions included pinned-pinned, clamped-clamped, free-free, clamped-free and clamped-pinned. Two linear tapers were considered, one with damping material thickest at the end with greatest clamping and the other with the reverse. It was found that boundary conditions influenced damping performance of the tapered systems, with clamped-free beams most affected and free-free beams least affected. When comparing the two tapered treatments against the same volume of damping material applied as a uniform layer, it was seen that the configuration with damping material thickest at the end with greatest clamping produced an increase in damping performance while the opposite configuration resulted in reduced performance.

An increase in performance of nearly 300% was achieved with clamped-free boundary conditions and damping material thickest at the clamped end.

Lundén performed analyses on the optimum distribution of unconstrained layer damping on beams [12] and frames [13]. It was found that the displacement response of a beam with a uniform damping layer, supported by springs, could be reduced a further 40% through optimal redistribution of the damping layer. In the case of vibrating frames, a further response reduction of 60% compared to a uniform layer treatment was possible.

Partial viscoelastic coatings applied to plates were analysed and evaluated experimentally by Stevens et al. [14–16]. In their work, an energy approach to free vibration was used to formulate a method for determining the effectiveness of partial and complete viscoelastic coatings applied to plates vibrating in the lower modes. Using plate mode shapes, system geometry and mechanical properties of the plate and coating, this method could be used to determine the natural frequencies and loss factors of plates with partial or complete damping layers. As this method was based on an energy approach, it was not restricted to any particular plate or damping layer geometries or plate boundary conditions. It was found that the accuracy of the method was subject to the choice of material properties for the damping materials. Also, the damping layers considered did not significantly alter the mode shapes of the plate from the undamped case. The results obtained from analysis and experiment on edge fixed square plates indicated that the use of partial coatings could be cost effective.

Optimum thickness distribution for unconstrained damping layer treatments on plates was explored by Yildiz and Stevens [17]. In their study, simply-supported and edge fixed plates with aspect ratios of 1.0 to 4.0 were considered. Optimum distributions of the thickness ratio that maximised the system loss factor were obtained through sequential unconstrained

minimisation techniques. Comprehensive tables detailing the optimal distribution of damping layer for each given aspect ratio, clamping condition and maximum admissible thickness ratio were presented. These tables also contained the expected performance increase over a uniform distribution in the first three modes. The results indicated that the system loss factor could be increased as much as 100% or more by optimising the thickness distribution of the damping treatment. The results presented were for a particular modulus ratio but were believed to be representative of those for plates with other modulus ratios, provided the ratios were much less than 1.

Another study on partial coverage of rectangular plates with unconstrained layer damping treatments was performed by Parthasarathy et al. [18]. A finite element approach was used to analyse the effectiveness of eleven configurations of partially applied damping layer treatments with the objective of realising maximum system damping with minimum mass of applied material. Two configurations with 11.11% (centralised) and 22.22% (slight variation of centralised) damping layer coverage area were found to have the first and second greatest system loss factors respectively. The analytical results were found to correlate well with experimental results produced with simply supported boundaries and clamped boundaries. For the same mass of applied damping material, partial coverage offered higher damping than full coverage. For the 11.11% configuration, a layer thickness ratio of greater than 10 yielded no appreciable increase in damping performance, unlike the 22.22% configuration which offered appreciable increases in modal damping up to a layer thickness ratio of 14. This work also showed that the presence of damping material in antinodal regions increased modal loss factors and decreased modal frequencies. The opposite effects were observed if damping material was present in the nodal regions.

Investigations into beams with uniform and partial unconstrained damping layer coverage were performed by Roy and Ganesan in 1996 [19]. The effect of damping layer distribution

on the dynamic stresses and displacements were studied with point harmonic excitations at the first three natural frequencies. Displacement amplitudes, stresses and system loss factors produced by a uniform ULD treatment were compared to those produced by several partial coverage configurations with the same volume of applied damping material. Three end condition cases were considered. Beams were either clamped at both ends, simply supported at both ends, or had one end clamped and the other free. For all cases, it was determined that the greatest performance increase was gained when the damping material was concentrated at the least number of locations rather than being evenly distributed, as the increased damping material thickness produced greater extensional strains and hence increased damping. For the case of clamping at both ends it was found that the greatest damping increase and displacement reduction was achieved with material applied only close to the ends. This was consistent for each of the first three bending modes. The authors concluded that this was due to the restraint of the slope at the ends producing greater strains in the damping layer. The added mass was also positioned at the point of minimum oscillation which reduced the kinetic energy of the system. For the simply supported configuration, optimal damping material placement was dependent on the resonant mode. The best performance for the first and third modes was found to be with the damping material concentrated on the middle of the beam, while the best performance for the second mode was found to be with the damping material concentrated between the ends and the centre of the beam. This result was consistent with the conclusions from Parthasarathy et al. [18] regarding placement of the UDL treatment on antinodal points. With one end clamped and the other free, stresses were reduced by up to 97% in the fundamental mode when the damping material was concentrated at the clamped end of the beam. Conversely, stresses were increased by up to 26 times in the fundamental mode if the damping material was located in the middle of the beam. In the second mode the best response was found to be with the material in the middle of the beam. This positioning was obviously unsuitable due to the increase in stress in the first mode. The next best response was with damping

material at the clamped end of the beam. The best response produced in the third mode was achieved with the damping material concentrated between the middle and the free end of the beam. This location coincided with the antinodal point of the third mode closest to the free end of the beam. From these results it was demonstrated that the configuration adopted for a partial damping layer treatment to control the vibration and stresses on a beam depend on both the boundary conditions of the beam and the mode in which the beam is vibrating.

A continuum finite element method was used by Lumsdaine and Scott to further investigate shape optimisation of unconstrained layers on beams and plates [20]. Results were obtained from realistic (frequency dependent) viscoelastic material data. The authors determined that for a given amount of damping material, the system loss factor could be improved by an order of magnitude in most cases using optimised placement of the material. They also showed that peak displacement could be reduced by as much as 98%. Substantial improvements were observed for many different structures and boundary conditions. In their work, shape optimisation was also performed for a wide range of damping layer volumes. The optimisation process showed great robustness, with the optimised layer achieving significantly greater damping effectiveness than the uniform damping layer in all cases. Both 'thick' and 'thin' beams were considered and it was found that for the thick beam the amount of improvement peaked as damping material volume reached 30% of the base layer volume. It was also shown that minimising the displacement at one given frequency near resonance, rather than at the resonant frequency, could result in a significantly worse global response if care was not taken. Additionally, only minor differences in the optimisation results were observed when frequency independent viscoelastic properties were used.

Theoretical predictions of the effect an added damping layer had on stresses in an aluminium alloy were performed by Bespalova and Kitaigorodskii [21]. It was found that

stresses within the two layer plate could be effectively reduced by dissipating energy in the flexible layer. The stress reduction was attributed to the substantial differences in the displacement behaviours of the two layers. Normal displacements were found to dominate in the load-bearing layer, while displacements in the soft damping layer were predominantly plane displacements. A 35 dB reduction in cumulative energy across the resonant frequencies was found possible with the materials considered in the study.

In 2003 Rao produced a summary of the applications of viscoelastic damping in the automotive and aerospace industries [22]. This work revealed that unconstrained treatments were predominantly used on motor vehicle floor panels and wheel bays, and were applied robotically as a spray to thicknesses between 1 and 3mm before being cured in an oven.

Parametric optimisation of damping layer thickness was performed using a genetic algorithm by Serabatir et al. in 2007 [23]. This optimisation method was used in conjunction with commercially available solid modelling and finite element software. The viscoelastic material properties were determined according to ASTM E756. Optimal damping solutions were validated experimentally for cantilever beam and L-shaped plate configurations using frequency response functions. The results indicated that the optimisation method used worked well and had potential for application to more complex geometries.

A brief assessment of unconstrained layer damping was included in work performed by Mead in 2007 [24]. This study was focused on the measurements of loss factors for beams and plates. In this work, Mead summarised that loss factors of beams treated with unconstrained layer damping could be determined from the decay rate of a flexural wave travelling along the beam.

An investigation into the effect of thick unconstrained layer damping treatments on beams was performed by Cortés and Elejabarrieta [25]. The authors derived a finite element model for homogenised flexural stiffness using Reddy-Bickford's theory of quadratic shear for thick beams. The model developed included the effects of shear strain which was absent from the model developed by Oberst and Frankenfeld [3]. The developed model and Oberst and Frankenfeld's model were compared to a 2D finite element model which considered extensional and shear strains, and longitudinal, transverse and rotational inertias. Thickness ratios of 1, 3 and 5 were used in each case. A fractional derivative model was used to characterise the viscoelastic material in order to account for variation of complex modulus with frequency. Also, to avoid the frequency dependence of the stiffness matrices, the authors used an iterative method they had previously developed to extract the eigenvalues and eigenvectors. For each of the models, the frequency response to a harmonic input force was calculated by superposition if modal contribution functions. The comparison of the two 1D models to the 2D model showed that the Oberst and Frankenfeld's model overdamped the amplitude of the resonant peaks for thickness ratios of 3 and 5, whereas the thick beam model did not significantly diverge from those of the 2D model for all thickness ratios studied. The authors concluded that the thick beam model provided sufficient accuracy to reproduce the mechanical behaviour of beams damped with a thick unconstrained damping layer and was suitable for practical applications.

Two estimation methods for determining structural loss factor in a cantilever beam were evaluated by Rak et al. [26]. The two methods, developed by Berthaut et al. [27] and McDaniel et al. [28, 29], were evaluated by comparing the produced loss factor values with those obtained experimentally by the Oberst beam method [3]. Experimental data showed that the wave field used in Berthaut's Inhomogeneous Wave Correlation method was incorrect and hence the values obtained were not reliable. Conversely, the experimental results indicated that McDaniel's method provided reliable estimation of loss factors over discrete

frequencies.

In 2010 Xiao and Sheng published a method for determining the dynamic characteristics of a steel beam with tapered damping layer treatment [30]. This so called Differential Transformation Method (DTM) was used to solve the Euler-Bernoulli beam model based on the equation of motion for a tapered composite beam. The results of the DTM were compared to those produced in ANSYS and it was found that the relative errors between these two methods were small. Furthermore, when the dimensions of the damped beam were large, the DTM was found to require far less computational time than ANSYS to determine the response.

1.2.2 Constrained Layer Damping

Constrained layer damping involves a viscoelastic damping layer bonded to a vibrating substrate and constrained by a stiff upper layer, thus making a three (or more) layer system.

The first research into constrained layer damping treatments was published in 1959 by Kerwin [4]. His work was initiated by the need for analysis of damping tape which was comprised of a viscoelastic material backed by a constraining foil layer that was being utilised in aircraft at the time. In this research he developed a theory for calculation of constrained layer damping performance for simply supported or infinite length beams assuming that shear deformation was the primary damping mechanism. Comparisons were made for variations in frequency, temperature, damping-application geometry and substrate thickness. Experimental data showed good correlation within certain limits of the variables involved and it was concluded that the assumption of a predominant shear mechanism was correct. Kerwin found that the theory couldn't accurately be applied when the constraining layer thickness approached the substrate thickness. It was also observed that the theory overpredicted the system loss factor for some temperature and frequency ranges, when the

square of the damping layer loss factor was very much less than 1 and a dimensionless shear parameter, g, became larger than 1. However, the simplified relation used in his calculations was adequate over a moderate frequency and temperature range to predict values of loss factor as a function of frequency, temperature, damping layer thickness and constraining layer thickness.

The use of multiple constraining layers was investigated by Ungar et al. [31]. They explored the effect of applying several layers of damping tape to an isotropic base beam. It was found that additional tape layers resulted in improved damping at all frequencies. The increase could be considered to be negligible at 'high' frequencies, but the increase at 'low' frequencies could be significant, especially for large numbers of tape layers. It was also demonstrated that it was essentially only the sum of all constraining layer thicknesses that determined the damping characteristics of a damping tape treatment with a given adhesive (damping) material. The number of tapes used and their relative thicknesses only had a small effect. In other words, a single layer of damping tape with a thicker foil was equivalent to several layers of tape with approximately the same weight.

These three authors also extended Kerwins earlier theoretical work to the case of three layered plates [7]. This comprehensive study established that the shear damping mechanism present in CLD treatments was more effective than the extensional damping mechanism of ULD treatments. The theoretical analysis, referred to as the Ross-Kerwin-Ungar (RKU) model, could be used to obtain the amount of damping for treatments involving shear and/or extensional damping in three-layer composite plates. The RKU model could also be extended to cases of multiple damping layers. It was determined that the performance of shear damping treatments was dependant on the loss factor of the damping layer material, how close the dimensionless shear parameter g was to its optimum value, and the magnitude of a dimensionless geometric parameter. The latter was found to be primarily

dependant on the extensional stiffness of the constraining layer, but could also be increased in several ways. One such way was to use a thick damping layer as this could significantly increase the damping performance due to the increased separation between the foil and plate. Treatments based on this idea have been called 'spacer-layer' treatments. Increasing the geometric parameter could also be achieved by using a thick constraining layer of soft light material such as plastic or foamed metal.

The effect of end constraints on beams with CLD treatment was examined by DiTaranto [32]. It was proposed that the damping of laminated beams was independent of non-dissipative boundary conditions and depended solely on the geometry of a beam's cross section and the properties of the damping material. Three and five layer beams were tested with free-free, free-free with shear bolts at each end, and fixed-fixed end conditions. A nine layer beam using different damping material than the other cases was also examined for the free-free case. The results showed good correlation between experimental values and the proposed theory.

DiTaranto also published a comprehensive investigation into the vibratory characteristics, natural frequencies and loss factors of a finite-length laminated beam [33]. In this work he derived an auxiliary equation to account for the effect of viscoelastic layers, and using this in conjunction with the ordinary bending equations encountered for homogeneous beams, was able to solve static and dynamic problems for laminated beams in the same manner as homogeneous beams. This resulted in a 6th order, complex, homogeneous differential equation. Solutions to this equation, subject to satisfying the boundary conditions, yielded the natural frequencies and associated system loss factors. This theory improved on Kerwin's work [4] which was limited by the condition that the beam was either simply supported and vibrating at a natural frequency, or was infinitely long so that the end effects could be neglected. DiTaranto concluded that the relationship between loss factor and frequency

was independent of non-dissipative boundary conditions but that other boundary conditions influenced the natural frequencies and hence system loss factor. The results of the freely-vibrating beam allowed the complete solution for the natural frequency and loss factor to be obtained for finite beams with non-dissipative boundary conditions.

Forced vibration of a three layer damped sandwich beam with arbitrary boundary conditions was examined by Mead and Markus [34]. They derived a 6th order differential equation of motion in terms of transverse displacement for a three-layer sandwich beam. Using this, mathematical expressions in terms of the transverse displacement were found for a variety of beam boundary conditions. Solutions of the differential equation using DiTarantos method [33] were shown to yield a special class of complex forced modes of vibration which were completely uncoupled. These modes were found to exist for beams with any boundary conditions but could only exist on their own in the presence of an externally applied harmonic transverse loading which was proportional to the local inertial loading of the mode. Use of these modes in the analysis of free vibration led to a simple series form of the solution.

Plunkett and Lee investigated cutting the constraining layer into appropriate lengths in order to achieve greater damping performance [35]. They noted that if the constraining layer was long, shear was greatest at the ends but very small away from them. Hence, a collection of small segments would give greater shear over the whole surface. The developed model was also suitable for the case of multiple segmented layers. Simplification of modelling multiple segmented layers was achieved by replacing a typical repetitive volume by an equivalent homogeneous material with the same force-deformation relationship. The longitudinal elastic modulus and transverse shear modulus were found for this equivalent material in terms the dimensions and material properties of the constituent layers of the nonhomogeneous material. The equivalent analysis was found to agree with experiment

and gave valid results if the layered system had dimensions which were large in comparison with those of an element of the constraining layer, and if the strain in the basic structure didn't vary rapidly with length. It was found that for the case of optimum element length of the constraining layer, energy dissipation depended primarily on the loss factor of the viscoelastic material and the stiffness of the constraining layer, and only indirectly on the shear modulus of the viscoelastic layer.

Mead and Markus [36] used an iterative numerical method to solve the differential equation for damped normal modes of a three-layer sandwich beam with clamped ends. This method was used to determine the characteristic equation for the resonant frequency, loss factors and modal roots. By examining the six modal roots it was observed that all roots had real and imaginary components. This implied that beams with different boundary conditions had different loss factor/resonant frequency relationships. They determined that the loss factor of an encastré damped sandwich beam varied with the shear parameter, geometric parameter and core loss factor in the same general way as that of a simply-supported beam. However, the maximum loss factor for the fundamental mode occurred at values of the shear parameter which were about four times the corresponding values for a simply supported beam. Mathematically, this was attributed to the existence of the imaginary parts of the roots which had previously been assumed to be real. Approximate values of the resonant frequencies for a given fully clamped sandwich beam could be satisfactorily estimated by using the computed values of the real part of the root only. Using the same method to calculate the loss factor at a fundamental mode resulted in an underestimate by a factor of about two at low frequencies, and an overestimate of about two at high frequencies. However, the maximum value of the loss factor was found very accurately using this approximate method.

Grootenhuis investigated a variety of multi-layer damping configurations for beams [37]. He determined that symmetric sandwich constructions could produce very high loss factors

but only over a limited frequency range unless the viscoelastic material had a shear modulus that varied linearly with frequency. It was observed that improved damping over a much wider frequency range could be achieved with multilayer asymmetric constructions with one damping layer much stiffer than the others. It was also noted that a multi-core sandwich (four-layers) could be as effective as a five-layer beam, and that unconstrained layer treatments could compete with sandwich constructions only when the ULD material was very stiff and could be applied in a thickness several times greater than the base layer. Grootenhuis stated that edge damping was useful for interrupting vibration transmission paths and controlling forced, non-resonant vibrations of beams and plates. It was concluded that viscoelastic damping materials should have a high loss factor and low to medium stiffness for edge damping and sandwich constructions, and should have loss factors and stiffnesses as high as possible for unconstrained layer treatments.

In 1979, Jones et al. established empirically that the behaviour of a multiple layer constrained damping treatment on a beam could be approximately represented in terms of an equivalent free layer damping treatment [38]. They found, to some degree of approximation, that the complex modulus of this equivalent treatment was only dependant on four parameters: the loss factor of the viscoelastic adhesive, the Young's modulus of the constraining layers, the ratio of the constraining layer thickness to the adhesive thickness and a dimensionless shear parameter, and did not depend on the beam to which the treatment was added. This provided a useful method for reducing the complex problem of predicting the effect of a multilayer treatment to the relatively simple problem of predicting the effect of a free layer.

Rao used an iterative approach to produce the exact solutions to the basic governing equations of sandwich beams for a variety of boundary conditions [39]. He presented the resulting frequency and loss factors of important modes in a series of graphs and formulae useful for

design purposes.

In 1982, Mead [40] compared the theories of flexural vibration of damped, three-layer sandwich beams that had been presented by Yan and Dowell [41], DiTaranto [33] and Mead and Markus [34]. By comparing the flexural wave speeds and loss factors computed from each theory, he concluded that the DiTaranto and Mead and Markus equations yielded reliable values provided the flexural wavelength was greater than about four face-plate thicknesses, and the Yan and Dowell equations yielded reliable values only at much greater wavelengths or when the central layer in the sandwich was very thick.

Johnson and Kienholz described a method for finite element modelling (FEM) of three-layer laminates containing a viscoelastic layer [42]. They estimated the modal damping ratios from undamped normal mode results and material loss factors, as first suggested by Ungar [43], by means of the modal strain energy method. The method was demonstrated on simple problems for three-layer beams, rings and plates. Good agreement was obtained with closed-form solutions for natural frequencies and modal loss factors.

Another finite element model for dynamic analysis of laminated beams treated with a constrained viscoelastic layer was presented by Sun, Sankar and V.S. Rao [44]. This model used a direct frequency response technique for analytical estimation of the damping and beam tip displacement. The authors found that for each mode of vibration, there existed a length, location and a thickness of damping tape, for a given thickness of the constraining layer, for which overall system damping was maximised.

Three theories for analysis of vibration and damping characteristics of cylindrical shells with CLD treatments were evaluated using the finite element method by Ramesh and Ganesan [45]. These theories were the discrete layer theory (DLT) [46], Wilkins's theory (WT)

[47] and Khatua's theory (KT) [48]. The analysis showed that at the lower circumferential modes and at a high shear parameter, extensional energy in the core was higher than shear energy so for accurate estimation of loss factor, extensional effects needed to be included in the core. This was included only in the DLT but could be added to the case of WT. KT gave good results for thin shells with a low shear parameter and mass but produced incorrect predictions for thicker shells with orthotropic facings. It was concluded that DLT or WT with extensional effects included were best suited to this class of problems.

Yu et al. examined the damping efficiency of the coating structure, attempting to strike a balance between damping capacity and overall stiffness [49]. Their investigation was based on the Reuss model [50] and the Hashin-Shtrickman [51] equation. The Reuss model used a method similar to that used by Jones et al. [38] to reduce a multilayer system to a simple substrate and coating configuration. Their findings showed an optimum thickness of the coating structure that maximised the product of storage modulus and loss factor. Increased modulus differences between the coating and substrate were found to increase the damping and strength of the coating structure.

1.2.3 Composite Damping

Composite damping treatments are a broad field and it is appropriate to define how the term 'composite' has been considered in this work.

Typically, composites are classified as a material that is comprised of more than one constituent material. Under this definition, both unconstrained and constrained layer treatments could be considered composites as they form a new material when combined with the substrate. However for the purposes of this investigation, it is convenient to define composite materials as those with more complex constructions, including the likes of fibre reinforcement and particle inclusions. As a general rule, any damping systems or treatments that aren't a simple metal-viscoelastic material combination will be classified as composite

damping materials. It is also important to note the distinction between composite materials that have been designed to increase their inherent damping capacity and those that have been designed as damping treatments. The latter are the focus of this section but the differences between these two areas are often indistinct so some crossover is to be expected.

Composite constructions commonly found in marine structures are sandwich panels. These arrangements are laminar, with a lightweight core material sandwiched by stiff face sheets which are typically layered fibre reinforced polymer. The result of these constructions are panels which have high stiffness to weight ratios, making them useful in marine application. Damping can be added to these systems with traditional ULD and CLD surface treatments, however one of the advantages of composite constructions is the ability to design the required material properties into the structure through constituent material selection and arrangement.

The damping behaviour of laminar structures comprised of viscoelastic material constrained between plies of fibre reinforced polymer composites were reviewed by Natarajan and Lewis in 1976 [52]. Carbon fibre reinforced polymer (CFRP) and glass fibre reinforced polymer (GRP) laminates were considered. Laminate configurations[1] of $[0]_8$, $[(0/90)_2]_S$, $[0/\pm 45/90]_S$, and $[90]_8$ were used in beam geometries. Where $[\theta_1/\pm\theta_2/\theta_3]_S$ is a laminate with fibre layer orientation θ stacked in the order: $\theta_1, +\theta_2, -\theta_2, \theta_3, \theta_3, -\theta_2, +\theta_2, \theta_1$. Experimental results indicated that when considering the CFRP and GRP layers alone, the greatest damping was found with the $[90]_n$ laminate arrangements. The $[0]_n$ arrangements were found to produce the lowest damping values. The authors suggested that this was due to the damping provided by the matrix material, which would have the greatest effect when the bending waves were perpendicular to the fibre direction. No such clear distinction between laminate configurations was apparent when the constrained viscoelastic layer beams

[1] Using laminate stacking notation, see [53].

were considered. The authors indicated that this was due to the uncertainties in assignment of mode numbers to the measured loss factors. The damping values obtained for the composite constrained layer laminates were observed to be similar to those of conventional steel CLD treatments, however, the composite laminates were lightweight, corrosion resistant, and could be designed for anisotropic damping and modulus characteristics. Loss factors obtained for the CLD composites were generally higher than those predicted by constrained layer laminate theories. The deviations between theoretical and experimental results increased with increasing loss factor contributions from the composite constraining plies.

The effect of fibre angle was explored in more detail by Mukhopadhyay and Kingsbury [54] in 1976. This work investigated the damping of simply supported sandwich plates with viscoelastic cores and asymmetric orthotropic facings in the fundamental mode of vibration. The influence of the facing anisotropy on the damping of harmonic transient loads was modelled analytically. The upper and lower facings were set with unidirectional fibre angles of θ and $-\theta$ respectively to produce the anisotropy about the core. This facing anisotropy produced coupling between the normal and shear effects (stress-coupling). It was found that maximum lateral deflection and total strain energy of the core were functions of θ, with maximum values obtained with values of θ in the range of approximately 30° to 45°. Maximum loss factor values for the composite plates were found to occur at values of $\theta = 0^\circ$.

The use of gradient interpenetrating polymer networks (IPNs) for damping materials was studied by Lipatov et al. [55, 56]. Gradient IPNs were defined as a mixture of network polymers in which the concentration of the components, and hence the material properties, varied over the cross section of the specimen. The authors found that there was significant change in the properties of the gradient system at different depths from the surface and that the resulting system had a broadened glass transition range, producing greater damping over a wider temperature range but reducing the maximum damping achieved.

Barrett re-examined the concept of anisotropic unidirectional fibre layers surrounding a core damping material for axially loaded cylinders [57] and flexurally loaded semi-infinite simply supported sandwich panels [58]. This work aimed to produce a new model which could account for addition of more compliant layers between the stiff face sheets and the damping material. The model developed by Mukhopadhyay and Kingsbury [54] was not used as the results produced by this analytical model were considered to be based on displacement fields that were too simple to fully categorise the dynamic response of the composite material. Panel stacking arrangements were of the form $[0_n/\theta_m/d/-\theta_m/0_n]$, where d was the damping layer and the θ_m and $-\theta_m$ layers were the compliant layers. Values of θ between 0° and 90° were used. It was concluded that these compliant interface layers could be used to increase the efficiency of the damping designs as they created a mechanism to increase the rate of shearing in the damping layer.

Olcott continued this line of research, exploring the stress-coupling effects produced when damping layers were co-cured with segmented stiffness layers to produce 'zig-zag' fibre patterns [59, 60]. Under axial loading, multiple areas of high shear strain would occur within the viscoelastic core at the points where the fibres changed from 'zig' to 'zag', as the fibres would attempt to align with the direction of applied load. It was concluded that significant increases in vibration damping properties could be achieved with only minor stiffness penalties. Various aspects surrounding modelling, experimentation and fabrication of the 'zig-zag' arrangement were subsequently explored by Trego et al. [61, 62].

In 1993, Alberts et al. patented a fibre enhanced viscoelastic damping material [63]. This damping treatment was comprised of multiple layers of uniformly spaced, aligned, short fibre segments surrounded by a viscoelastic matrix. The material was designed to combine the effects of a multiple constrained layer treatment with the benefits of optimal constrained layer segment length [35], while reducing overall weight through the use of fibres rather than

metal constraining layers.

Alberts and Xia went on to produce a micromechanical model for a fibre enhanced viscoelastic damping polymer that took into account fibre segment length and relative motion between fibres [5]. From this, they developed closed form expressions for the effective storage and loss properties of the damping material and an optimal relation between design parameters such as the length, diameter, spacing, and Youngs modulus of fibres and the shear modulus of the viscoelastic matrix. The theoretical results were compared to a finite element model with good agreement. Comparing the composite treatment with a conventional constrained layer treatment showed that the enhanced polymer provided significant improvement in the damping performance.

The stress-coupling fibre geometry initially studied by Olcott [59] was developed further by Pratt et al. [64] with the use of continuous sinusoidal fibre patterns in the constraining layers. This was a logical step from a manufacturing perspective, as production of continuous woven fibres provided a simpler production method than the segmented fibre arrangement. It was found that the sinusoidal fibres produced higher stiffness values than the segmented design under axial loading. Greater damping values were also possible and the trends observed indicated that an optimal fibre wavelength existed for different shear moduli of the viscoelastic core. Further studies were made on this material and particularly on its use in geometries commonly found in aerospace structures [65–67].

A method previously developed for determination of elastic and damping parameters of orthotropic plates was applied to laminated composite plates by Talbot and Woodhouse [68]. It was verified that thin-plate bending theory could be used to predict the low frequency vibrational behaviour of free-edged carbon fibre reinforced polymer (CFRP) laminates and that laminate theory was capable of modelling elastic behaviour with sufficient accuracy to

enable frequency and mode shape predictions to be made. Estimates of damping constants were found to be less accurate. It was also demonstrated that the elastic and damping properties of the plies of a laminate could be deduced from measurements on the complete laminate, using an inverse approach.

The optimal design of viscoelastic composite microstructures was explored by Yi et al. with the aim of improving stiffness and damping characteristics [69]. This work presented an inverse homogenisation approach as a topology optimisation problem of two phase composites. An artificial two phase material model with repeating microstructure was used to simplify the problem. Numerical examples showed that improvements in the damping characteristics could be achieved by designing topological structures of the composites. Particularly, the optimisation of the two materials investigated resulted in increased damping over a wider range of frequencies but a reduced maximum damping level. It was also found that 'mechanism-like' and 'wavy' structures had a crucial role in improving damping by providing sufficient deformation in the viscoelastic phase while maintaining a desired level of stiffness.

Jung and Aref examined the feasibility of combining honeycomb and solid viscoelastic materials for structural damping purposes [6]. The proposed treatment was comprised of repeating sections of polymer honeycomb structure and solid viscoelastic material constrained between fibre reinforced polymer (FRP) laminates subject to in-plane shear. The authors established the relationship between geometric parameters, including area and thickness, and frequency using experimental and numerical results. The system was found to produce greater energy dissipation capacity than other damping cases with the added advantage of damping and stiffness customisation through alteration of viscoelastic and honeycomb proportions.

A comprehensive review of vibration damping in composite sandwich structures was performed by Zhuang and Crocker in 2005 [70]. Nine major conclusions were drawn from this review.

1. Sixth-order models were found to produce more accurate results than fourth-order models.

2. From a theoretical standpoint, the modal strain energy (MSE) method is better than the Ross-Ungar-Kerwin model as it includes damping in all elements. However, this method requires preliminary information on the damping in all layers.

3. Finite element models are very effective but some approximations have to be made because some materials are hard to model.

4. The Ross-Ungar-Kerwin model indicates that the loss factor has a maximum value when a three-layer sandwich structure is symmetric about the neutral axis.

5. If the constraining layer is thinner than the damping layer, then the system damping has a maximum value when the shear modulus of the core has an optimal value in the intermediate range.

6. The significance of higher order effects varies for different configurations of sandwich structures.

7. Damping in different joints varies. For bonded joints, if the viscoelastic layer is much softer than the constraining layer, the total loss factor varies little with the shear modulus of the damping layer. For bolted joints, as the bolt diameter decreases, the damping increases.

8. Most multi-layer structures (e.g. four or five layer sandwiches) normally possess more damping than three-layer sandwich structures. They also have a wider high damping range in terms of the core shear modulus.

9. A spacer with a higher shear modulus than the damping layer can be inserted beneath the damping layer to increase the shear stress in the damping layer and, thus, to increase the energy dissipation in the whole structure.

An iterative modal stain energy approach was used by Zhang and Chen [71] in a three-dimensional finite element model to account for the frequency dependence of the viscoelastic material properties of a damped composite beam. This work also accounted for the damping contributions of the fibre reinforced layers within the model. Various damping layer locations and stacking arrangements were considered. Compliant layers similar to those used in [57] were also studied with the notable difference of being symmetric rather than asymmetric about the damping layer. It was concluded that the layup sequence, the mode of vibration, and the ply angle of compliant layers within the laminate influenced the modal frequencies and loss factors. Of the lay-up configurations considered, it was found that an appropriate number of compliant layers and an increasing compliant ply angle were beneficial in increasing the flexural modal loss factor. The effect of the compliant layers was also found to be more significant at higher flexural modes.

A unit cell based finite element procedure for determining the loss factor response of multiphase composite materials was proposed by Patel et al. [72]. It was demonstrated that with careful selection of the viscoelastic constituents and their morphology, a flat loss factor response over a wide frequency range could be obtained. Multiple layers with different relaxation times were particularly useful for modulating the damping response.

The effect of adding granular viscoelastic particles to cavities in aluminium and sandwich beams with regard to the system damping performance was investigated by Park and Palumbo [73]. The comparison between measured and predicted values suggested that the acoustic-structure interaction between the frame of the lightweight particles and the structure increased the vibration damping. It was found that considerable vibration reduction

was achieved with the particle damping. Results from testing different types of particles indicated that the frequency at which maximum damping occurred and the amount of damping obtained depended on properties of the particles such as size, mass and type of polymer. This indicated that particles could be designed to target vibration reduction at particular frequencies. The Rayleigh-Ritz method was found to be an effective tool for this evaluation.

An easily implemented method to measure relevant elastic and damping properties of sandwich structure constituent materials, well suited to those with a heterogeneous core (e.g honeycomb), was proposed by Rebillat and Boutillon [74]. The method enabled out-of-plane measurement of complex moduli and produced reliable and repeatable results. The method did not require the full field measurements needed by similar techniques, making it simpler to implement and faster to execute. As the proposed method did not require complex experimental apparatus, it was found to be well suited to the in-line control of the production of sandwich materials.

From the brief overview of using viscoelastic materials to increase damping performance of metallic and composite constructions, it is clear that the field is very broad. Many materials, modelling techniques and test methods are available for exploration into enhancing the structural vibration damping properties of structures used in the marine industry.

1.3 Contribution

The work reported in this thesis falls into two areas:

1. Measurement and application of ULD treatements to metal panels (Chapter 2 and Chapter 3)

2. Modelling, experimentation and implementation of a composite damping arrangement for composite sandwich constructions (Chapter 4 and Chapter 5)

In the first area, the principles behind viscoelasticity and comparison of two measurement techniques to determine material damping properties provide useful insight. However, the main contribution is an investigation into application of ULD treatments to metal panels. Previous studies identified the effect of UDL thickness, partial coverage of a substrate, and even optimising the damping material distribution for a range of plate geometries. However no studies have been performed to compare the relative influence of variables or their interactions on the system damping performance. The relative influence of several key variables, namely substrate material, damping layer thickness, ambient temperature, panel geometry and boundary conditions were investigated experimentally using Design of Experiments methodology.

In the second area, a finite element model was developed to study the modal damping behaviour of a composite damping arrangement that expands upon the stress-coupled designs of Olcott [59], Trego et al. [61], Pratt et al. [64], and others [65, 66]. These previous designs showed that increased damping performance was achievable using deliberate asymmetry and changing fibre angles in composite layers surrounding a viscoelastic core. The concept was developed from 'zig-zag' patterns to continuous sine wave patterns and applied to a number of composite geometries. In some of the later work on the sine wave fibre patterns, it was identified that the pattern wavelength influenced the frequency at which maximum damping occurred and the maximum fibre angle influenced the maximum damping values achieved [75, 76]. In all of the studies involving patterned fibre layers, only constant sinusoid patterns were studied. The second area explores the modal damping behaviour and trends of more complicated fibre patterns using a finite element model developed in MATLAB. The model accounts for the damping provided by the composite layers and the frequency dependence of both the viscoelastic layer material properties and the composite layer material properties. The model is validated through experiment and a study is performed on implementation of these complex patterned fibre CLD treatments to

typical composite sandwich geometries found in marine structures.

Chapter 2

Measurement of Viscoelastic Damping Performance

2.1 Introduction

When investigating or designing damping treatments, it is important to understand the damping mechanisms and relevant material properties involved in order to obtain the desired performance from the damping system. This chapter details the dynamic behaviour of viscoelastic materials and compares two experimental methods used to determine the dynamic mechanical properties of viscoelastic damping materials.

2.2 Viscoelasticity

2.2.1 Basic Phenomena

Viscoelastic materials display characteristics of both elastic and viscous responses. Under cyclical loading elastic materials deform instantaneously, or in other words, the stress and strain are in phase. This behaviour is described by Hooke's law of linear elasticity, assuming

small strains, where strain is proportional to stress:

$$\sigma = E\varepsilon \ . \tag{2.1}$$

In viscous materials, shear stress obeys $\sigma = \mu\frac{d\varepsilon}{dt}$ and strain lags stress by 90°. Viscoelastic materials fall between these two behaviours, with the strain lagging the stress by phase angle δ, as seen in figure 2.1 (sourced from [77]), where $0° < \delta < 90°$.

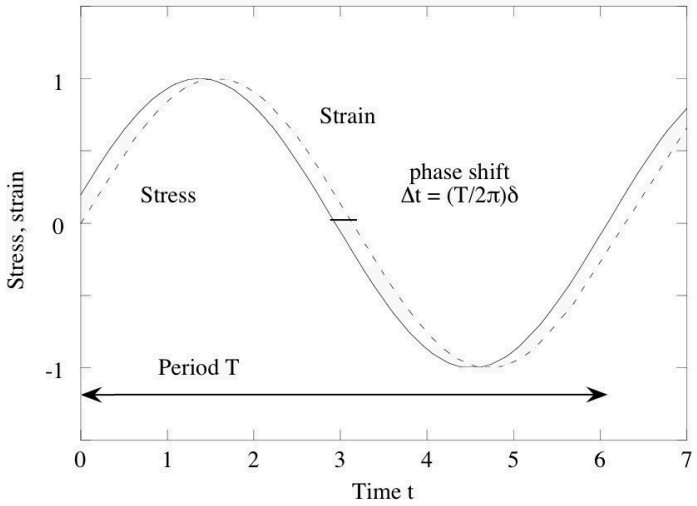

Figure 2.1: Stress-strain phase shift ([77])

As a consequence, the Young's modulus of the material becomes complex:

$$E^* = E' + iE'' \ . \tag{2.2}$$

This behaviour is the result of mechanical energy being transformed into thermal energy through each cycle of deformation. The tangled polymer molecules within the viscoelastic material produce heat during the straining and recovery of the molecular structure as the polymer chains rub against one another, stretch, and recover.

In Equation 2.2 the real component of the complex Young's modulus is termed the storage modulus (E') and represents the energy stored in the material per cycle. The imaginary component is termed the loss modulus (E'') and represents the energy dissipated per cy-

cle. The ratio of these values provides a dimensionless measure of a material's damping performance. This value is called damping loss factor (η) or loss tangent ($\tan\delta$)

$$\eta = \tan\delta = \frac{E''}{E'} \ . \tag{2.3}$$

Using this ratio, Equation 2.2 can be re-written:

$$E^* = E'(1 + i\eta) \ . \tag{2.4}$$

2.2.2 Simple Models

Viscous Damping

A mechanical analogy for viscoelastic behaviour is a spring-damper system. Figure 2.2 below shows three mechanical models for viscoelastic behaviour. These models fall under the category of viscous damping as the damping present in the system is modelled with viscous dashpots.

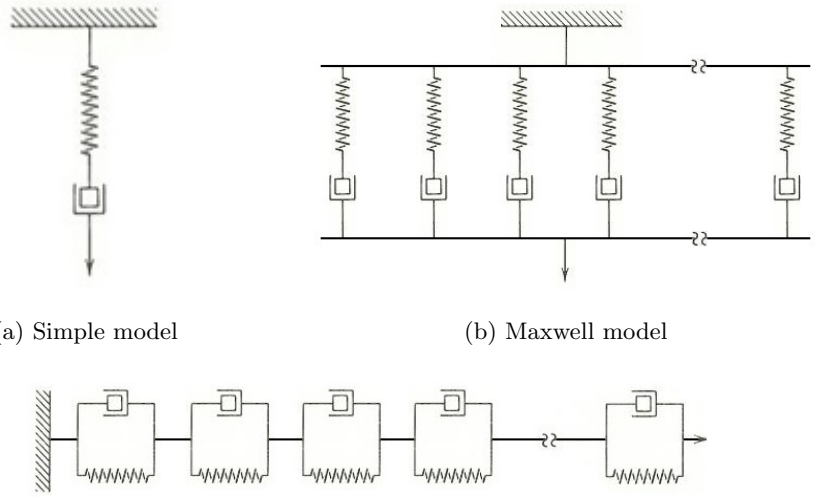

(a) Simple model

(b) Maxwell model

(c) Voigt model

Figure 2.2: Mechanical analogies for viscoelasticity

The equation of motion for the simple single degree of freedom system shown in Figure 2.3

undergoing steady state harmonic excitation ($F(t) = F\cos\omega t$) is defined

$$m\ddot{x}(t) + c\dot{x}(t) + kx(t) = F\cos\omega t\ , \tag{2.5}$$

where

m = mass [kg] ,

c = damping [Ns.m^{-1}] ,

k = stiffness [N.m^{-1}] ,

F = harmonic force amplitude [N] ,

ω = forcing frequency [rad.s^{-1}] .

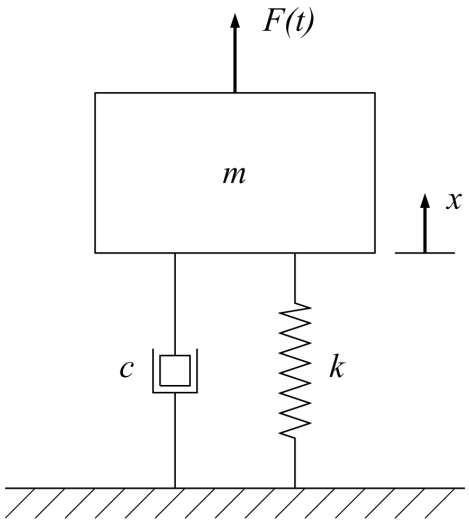

Figure 2.3: Single degree of freedom system with viscous damping

The complete solution to this equation is the sum of the complimentary solution (transient behaviour) and the particular solution (steady state behaviour). The complimentary solution is defined

$$x_c = e^{-at}(C_1\sin\omega_{_D}t + C_2\cos\omega_{_D}t)\ , \tag{2.6}$$

where

$$a = \frac{c}{2m} \tag{2.7}$$

and the damped natural frequency (ω_D) of the system is

$$\omega_{_D} = \sqrt{\frac{k}{m} - \left(\frac{c}{2m}\right)^2} \,. \tag{2.8}$$

The arbitrary constants C_1 and C_2 are obtained by substituting initial conditions into the complete solution of the equation. The particular solution x_p is any function $x(t)$ that satisfies Equation 2.5. A particular solution to this equation is

$$x_p = \frac{F\cos(\omega t - \varphi)}{\sqrt{(k - m\omega^2)^2 + \omega^2 c^2}} \,, \tag{2.9}$$

with

$$\varphi = \tan^{-1}\left(\frac{c\omega}{k - m\omega^2}\right) \,. \tag{2.10}$$

This gives the complete solution of Equation 2.5:

$$x = x_c + x_p = e^{-at}(C_1 \sin\omega_D t + C_2 \cos\omega_D t) + A_1\cos(\omega t - \varphi) \,, \tag{2.11}$$

with

$$A_1 = \frac{F}{\sqrt{(k - m\omega^2)^2 + \omega^2 c^2}} \,. \tag{2.12}$$

The simple viscous model is convenient as it provides the only known simple solution for transient response (the complimentary solution). However, in many situations, the steady state response (particular solution) is of primary concern. Hysteretic damping provides an alternative method for modelling viscoelastic damping behaviour of steady state vibrations.

Hysteretic Damping

Hysteretic damping utilises complex values of stiffness to model damping present in a system. The principal difference between viscous and hysteretic damping is that for a viscous system, the energy dissipated per cycle depends linearly on the frequency of oscillation, where for the hysteretic case it is independent of the frequency (static hysteresis). A simple hysteretic model is shown in Figure 2.4.

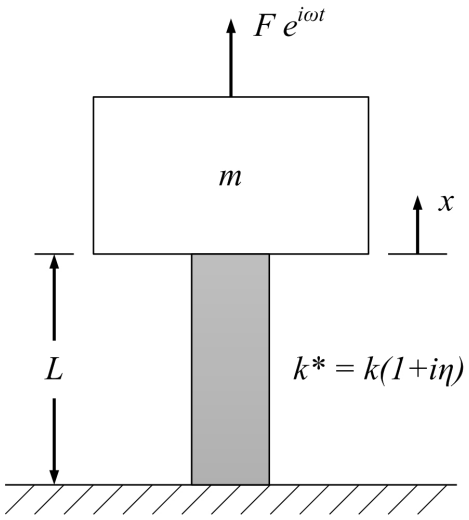

Figure 2.4: Single degree of freedom system with hysteretic damping

If the viscous damping coefficient in Equation 2.5 is set as $c = k\eta/\omega$, then the steady state solution shown in Equation 2.9 becomes

$$x = x_p = A_1 \cos(\omega t - \varphi) \,, \tag{2.13}$$

where

$$A_1 = \frac{F}{\sqrt{(k - m\omega^2)^2 + k^2\eta^2}} \tag{2.14}$$

and

$$\varphi = \tan^{-1}\left(\frac{k\eta}{k - m\omega^2}\right) \,. \tag{2.15}$$

Using Euler's convention: $e^{i\omega t - \varphi} = \cos(\omega t - \varphi) + i\sin(\omega t - \varphi)$, then

$$x = \mathrm{Re}\left[A_1 e^{i(\omega t - \varphi)}\right] \tag{2.16}$$

and

$$\dot{x} = \mathrm{Re}\left[A_1 i\omega e^{i(\omega t - \varphi)}\right] = i\omega x \,. \tag{2.17}$$

These values can be substituted into Equation 2.5 to give the equation of motion for the hysteretic damping system

$$m\ddot{x} + k(1 + i\eta)x = \mathrm{Re}(Fe^{i\omega t}) \,, \tag{2.18}$$

or

$$m\ddot{x} + k^* x = \mathrm{Re}(Fe^{i\omega t}) \,, \tag{2.19}$$

with $k^* = k(1 + i\eta)$ accounting for both stiffness and damping.

2.2.3 Effect of Temperature and Frequency

The behaviour of viscoelastic materials is dependant on temperature and excitation frequency. At low temperatures, the material is stiff and mobility between molecule chains is limited. Consequently, values of the loss factor are low as the storage modulus dominates the loss modulus. This is referred to as the glassy region. As temperature increases, the molecular mobility also increases resulting in greater values of loss factor. At high temperatures the material exhibits rubber-like properties and loss factor values decrease with increasing temperature as the polymer approaches its melting point.

The region between the glassy region and rubber-like region is designated the transition region. Within the transition region, values of loss factor increase with increasing temperature until the glass transition temperature (T_g) is reached, this is the point of maximum damping and further increases in temperature result in decreasing loss factor until the rubber-like region is reached. The generalised temperature dependant behaviour of viscoelastic materials is shown in Figure 2.5.

Excitation frequency produces a similar effect on the damping performance of viscoelastic materials. High frequency excitation produces behaviour similar to that at low temperatures while low frequency excitation mimics high temperature behaviour. This is illustrated in Figure 2.6.

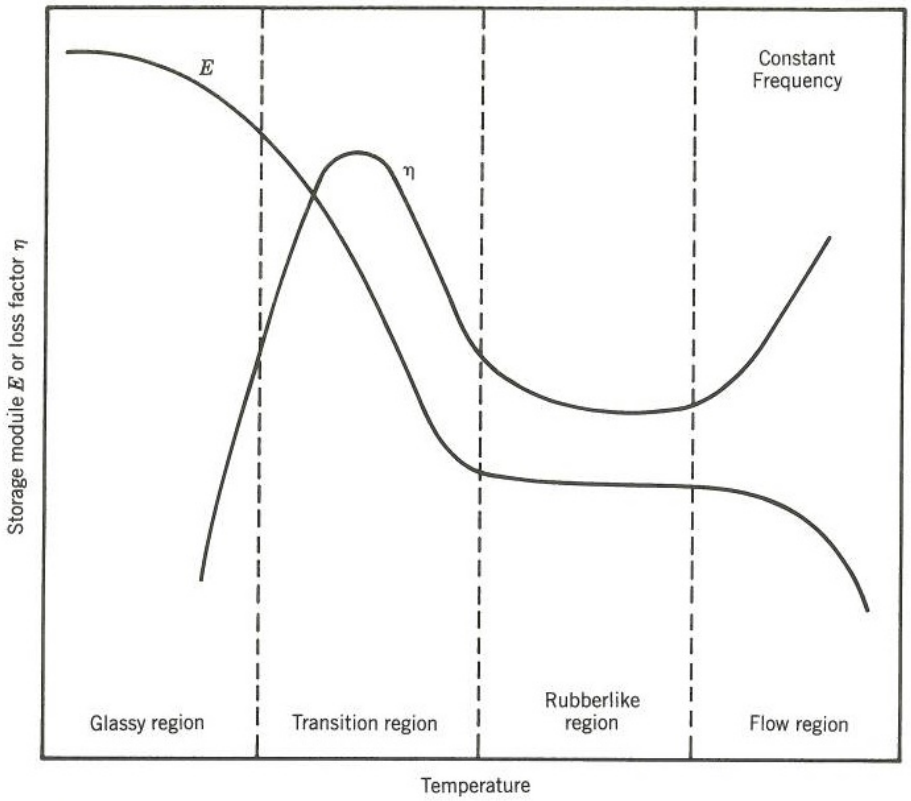

Figure 2.5: Variation of the storage modulus and loss factor with temperature (from [2])

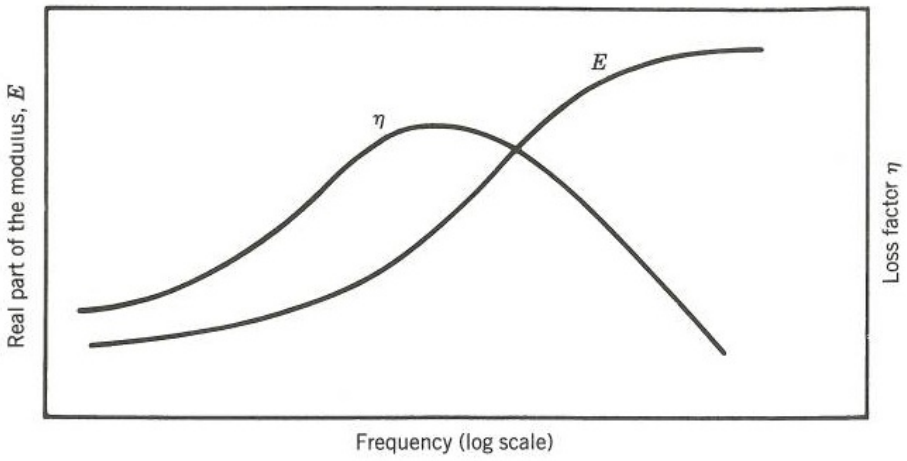

Figure 2.6: Variation of the storage modulus and loss factor with frequency (from [2])

2.3 Oberst Beam Method

It is necessary to measure the loss factor of damping materials over a range of temperatures and excitation frequencies in order to determine the conditions under which the material will provide the greatest damping performance. The Oberst beam technique [3] for determining loss factor is used in international standards ISO 6721-3 [78] and ASTM E756 [79]. Two test rigs were designed and constructed to perform measurements that met the requirements of these standards.

2.3.1 Measurement Principles

Loss factor is calculated through analysis of the modal behaviour of the beam system in question. In both standards, a pink noise signal supplied by an electromagnetic transducer is used to excite an elastic base beam coated in the damping material being tested. The dynamic response of the beam system is measured with a non-contact capacitive transducer and the frequency domain modal response is recorded. Loss factor is calculated at the resonant frequencies using the half-power bandwidth technique.

Half-power Bandwidth

A common method of determining damping is to measure the frequency bandwidth between points on the response curve, for which the response is some fraction of the resonant response of the system, such as the points 1 and 2 illustrated in Figure 2.7. Using this curve and the damping model shown in Figure 2.4, it is possible to derive the equation for the loss factor from the system mechanics. The equation of motion for this system is given in Equation 2.18. The amplitude of vibration of this system is defined by Equation 2.14. Peak amplitude is achieved at the resonant frequency

$$\omega_r = \sqrt{\frac{k}{m}}\,. \tag{2.20}$$

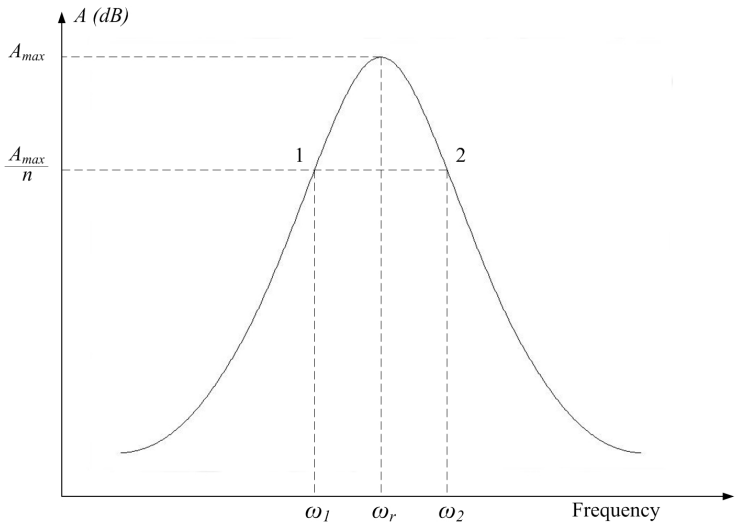

Figure 2.7: Fractional-power bandwidth

Substituting this resonant frequency into Equation 2.14 yields the peak amplitude

$$A_{max} = (x_p)_r = \frac{F}{k\eta} \,. \tag{2.21}$$

The points 1 and 2 in Figure 2.7 can be computed by equating the vibration amplitude in Equation 2.14 to A_{max}/n :

$$\frac{F}{\sqrt{(k - m\omega^2)^2 + k^2\eta^2}} = \frac{F}{nk\eta} \,. \tag{2.22}$$

Rearrangement produces the quadratic equation

$$m\omega^2 + k\left(-1 + \eta\sqrt{n^2 - 1}\right) = 0 \,. \tag{2.23}$$

Solving this equation for ω_1 and ω_2 yields

$$\omega_{1,2} = \sqrt{\left(\frac{k}{m}\right)\left(1 \mp \eta\sqrt{n^2 - 1}\right)} \,. \tag{2.24}$$

Hence, for $n = \sqrt{2}$

$$\frac{\Delta\omega}{\omega_r} = \sqrt{1 + \eta} - \sqrt{1 - \eta} \,, \tag{2.25}$$

and for $\eta \ll 1$

$$\frac{\Delta\omega}{\omega_r} \simeq \left(1 + \frac{\eta}{2}\right) - \left(1 - \frac{\eta}{2}\right) = \eta \,. \tag{2.26}$$

On a logarithmic scale this results in $20 \log_{10} \frac{1}{\sqrt{2}} = -3.01$ dB from the peak resonance value. This enables simple calculation of the loss factor using the plot shown in Figure 2.8 and the relationship in Equation 2.27:

$$\eta_c = \frac{\Delta f}{f_c} \,. \tag{2.27}$$

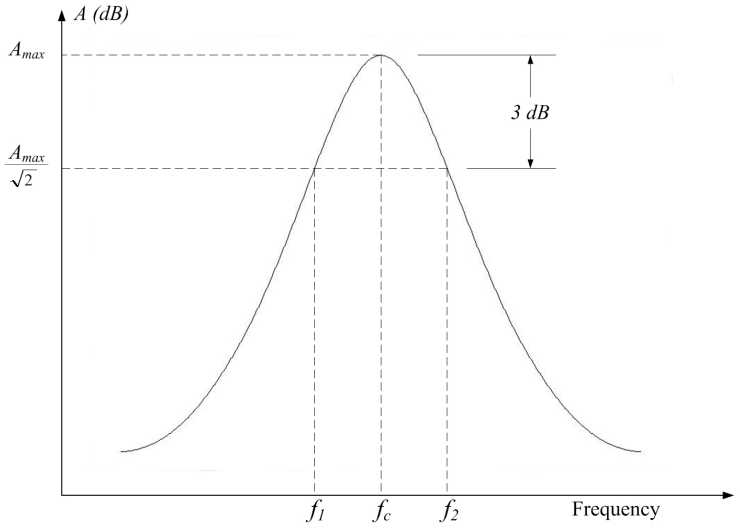

Figure 2.8: Half-power bandwidth at resonant frequencies

Measurements of η_c can be performed at multiple modes in order to establish the effect of frequency on the damping performance of a material. Figure 2.9 shows an example frequency response curve for a damped beam.

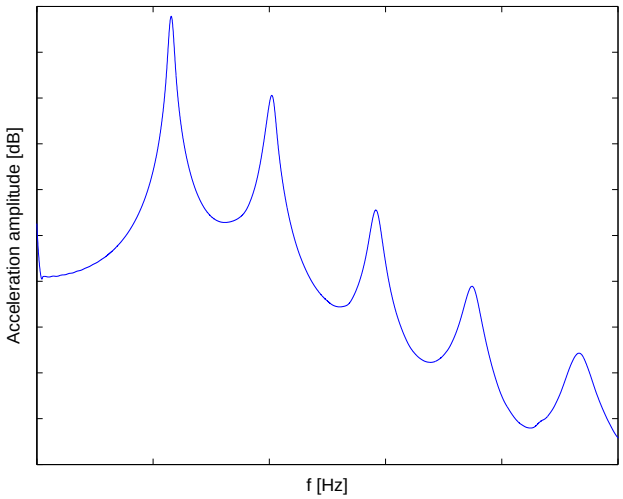

Figure 2.9: Example frequency response curve for a damped beam

2.3.2 ASTM Standard

ASTM E756 [79] involves comparing the dynamic response of an elastic base beam to that of the same beam with damping material applied. The material loss factor is calculated from this comparison using the method outlined in Oberst and Frankenfeld's work [3]. The base beam with damping layer is shown in Figure 2.10.

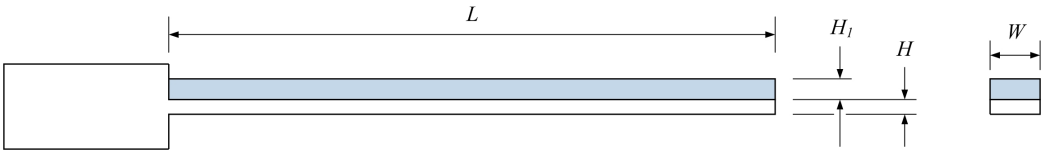

Figure 2.10: Beam damped on one side (Oberst)

Test Rig Design

A test rig was designed and constructed to meet the requirements for testing a material's loss factor to ASTM E756. The testing apparatus consisted of a rigid test fixture to hold the test specimen, an environmental chamber to control temperature, and vibration trans-

ducers with associated instrumentation for generating the excitation signal and measuring the response signal.

A cantilever beam arrangement was specified by the standard and the test fixture was required to consist of a massive, rigid structure to provide a clamp for the root end of the beam. Mounting points for the excitation and response transducers were also needed. The elastic base beam and root section were machined from a solid bar to achieve the required clamping condition for the test specimen. The transducer mounts were attached to a rail in order to facilitate a variety of excitation and response measurement positions. The test fixture is shown in Figure 2.11 and construction drawings are presented in Appendix A.7. The testing configuration is shown in Figure 2.12.

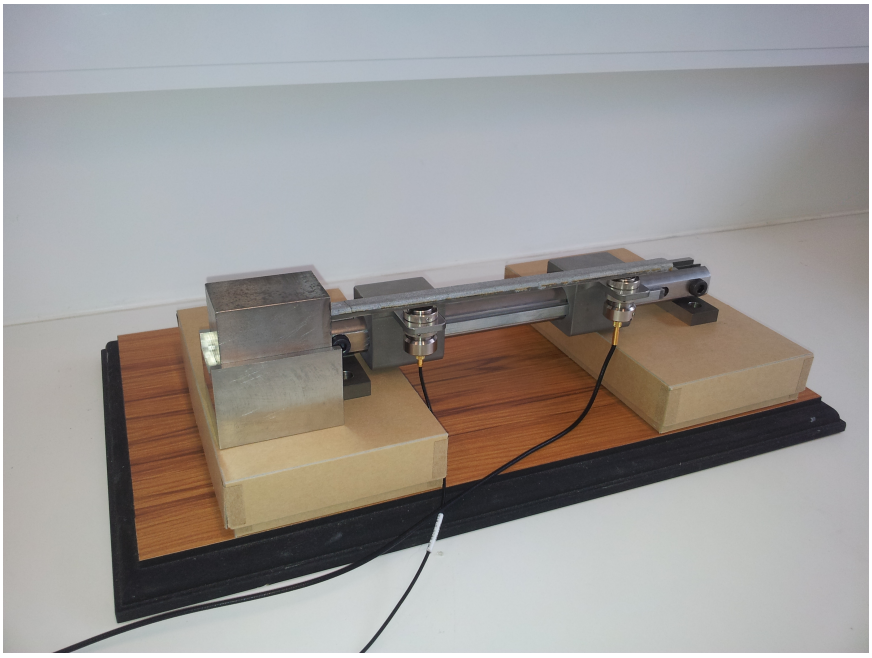

Figure 2.11: ASTM testing fixture

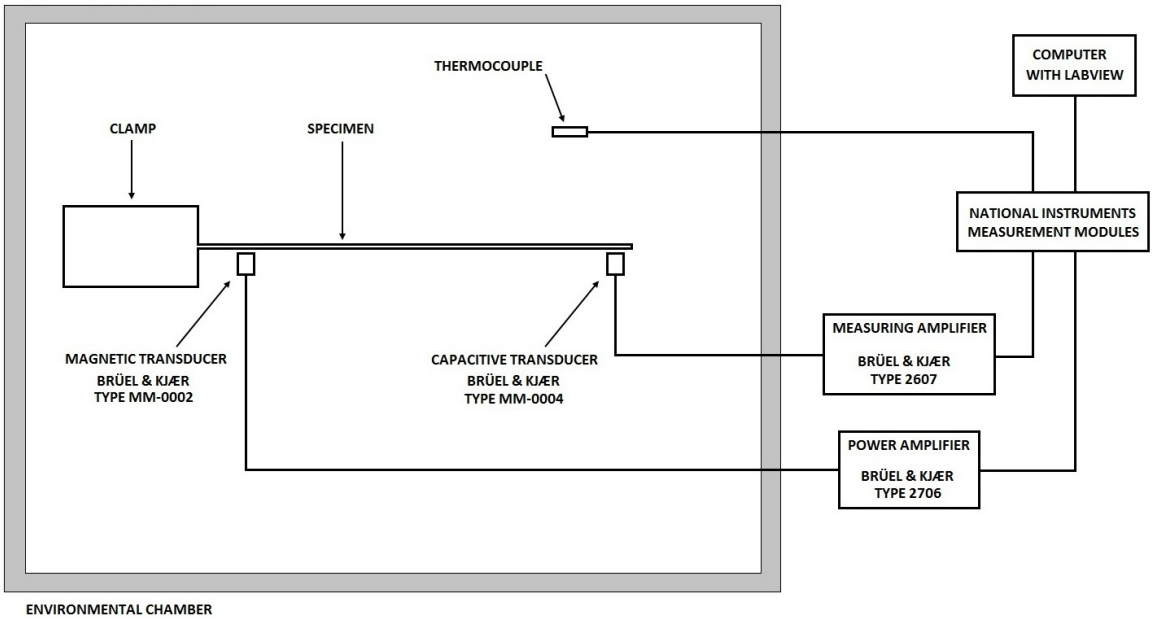

Figure 2.12: ASTM testing configuration

Instrumentation

National Instruments (NI) modules were selected to drive and record the required response of the test assembly. The pink noise excitation signal was generated with a NI 9263 module. This signal was amplified with a Brüel & Kjær (B&K) Type 2706 power amplifier and fed to a B&K magnetic transducer to excite the elastic base beam over a broad frequency range. The dynamic response of the beam was measured with a B&K capacitive transducer connected to a B&K measuring amplifier and an NI 9234 module. Ambient temperature was measured with a resistance temperature detector (RTD) connected to a NI 9217 module. The NI program LabVIEW was used to automate the excitation and measurement modules and record the dynamic response. This measurement data was then input into MATLAB for post-processing. The MATLAB code calculated the required material properties and determined the material loss factor using the equations is described below.

Method and Calculations

All equations contained within this section were obtained from ASTM E756 [79] but were originally derived by [3] using the Euler-Bernoulli theory of bending.

The first stage of the method required determination of the Young's modulus of the base beam. Measuring the dynamic response of the base beam with no damping material applied allowed the Young's modulus of the base beam to be calculated using

$$E = \frac{12\rho l^4 f_n^2}{H^2 C_n^2} \ , \tag{2.28}$$

where

E = Young's modulus of beam material [Pa] ,

ρ = density of beam [kg.m^{-3}] ,

l = length of beam [m] ,

f_n = resonant frequency of the base beam for mode n [Hz] ,

n = mode number $(1, 2, 3, ...)$,

H = thickness of base beam in vibration direction [m] ,

C_n = coefficient for mode n, of uniform clamped-free beam ,

and

$C_1 = 0.55959$,

$C_2 = 3.5069$,

$C_3 = 9.8194$,

$C_4 = 19.242$,

$C_5 = 31.8019$,

$C_n = (\pi/2)(\mathrm{n} - 0.5)^2$, for $n > 3$.

In order to achieve sufficient resolution of the resonant peaks produced by the dynamic

response, the excitation and measurement transducers would sometimes need to be shifted to various locations on the beam to better excite and measure particular resonant modes. The offset distance between the transducers and the base beam was also found to affect the clarity of the measured dynamic response. Particular care was taken to find the offset distance that gave the strongest response signal.

The next stage of the method was to measure the response of the damped beam. Damping material was applied to the base beam with a pressurised sprayer, allowed to dry, and then machined to achieve a consistent damping layer thickness. The damped beam was then excited and the dynamic response measured. Sufficient samples of the dynamic response were recorded to achieve a smooth response curve and reduce the associated measurement error. Using Equation 2.27 and Equation 2.28, the damping material's Young's modulus and loss factor were calculated with:

$$E_1 = \frac{E}{2T^3}\left((\alpha - \beta) + \sqrt{(\alpha - \beta)^2 - 4T^2(1 - \alpha)}\right) , \tag{2.29}$$

and

$$\eta_1 = \eta_c \left(\frac{(1 + MT)(1 + 4MT + 6MT^2 + 4MT^3 + M^2T^4)}{(MT)(3 + 6T + 4T^2 + 2MT^3 + M^2T^4)} \right) , \tag{2.30}$$

where

E_1 = Young's modulus of the damping material [Pa] ,

E = Young's modulus of the beam material [Pa] ,

$T = H_1/H$, thickness ratio ,

H_1 = thickness of the damping material [m] ,

H = thickness of the base beam in vibration direction [m] ,

$\alpha = (f_c/f_n)^2(1 + DT)$, resonant frequency ratio function ,

f_c = resonant frequency of the damped beam for mode c [Hz] ,

c = mode number (1, 2, 3, ...) for damped beam ($c = n$) ,

f_n = resonant frequency of the base beam for mode n [Hz] ,

$D = \rho_1/\rho$, density ratio ,

ρ_1 = density of the damping material [kg.m^{-3}] ,

ρ = density of the base beam [kg.m^{-3}] ,

$\beta = 4 + 6T + 4T^2$, thickness ratio function ,

η_1 = loss factor of the damping material ,

$\eta_c = \Delta f_c / f_c$, loss factor of mode c for the damped beam ,

Δf_c = half-power bandwidth of mode c of the damped beam [Hz]) ,

$M = E_1/E$, Young's modulus ratio .

For measurements of material loss factor over a range of temperatures, ASTM E756 required that the test specimen be held at each desired temperature point for a minimum of 30 minutes to ensure the damping layer reach the correct temperature before measuring the response.

2.3.3 ISO Standard

ISO 6721-3 [78] provides the methodology for measuring the loss factor of a damping layer treatment applied to an elastic base beam. Two methods are covered by the standard, both use the beam dynamic modal response to determine the loss factor. Method A is a cantilever beam arrangement similar to that in ASTM E756 and method B is a freely suspended beam arrangement. ISO 6721-3 calculates the loss factor of the metal-viscoelastic system. The damping material loss factor is not calculated as in the ASTM standard.

Test Rig Design

Method B was selected for testing as the standard indicated that this method was particularly suitable for testing layered damping materials. The test fixture was comprised of two parallel rails, the lower rail housing the excitation and measurement transducers to facilitate multiple measurement positions. The upper rail provided attachment points for the fibres used to suspend the test specimen, and allowed a variety of suspension positions. The test

fixture is shown in Figure 2.13 and construction drawings are presented in Appendix A.7. The testing configuration conforming to ISO 6721-3 is shown in Figure 2.14.

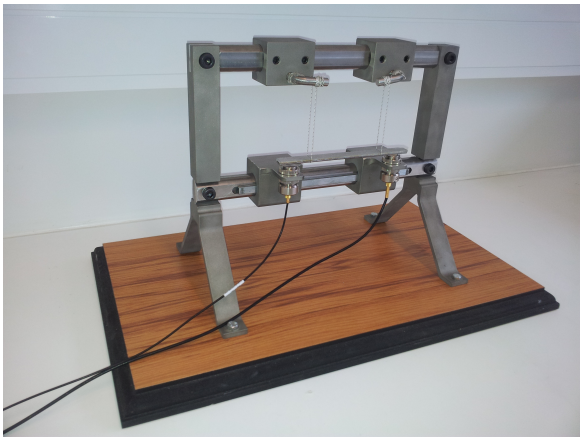

Figure 2.13: ISO testing fixture

Instrumentation

The same instrumentation set up and LabVIEW control code used for the ASTM test rig was also used for the ISO test rig:

Excitation

- Pink noise generator - NI 9263 module
- Excitation amplifier - Brüel & Kjær type 2706 power amplifier
- Excitation transducer - Brüel & Kjær type MM-0002 magnetic transducer

Measurement

- Measurement transducer - Brüel & Kjær type MM-0004 capacitive transducer
- Measurement amplifier - Brüel & Kjær type 2607 measuring amplifier
- Signal analyser - NI 9234 module

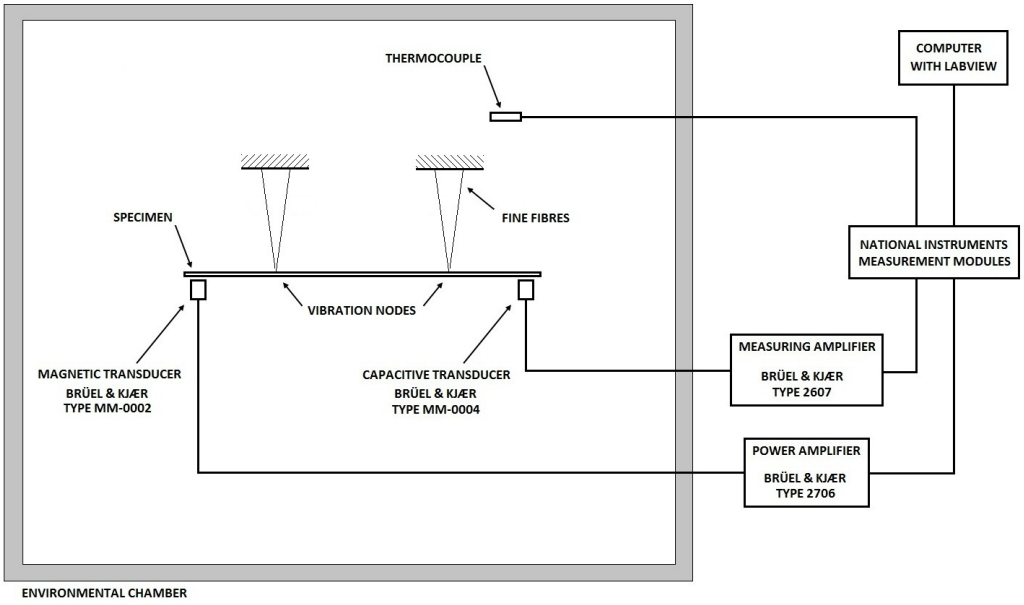

Figure 2.14: ISO testing configuration

- Temperature transducer - RTD
- Temperature acquisition system - NI 9217 module

Method and Calculations

All equations contained within this section were obtained from ISO 6721-3 [78]. As with the ASTM method, these equations were originally derived by Oberst and Frankenfeld [3] using the Euler-Bernoulli theory of bending.

The test specimen was suspended from the upper rail of the test fixture with inelastic fibres. The fibres were positioned at mode vibration nodes closest to the ends of the test beam to minimise the influence of the suspension method on the measured mode vibration response. Each measured mode required different suspension points. The distance between the ends of the test beam and the nearest mode vibration node were calculated using one of the two following relationships:

$L_n/l = 0.224$ for $n = 1$, or

$L_n/l = 0.660/(2n + 1)$ for $n > 1$,

where

L_n = distance from the node location of mode n to each beam end [m] ,

l = the length of the test specimen [m] ,

n = the bending mode number .

Modes 2 and 3 of the base beam used were found to give responses with good resolution. Resolution of the desired mode could also be increased with careful placement of the excitation and measurement transducers. The dynamic response of the damped beam was used to calculate the beam's loss factor using Equation 2.27. Flexural storage modulus is given by:

$$E'_f = \left(\frac{4\pi l^2\sqrt{3\rho_d}}{h}\right)^2 \left(\frac{f_c}{k_c^2}\right)^2 , \tag{2.31}$$

where

E'_f = flexural storage modulus [Pa] ,

l = length of the damped beam [m] ,

ρ_d = density of damped beam [kg.m^{-3}] ,

h = thickness of the damped beam [m] ,

f_c = resonance frequency of the damped beam for mode c [Hz] ,

k_c = numerical factor for mode c, given by one of the following equations:

$k_1^2 = 22.4$ for $c = 1$,

$k_2^2 = 61.7$ for $c = 2$,

$k_c^2 = (c + 0.5)^2\pi^2$ for $c > 2$.

The flexural loss modulus could then be calculated using

$$E''_f = E'_f\eta_c . \tag{2.32}$$

For measurements of loss factor over a range of temperatures, ISO 6721-3 required that the tests be performed at incremental temperature steps or at a rate of change of temperature slow enough to allow temperature equilibrium to be reached throughout the entire specimen. Temperature rates of 1 °C.minute^{-1} to 2 °C.minute^{-1}, or temperature step intervals of 2 °C to 5 °C held for 3 minutes to 5 minutes were recommended by this standard.

2.4 Dynamic Mechanical Analysis

Another method for determining the dynamic material properties of damping layer treatments is through the use of a dynamic mechanical analyser (DMA). The dynamic material properties of the damping material are measured by exciting a sample of the material with a constant force sinusoidal load and measuring the strain response. Measurements are made over a range of controlled frequencies and temperatures. A TA Instruments Q800 DMA was used for all measurements.

2.4.1 Measurement Environment

A variety of clamping fixtures were available with the TA DMA. A dual cantilever arrangement was selected to best replicate the flexural excitation that unconstrained layer damping treatments undergo during use. A simplified schematic of the clamp arrangement is illustrated in Figure 2.15. Measurements were able to be made over a temperature range from -150 °C to 300 °C. Sub-ambient temperatures were achieved using a liquid nitrogen cooling system and heating rates of 0.1 °C.min^{-1} to 20 °C.min^{-1} were possible. The frequency excitation signal was limited to 0.01 Hz-200 Hz, although it was found that frequencies over 140 Hz produced unreliable results. The sample could be excited at several frequencies simultaneously using superposition of the excitation signals. The limited excitation frequency range available was inadequate at providing a complete understanding of a damping treatment, particularly for design purposes. For this reason the dynamic response of the damping material over a wider frequency range was obtained using the time-temperature superposi-

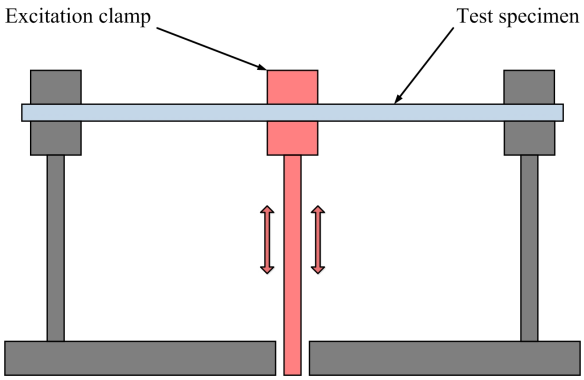

Figure 2.15: DMA dual cantilever clamp arrangement

tion principle.

2.4.2 Time-Temperature Superposition Principle

The inverse relationship between the temperature and frequency effects on dynamic material properties is used to establish the time-temperature superposition principle (TTSP) [2, 80]. By this principle, measurements of damping properties as a function of frequency made at different temperatures can be collapsed onto one master curve using an appropriate shift factor. Hence, measurements made over a limited frequency range can be expanded to a larger frequency range if they are also made over a wide temperature range. Figure 2.16 illustrates the principle.

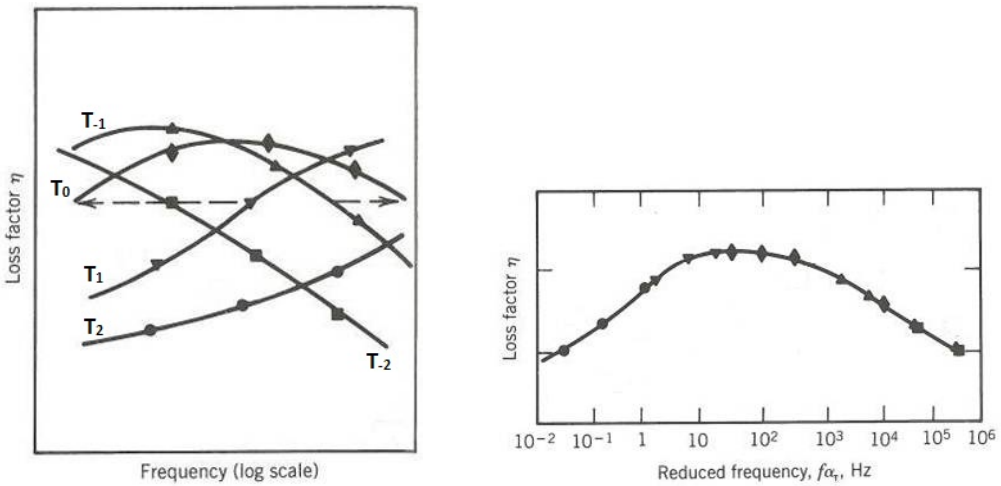

(a) Loss factor at various temperatures

(b) Loss factor master curve

Figure 2.16: Application of time-temperature superposition principle (adapted from [2])

In order to create such a master curve, it is necessary to determine the horizontal shift factor $\alpha_{_T}$ which is used for the reduced frequency $f\alpha_{_T}$. The Williams-Landel-Ferry (WLF) equation [81] is used to calculate this shift factor:

$$\log(\alpha_{_T}) = \frac{-C_1(T - T_0)}{C_2 + (T - T_0)} \,, \tag{2.33}$$

where

$\alpha_{_T}$ = horizontal shift factor of curve at temperature T ,

T_0 = the reference temperature that other curves are fitted to [K] ,

T = the temperature of the curve to be shifted [K] ,

C_1, C_2 = empirical constants used to adjust the curve shifting values .

The work by Williams et al. [81] specified that reference temperatures were limited to the range $T_g \leq T_0 \leq T_g + 100$ [K]. It was also stated that if the glass transition temperature T_g is selected as the reference temperature, for most amorphous (non-crystalline) polymers C_1 and C_2 could usually be assumed to take on values of:

$$C_1^g = 17.44, \qquad C_2^g = 51.6 \,.$$

This yields Equation 2.34

$$\log(\alpha_{_T}) = -17.44\frac{T - T_g}{51.6 + T - T_g} \ . \tag{2.34}$$

However in subsequent work, Ferry [1] found that variation from one polymer to another was too great to permit use of these values except as a last resort. He proposed a better approximation where values of $C_1^s = 8.86$ and $C_2^s = 101.6$ were used in conjunction with a reference temperature T_s, which was allowed to be an adjustable parameter. T_s generally fell about 50 °K above T_g.

$$\log \alpha_{_T} = -8.86\frac{T - T_s}{101.6 + T - T_s} \tag{2.35}$$

The WLF equation is not always sufficient for constructing the master curves of viscoelastic damping materials. Many materials have fillers and polymer blends which add complexity to the curve shifting required to produce the desired master curves. It is sometimes necessary to introduce a vertical shift factor to account for variations of density with temperature [82, 83]. In simple viscoelastic materials, vertical shift factors are close to unity. However, in viscoelastic materials with crystalline structures or those with fillers added, larger vertical shift factors may be required to create continuous master curves. Such shift factors can be calculated using:

$$b_{_T} = \frac{T_0\rho_0}{T\rho} \ , \tag{2.36}$$

where

$b_{_T}$ = vertical shift factor of curve at temperature T ,

T_0 = the reference temperature that the other curves are fitted to [K] ,

T = the temperature of the curve to be shifted [K] ,

ρ_0 = density of the damping material at temperature T_0 [kg.m^{-3}] ,

ρ = density of the damping material at temperature T [kg.m^{-3}] .

The TA Q800 DMA used for all testing produced master curves of loss factor, storage modulus and loss modulus from measured data using the WLF equation. Vertical shift factors were also able to be produced using Equation 2.36 and required the sample density to be supplied to the software. Vertical shifting was not utilised during this study.

2.5 Method Comparison

It was useful to compare the results found from DMA measurements to those found using the Oberst beam technique. Measurements were made on a commercially available damping compound which was comprised of a styrene-acrylic co-polymer emulsion with a calcium carbonate filler.

2.5.1 Oberst Beam Measurements

ASTM E756 was selected as the material loss factor could be calculated with this method. The test configuration described in Section 2.3.2 had not yet been constructed so an alternative rig was used. The test configuration used is shown in Figure 2.17.

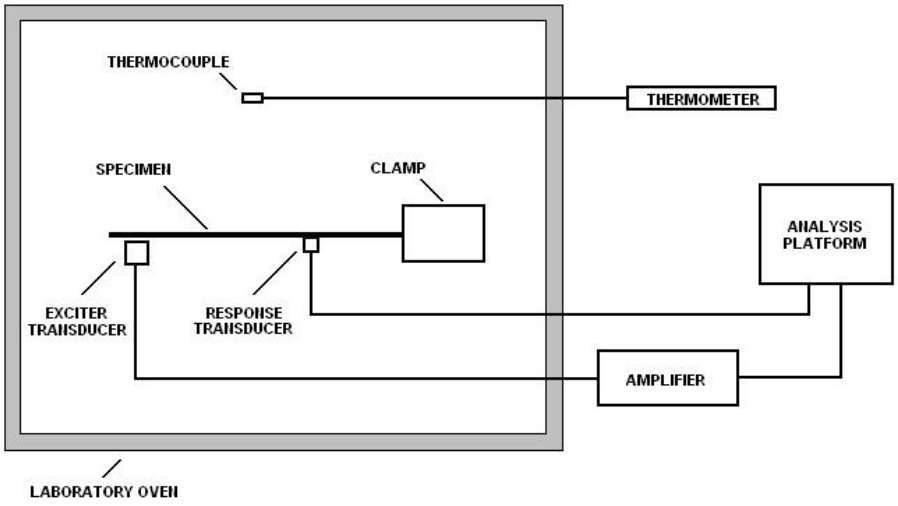

Figure 2.17: ASTM test configuration for method comparison

As in the standard, measurements of vibratory response were made on a steel beam which was clamped at one end and free at the other. The dimensions of the base beam were 300 mm × 25 mm × 1 mm. Once clamped, the free length of the beam was reduced to 216.2 mm.

The beam was excited using a electromagnet placed near the free end of the beam and the response was measured with a B&K accelerometer attached to the underside of the beam.

A pink noise excitation signal, of frequency range 0 - 600 Hz, was generated using a B&K PULSE analyser platform and amplified before being fed to the electromagnet. The PULSE system was also used to analyse the response signal in the frequency domain.

The beam-clamp arrangement, exciter, receiver and temperature probe were placed into a laboratory oven to facilitate measurements over a range of temperatures. Sub-ambient temperatures were not achievable with the equipment available, consequently the lowest temperature achievable during testing was the ambient temperature at the time of testing.

Frequency domain measurements of the dynamic response were first made on the base beam at ambient temperature. The third mode of vibration was then examined in order to calculate the Young's modulus of the base beam using Equation 2.28. Measurement of the third mode was recommended by the ISO standard and the accelerometer was placed in a position to best capture the response of this mode. The frequency domain response of the base beam is shown in Figure 2.18.

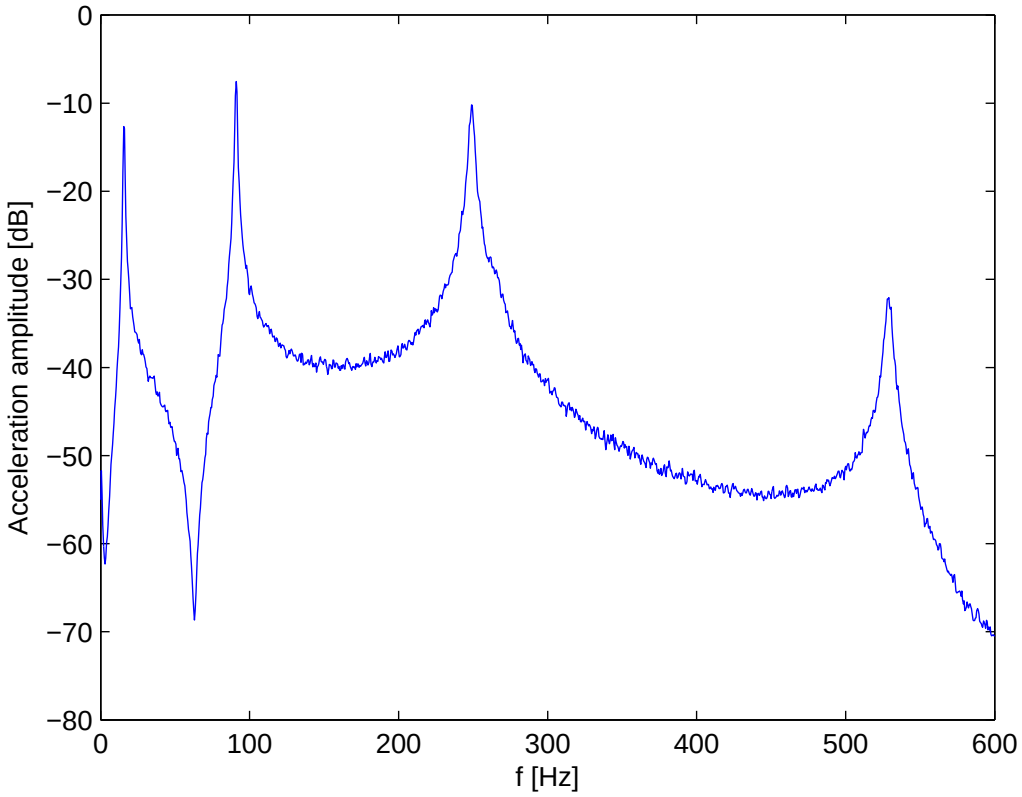

Figure 2.18: Base beam modal response

The resonant frequency of the third mode was found to be 249 Hz. The mass of the base beam was measured and the density calculated as 7362 kg.m^{-3}. Using Equation 2.28, the Young's modulus of the base beam was calculated to be 124.13 GPa.

A 2 mm layer of damping material was applied to one side and along the free length of the base beam (216.2 mm). The damping layer was allowed to cure over a period of three days. Damped beam measurements were made at multiple ambient temperatures, with the lowest being 14°C, and then at elevated temperatures ranging from 25 °C to 50 °C in 5 °C increments. The damped beam was held for 30 minutes at each temperature point to ensure thermal equilibrium within the damping layer. The dynamic response was then measured in

the frequency domain and the third mode of vibration was again examined to perform the required calculations. The density of the damping material was found to be 1942 kg.m^{-3}. Using this value and Equations 2.29 and 2.30, the flexural storage modulus and loss factor of the damping material were determined at each temperature point.

2.5.2 Dynamic Mechanical Analysis Measurements

The TA Q800 DMA, seen in Figure 2.19a, was configured with a bending probe to simulate the flexural vibrations experienced by the damping material in real world use. The probe consisted of a dual-cantilever arrangement where the ends of the test sample were clamped and the centre was attached to the oscillatory exciter as seen in Figure 2.19b.

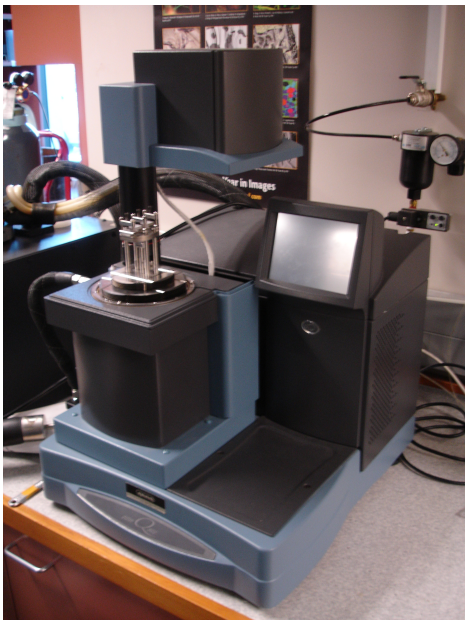

(a) TA Q800 DMA

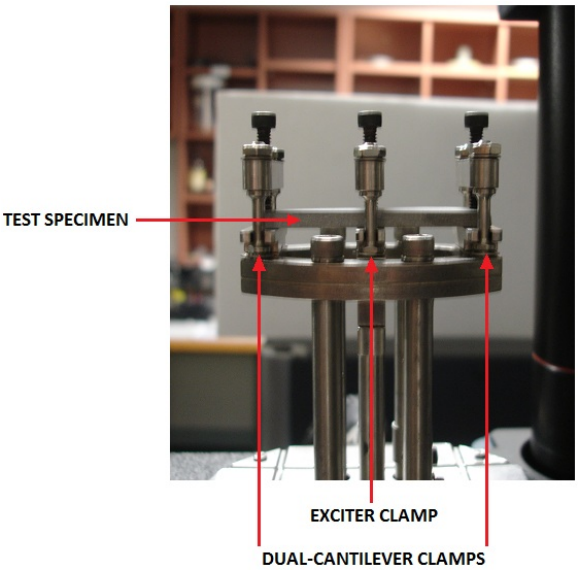

(b) DMA bending probe arrangement

Figure 2.19: TA Q800 DMA testing arrangement

Test samples for the DMA were prepared by applying the damping material to a steel panel coated in a release agent. The material was left to cure for three days before being removed from the panel. Test specimens were then cut from this sheet. Sample dimensions of 55 mm × 11 mm × 4 mm were used in this test. The temperature of each test piece was lowered

to -100 °C before being clamped to minimise deformation of the sample at the clamping points. The specimen was excited simultaneously at frequencies 1, 2, 5, 10 and 20 Hz using frequency superposition. A temperature range of -100 °C to 100 °C and heating rate of 2 °C.min^{-1} was used. The DMA analysis software was used to display curves of loss factor versus temperature and construct a material loss factor master curve.

2.5.3 Results

Values of material loss factor versus temperature obtained from the ASTM and DMA tests are shown in Figure 2.20.

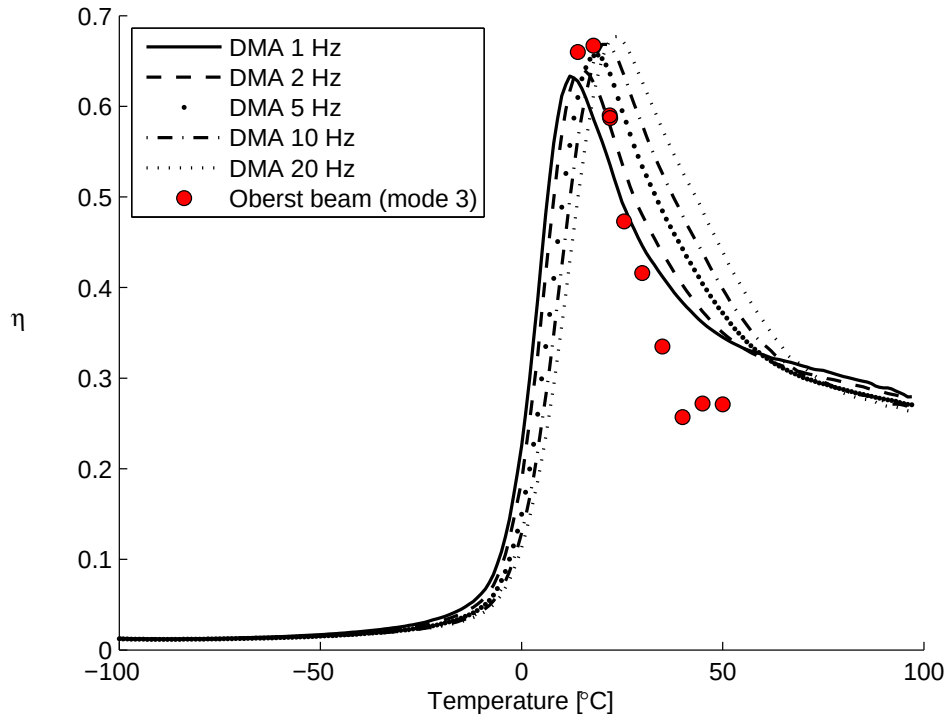

Figure 2.20: Material loss factor data from Oberst beam and DMA tests

It was apparent that the DMA curve at 5 Hz gave the closest approximation to the Oberst beam results. Figure 2.21 and Table 2.1 give a clearer comparison of the 5 Hz DMA measurements and the Oberst beam measurements.

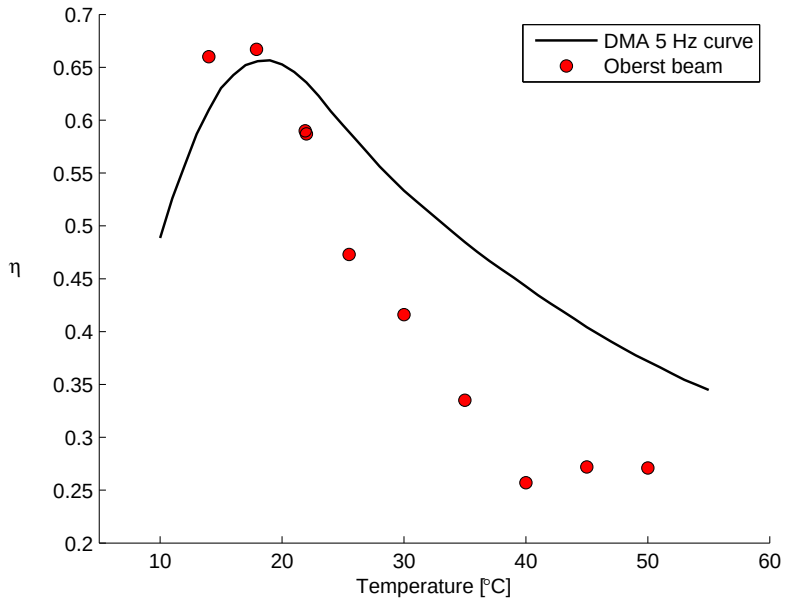

Figure 2.21: Oberst beam and 5 Hz DMA data comparison (closer view of Figure 2.20)

Temperature	Oberst beam					DMA	Difference
[°C]	f_{c3} [Hz]	Δf_{c3} [Hz]	η_c	E_1 [MPa]	η_1	η_1	(%)
14.0	266.25	74.25	0.279	1553	0.660	0.610	-7.6
17.9	248.25	56.50	0.228	1076	0.667	0.655	-1.8
21.9	240.75	42.75	0.178	889	0.590	0.636	7.9
22.0	241.25	43.00	0.178	901	0.587	0.637	8.5
25.5	236.25	30.75	0.130	780	0.473	0.589	24.5
30.0	231.75	23.88	0.103	673	0.416	0.533	28.1
35.0	229.00	16.63	0.077	609	0.335	0.485	44.8
40.0	227.25	12.75	0.056	568	0.257	0.443	72.4
45.0	225.25	12.50	0.056	523	0.272	0.403	48.2
50.0	223.25	11.50	0.052	477	0.271	0.372	37.3

Table 2.1: Result comparison between Oberst beam data and DMA 5 Hz data

Analysis of the results presented in Figures 2.20 - 2.21, and Table 2.1, indicated that both the DMA and Oberst beam methods provided material loss factors within 2% of one another at the glass transition temperature. It is also apparent that the percentage difference between results increased at higher temperatures. Differences in the results may have been due to inherent differences between the two methods; specifically clamping arrangements, excitation frequencies, and the times which the test specimens were held at each temperature. The rate at which the temperature was increased during the DMA test may have introduced error into the temperature values reported in the results. Further testing using the Oberst beam method at temperatures lower than the glass transition temperature would be necessary to determine whether differences in values followed the same trend at lower temperatures.

The material loss factor master curve produced by the DMA with a reference temperature of 18 °C is shown in Figure 2.22.

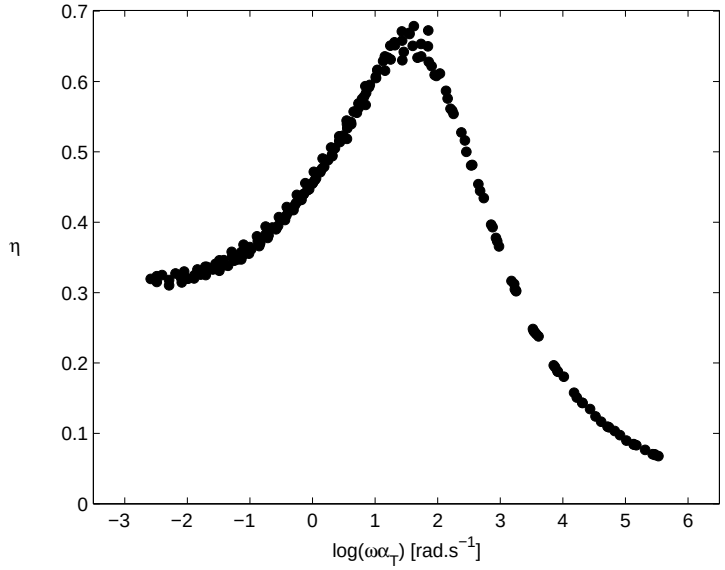

Figure 2.22: Material loss factor master curve

It can be seen that there is noticeable scatter in the master curve values at low frequencies and particularly at the peak damping values. This is likely due to the limitations of the WLF equation when dealing with a co-polymer that contains particulate fillers [1, 82–84]. The noticeable scatter diminishes at frequencies greater than approximately $\log(\omega\alpha_T) = 1.9\,\text{rad.s}^{-1}$, which is equivalent to a frequency of approximately 12.5 Hz.

Whilst it is clearly necessary for a material designer to gain useful and accurate data from a test, the time taken to perform the test and process the results is also an important factor, particularly in the commercial sector. An advantage of using the DMA was the ability to perform tests over a wide range of temperatures in a relatively short period of time, and generate useful data with minimal post-processing by the tester. Conversely, when testing to the ASTM standard, it was not uncommon for a measurement at a single temperature point to take 45 minutes due to the thermal hold time requirement. This method also required an operator to perform each test measurement, alter the temperature and manually select data during post-processing, which further increased the time taken for testing.

2.5.4 Concluding Remarks

The Oberst beam method is well established and used in ISO and ASTM standards. This method requires considerable user input to make measurements and produce useful results.If testing were performed according to either the ISO or ASTM standards, obtaining values at multiple temperatures significantly increases the duration of the testing.

Testing with a DMA produced values of material loss factor that varied appreciably from those obtained using the Oberst beam method. However, values of glass transition temperature were found to be fairly well matched and values of loss factor at the glass transition temperature were found to be within 2% using either method. The DMA was able to measure data over a much larger temperature range in a short period of time and useful

results were produced with minimal user input. These attributes make testing with a DMA excellent for comparing the relative performance of different damping materials including rapid testing of prototype materials.

Further testing may be required to establish a more complete understanding of the limitations of each test method.

2.6 Summary

Unconstrained layer damping is commonly used to reduce resonant structural vibration. The performance of viscoelastic damping materials used for such treatments is measured by the material loss factor metric (η or $\tan\delta$). Methods of measuring material loss factor include the Oberst beam technique, which is used in ISO and ASTM standards, and measurement using a Dynamic Mechanical Analyser (DMA).

Two test rigs were constructed to facilitate measurement of material loss factor in accordance with both ISO and ASTM standards. Of the two international standards, the ASTM standard included calculation of the material loss factor from measurements of loss factor on a substrate beam covered with damping material. The ISO standard produced measurements of the loss factor of the substrate beam and damping layer combination only.

Results from tests made using a DMA were compared to those performed using the Oberst beam technique. The DMA produced similar peak damping values and glass transition temperatures to the Oberst beam results but material loss factor values varied significantly at temperatures higher than the glass transition temperature.

The DMA was found to be well suited to measurements of material loss factor over a wide range of temperatures, requiring significantly less time and user input to achieve measure-

ment data compared to the ISO and ASTM tests. Based on the measured peak damping behaviour seen in Figures 2.20 and 2.21, it was concluded that the DMA would be excellent for testing relative performance between two materials, making it a useful method in the prototype stages of damping material design.

The ISO and ASTM rigs constructed, along with associated testing equipment and code, provide facilities for commercial testing of damping materials.

Chapter 3

Unconstrained Layer System Damping Performance

3.1 Introduction

When a damping treatment is applied to a system, the damping performance is characterised in much the same way as that of the damping material alone. However, the damping behaviour of the new system is rather more complex than that of the damping material. Conditions such as substrate material, system geometry, boundary conditions, damping layer placement and thickness affect the overall system response. It is important to have an understanding of these behaviours in order to obtain the best performance from a system requiring damping treatment. The effect of many of these key variables on system damping performance have been explored by numerous researchers (see Section 1.2.1), however studies that rank the relative influence of variables on the overall damping performance of a system are scarce. Such a study is the focus of this chapter.

3.2 Experimental Design

When investigating the influence of several variables on a single performance metric, efficient experimental design can be employed in order to gain the required data set, while preventing an excessive number of test iterations.

A common approach in experimentation is changing one variable at a time while keeping all others constant to see the effect of that variable. This method requires a large number of resources to gain a limited amount of data, particularly for processes that are sensitive to a range of variables. Experiments performed using this method can be uneconomic, time-consuming and can lead to false optimum conditions if care is not taken. Design of Experiments (DOE) methodology provides a more efficient method for experimental investigations involving multiple variables [85].

3.2.1 Design of Experiments

Design of Experiments is a method of planning, designing and analysing an experiment so that valid and objective conclusions can be drawn. This method integrates statistical methods into the experimental design methodology in order to draw sound conclusions. It is important to have a good understanding of the process under investigation and the constraints of this experimental method in order to properly design an experiment.

The investigation performed in this section involved changing controllable variables which were known to have an effect on the damping performance of a system, and measuring the resulting system loss factor.

The size of an experiment set is determined by the number of variables studied and the number of levels of each variable. The levels of a variable refer to the range of values chosen for each variable. The DOE method is usually limited to two levels of each variable. Two

level designs account for linear effects of variables. Three level DOE designs are possible and can be used when non-linear effects are expected, however this type of design typically reduces the number of variables that are able to be studied due to the significant increase in experiments associated with three variable levels.

Using the DOE method, an experiment design is categorised as either a full factorial design or a fractional factorial design. A full factorial design allows interactions between all variables and combined variable effects to be studied. The number of experiments in a full factorial design is given by 2^k for a two level design, where k is the number of variables to be studied. This can lead to a significant number of test configurations for processes where the study of multiple variables is desired.

Using a fractional factorial design, the number of experiments required to obtain useful information can be substantially reduced. The number of experiments in a fractional factorial design is given by $2^{(k-p)}$ for two level designs, where $1/2^p$ represents the fraction of the full factorial 2^k. For example, $2^{(5-2)}$ is a 1/4th fraction of a 2^5 full factorial design, which allows study of 5 variables at two levels with only 8 experiments instead of 32.

The reduced number of experiments with fractional designs is achieved through deliberate confounding of variables. Confounding refers to the combining influences of two or more variable effects on one measured effect. As it is not possible to distinguish which of the confounded variables has the greatest influence on the measured response, use of fractional designs relies on the assumption that single variables will have a greater effect than combined variable influences. Effects which are confounded are termed aliases and a list of confounded variables which occur in an experimental design is called an alias structure or confounding pattern.

3.2.2 Influential Parameters

When selecting variables to study, it was necessary to consider the typical uses of unconstrained layer damping (ULD) treatments in the marine industry in order to explore meaningful variables. Within metallic marine structures, vibration damping treatments are typically applied to areas of high vibration transmission or sound radiation [86]. Metal plates can be particularly efficient radiators of sound due to their low flexural stiffness, large surface area and elastic material behaviour. Consequently, the dynamic behaviour of damped, thin rectangular metal plates was studied. The effect of plate material on damping performance was of interest, along with edge clamping conditions, damping layer thickness and ambient temperature. Two plate sizes were also investigated. While variables such as partial damping layer coverage or optimal damping layer placement were not included in the investigation, the variables selected were considered to be important at a basic application level within marine structures.

The levels of each of the five variables were selected to replicate values found in common application, where possible. Plate sizes were constrained to dimensions imposed by the testing facilities available. Temperatures above the glass transition temperature of the damping material were selected to avoid the non-linear behaviour associated with temperatures either side of the glass transition peak. The levels of each variable are displayed in Table 3.1 and are denoted as either 'high' or 'low'. For convenience, high and low variable levels are labelled +1 and -1 respectively in later sections. The 'C' and 'SS' values for the boundary conditions refer to clamped and simply-supported edge conditions respectively.

Variable	Designation	Low level (-1)	High level (+1)
Damping layer thickness [mm]	A	1.25	2.5
Ambient temperature [°C]	B	20	30
Boundary conditions	C	SS-SS-SS-SS	C-C-C-C
Plate size [mm]	D	$600 \times 600 \times 1.25$	$1545 \times 945 \times 1.25$
Plate material	E	Aluminium	Steel

Table 3.1: Experiment variable level values

3.2.3 Design Matrix

A $2^{(5-2)}$ fractional factorial experiment design [85] was selected to meet time and resource constraints. The reduction of test configurations was achieved through confounding of single variable interactions with combined two and three variable interactions. The design generators selected for the experiment were:

$$\mathrm{D} = \mathrm{BC} \qquad \text{and} \qquad \mathrm{E} = \mathrm{ABC}\ .$$

Using the identity element (I), which can be considered as a pseudo identity matrix, and the rules:

$$I = \mathrm{A}^2 = \mathrm{B}^2 = \mathrm{C}^2 = \mathrm{D}^2 = \mathrm{E}^2 \qquad \text{and} \qquad I \times I = I,\ \mathrm{A} \times I = \mathrm{A},\ \mathrm{B} \times I = \mathrm{B} \text{ etc.},$$

the defining relationship of the confounding structure could be created:

$$\mathrm{BCD} = \mathrm{B}^2\mathrm{C}^2 = I\ , \qquad \mathrm{ABCE} = \mathrm{A}^2\mathrm{B}^2\mathrm{C}^2 = I\ , \qquad \text{and} \qquad I = \mathrm{ADE}\ .$$

In order to find the aliases of A, both sides of the defining relation were multiplied by A.

$$\mathrm{A} \times I = \mathrm{A} = \mathrm{A} \times \mathrm{ABCE} = \mathrm{A}^2\mathrm{BCE} = \mathrm{BCE} = \mathrm{DE}\ , \qquad (\text{as } \mathrm{A}^2 = I).$$

Aliases of B, C, D and E could then be generated:

$$\mathrm{B} \times I = \mathrm{B} = \mathrm{CD} = \mathrm{ACE} \ ,$$

$$\mathrm{C} \times I = \mathrm{C} = \mathrm{BD} = \mathrm{ABE} \ ,$$

$$\mathrm{D} \times I = \mathrm{D} = \mathrm{BC} = \mathrm{AE} \ ,$$

$$\mathrm{E} \times I = \mathrm{E} = \mathrm{AD} = \mathrm{ABC} \ .$$

The two variable influences that weren't confounded with single variable interactions were also included in the structure:

$$\mathrm{AB} \times I = \mathrm{A^2B^2CE} = \mathrm{CE} = \mathrm{BDE} = \mathrm{ACD} \ ,$$

$$\mathrm{AC} \times I = \mathrm{A^2BC^2E} = \mathrm{BE} = \mathrm{ABD} = \mathrm{CDE} \ .$$

The alias structure is summarised in Table 3.2 and the resulting design matrix is shown in Table 3.3, with high variable levels designated +1 and low levels -1.

Base variable(s)	Confounded with		
A	DE	BCE	-
B	CD	ACE	-
C	BD	ABE	-
D	BC	AE	-
E	AD	ABC	-
AB	CE	BDE	ACD
AC	BE	ABD	CDE

Table 3.2: Experiment confounding pattern

Configuration	A	B	C	D	E
1	-1	-1	-1	+1	-1
2	+1	-1	-1	+1	+1
3	-1	+1	-1	-1	+1
4	+1	+1	-1	-1	-1
5	-1	-1	+1	-1	+1
6	+1	-1	+1	-1	-1
7	-1	+1	+1	+1	-1
8	+1	+1	+1	+1	+1

Table 3.3: Experiment design matrix

The design matrix was reorganised to group the low and high levels of variable B (ambient temperature) together in order to streamline the testing process. The resulting experiment layout is displayed in Table 3.4.

Test number	ULD thickness [mm]	Ambient temperature [°C]	Boundary conditions	Plate size [mm]	Plate material
1	2.5	20	C-C-C-C	600 × 600	Aluminium
2	2.5	20	SS-SS-SS-SS	1545 × 945	Steel
3	1.25	20	SS-SS-SS-SS	1545 × 945	Aluminium
4	1.25	20	C-C-C-C	600 × 600	Steel
5	1.25	30	SS-SS-SS-SS	600 × 600	Steel
6	1.25	30	C-C-C-C	1545 × 945	Aluminium
7	2.5	30	SS-SS-SS-SS	600 × 600	Aluminium
8	2.5	30	C-C-C-C	1545 × 945	Steel

Table 3.4: Experiment schedule

3.3 Experimental Method

3.3.1 Measurement Method

The performance metric to be measured was the system loss factor. A vibration decay method similar to the method described in international standard ISO 10848-1 [87] was employed. The method involved producing an impulse excitation by striking the test plate with an impact hammer and measuring the surface vibration decays to determine the structural reverberation time. Structural reverberation time is defined as the time in seconds required for the velocity or acceleration level in a structure to decrease by 60 dB after the vibration excitation source has stopped. The velocity decays were measured with four accelerometers connected to a Brüel & Kjær PULSE analyser platform. The system loss factor, η_{sys}, was calculated with the relation between frequency f [Hz] and structural reverberation time T_s [s]:

$$\eta_{sys} = \frac{2.2}{fT_s} \,. \tag{3.1}$$

3.3.2 Undamped Plate Response

The blank steel and aluminium plates were tested prior to addition of the damping material. This was done to provide a reference damping measurement which could be compared to the performance of the damped plates.

3.3.3 Sample Preparation

Damped plate test samples were produced using a method similar to techniques commonly used in industrial application. Base plates were laid flat and the edges enclosed to produce a dam that would hold the damping compound within the required area. Damping compound was then applied to the plates with a pressurised spray gun.

The plates were then left to dry for 5 days to ensure proper curing of the damping layer.

A CNC mill was used to machine the surface of the damping layer to ensure an accurate damping layer thickness was achieved. While machining of the ULD treatment is not common practice, it was considered necessary for accurate and repeatable results.

3.3.4 Experimental Conditions

Clamping

The plates were fixed between two aluminium frames that were then clamped into an opening between a reverberation room and a semi-anechoic chamber with the damping layer facing into the semi-anechoic chamber. Sound absorption material was added to the reverberation room to minimise any reflected acoustic energy that might add error to the measured results. The general arrangement for the two boundary conditions is shown in Figure 3.1.

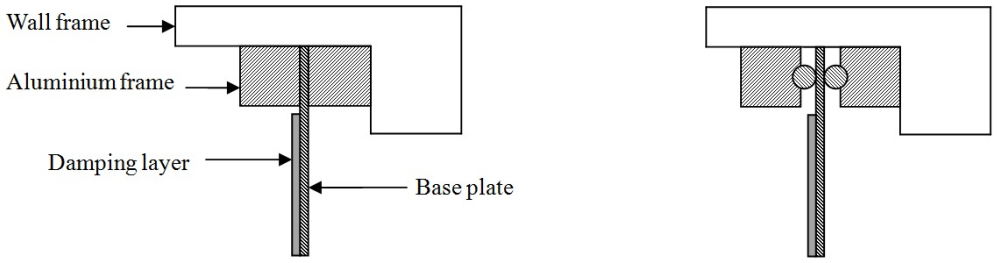

(a) Clamped (b) Simply-supported

Figure 3.1: Boundary condition cross-sections

Figure 3.2 shows the plate, frame and clamping assembly. Construction drawings for the two frames are included in Appendix A.8

Figure 3.2: Test specimen in situ

Excitation and Response Measurement

The surface acceleration reverberation time of each damped and undamped plate was measured using four accelerometers connected to a Brüel & Kjær PULSE analyser. Values were recorded at one-third octave band centre frequencies from 25 Hz to 10 kHz. Impact excitation of the plates was achieved using a PCB 086C03 impact hammer. Two groupings of the accelerometers were used for each plate and two impact locations were used for each accelerometer grouping. It was assumed that the various accelerometer and excitation positions would be sufficient to capture the vibratory response of each plate. Each measurement set was performed three times on all plates. This resulted in 48 measured reverberation decays for each plate.

Temperature

The required temperatures for each test configuration were achieved within the semi-anechoic chamber using a thermostat controlled fan heater. The thermostat sensor was placed adjacent to the surface of the damping layer and the heater was positioned facing away from the plate to allow uniform heating of the damping layer.

Once the experiment configuration temperature point had been reached, each test specimen was left for a minimum of 30 minutes to allow the damping material to equilibrate with the temperature of the chamber. Table 3.4 shows the required temperatures for each experiment configuration.

3.4 Results and Discussion

3.4.1 Reference Damping Performance

The reverberation decays of the undamped plates were used to determine the reference damping performance using Equation 3.1. Figures 3.3 and 3.4 show the damping performance of the 600 mm × 600 mm and 1545 mm × 945 mm plates respectively. Tables 3.5 and 3.6 summarise the average and maximum damping values for each of the plates, where the term average is defined as the arithmetic mean.

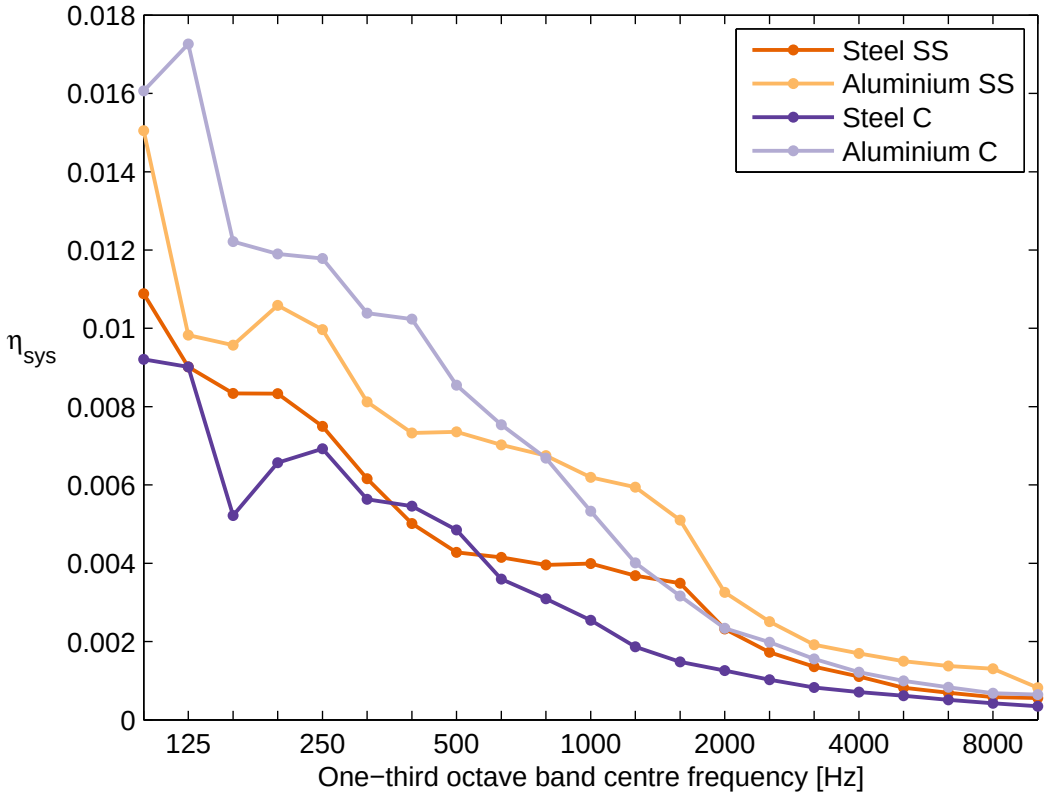

Figure 3.3: System loss factor of undamped 600 mm × 600 mm plates

Plate configuration		η_{sys}	
		Average	Maximum
Steel	simply-supported	0.0042	0.0109
Aluminium	simply-supported	0.0059	0.0150
Steel	clamped	0.0034	0.0092
Aluminium	clamped	0.0064	0.0173

Table 3.5: System loss factors of undamped 600 mm × 600 mm plates

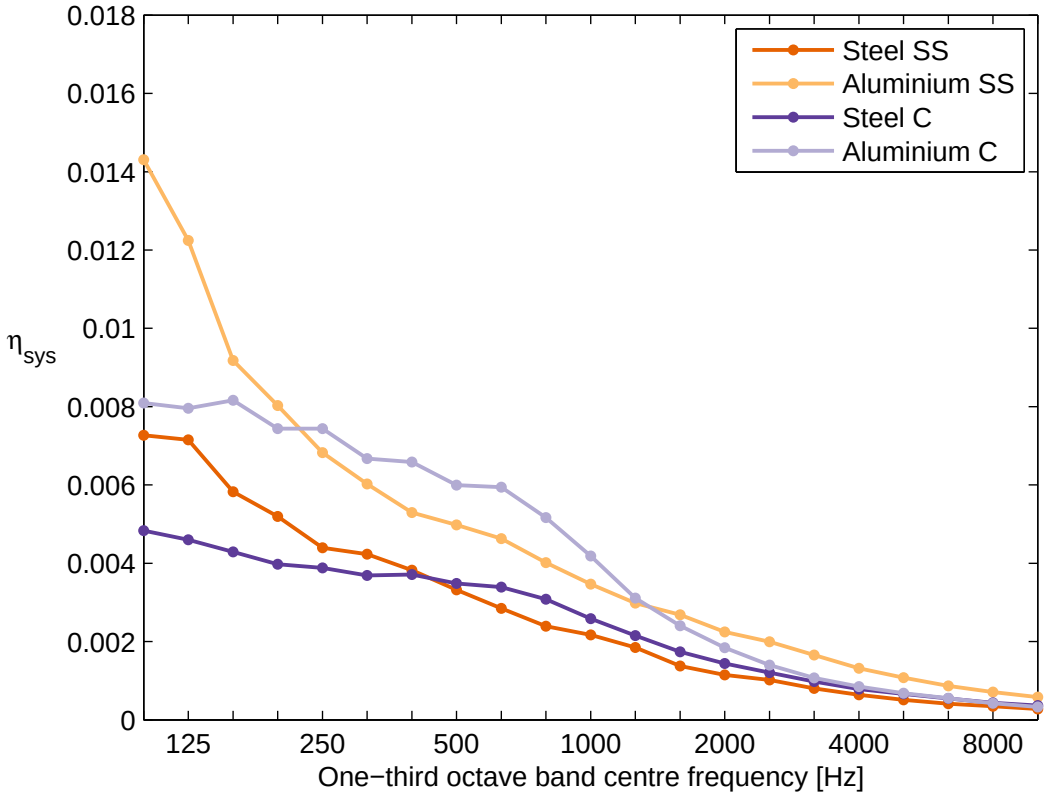

Figure 3.4: System loss factor of undamped 1545 mm × 945 mm plates

Plate configuration		η_{sys}	
		Average	Maximum
Steel	simply-supported	0.0027	0.0073
Aluminium	simply-supported	0.0045	0.0143
Steel	clamped	0.0025	0.0048
Aluminium	clamped	0.0041	0.0082

Table 3.6: System loss factor of undamped 1545 mm × 945 mm plates

Typical values of material loss factor for aluminium and steel were expected to be very small ($\simeq$ 0.001 [79]) due to their elastic material properties. However, the clamping ar-

rangement introduced areas where interfacial friction removed mechanical energy from the system, thereby increasing the damping performance.

The greatest maximum system loss factor of all of the undamped plates was achieved by the clamped aluminium 600 mm × 600 mm configuration with a value of $\eta_{sys} = 0.0173$. This appeared to deviate from the trend of the simply supported plates producing slightly higher values of loss factor over their clamped counterparts. It can also be seen that the aluminium plates produced greater values of loss factor compared to the steel plates in both clamped and simply supported cases. Greater damping with the simply supported configurations may have been due to the larger number of interface surfaces in the clamping arrangement, resulting in a greater area of friction action. An audible rattle was also observed during several of the simply supported tests indicating non-uniform clamping. This behaviour was also likely to have resulted in a measured increase in damping performance.

3.4.2 Damped Plate Response

Tests carried out on the eight damped plate configurations yielded values of system loss factor for each one-third octave band centre frequency from 25 Hz to 10 kHz. These values were produced using measurements of structural reverberation time and Equation 3.1. Due to large variations in some of the lower frequency measured data, only results between 100 Hz and 10 kHz were considered.

Damping Behaviour

Figure 3.5 shows the damping performance measured from the eight damped plate configurations tested. The average and maximum loss factor values of each test configuration are displayed in Table 3.7. A comparison between the lowest damping performance of the damped plates (configuration 5) with the highest damping performance of the undamped plates (aluminium 600 mm × 600 mm C) is shown in Figure 3.6 and Table 3.8.

Plate configurations are show in Table 3.4.

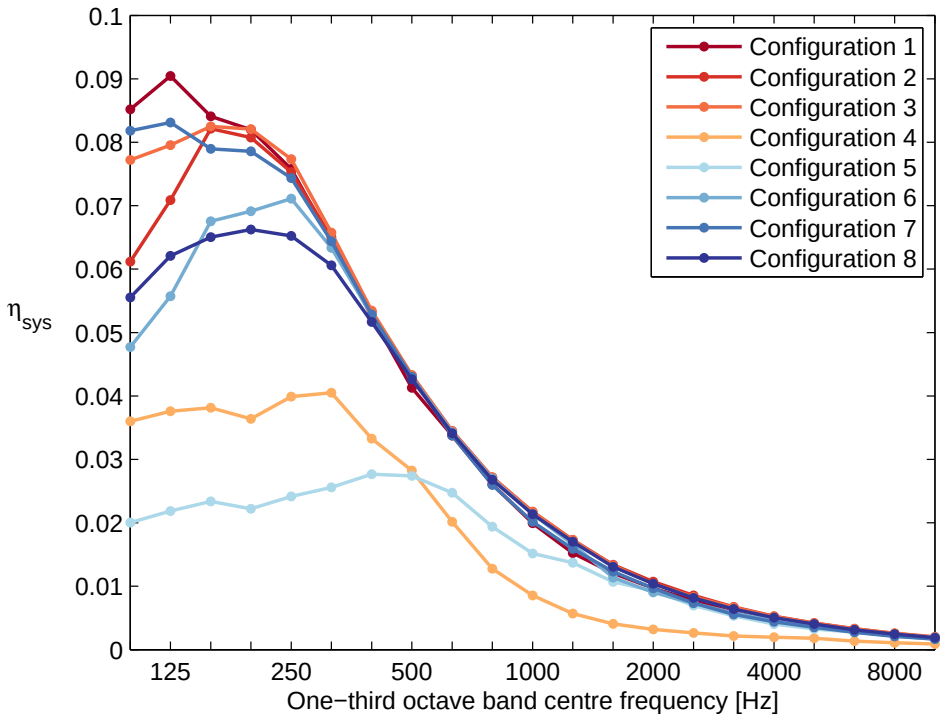

Figure 3.5: System loss factor of the eight damped plate configurations

Configuration	Average η_{sys}	Maximum η_{sys}
1	0.0344	0.0904
2	0.0328	0.0821
3	0.0342	0.0825
4	0.0170	0.0405
5	0.0148	0.0277
6	0.0294	0.0711
7	0.0334	0.0831
8	0.0297	0.0662

Table 3.7: Average and maximum damping of damped plate tests

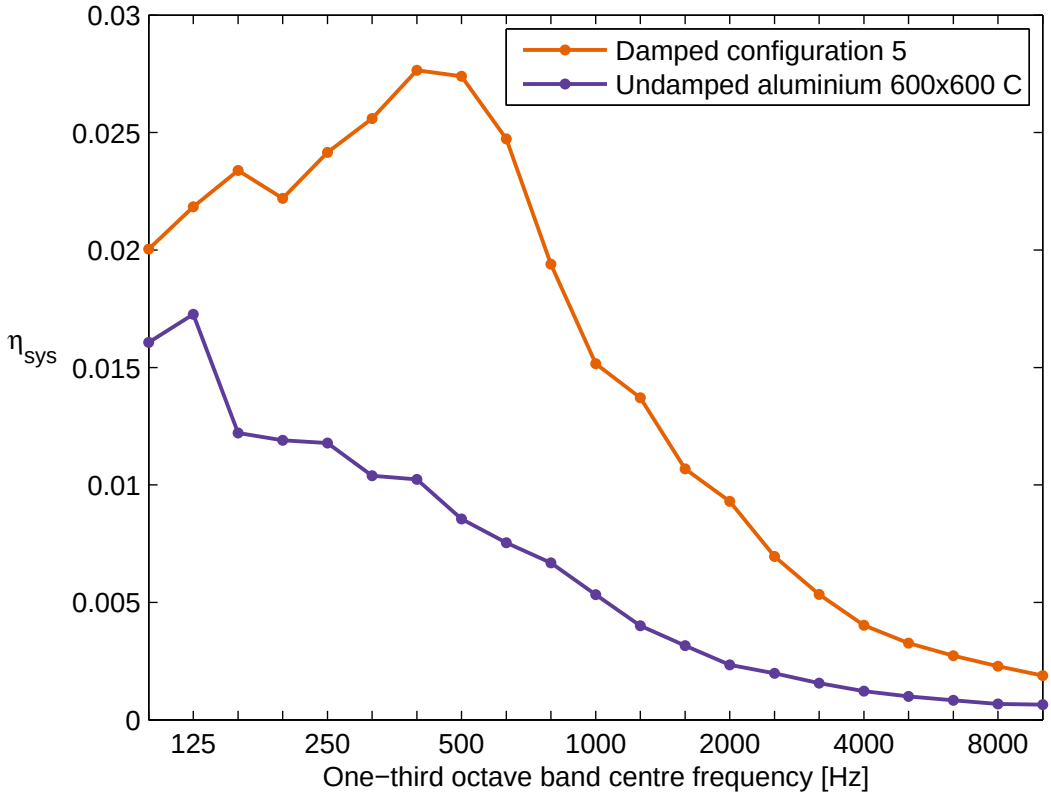

Figure 3.6: Comparison between lowest damped and greatest undamped plate performances

Configuration	Average η_{sys}	Maximum η_{sys}
Undamped aluminium clamped 600 mm × 600 mm	0.0064	0.0173
Damped configuration 5 (see Table 3.4)	0.0148	0.0277

Table 3.8: Average and maximum damping of lowest damped and greatest undamped plate performances

Influence of Variables

The influence of each DOE variable and the unconfounded two-factor interactions were calculated using the difference in average results produced by configurations where the variable in question was at a high level, and configurations where the variable was at a low level [85]. Equation 3.2 gives a generalised version of this process:

$$I_X = \overline{\eta}_{high} - \overline{\eta}_{low} \ , \tag{3.2}$$

where

I_X = Influence of variable X,

$\overline{\eta}_{high}$ = Average system loss factor of test configurations at high level of variable X,

$\overline{\eta}_{low}$ = Average system loss factor of test configurations at low level of variable X.

An example calculation can be made with reference to Table 3.4. The influence of variable B (ambient temperature) is given by

$$I_B = \frac{\eta_5 + \eta_6 + \eta_7 + \eta_8}{4} - \frac{\eta_1 + \eta_2 + \eta_3 + \eta_4}{4} \ , \tag{3.3}$$

where

η_i = System loss factor from test configuration i.

The influence of two-factor interactions was calculated in a similar manner. The high and low values of two-factor interactions were determined by multiplying the two variable levels together for each test configuration. For example, if the influence of the two-factor interaction AB is examined, a low level of both A and B is considered a high level of AB, along with a high level of both A and B. Conversely, a high level A paired with a low level of B, or vice versa, results in a low level of AB. This yields the following equation for the influence of AB:

$$I_{AB} = \frac{\eta_3 + \eta_4 + \eta_7 + \eta_8}{4} - \frac{\eta_1 + \eta_2 + \eta_5 + \eta_6}{4} \ . \tag{3.4}$$

As a loss factor value was obtained at each one-third octave band centre frequency for every test configuration, it was necessary to select a meaningful single value of η_{sys} from each test configuration to calculate the influence of each variable.

Both the average η_{sys} and maximum η_{sys} values across the frequency range were considered to determine whether differing influences were observed between the two performance metrics. These values are shown in Table 3.7.

The influence of each variable using the average and maximum system loss factor values are shown in Figures 3.7 and 3.8 respectively. The calculated values of influence were normalised by the maximum influence value to better display the relative performance of each variable. Error bars indicate one standard deviation for the calculated values.

It was also possible to compare results from individual one-third octave bands to track how the influence of each variable changed with frequency. Figure 3.9 shows the results from these calculations which were also normalised by the maximum influence value.

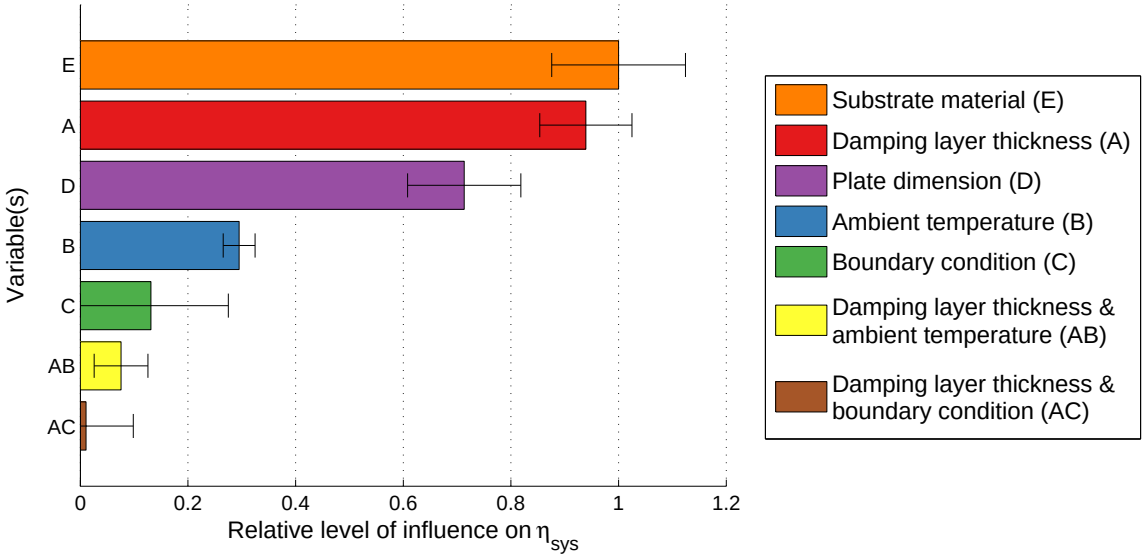

Figure 3.7: Influence of variables on damping performance using one-third octave band average η_{sys} values

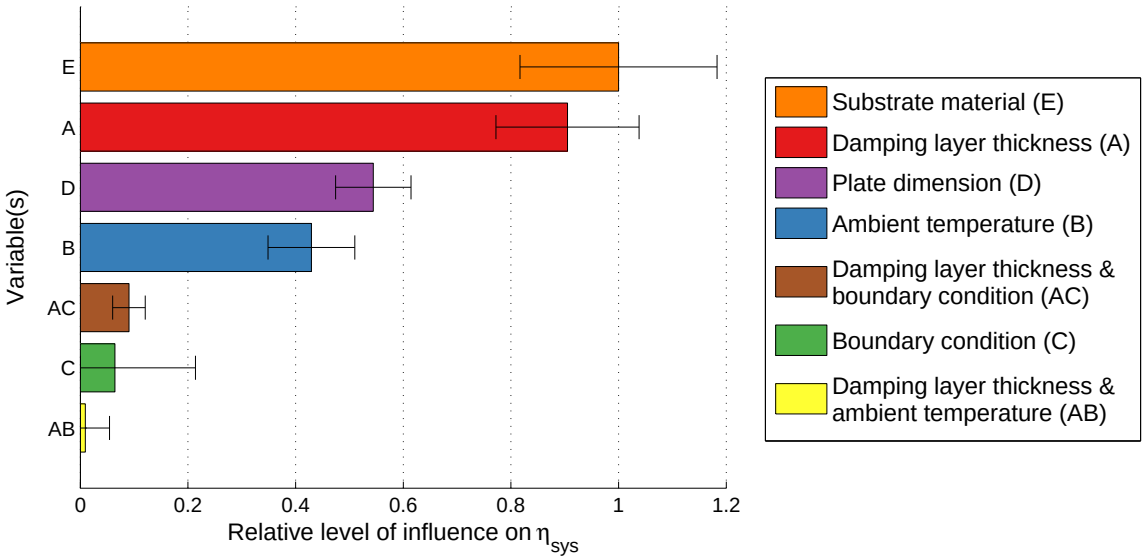

Figure 3.8: Influence of variables on damping performance using maximum η_{sys} values

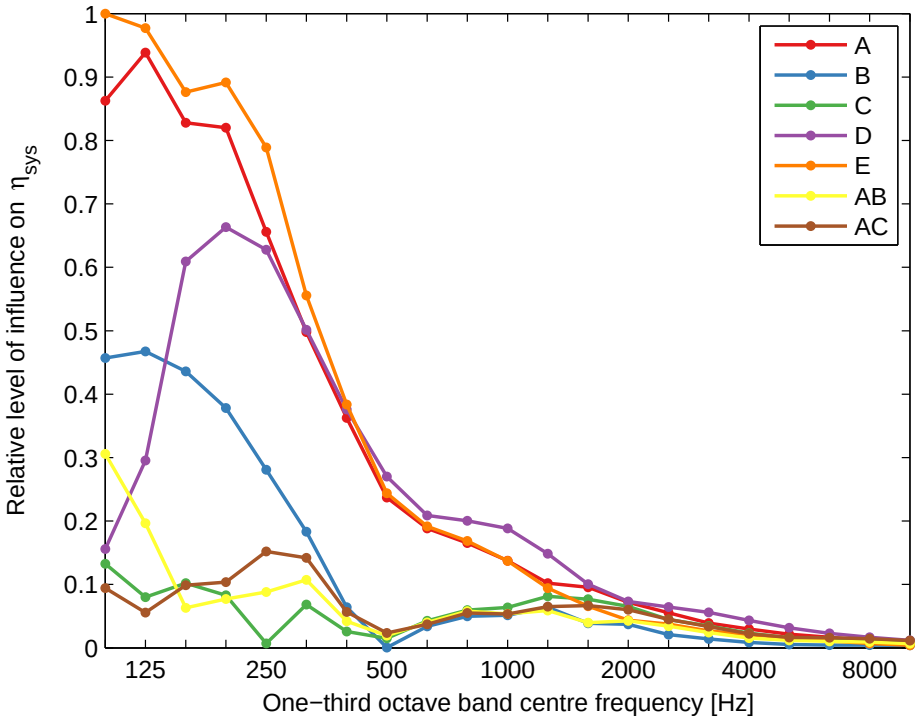

Figure 3.9: Change of variable influence with frequency

From Figures 3.7 and 3.8 it is clear that the substrate material (E) consistently had the greatest influence on the damping performance of the overall system, followed closely by the damping layer thickness (A) and the plate dimension (D). Plate boundary conditions (C) and the two-factor interactions, AB and AC, were found to have negligible influence on the system loss factor. The minimal influence of the two-factor interactions indicated that the initial confounding assumption of single variables providing greater influence was reasonable. Figure 3.9 indicated that plate dimension became the most influential variable at frequencies 500 Hz and above. It also showed that there was clear separation of variable influence at frequencies approximately 1000 Hz and below, but influence levels tended to converge at higher frequencies.

The gradient between high and low values of each variable indicated the setting which

provided the greater system loss factor value. Variable gradients produced using average values of η_{sys} from each one-third octave band are displayed in Figure 3.10. A positive gradient indicated that greater damping was achieved by the high level of a variable, and a negative gradient indicated that the low level of a variable produced the greater damping performance. The gradient magnitude also indicated the degree of influence. A small gradient magnitude indicated that there was little change in the damping performance between high and low levels of a variable, and hence that variable has little influence on damping performance. The opposite was true for large gradient magnitudes.

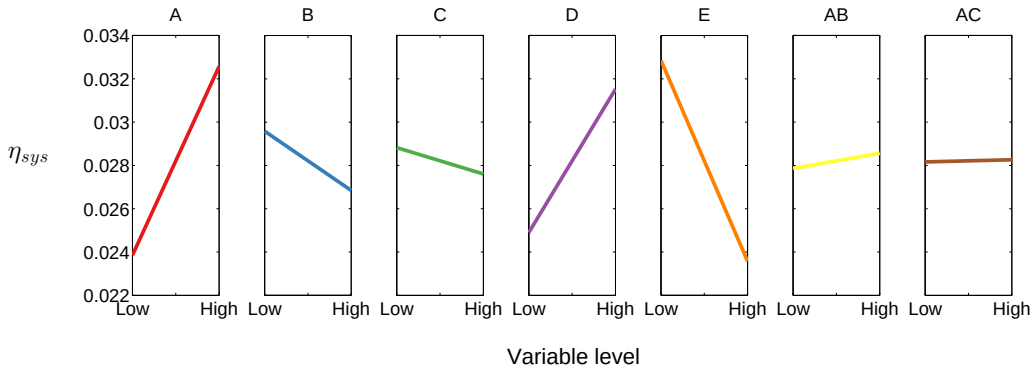

Figure 3.10: Influence gradients using one-third octave band average η_{sys} values

The results show that greater damping was achieved with:

- the thicker damping layer
- the lower temperature
- simply supported boundary conditions
- the larger plate size
- the aluminium base plate

These results were consistent with several expected outcomes. A thicker damping layer would result in a greater level of damping up to a particular thickness ratio [7]. The glass

transition temperature (maximum damping point) of the damping material used was approximately 18 °C [88], so 20 °C was expected to produce higher damping as it is the closest to this temperature point.

A notable result from the experiment was the influence of substrate material outperforming a doubling of the damping layer thickness. The significant increase in damping performance using an aluminium base plate over a steel base plate was most likely due to the differences in stiffness between the two materials. A plate with lower bending stiffness would produce greater displacement amplitudes compared to a stiffer plate given the same input excitation energy. Larger vibration amplitudes would result in greater extensional straining in the ULD layer and consequently a greater damping efficiency. This behaviour could also be observed with the plate size variable. The large plate systems would facilitate greater deflections than their smaller counterparts, and would consequently produce greater damping performance.

Another significant result from the experiment was the relatively low influence of boundary conditions. Simply-supported edges provided only a 1.04 factor increase in damping over clamped edges. This outcome was important from a treatment application point of view as it indicated that similar damping performance could be expected regardless of plate clamping arrangements for ULD treatments. However, due to the clamping arrangements used in testing, the values used to produce these results may have been less reliable than other variables studied in the experiment.

The simply-supported boundary conditions were achieved using rods rather than true knife edge supports. Consequently the deflection of the plates about the contact points may have followed the curvature of the rod surfaces. Alignment of the simply-supported clamps either side of the plates was unlikely to have been perfect, producing further deviations from

true simply-supported boundary condition behaviour. The damping performance measured during tests in the simply-supported configuration may have been greater than otherwise expected due to the clamping quality. An audible rattle was apparent in many of the simply-supported tests and the clamp arrangement introduced multiple areas where inter-facial friction could increase damping performance. The variability in the results produced for the boundary condition variable was also clear in Figures 3.7 and 3.8. Performance of the plate edge condition fixtures used in the experiment is explored in Section 3.4.3 below.

The two level designs used in this experiment accounted for linear effects of variables. The variable levels for damping layer thickness and ambient temperature were selected in part to produce linear responses. However, it was unknown whether the other variables deviated from the assumed linear response behaviour. This was perhaps most important for the plate size variable as the aspect ratios of the two levels selected were not linearly related. Edge condition and substrate material, both being qualitative rather than quantitative variables, had discrete levels and consequently the linearity of the response could not be predicted.

3.4.3 Edge Condition Check

Behaviour of the edge condition fixtures was explored by measuring the frequency response of undamped aluminium and steel plates fixed in the simply-supported frames and clamped frames (see Figure 3.1 and Appendix A.8). The measured resonant frequencies produced by these experiments was compared to a variety of analytically predicted modal frequencies for these plate materials, geometries and edge conditions.

Analytical Models

Several analytical models for resonant plate vibration were considered for both simply-supported and clamped edge conditions. Multiple analytical models were considered to obtain a range of predicted modal frequency results. The models presented in the books by

Leissa [89] and Pilkey [90] were used. These included models for simply-supported edge conditions by Warburton, Leissa, Pilkey and Janich, and models for clamped edge conditions by Warburton, Pilkey, Janich, Galin and Bolotin. Common variables used in the models included:

ω_{mn} = modal frequency [rad.s^{-1}] ,

m, n = mode indexes (1, 2, 3, ...) ,

a = plate length [m] ,

b = plate width ($b < a$) [m] ,

β = aspect ratio, a/b ,

ρ_s = surface density [kg.m^{-2}] ,

D = plate flexural rigidity [Pa m^3], which is defined by

$$D = \frac{Eh^3}{12(1-\nu^2)} \,, \tag{3.5}$$

where

E = elastic modulus [Pa] ,

h = plate thickness [m] ,

ν = Poissons ratio .

Standard values of elastic modulus and Poisson's ratio of aluminium and steel were used [91]. Density values were calculated from the measured mass of the plates. These values are displayed in Table 3.9. The surface density, ρ_s, required in the models was calculated by multiplying the measured material volumetric densities, ρ, by the thickness of the modelled plates.

Material	E [GPa]	ν	ρ [kg.m^{-3}]
Aluminium	69	0.33	2670
Steel	207	0.30	7575

Table 3.9: Model material property values

The plate dimensions arising from the two plate sizes and two edge condition test fixtures are detailed in Table 3.10.

Plate	Edge Conditions	
	Simply-supported	Clamped
Small	569 mm × 569 mm	544 mm × 544 mm
Large	1520 mm × 919 mm	1495 mm × 895 mm

Table 3.10: Plate dimensions for each edge condition test fixture

The analytical models used for simply-supported and clamped plate modal frequencies are summarised in Table 3.11. The variables contained within each model are defined in Appendix A.1.

Model	Simply-supported	Clamped
Warburton	$\omega_{mn}^2 = \frac{\pi^4 D}{a^4 \rho_s}\left(m^4 + n^4\beta^4 + 2\beta^2\left(\nu m^2 n^2 + (1-\nu)m^2 n^2\right)\right)$	$\omega_{mn}^2 = \frac{\pi^4 D}{a^4 \rho_s}\left(A_x^4 + A_y^4\beta^4 + 2\beta^2\left(\nu B_x B_y + (1-\nu)B_x B_y\right)\right)$
Janich	$\omega_{11}^2 = \frac{\pi^4 DA}{a^4 \rho_s B}$	$\omega_{11}^2 = \frac{\pi^4 DA}{a^4 \rho_s B}$
Pilkey	$\omega_{mn} = \frac{\lambda_{mn}}{a^2}\sqrt{\frac{D}{\rho_s}}$	$\omega_{mn} = \frac{\lambda_{mn}}{a^2}\sqrt{\frac{D}{\rho_s}}$
Leissa	$\omega_{mn} = \left(\left(\frac{m\pi}{a}\right)^2 + \left(\frac{n\pi}{b}\right)^2\right)\sqrt{\frac{D}{\rho_s}}$	–
Galin	–	$\omega_{11} = 12\sqrt{\frac{7}{2}\left(\frac{1}{a^4} + \frac{4}{7a^2b^2} + \frac{1}{b^4}\right)}\sqrt{\frac{D}{\rho_s}}$
Bolotin[a]	–	$\omega_{mn}a^2\sqrt{\frac{\rho_s}{D}} = \begin{bmatrix} 35.10 & 72.90 & 131.63 & 210.35 \\ & 107.47 & 164.39 & 242.20 \\ & & 219.32 & 295.69 \\ & & & 370.66 \end{bmatrix}$

Table 3.11: Summary of the analytical modal frequency models used for simply-supported and clamped plates

[a]For further details of Bolotin's method, see [92]

Excitation and Response Measurement

The frequency response of the undamped plates was measured using the same accelerometer configuration, impact excitation method and testing equipment as used for the damped plate testing. Multiple impacts were used for each set of accelerometer locations in order to excite as many modes as possible. The acceleration amplitudes were passed through a Fourier transform to obtain the frequency domain response. Eight responses were measured for each plate over a frequency range of 0-800 Hz. The highest measurement sampling rate was used to maximise the response resolution.

Modal Response Comparison

The performance of the frame clamping arrangements were tested by comparing the measured modal responses of the undamped metal plates with values predicted by the various analytical models.

To better compare the measured and modelled modal frequencies, a response frequency range of 0-300 Hz was used for the small plates, and a frequency range of 0-100 Hz was used for the large plates.

Figures 3.11 - 3.18 show the response comparisons and Tables 3.12 - 3.19 show the five dominant measured modal resonances and the closest modelled modal frequencies.

The modelled resonant frequencies for the simply-supported plates were identical for all analytical models considered but differed between clamped plate models. In the clamped plate cases, the individual models were displayed within the figures.

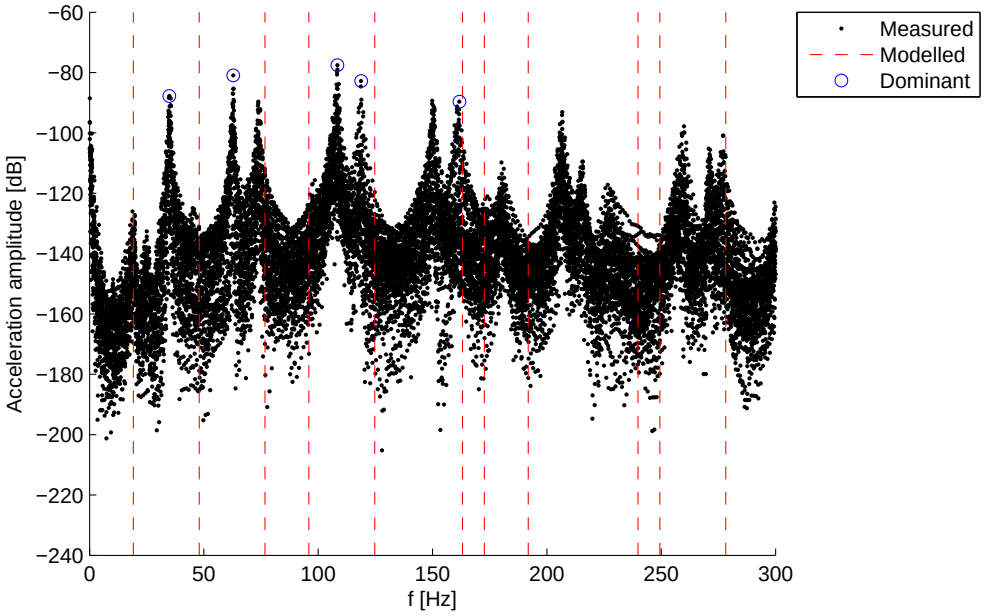

Figure 3.11: Frequency response of the small simply-supported steel plate

Dominant measured modal frequencies [Hz]	Nearest modelled modal frequency [Hz]	Model and mode number [Hz]
34.9	48.0	All models (1,2)
62.9	76.8	All models (2,2)
108.4	95.9	All models (1,3)
118.8	124.7	All models (2,3)
161.8	163.1	All models (1,4)

Table 3.12: Results for the small simply-supported steel plate

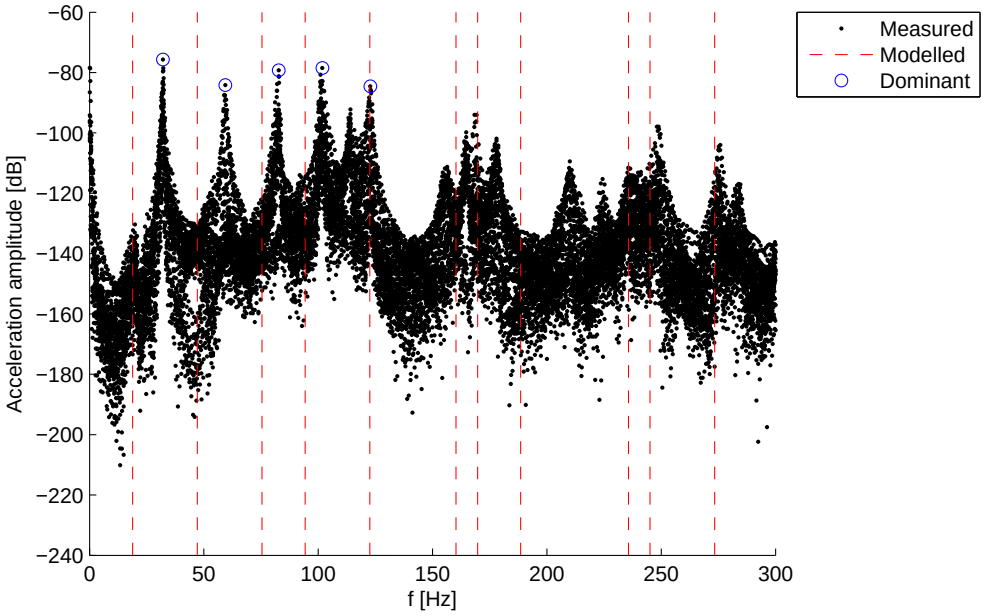

Figure 3.12: Frequency response of the small simply-supported aluminium plate

Dominant measured modal frequencies [Hz]	Nearest modelled modal frequency [Hz]	Model and mode number [Hz]
32.1	18.9	All models (1,1)
59.4	47.1	All models (1,2)
82.8	75.4	All models (2,2)
101.8	94.3	All models (1,3)
122.8	122.6	All models (2,3)

Table 3.13: Results for the small simply-supported aluminium plate

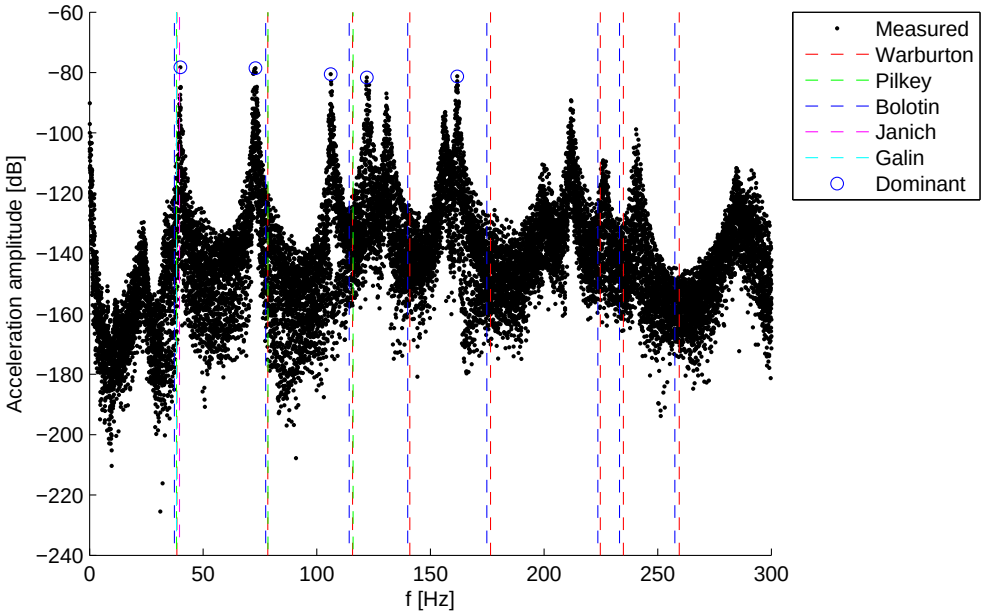

Figure 3.13: Frequency response of the small clamped steel plate

Dominant measured modal frequencies [Hz]	Nearest modelled modal frequency [Hz]	Model and mode number [Hz]
40.0	39.6	Janich (1,1)
73.0	77.5	Bolotin (1,2)
106.1	114.3	Bolotin (2,2)
122.0	115.9	Pilkey (3,3)
161.8	174.8	Bolotin (2,3)

Table 3.14: Results for the small clamped steel plate

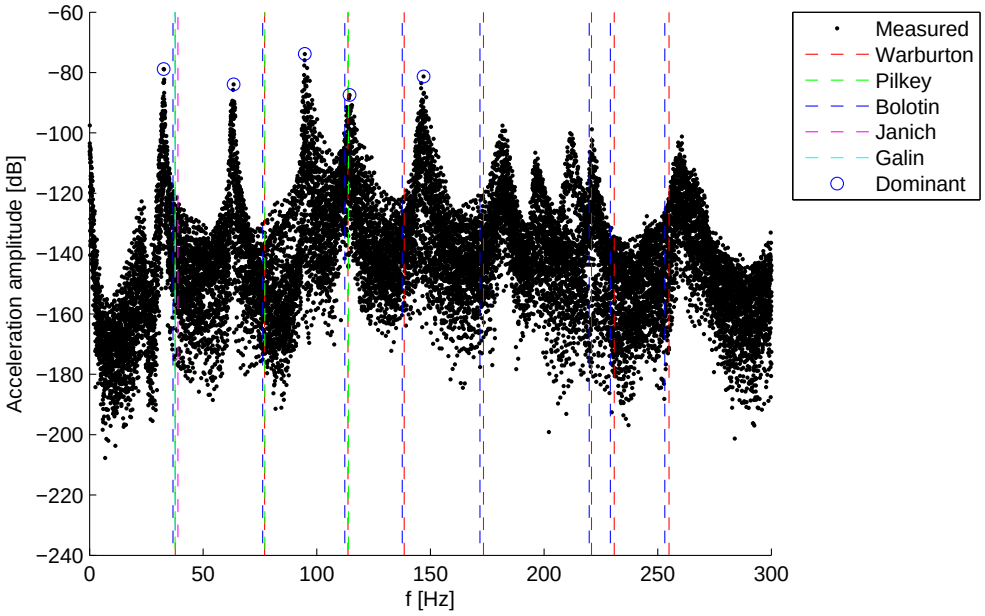

Figure 3.14: Frequency response of the small clamped aluminium plate

Dominant measured modal frequencies [Hz]	Nearest modelled modal frequency [Hz]	Model and mode number [Hz]
32.6	36.7	Bolotin (1,1)
63.4	76.2	Bolotin (1,2)
94.8	112.3	Bolotin (2,2)
114.4	113.9	Pilkey (3,3)
147.0	138.5	Warburton (1,3)

Table 3.15: Results for the small clamped aluminium plate

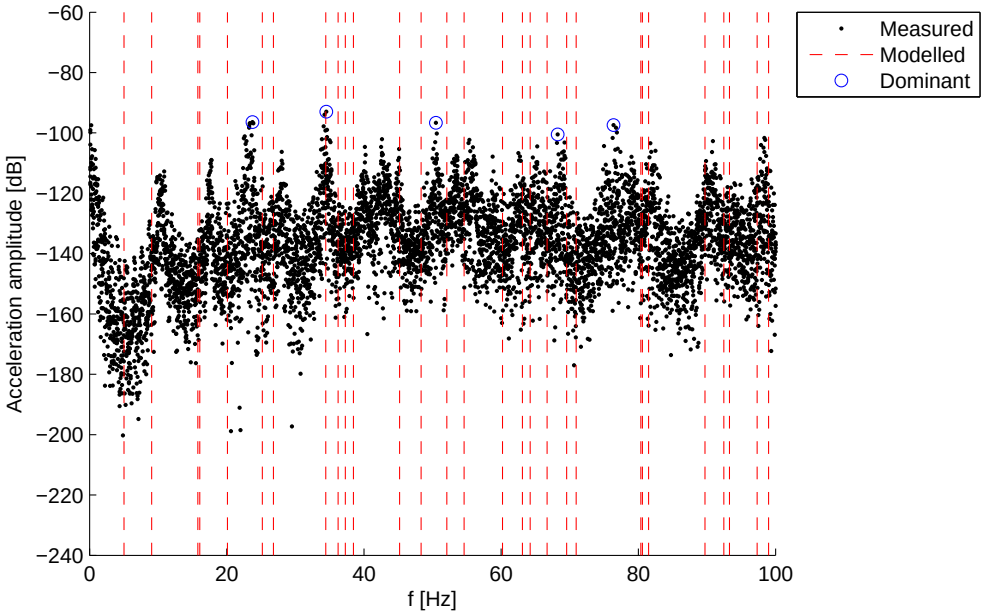

Figure 3.15: Frequency response of the large simply-supported steel plate

Dominant measured modal frequencies [Hz]	Nearest modelled modal frequency [Hz]	Model and mode number [Hz]
23.8	25.2	All models (4,1)
34.5	34.4	All models (1,3)
50.5	52.1	All models (6,1)
68.25	69.6	All models (7,1)
76.4	80.4	All models (4,4)

Table 3.16: Results for the large simply-supported steel plate

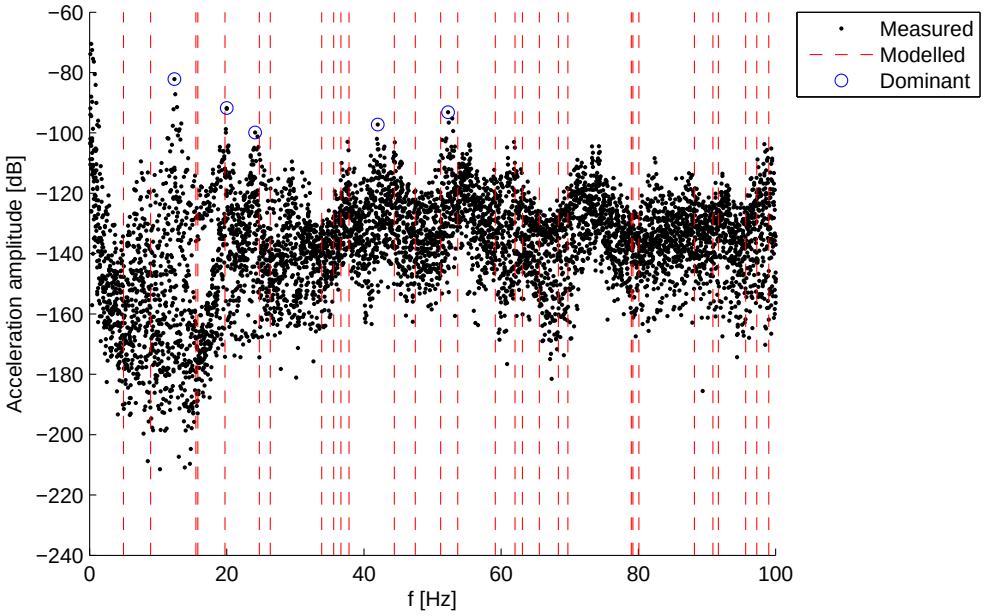

Figure 3.16: Frequency response of the large simply-supported aluminium plate

Dominant measured modal frequencies [Hz]	Nearest modelled modal frequency [Hz]	Model and mode number [Hz]
12.4	15.5	All models (3,1)
20.0	19.7	All models (2,2)
24.1	24.8	All models (4,1)
42.0	44.4	All models (3,3)
52.3	51.2	All models (6,1)

Table 3.17: Results for the large simply-supported aluminium plate

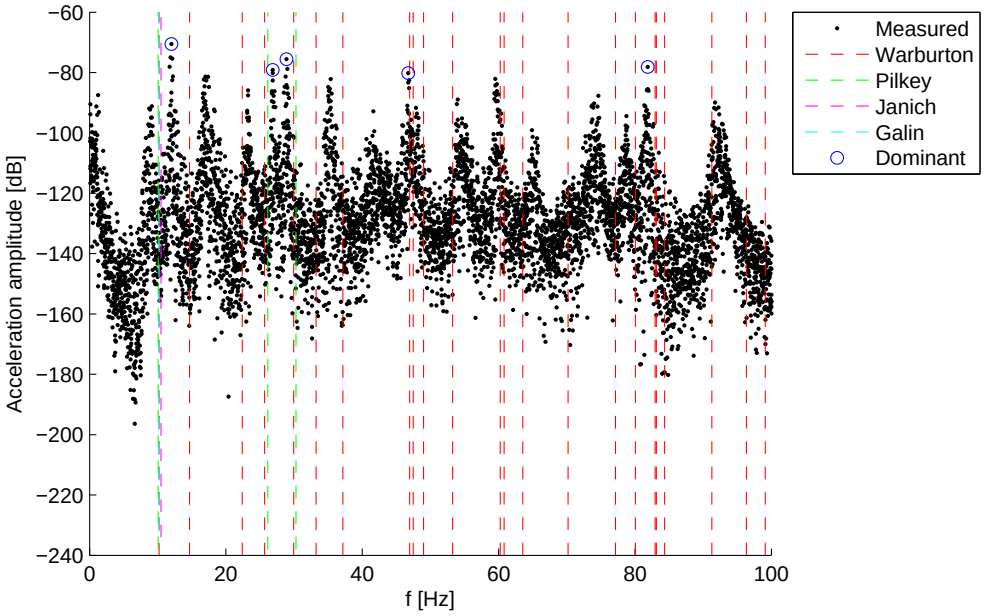

Figure 3.17: Frequency response of the large clamped steel plate

Dominant measured modal frequencies [Hz]	Nearest modelled modal frequency [Hz]	Model and mode number [Hz]
12.0	10.5	Janich (1,1)
26.9	26.1	Pilkey (2,2)
28.9	29.9	Warburton (2,2)
46.8	47.0	Warburton (5,1)
81.9	83.0	Warburton (7,1)

Table 3.18: Results for the large clamped steel plate

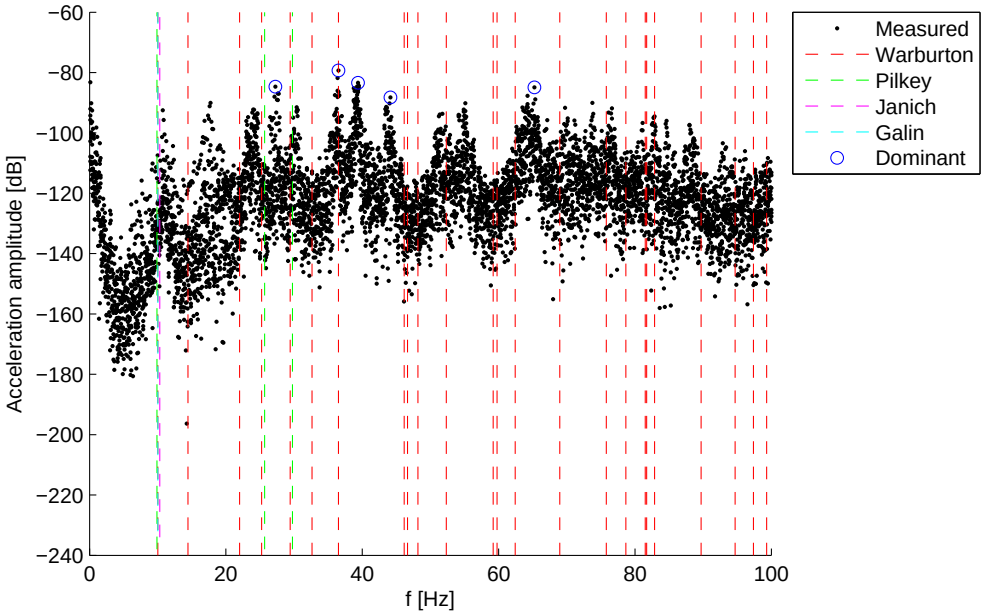

Figure 3.18: Frequency response of the large clamped aluminium plate

Dominant measured modal frequencies [Hz]	Nearest modelled modal frequency [Hz]	Model and mode number [Hz]
27.3	25.7	Pilkey (2,2)
36.5	36.5	Warburton (3,2)
39.4	36.5	Warburton (3,2)
44.1	46.1	Warburton (5,1)
65.3	62.4	Warburton (6,1)

Table 3.19: Results for the large clamped aluminium plate

From these figures and tables it is clear that the analytical models and measured responses often did not match. This behaviour was not limited to any particular configuration, although the measured responses of the large plates were more likely to lie close to predicted values due to their asymmetric aspect ratios producing a greater range of modes in the frequency range considered. In many cases less dominant resonances appeared to agree well with predicted values.

As mode shapes were not measured during experimentation, it was not possible to know with any certainty whether modelled and measured resonances which lay close to one another were behaviour caused by the same mode shape, or whether they were different modes which happened to coincide. This was particularly true for the numerous modes predicted for the large plates.

Differences between the measured and predicted resonances may have been due to the assumed material properties used in the models or the difficulty in achieving true clamped and simply-supported edge conditions during testing. The audible rattle observed in several of the simply supported tests indicating non-uniform clamping.

These results show that the experimental test fixture used deviated from truly simply-supported and clamped edge conditions. This behaviour may have affected the boundary condition influence (variable C) found in the previous DOE study. It may also explain the large variability in variable C seen in Figrues 3.7 and 3.8.

3.5 Summary

The relative influence of five variables on the system damping performance of metal plates was investigated using Design of Experiments methodology. Damping layer thickness, ambient temperature, boundary conditions, plate size and substrate material were each studied at two levels. A fractional factorial design was employed to reduce the number of test configurations required to gain useful data and meet time and resource constraints. The fractional design resulted in eight test configurations.

The clamping arrangements used were evaluated by comparing the resonant response of the various undamped plate and clamp configurations to several analytical models for plate natural frequencies. Some responses were well matched to the modelled results, while others deviated from the predicted responses. Large deviations between measured and modelled responses were attributed to non-uniform clamping and the material properties used in the models.

Values of system loss factor were obtained using an impulse decay method similar to that outlined in ISO 10848-1 [87]. Forty eight vibration decay measurements were recorded for each test configuration.

Of the five variables studied, substrate material was found to have the greatest influence on both one-third octave band average damping and maximum damping performance of the plate systems. Aluminium plates produced a 1.39 fold increase in average damping and 1.51 fold increase in maximum damping over the steel plate configurations.

Damping layer thickness was found to be the second most influential variable, with a 2:1 damping layer to substrate layer thickness ratio producing a 1.37 fold increase in average damping and a 1.45 fold increase in maximum damping over a 1:1 thickness ratio.

When tracking variable influence over each one-third octave band, it was found that the influence of plate dimension overtook the substrate material variable for frequencies 500 Hz and above. This result is perhaps less significant than it first appears as the two plate dimension levels selected were constrained by the testing facilities at hand and consequently were not dimensions that would likely be found in practice.

An interesting result from the study was that boundary conditions had little influence on the measured system loss factor. Simply-supported edge conditions yielded an increase in damping performance by a factor of 1.04 for average damping and 1.03 for maximum damping over fully clamped edge conditions. However, the simply-supported clamping arrangements used during testing may have added measurable dissipative effects through interfacial friction making this result inconclusive.

The unconfounded two-factor interactions, AB and AC, were found to have little influence on the system damping performance. For a fuller understanding of the two and three-factor interactions involved with this experiment a full factorial design would be required.

Chapter 4

Patterned Fibre Composite Constrained Layer Damping

4.1 Introduction

The use of composite materials is becoming increasingly prevalent in a wide range of industries. Many of the application areas for such materials are in structures and environments where high levels of vibration are also present. This is particularly true in the marine industry with vibration excitation provided by numerous and varied sources.

A method of increasing the damping characteristics of composite constructions is through inclusion of viscoelastic damping layers within a laminate lay-up. The damping performance of these constructions is influenced by the shear strains within the viscoelastic layers in the same way as constrained layer damping (CLD) surface treatments. Use of asymmetric orthotropic layers surrounding a viscoelastic core produces coupling between extension and twist behaviours. This coupling can be used to induce in-plane transverse shear strains. Previous research into the use of 'zig-zag' and continuous sinusoidal fibre patterns in such a configuration found that the damping performance of these composite damping materials

was affected by the fibre pattern wavelength and maximum fibre angle [59, 62, 75, 76]. The pattern wavelength tended to shift the frequency at which maximum damping occurred, while the maximum fibre angle shifted the maximum damping value achieved. Previous research only considered simple constant sine wave patterns. An example is shown in Figure 4.1.

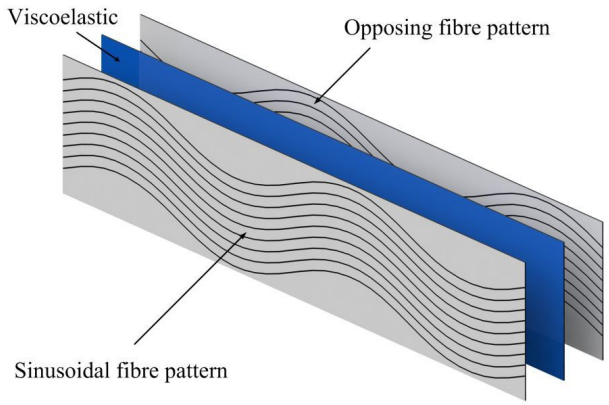

Figure 4.1: Simple sinusoidal fibre pattern

It is of interest to explore what effect more complex fibre patterns have on the damping spectrum of composite sandwich arrangements with a viscoelastic core material. An example of a more complex pattern is shown in Figure 4.2.

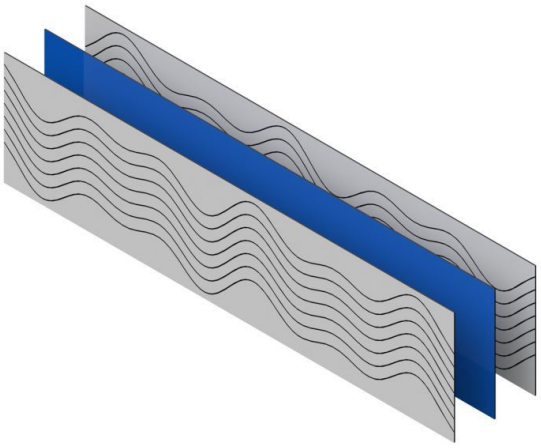

Figure 4.2: Complex sinusoidal fibre pattern

The finite element (FE) method is a tool that can be used to simulate the behaviour of materials and structures. This makes it useful for the development and evaluation of new materials, particularly when the cost of the materials or their fabrication prohibits extensive experimental evaluation.

The proposed composite damping treatment, termed complex patterned fibre constrained layer damping (CPF-CLD), presents fabrication challenges which prohibit economic production of large volumes of test specimens. Hence, finite element analysis (FEA) is an excellent technique for an investigation of this composite damping material.

Numerous commercial FEA packages exist, however these tend to be limited in the damping models available for dynamic studies. ANSYS 14 was available and could be modified to account for the damping requirements of the study using the code interface ANSYS Classic. However, alteration of fibre geometries between patterns would be laborious. Consequently the model was constructed in MATLAB allowing exact control over the entire model. Constructing the model from code also provided a greater understanding of the principles involved with FE modelling.

This chapter details the development of a finite element model (FEM) in MATLAB for the CPF-CLD material, validation of the model through experiment, and an exploration of the modal damping behaviour of various complex fibre patterns.

4.2 Model Development

The CPF-CLD material varies from conventional composite laminate constructions in several significant areas:

- Structural properties vary along the length of the sample depending on the local fibre angle

- In-plane transverse shear strains are present due to the fibre angle phase shift between layers
- The mid ply is viscoelastic with damping and stiffness properties that vary significantly with excitation frequency
- The fibre reinforced composite face sheets would provide some material damping to the system and would also exhibit frequency dependent material properties

Element types, material models and other analysis parameters had to be correctly selected in order to properly reflect these characteristics in the model.

When modelling the dynamic behaviour of composite laminate structures, the element types selected usually fall into shell or solid element categories. Two classifications of element models are available, smeared laminate models (SLMs) or discrete laminate models (DLMs).

In SLM, individual lamina properties are combined to produce a set of equivalent laminate properties which are used to determine the global behaviour of the laminate. This approach is useful for modelling large, multi-layer systems, as the element degrees of freedom do not increase with additional layers. However, an SLM is not suitable for use with constrained viscoelastic layers because it does not allow for differential motion between plies of a laminate, behaviour which is certainly present in CPF-CLD arrangements. For this reason a discrete laminate model was developed, with individual elements representing laminae within the layered structure.

Texts on finite element modelling by Zienkiewicz and Taylor [93] and Cook et al. [94] were used in the development of the model, and reference was made to previous models of sinusoidal fibre pattern behaviour [95].

4.2.1 Element Type

It was important to consider the behaviour the model was expected to predict when selecting the element type. In this case bending and lateral in-plane displacement were of interest in order to capture the strain within the viscoelastic core.

Shell elements are often used when two dimensions of a structure are much greater than the third, as is the case with a thin beam or plate. They are also useful when significant bending or rotation is involved as both translational and rotational degrees of freedom are generally used. However, these elements are positioned at the centre of each layer and consequently do not properly capture lateral movement close to layer interfaces as there are no shared nodes between the layers.

Solid elements provide an element structure with shared nodes between layers. This element type generally uses translational degrees of freedom only. As bending vibration was the focus of this model, it was important to ensure that the solid elements were arranged appropriately to properly model the bending behaviour. Bending can be captured in solid elements, with translational degrees of freedom only, provided there is a minimum of three elements in the thickness direction. Fewer elements can result in a higher predicted bending stiffness than exists in reality.

Solid elements were selected for the model in order to account for transverse in-plane shear effects. In order to prevent shear locking, quadratic interpolation functions were used in the plane of the laminate and linear interpolation functions through the thickness. This configuration was achieved by stacking conventional 8 node plane elements, sometimes called Serendipity-8 elements, to form 16 node brick elements. The 'brick-16' arrangement is shown in Figure 4.3.

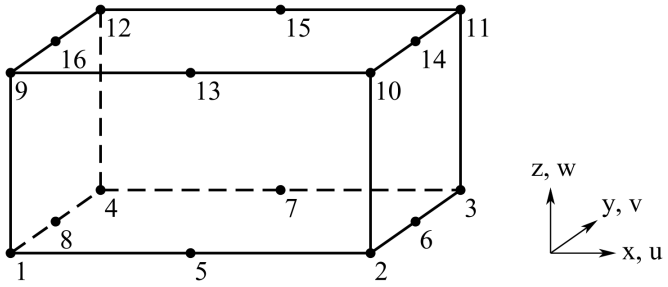

Figure 4.3: 'Brick-16' solid element

Three of these 'Brick-16' elements were stacked to represent the three layers present in the laminate construction. This produced a layered brick with 32 nodes, shown in Figure 4.4. Each node of the brick had three translational degrees of freedom only. Rotational degrees of freedom were not included as it was assumed bending would be properly accounted for by the three layers of solid elements used to represent the three layers of the beam. This assumption was validated with bending comparisons (see Section 4.3.1).

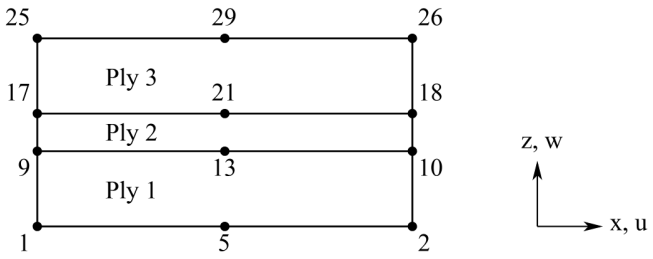

Figure 4.4: Stacked 'Brick-16' solid elements

Isoparametric Element Formulation

Isoparametric formulation facilitates solid elements taking non-rectangular shapes which may result from the structure's deformation. This is achieved by transforming a deformed solid element into a coordinate system where the solid element becomes a cube. An example of this can be seen in Figure 4.5. The new element coordinate system is defined by directions

ξ, η, and ζ which map to the global coordinate system directions x, y, and z respectively.

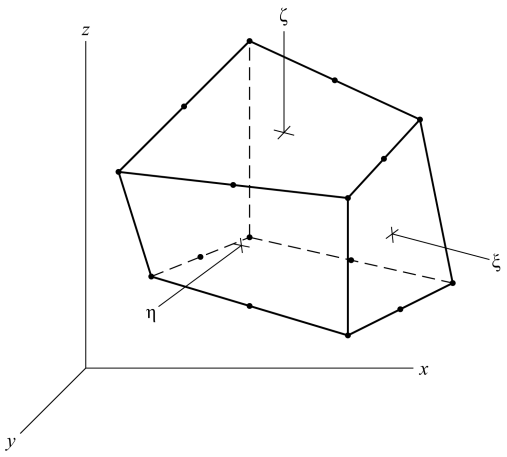

Figure 4.5: Non-rectangular hexahederal solid element

The transformation also normalises the dimensions of the element in order to simplify any differences between these values in the global coordinate system. Element edge lengths in the element coordinate system are all set to 2, with the origin located at the centre of each element. Thus, nodes are located at values of -1, 0, +1 in the ξ and η directions, and at -1 and +1 in the ζ direction.

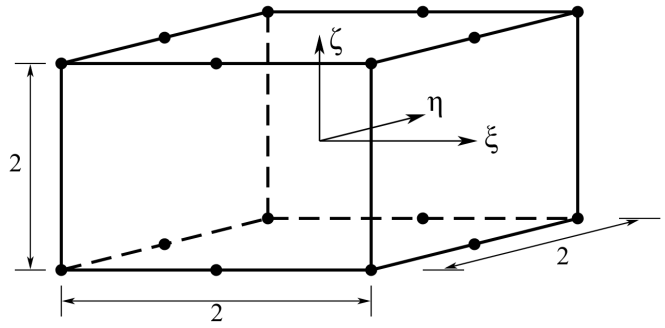

Figure 4.6: Element transformed into the element coordinate system

Interpolation Functions

The use of quadratic interpolation functions in the laminate plane and linear interpolation in the thickness direction was selected to prevent shear locking in the model. These functions were used to determine the distribution of nodal contributions through each 16-node element. The functions were built upon the layering of 8-node shell elements to create a 16-node solid element. The interpolation functions for an 8-node shell element are shown in Equation 4.1.

$$\begin{Bmatrix} W_1 \\ W_2 \\ W_3 \\ W_4 \\ W_5 \\ W_6 \\ W_7 \\ W_8 \end{Bmatrix} = \frac{1}{4} \begin{Bmatrix} (1-\xi)(1-\eta)(-\xi-\eta-1) \\ (1+\xi)(1-\eta)(\xi-\eta-1) \\ (1+\xi)(1+\eta)(\xi+\eta-1) \\ (1-\xi)(1+\eta)(-\xi+\eta-1) \\ 2(1-\xi^2)(1-\eta) \\ 2(1+\xi)(1-\eta^2) \\ 2(1-\xi^2)(1+\eta) \\ 2(1-\xi)(1-\eta^2) \end{Bmatrix} \tag{4.1}$$

As each 16-node element was equivalent to two of these shell elements stacked on one another, interpolation in the thickness direction needed to be accounted for. The requirement of each of the 16 interpolation functions was to be equal to 1 when the coordinates of its corresponding node were input, and 0 otherwise. To meet this requirement for interpolation in the thickness direction Equation 4.2 was used where h_p was the element thickness:

$$z = \frac{\zeta + 1}{2} h_p \, . \tag{4.2}$$

Using this relationship between the global thickness direction (z) and the element thickness direction (ζ), it was possible to produce the full set of interpolation functions for each 16-node element:

$$\left\{\begin{array}{c} N_1 \\ \vdots \\ N_8 \\ N_9 \\ \vdots \\ N_{16} \end{array}\right\} = \left\{\begin{array}{c} W_1 \frac{h_p - z}{h_p} \\ \vdots \\ W_8 \frac{h_p - z}{h_p} \\ W_1 \frac{z}{h_p} \\ \vdots \\ W_8 \frac{z}{h_p} \end{array}\right\}. \tag{4.3}$$

The expanded version of Equation 4.3 shows the interpolation functions in their standard form:

$$\left\{\begin{array}{c} N_1 \\ N_2 \\ N_3 \\ N_4 \\ N_5 \\ N_6 \\ N_7 \\ N_8 \\ N_9 \\ N_{10} \\ N_{11} \\ N_{12} \\ N_{13} \\ N_{14} \\ N_{15} \\ N_{16} \end{array}\right\} = \frac{1}{8} \left\{\begin{array}{c} (1-\xi)(1-\eta)(-\xi-\eta-1)(1-\zeta) \\ (1+\xi)(1-\eta)(\xi-\eta-1)(1-\zeta) \\ (1+\xi)(1+\eta)(\xi+\eta-1)(1-\zeta) \\ (1-\xi)(1+\eta)(-\xi+\eta-1)(1-\zeta) \\ 2(1-\xi^2)(1-\eta)(1-\zeta) \\ 2(1+\xi)(1-\eta^2)(1-\zeta) \\ 2(1-\xi^2)(1+\eta)(1-\zeta) \\ 2(1-\xi)(1-\eta^2)(1-\zeta) \\ (1-\xi)(1-\eta)(-\xi-\eta-1)(1+\zeta) \\ (1+\xi)(1-\eta)(\xi-\eta-1)(1+\zeta) \\ (1+\xi)(1+\eta)(\xi+\eta-1)(1+\zeta) \\ (1-\xi)(1+\eta)(-\xi+\eta-1)(1+\zeta) \\ 2(1-\xi^2)(1-\eta)(1+\zeta) \\ 2(1+\xi)(1-\eta^2)(1+\zeta) \\ 2(1-\xi^2)(1+\eta)(1+\zeta) \\ 2(1-\xi)(1-\eta^2)(1+\zeta) \end{array}\right\}. \tag{4.4}$$

Each node had three translational degrees of freedom. Interpolation functions were applied to each degree of freedom resulting in a 3×48 interpolation function matrix of the form

$$[\mathbf{N}] = \begin{bmatrix} N_1 & \cdots & N_{16} & 0 & \cdots & 0 & 0 & \cdots & 0 \\ 0 & \cdots & 0 & N_1 & \cdots & N_{16} & 0 & \cdots & 0 \\ 0 & \cdots & 0 & 0 & \cdots & 0 & N_1 & \cdots & N_{16} \end{bmatrix} . \tag{4.5}$$

The interpolation functions were used to define locations and displacements within each element using the relations in Equations 4.6 and 4.7 respectively:

$$\begin{Bmatrix} x \\ y \\ z \end{Bmatrix} = \begin{Bmatrix} \sum N_i x_i \\ \sum N_i y_i \\ \sum N_i z_i \end{Bmatrix} = [\mathbf{N}]\{\mathbf{c}\} , \tag{4.6}$$

$$\begin{Bmatrix} u \\ v \\ w \end{Bmatrix} = \begin{Bmatrix} \sum N_i u_i \\ \sum N_i v_i \\ \sum N_i w_i \end{Bmatrix} = [\mathbf{N}]\{\mathbf{a}\} , \tag{4.7}$$

where nodal locations and displacements were defined by Equations 4.8 and 4.9:

$$\{\mathbf{c}\} = \{x_1 \cdots x_{16} \;\; y_1 \cdots y_{16} \;\; z_1 \cdots z_{16}\}^T , \tag{4.8}$$

$$\{\mathbf{a}\} = \{u_1 \cdots u_{16} \;\; v_1 \cdots v_{16} \;\; w_1 \cdots w_{16}\}^T . \tag{4.9}$$

Element Property Matrices

In order to perform finite element analysis the matrices defining the element properties, such as stiffness and mass, were required. These matrices were of the form

$$\int_V [\mathbf{\Pi}] \, dV , \tag{4.10}$$

where $[\mathbf{\Pi}]$ depended on the interpolation function matrix $[\mathbf{N}]$ or its derivatives with respect to global coordinates.

Transformation between the element coordinate system and the global coordinate system was achieved using the Jacobian matrix [**J**]. This matrix was used to map the physical lengths ∂x, ∂y and ∂z to the reference lengths $\partial \xi$, $\partial \eta$ and $\partial \zeta$. Equation 4.11 gives the form of the Jacobian matrix, where comma separated subscripts indicate partial derivatives in that dimension:

$$[\mathbf{J}] = \begin{bmatrix} x_{,\xi} & y_{,\xi} & z_{,\xi} \\ x_{,\eta} & y_{,\eta} & z_{,\eta} \\ x_{,\zeta} & y_{,\zeta} & z_{,\zeta} \end{bmatrix} = \begin{bmatrix} \sum N_{i,\xi} x_i & \sum N_{i,\xi} y_i & \sum N_{i,\xi} z_i \\ \sum N_{i,\eta} x_i & \sum N_{i,\eta} y_i & \sum N_{i,\eta} z_i \\ \sum N_{i,\zeta} x_i & \sum N_{i,\zeta} y_i & \sum N_{i,\zeta} z_i \end{bmatrix} . \tag{4.11}$$

In general the derivatives of a variable ϕ (e.g. $\phi = u$, v or w), with respect to the element coordinate system, were defined as

$$\begin{aligned} \frac{\partial \phi}{\partial \xi} &= \frac{\partial \phi}{\partial x}\frac{\partial x}{\partial \xi} + \frac{\partial \phi}{\partial y}\frac{\partial y}{\partial \xi} + \frac{\partial \phi}{\partial z}\frac{\partial z}{\partial \xi} , \\ \frac{\partial \phi}{\partial \eta} &= \frac{\partial \phi}{\partial x}\frac{\partial x}{\partial \eta} + \frac{\partial \phi}{\partial y}\frac{\partial y}{\partial \eta} + \frac{\partial \phi}{\partial z}\frac{\partial z}{\partial \eta} , \\ \frac{\partial \phi}{\partial \zeta} &= \frac{\partial \phi}{\partial x}\frac{\partial x}{\partial \zeta} + \frac{\partial \phi}{\partial y}\frac{\partial y}{\partial \zeta} + \frac{\partial \phi}{\partial z}\frac{\partial z}{\partial \zeta} . \end{aligned} \tag{4.12}$$

Use of the Jacobian matrix [**J**] and its inverse [**Γ**] allowed transformation between the derivatives of the element and global coordinate systems, as shown in Equations 4.13 and 4.14.

$$\begin{Bmatrix} \phi_{,\xi} \\ \phi_{,\eta} \\ \phi_{,\zeta} \end{Bmatrix} = [\mathbf{J}] \begin{Bmatrix} \phi_{,x} \\ \phi_{,y} \\ \phi_{,z} \end{Bmatrix} \tag{4.13}$$

$$\begin{Bmatrix} \phi_{,x} \\ \phi_{,y} \\ \phi_{,z} \end{Bmatrix} = [\mathbf{\Gamma}] \begin{Bmatrix} \phi_{,\xi} \\ \phi_{,\eta} \\ \phi_{,\zeta} \end{Bmatrix} \tag{4.14}$$

Having established these transformations, the general form of the element stiffness and

mass matrices could be defined using the element coordinate system. The element stiffness matrix, $[\mathbf{k}^*]$, was defined by

$$\underset{48\times48}{[\mathbf{k}^*]} = \int_{-1}^{1}\int_{-1}^{1}\int_{-1}^{1} \underset{48\times6}{[\mathbf{B}]}^T \underset{6\times6}{[\mathbf{E}^*]} \underset{6\times48}{[\mathbf{B}]}\ J\ d\xi\ d\eta\ d\zeta\ , \tag{4.15}$$

where

$[\mathbf{B}]$ = the element strain matrix ,

$[\mathbf{E}^*]$ = the complex material constitutive matrix ,

J = the determinant of the Jacobian matrix, $det[\mathbf{J}]$.

The element strain matrix was defined as

$$[\mathbf{B}] = \begin{bmatrix} N_{1,x} & \cdots & N_{16,x} & \mathbf{0} & & & \mathbf{0} & \\ & \mathbf{0} & & N_{1,y} & \cdots & N_{16,y} & \mathbf{0} & \\ & \mathbf{0} & & & \mathbf{0} & & N_{1,z} & \cdots & N_{16,z} \\ & \mathbf{0} & & N_{1,z} & \cdots & N_{16,z} & N_{1,y} & \cdots & N_{16,y} \\ N_{1,z} & \cdots & N_{16,z} & & \mathbf{0} & & N_{1,x} & \cdots & N_{16,x} \\ N_{1,y} & \cdots & N_{16,y} & N_{1,x} & \cdots & N_{16,x} & & \mathbf{0} & \end{bmatrix} . \tag{4.16}$$

The material constitutive matrix $[\mathbf{E}^*]$ was dependent on the material properties of the element under consideration and the orientation of the material within the element. The constitutive matrix was complex due to the complex material properties used in the model. Material property transformations were applied to $[\mathbf{E}^*]$ for the outer two plies in order to account for the varying fibre orientation along the length of the structure studied. Both the complex material properties and property transformations are discussed in greater depth in Section 4.2.2.

The element mass matrix, $[\mathbf{m}]$, was defined by

$$\underset{48\times48}{[\mathbf{m}]} = \int_{-1}^{1}\int_{-1}^{1}\int_{-1}^{1} \rho \underset{48\times3}{[\mathbf{N}]^T} \underset{3\times48}{[\mathbf{N}]}\ J\ d\xi\ d\eta\ d\zeta\ , \tag{4.17}$$

where

ρ = density of the material within the element [kg.m^{-3}] .

As the element mass matrix was calculated using the same interpolation functions as used in the computation of the element stiffness matrix, the mass matrix was classed as 'consistent'.

An explicit element damping matrix was not required as the damping behaviour was incorporated by the imaginary terms of $[\mathbf{k}^*]$.

The integration required to evaluate $[\mathbf{k}^*]$ and $[\mathbf{m}]$ was performed using Gauss Quadrature [93, 94]. The general form for this numerical integration in three dimensions is

$$I = \int_{-1}^{1}\int_{-1}^{1}\int_{-1}^{1} \Pi(\xi,\eta,\zeta)\ d\xi\ d\eta\ d\zeta \approx \sum_i \sum_j \sum_k W_i W_j W_k\ \ \Pi(\xi_i,\eta_j,\zeta_k)\ , \tag{4.18}$$

where the function $\Pi(\xi,\eta,\zeta)$ is sampled at set points (ξ_i,η_j,ζ_k) within each element and multiplied by corresponding weighting functions W_i, W_j and W_k.

As quadratic interpolation functions were used in the laminate plane and linear functions in the thickness direction, three Gauss points were used in the ξ and η directions, and two Gauss points in the ζ direction. These Gauss points and associated weighting functions were

$$\begin{aligned}
\xi &= \{-\sqrt{0.6},\ \ 0,\ \ \sqrt{0.6}\}\ , & W_\xi &= \{5/9,\ \ 8/9,\ \ 5/9\}\ , \\
\eta &= \{-\sqrt{0.6},\ \ 0,\ \ \sqrt{0.6}\}\ , & W_\eta &= \{5/9,\ \ 8/9,\ \ 5/9\}\ , \\
\zeta &= \{-\sqrt{0.3},\ \ \sqrt{0.3}\}\ , & W_\zeta &= \{1,\ \ 1\}\ .
\end{aligned}$$

The numerical integration procedure used to generate each element stiffness and mass matrix followed the procedure outlined in Figure 4.7.

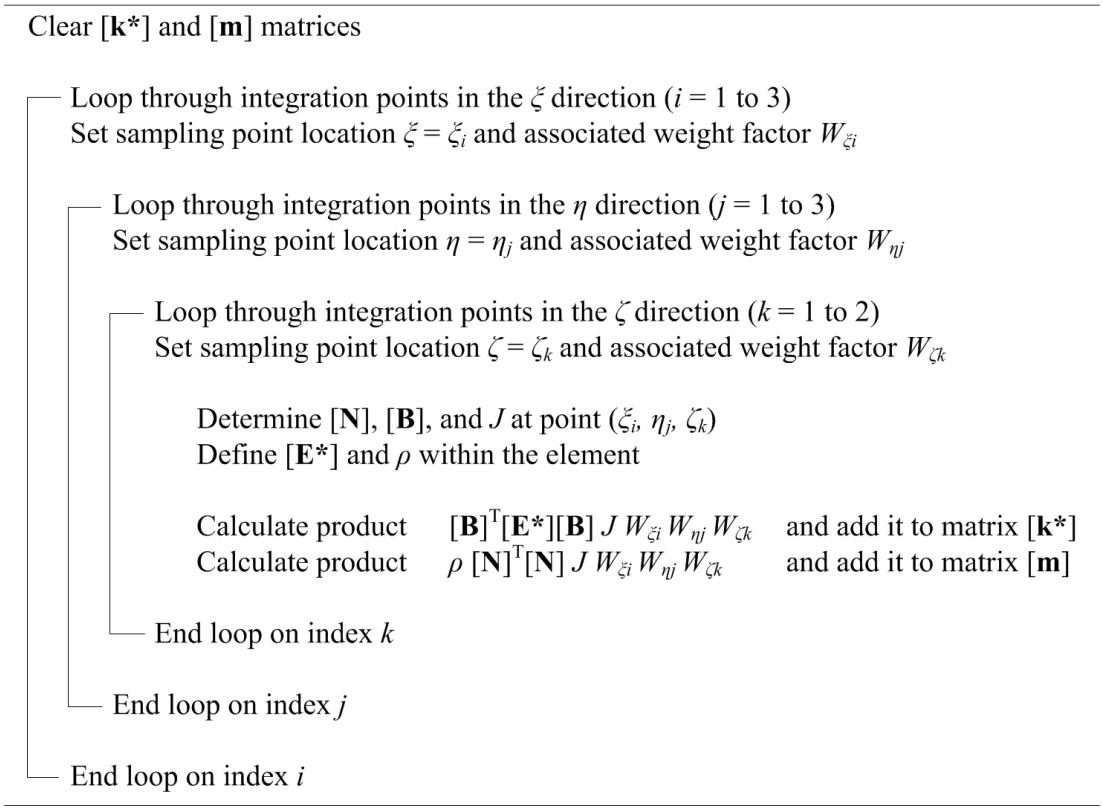

Figure 4.7: Computational procedure for generating element stiffness and mass matrices

4.2.2 Material Models

Calculation of the element stiffness matrices required the use of appropriate material models for the constituent materials. The fibre layers were modelled as a transversely isotropic material while the damping layer was assumed to be isotropic. The damping properties for both of these material types were accounted for using complex constitutive matrices [$\mathbf{E}^*$]. The complexity of the stiffness matrices was a result of complex material properties within the constitutive equations for each of the materials. Many of these properties were also frequency dependent and models for the frequency dependent behaviour were required in

order to produce a useful finite element model.

As seen in Equation 4.15, the complex 6×6 material constitutive matrix $[\mathbf{E}^*]$ was used to derive the 48×48 stiffness matrix $[\mathbf{k}^*]$ for each 'brick-16' element. For the isotropic viscoelastic damping material (VEM) the material constitutive matrix was defined as

$$[E^*]_{VEM} = \frac{2G'_v(1+i\eta_v)}{1-2\nu_v} \begin{bmatrix} 1-\nu_v & \nu_v & \nu_v & 0 & 0 & 0 \\ \nu_v & 1-\nu_v & \nu_v & 0 & 0 & 0 \\ \nu_v & \nu_v & 1-\nu_v & 0 & 0 & 0 \\ 0 & 0 & 0 & \frac{1-2\nu_v}{2} & 0 & 0 \\ 0 & 0 & 0 & 0 & \frac{1-2\nu_v}{2} & 0 \\ 0 & 0 & 0 & 0 & 0 & \frac{1-2\nu_v}{2} \end{bmatrix}. \quad (4.19)$$

This is an adaptation of Hooke's Law for an isotropic material in three dimensions, where damping is accounted for with use of the complex shear modulus. The shear modulus form of Hooke's Law was selected as the viscoelastic layer would be operating in a shear arrangement and it was assumed that greater accuracy would be achieved if this form of the equation was used along with the appropriate shear properties obtained from experiment.

Both the storage modulus [1] (G'_v) and loss factor (η_v) of the damping material were functions of frequency. The frequency dependence of these properties was measured from dynamic experiments (see Section 4.3.3) and added to the model (see Section 4.2.4). The Poisson's ratio may also have been somewhat frequency dependent, however there was no practical way of measuring this and literature indicated that the imaginary part of a viscoelastic material's Poisson's ratio is usually very small [2, p. 77]. Consequently it was assumed to be constant.

[1] In this case storage modulus refers to the real part of complex shear modulus, rather than the real part of complex elastic modulus.

It is worth noting that the finite element model assumed perfect bonding between the fibre reinforced layers and the damping layer. This behaviour may not be exactly achieved in practice, depending on the bonding between the layers during infusion. Deviation from perfect inter-facial bonding within the model was approximated by encompassing this behaviour in the material properties of the VEM. Measurement or the damping layer properties was performed using a shear method where the test sample was prepared from a section of the damped composite arrangement. Using this sample arrangement the measurements for shear modulus and loss factor of the damping tape included bonding effects with the fibre layer. More detail is provided in Section 4.3.3.

The element stiffness matrices for the fibre layers were calculated using the general orthotropic material constitutive equations with the $2-3$ $(y-z)$ plane as a plane of symmetry. Transformation of the material constitutive matrix was required as the fibre orientation within each element was dependent upon where the element lay along the fibre pattern. Constitutive relations for orthotropic materials are typically described using the compliance matrix $[\mathbf{S}]$ which is defined as the inverse of the stiffness matrix $[\mathbf{Q}]$, or $\{\varepsilon\} = [\mathbf{S}]\{\sigma\}$. The compliance matrix for an orthotropic material is defined in the stress-strain relationship

$$\begin{Bmatrix} \varepsilon_1 \\ \varepsilon_2 \\ \varepsilon_3 \\ \gamma_{23} \\ \gamma_{31} \\ \gamma_{12} \end{Bmatrix} = \begin{bmatrix} \frac{1}{E_1} & -\frac{\nu_{21}}{E_2} & -\frac{\nu_{31}}{E_3} & 0 & 0 & 0 \\ -\frac{\nu_{12}}{E_1} & \frac{1}{E_2} & -\frac{\nu_{32}}{E_3} & 0 & 0 & 0 \\ -\frac{\nu_{13}}{E_1} & -\frac{\nu_{23}}{E_2} & \frac{1}{E_3} & 0 & 0 & 0 \\ 0 & 0 & 0 & \frac{1}{G_{23}} & 0 & 0 \\ 0 & 0 & 0 & 0 & \frac{1}{G_{31}} & 0 \\ 0 & 0 & 0 & 0 & 0 & \frac{1}{G_{12}} \end{bmatrix} \begin{Bmatrix} \sigma_1 \\ \sigma_2 \\ \sigma_3 \\ \sigma_{23} \\ \sigma_{31} \\ \sigma_{12} \end{Bmatrix}. \tag{4.20}$$

In the special case of transverse isotropy, with the $2-3$ plane as a plane of symmetry, the following relations are true:

$$E_3 = E_2 \ , \qquad -\frac{\nu_{21}}{E_2} = -\frac{\nu_{12}}{E_1} \ ,$$
$$G_{31} = G_{12} \ , \qquad -\frac{\nu_{31}}{E_3} = -\frac{\nu_{13}}{E_1} \ ,$$
$$\nu_{13} = \nu_{12} \ , \qquad -\frac{\nu_{32}}{E_3} = -\frac{\nu_{23}}{E_2} \ .$$

Applying these relations and complex stiffness values yields

$$[\mathbf{S}^*]_{CFRP} = \begin{bmatrix} \frac{1}{E_1^*} & -\frac{\nu_{12}}{E_1^*} & -\frac{\nu_{12}}{E_1^*} & 0 & 0 & 0 \\ -\frac{\nu_{12}}{E_1^*} & \frac{1}{E_2^*} & -\frac{\nu_{23}}{E_2^*} & 0 & 0 & 0 \\ -\frac{\nu_{12}}{E_1^*} & -\frac{\nu_{23}}{E_2^*} & \frac{1}{E_2^*} & 0 & 0 & 0 \\ 0 & 0 & 0 & \frac{1}{G_{23}^*} & 0 & 0 \\ 0 & 0 & 0 & 0 & \frac{1}{G_{12}^*} & 0 \\ 0 & 0 & 0 & 0 & 0 & \frac{1}{G_{12}^*} \end{bmatrix} , \tag{4.21}$$

where

$$E_i^* = E_i'(1 + i\eta_i) \ ,$$
$$G_{ij}^* = G_{ij}'(1 + i\eta_{ij}) \ .$$

The material constitutive matrix could then be defined by

$$[\mathbf{Q}^*]_{CFRP} = [\mathbf{S}^*]_{CFRP}^{-1} \ . \tag{4.22}$$

The extensional storage moduli (E_1' and E_2') and their associated loss factors (η_1 and η_2), along with the shear storage moduli (G_{12}' and G_{23}') and their associated loss factors (η_{12} and η_{23}), were functions of frequency. As with the frequency dependent properties of the VEM, the frequency dependence of these properties were measured using dynamic experiments (see Section 4.3.3) and added to the finite element model (see Section 4.2.4).

A transformation of the CFRP material constitutive matrix was required before the element stiffness matrix could be calculated. Transformation of the material properties were required in order to account for the fibre angle within the element in question. The fibre

pattern present in the CFRP layers resulted in a continuously varying fibre angle along the length of the structure.

Due to the complexity of the fibre patterns under study it was convenient to define the fibre angle at set intervals along the length of the beam. Setting this discretisation interval to half the length of an element in the pattern direction allowed the fibre angle to be determined at each element node. These values were used in the calculation of the element stiffness matrices.

Defining the fibre angle at each node would result in a small error due to the use of node fibre angle at the Gauss points within each element during calculation of $[\mathbf{k}^*]$. Sufficient elements in the pattern direction were required in order to reduce this error and produce a global fibre pattern that approached the behaviour that would be exhibited by the constantly varying fibre pattern. A mesh refinement process was used to determine a sufficient number of elements in the length direction, this is discussed in Section 4.3.1.

Using the angle at each point of interest within the element, the transformed material property matrix for the CFRP was determined using

$$[\mathbf{E}^*]_{CFRP} = [\mathbf{T}]^T [\mathbf{Q}^*]_{CFRP} [\mathbf{T}] \,, \tag{4.23}$$

where the transformation matrix $[\mathbf{T}]$ was defined using $m = \cos(\theta)$ and $n = \sin(\theta)$ as

$$[\mathbf{T}] = \begin{bmatrix} m^2 & n^2 & 0 & 0 & 0 & -mn \\ n^2 & m^2 & 0 & 0 & 0 & mn \\ 0 & 0 & 1 & 0 & 0 & 0 \\ 0 & 0 & 0 & m & n & 0 \\ 0 & 0 & 0 & -n & m & 0 \\ 2mn & -2mn & 0 & 0 & 0 & m^2 - n^2 \end{bmatrix} . \tag{4.24}$$

The constituent material properties used in the material models for the CFRP and VEM were obtained from experiment. The measurement techniques and results can be found in Section 4.3.3.

The fibre volume fraction was not used in any of the material property calculations. This was due to the manufacturing method producing twisted fibre strands and variable fibre distribution within the fibre layers. These characteristics had an unknown affect on the stiffness and damping properties. Consequently, bulk material properties were deemed a better representation for the material property calculations and it was these values that were measured and applied to the model.

4.2.3 Global Assembly

The three-layered beam model used in this investigation was built from 32-node bricks formed by stacking three 16-node bricks on one another (see Figure 4.4). In the global model these 32-node bricks were numbered as individual elements, with the 16-node brick elements within them designated as plies. These elements were numbered in rows, advancing along the length of the beam in the fibre pattern direction (x) before initiating further rows in the width direction (y). Figure 4.8 shows the element numbering arrangement.

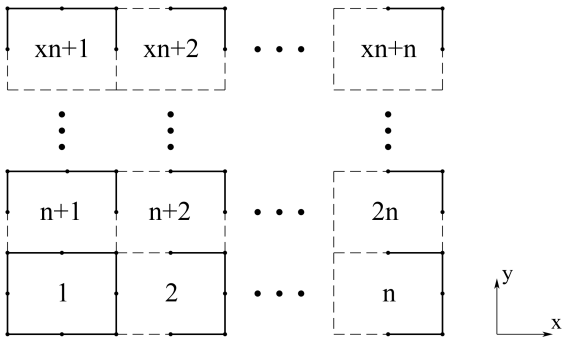

Figure 4.8: Order of element arrangement

As many nodes were shared between the 32-node bricks, a method of numbering the nodes was required. Figure 4.9 shows how the nodes were added. Numbering of the added nodes followed the same pattern as that shown in Figures 4.3 and 4.4, skipping the existing nodes.

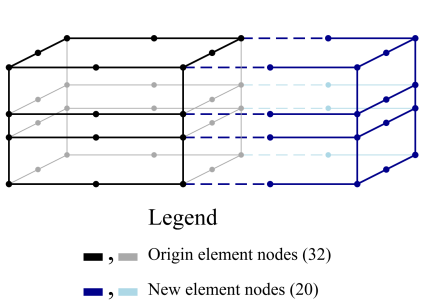

(a) Element 2

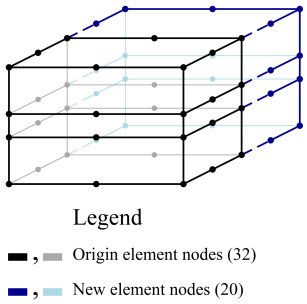

(b) Element n+1

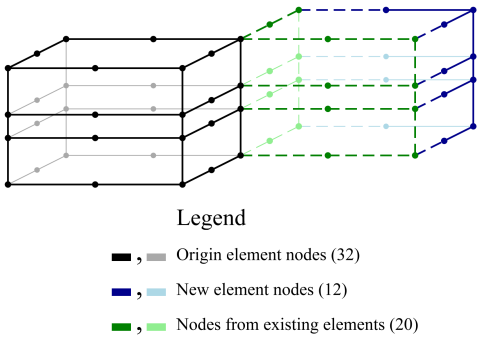

(c) Element n+2

Figure 4.9: Element build order

Once all 32-node brick elements and their corresponding nodes had been numbered in the global domain, the global stiffness [$\mathbf{K}^*$] and mass [$\mathbf{M}$] matrices could be constructed. This was achieved through nodal superposition of the element stiffness [$\mathbf{k}^*$] and mass [$\mathbf{m}$] matrices corresponding to shared nodal degrees of freedom. The global stiffness and mass matrices were symmetric, sparse and of size $DOF \times DOF$, where the number of degrees of freedom (DOF) of the system was three times the number of nodes within the structure. The *sparse* function in MATLAB was used to assemble the [$\mathbf{K}^*$] and [$\mathbf{M}$] matrices using

triplet notation to achieve the required superposition of stiffness and mass values.

The total mass of the structure could be calculated by summing all the elements of [**M**] and dividing the result by the degrees of freedom of each node (i.e. 3).

4.2.4 Iterative Damping Analysis

Damping performance of the beams under consideration was desired as a function of frequency. The equation of motion of the multiple degree of freedom system produced by the model was

$$[\mathbf{M}]\{\ddot{\mathbf{a}}\} + [\mathbf{K}^*]\{\mathbf{a}\} = \{\mathbf{f}(t)\} \, . \tag{4.25}$$

Due to the way the shape function matrix [**N**] and strain matrix [**B**] were arranged, the displacement vector $\{\mathbf{a}\}$ was arranged in the form

$$\{\mathbf{a}\} = \{u_1 \ , \ \cdots \ , \ u_n \ , \ v_1 \ , \ \cdots \ , \ v_n \ , \ w_1 \ , \ \cdots \ , \ w_n\}^T \, , \tag{4.26}$$

where n was the number of nodes in the system. The acceleration vector $\{\ddot{\mathbf{a}}\}$ and force vector $\{\mathbf{f}\}$ also followed this structure.

Analysis of the damping performance was performed in the frequency domain using modal analysis. The forcing vector and displacement vector from Equation 4.25 could be expressed in the frequency domain using a Laplace transform and the general solution $s = i\omega$. This resulted in $\{\mathbf{f}(t)\} = \{\mathbf{F}\}e^{i\omega t}$ and $\{\mathbf{a}(t)\} = \{\mathbf{A}\}e^{i\omega t}$, where $\{\mathbf{F}\}$ was the vector of the force amplitudes applied to the degrees of freedom of the model, $\{\mathbf{A}\}$ was the vector of the displacement amplitudes, and ω was the excitation frequency. Applying these relationships to Equation 4.25 resulted in

$$\Big([\mathbf{K}^*] - \omega^2[\mathbf{M}]\Big)\{\mathbf{A}\}\, e^{i\omega t} = \{\mathbf{F}\}\, e^{i\omega t} \, . \tag{4.27}$$

In the case of unforced vibration, Equation 4.27 simplified to

$$\Big([\mathbf{K}^*] - \omega^2[\mathbf{M}]\Big)\{\mathbf{A}\} = \{\mathbf{0}\} \, . \tag{4.28}$$

This is the general linear eigenvalue problem and solution of this problem provides the eigenvalues and eigenvectors of the system. There will be m combinations of ω_i and $\{\phi_i\}$ that will satisfy this equation, where m is the number of DOF of the system, ω_i is the i^{th} modal frequency, and $\{\phi_i\}$ the i^{th} mode shape. The eigen-problem is displayed using the relation $\lambda = \omega^2$ for the eigenvalues and $\{\phi\} = \{\mathbf{A}\}$ for the eigenvectors:

$$\Big([\mathbf{K}^*] - \lambda_i \mathbf{M}]\Big)\{\phi_i\} = \{\mathbf{0}\} \,. \tag{4.29}$$

The stiffness and mass matrices could be separated using the following steps:

$$\{\phi_i\}^T \Big([\mathbf{K}^*] - \lambda_i [\mathbf{M}]\Big)\{\phi_i\} = \{\mathbf{0}\} \,, \tag{4.30}$$

$$\{\phi_i\}^T \, [\mathbf{K}^*] \, \{\phi_i\} - \lambda_i \, \{\phi_i\}^T \, [\mathbf{M}] \, \{\phi_i\} = \{\mathbf{0}\} \,, \tag{4.31}$$

$$\{\phi_i\}^T \, [\mathbf{K}^*] \, \{\phi_i\} = \lambda_i \, \{\phi_i\}^T \, [\mathbf{M}] \, \{\phi_i\} \,. \tag{4.32}$$

Typically the stiffness matrix in Equation 4.32 would be real which would result in real eigenvalues and eigenvectors. However as the stiffness matrix is complex, the resulting eigenvalues and eigenvectors were also complex. Equation 4.32 can be arranged into the form

$$[\mathbf{K}^*][\mathbf{\Phi}^*] = [\mathbf{M}][\mathbf{\Phi}^*][\mathbf{\Lambda}^*] \,, \tag{4.33}$$

where

$$[\mathbf{\Phi}^*] = \Big[\, \{\phi^*_{\mathbf{1}}\}, \, \{\phi^*_{\mathbf{2}}\}, \, \cdots, \, \{\phi^*_{\mathbf{n}}\} \, \Big] \,, \tag{4.34}$$

and

$$[\mathbf{\Lambda}^*] = \begin{bmatrix} \lambda^*_1 & & & 0 \\ & \lambda^*_2 & & \\ & & \ddots & \\ 0 & & & \lambda^*_n \end{bmatrix} .$$

The Iterative Complex Eigensolution (ICE) algorithm [96] was used to calculate the modal frequencies and corresponding damping loss factors. This method evolved from the Modal Strain Energy (MSE) approach first introduced by Ungar and Kerwin [43] and applied to

FE analysis by Johnson and Kienholz [42]. The definition for the loss factor of mode r using the MSE approach was

$$\eta_r = \frac{\{\phi_r\}^T \mathrm{Im}[\mathbf{K}^*]\{\phi_r\}}{\{\phi_r\}^T \mathrm{Re}[\mathbf{K}^*]\{\phi_r\}} , \tag{4.35}$$

where the eigenvector of mode r ($\{\phi_r\}$) was determined using the real part of the stiffness matrix only.

The ICE method differed from the MSE approach by using the complex stiffness matrix to determine complex eigenvalues and eigenvectors, which were then used to define the damping performance. The damping loss factor for mode r was found using

$$\eta_r = \frac{\mathrm{Im}(\lambda_r^*)}{\mathrm{Re}(\lambda_r^*)} . \tag{4.36}$$

This produced identical results as using the MSE approach with complex eigenvectors:

$$\eta_r = \frac{\{\phi^*{}_r\}^T \mathrm{Im}[\mathbf{K}^*]\{\phi^*{}_r\}}{\{\phi^*{}_r\}^T \mathrm{Re}[\mathbf{K}^*]\{\phi^*{}_r\}} . \tag{4.37}$$

As the stiffness matrix was a function of frequency an iterative algorithm was required to account for the change in material properties with changing modes of interest. Figure 4.10 shows the process used to determine the loss factor of each mode of interest. The convergence criteria $\Delta_{\max}$ was set as 0.01%.

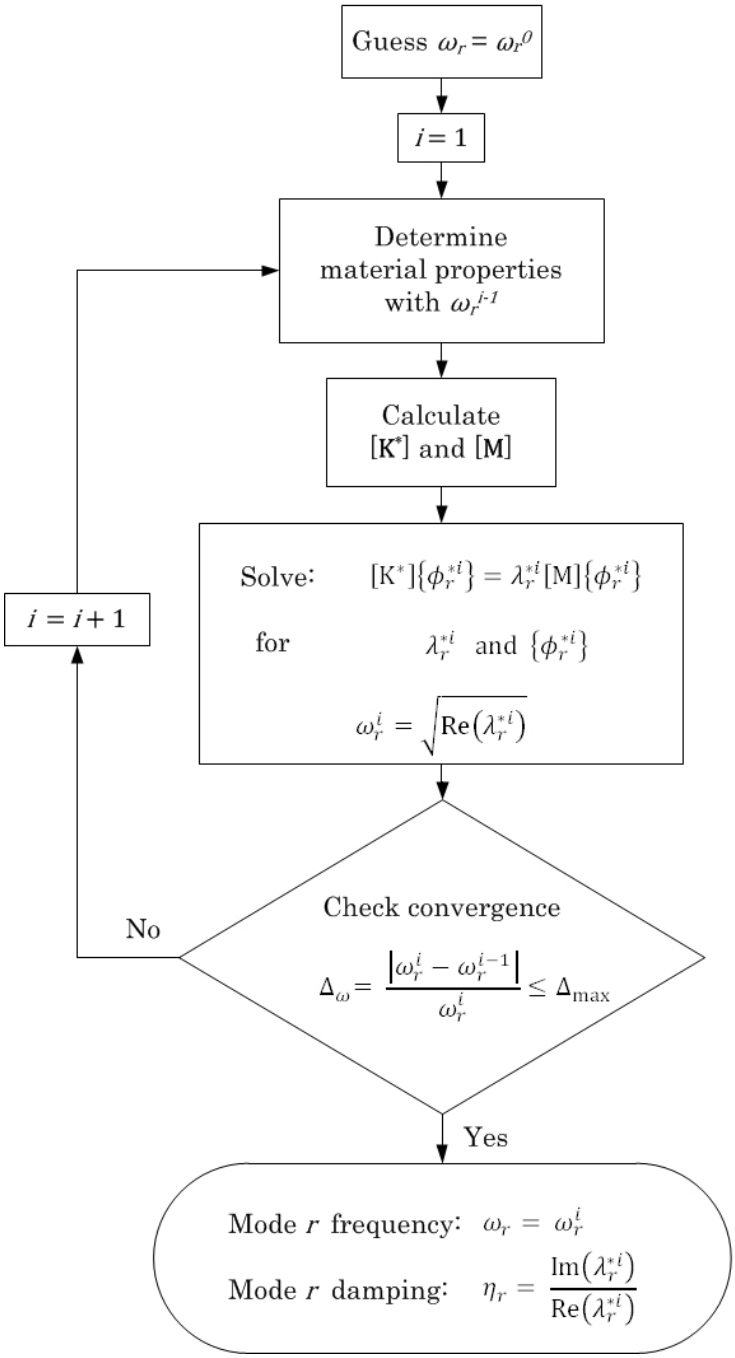

Figure 4.10: Iterative algorithm to determine modal damping

The complex eigenvalues and eigenvectors of the system in Equation 4.32 were calculated using the MATLAB function *eigs*:

$$[\ \underset{m\times p}{\mathbf{\Phi}^*}\ ,\ \underset{p\times p}{\mathbf{\Lambda}^*}\ ] = eigs(\ \underset{m\times m}{[\mathbf{K}^*]}\ ,\ \underset{m\times m}{[\mathbf{M}]}\ ,\ p\ ,\ 0\ )\ . \tag{4.38}$$

This allowed the first p eigenvalues and eigenvectors of the system to be calculated. As the structure was unrestrained, the first six modes would be rigid body modes. Consequently, the first six eigenvectors and their corresponding eigenvalues were discarded from the analysis.

In the cases where simply supported or fixed conditions were desired, zero values of nodal displacement were achieved in the required global degrees of freedom by removing the corresponding rows and columns in $[\mathbf{K}^*]$ and $[\mathbf{M}]$ before solving the eigen-problem. The zero displacement values of these degrees of freedom were then re-inserted into the eigenvectors to achieve the correct vector length. No rigid body modes were present in these cases so all eigenvectors were retained.

4.2.5 Further Analyses

Strain and stress within the model could be calculated from nodal displacements $\{\mathbf{a}\}$, the element strain matrix $[\mathbf{B}]$, and the material constitutive matrix $[\mathbf{E}^*]$.

Values of stress and strain were calculated at the Gauss points within each element to avoid errors associated with sampling at the boundaries of each element [93, p. 376].

The strain at each Gauss point within an element was calculated using

$$\underset{6\times 1}{\{\varepsilon\}} = \underset{6\times 48}{[\mathbf{B}]}\ \underset{48\times 1}{\{\mathbf{a}\}}\ . \tag{4.39}$$

The corresponding stress could then be calculated using

$$\underset{6\times1}{\{\sigma\}} = \underset{6\times6}{[\mathbf{E}^*]}\ \underset{6\times1}{\{\varepsilon\}}\ . \tag{4.40}$$

With these values, it was also possible to calculate the strain energy density (U_0) using

$$U_0 = \frac{1}{2}\{\sigma\}^T\{\varepsilon\} \tag{4.41}$$

Each of these values could be used in better understanding the stress and strain behaviour within the modelled structures.

4.3 Verification and Validation

In order to determine whether the finite element model produced results that accurately predicted real world behaviour of the three layer patterned fibre beams, the model required verification and validation. At several stages during the model development verification was performed to assess model behaviour and the final model was validated through comparison with experimental results. A fabrication method for production of test specimens was devised and the constituent material properties of the resulting test specimens were evaluated to determine the values required for input into the model.

4.3.1 Model Assessment During Development

Verification was employed during development of the model to ensure that the element arrangement, stiffness matrix assembly and stress and strain calculations were producing reasonable results. The behaviour of the model was assessed for extensional loading, cantilever loading and modal deformation.

Extension and Bending

It was important to ensure that the three layered element arrangement was able to accurately capture the proper flexure and extension behaviours of a material. Tests for both

extension and bending were applied.

In both of these investigations, uniformly distributed loads (UDLs) were used in the model. As uniformly distributed loads act over an area or length and the beam was modelled by discrete nodes, it was important to ensure that the nodes under external load had the correct point force distribution to produce a truly uniformly distributed load. Appendix A.2 details the equations used for the UDL analysis.

The extension behaviour was tested by assuming an isotropic material (steel) under uniformly distributed loading of one end face of the beam, with the opposite end face fixed in the direction of applied load. Beam dimensions of 600 mm × 100 mm × 1.5 mm were used along with a Young's Modulus of 210 GPa and Poisson's ratio of 0.3. Stress and strain through the beam and end displacement values exactly matched those calculated by hand.

Bending was examined by modelling a cantilever beam with a uniformly distributed load acting along the free end upper edge. When using solid elements, it is typically assumed that three elements thickness will correctly account for bending, however as different materials were being used in each of the layers for this model, it was important to determine whether the variation in properties through the thickness would affect the bending behaviour. For this reason the outer layers of the beam were set as steel (E = 210 GPa) and the mid-layer was set as Aluminium (E = 69 GPa). Analytical calculations for end deflection were performed using

$$\delta = \frac{FL^3}{3(E_1I_1 + E_2I_2 + E_3I_3)} \,, \tag{4.42}$$

where F was the equivalent point force acting on the end of the beam, L was the length of the beam, E_i was the elastic modulus of layer i and I_i was the second moment of area of layer i. Parallel axis theorem was used to account for the offset of the outer layers from the beam centroid.

For a beam of dimensions 600 mm, width of 100 mm, outer layer thickness of 0.7 mm, core layer thickness of 0.1 mm and an applied load of 10 N acting in the negative z-direction, an end deflection of 121.9 mm was calculated. The model predicted an end deflection of 119.3 mm, producing an error of 2.2%. This error was deemed acceptable for the accuracy desired from the model.

Mesh Refinement

As the fibre angle in the model was discretised, it was important to ensure that a sufficient number of elements were included in the mode in order to properly capture the behaviour of each fibre pattern. It was also necessary to determine at which point model results ceased changing, within some error range, with increasing numbers of elements.

A mesh independence analysis was performed to assess these behaviours. Elements were constructed with equal edge lengths in the laminate plane and a fixed edge length in the thickness direction. The number of elements in the length direction was increased with each iteration until the percentage change in the damping loss factor of bending modes 1 through 4 was less than 0.1% for all patterns. This criteria was met with 30 elements in the width direction (192 elements in the length direction), producing an element aspect ratio of 12.5 : 1 in the thinnest layer. The convergence rate of the mode frequency and damping values are shown in Appendix A.3.

Modal Behaviour

The mode shapes produced by the model were also examined. This check was performed in order to determine whether the bending and twist modes were falling in the correct order and the correct shapes were being produced. The results from the model were compared to standard shapes found in literature and were found to match.

4.3.2 Fabrication of Test Specimens

Pattern Selection

A set of patterns to study was required before fabrication could begin. The major considerations for this investigation were manufacturability and comparison to the earlier work performed. It was also advantageous for the patterns to fit a Design of Experiments [85] schedule in order to facilitate later investigations. Combining simple sinusoidal patterns provided a method for comparison of more complex patterns. The two parameters, pattern wavelength and maximum fibre angle, used in previous studies were again employed for this work. Four patterns were selected, two used superposition of sine waves, and two used swept sine waves. A maximum fibre angle of 30° was selected for each pattern. The pattern specifications can be seen in Table 4.1. These values were selected as they had previously been investigated for constant sinusoids [65, 66, 76].

	Pattern 1	Pattern 2	Pattern 3	Pattern 4
Waveform	$\lambda_1 + \lambda_2$	$\lambda_1 + \lambda_2$	$\lambda_1 \rightarrow \lambda_2$	$\lambda_1 \rightarrow \lambda_2$
λ_1 (mm)	125	125	125	125
λ_2 (mm)	50	75	50	75
θ_{max} (°)	30	30	30	30

Table 4.1: Fibre pattern details

The two superposition patterns were created using

$$y = A(\sin(k_1 x + \phi_1) + \sin(k_2 x + \phi_2)) \,, \tag{4.43}$$

where k_1 and k_2 are the wave numbers of the two sine waves, and the phase angle (ϕ_1 and ϕ_2) of both sine waves was set as 0°. The wave number was defined by $k_i = \frac{2\pi}{\lambda_i}$, where λ_i was the fibre wavelength. The waveform amplitude was selected to ensure that the maximum

fibre angle didn't exceed 30°, using the gradient of the pattern:

$$\frac{dy}{dx} = A(k_1 \cos(k_1 x) + k_2 \cos(k_2 x)) = \tan(\theta) \; . \tag{4.44}$$

Knowing that θ_{max} occurs at $\cos(k_1 x) = \cos(k_2 x) = 1$, the amplitude constant could be defined as

$$A = \frac{\tan(\theta_{max})}{k_1 + k_2} \; . \tag{4.45}$$

The two swept sine patterns were created as linear wavelength sweeps from λ_1 to λ_2. The patterns were defined by a chirp function with a modified amplitude variable which was used to limit the maximum fibre angle to 30°:

$$y = A(\sin(\phi_1 + 2\pi(f_1 x + \frac{k_{swept}}{2} x^2))) \; . \tag{4.46}$$

The wave number for the linear sweep was defined as

$$k_{swept} = \frac{f_2 - f_1}{L} \; , \tag{4.47}$$

where f_1 was the initial pattern frequency, f_2 was the final pattern frequency and L was the total length of the pattern.

Using the gradient of the chirp function to control the maximum fibre angle, it could be seen that the amplitude of the pattern would be a function of x:

$$\frac{dy}{dx} = 2\pi A(f_1 + k_{swept} x) \cos(\phi_1 + 2\pi(f_1 x + \frac{k_{swept}}{2} x^2)) = \tan(\theta) \; . \tag{4.48}$$

Rearranging for amplitude gave

$$A = \frac{\tan(\theta_{max})}{2\pi(f_1 + k_{swept} x)} \; . \tag{4.49}$$

At the beginning of the wave pattern ($x = 0$) the denominator was $2\pi f_1$. At the end of the

pattern ($x = L$) the denominator is $2\pi f_2$. For convenience the pattern was discretised into n points. This allowed the amplitude to be defined as

$$A_i = \frac{\tan(\theta_{max})}{2\pi f_i} \,, \tag{4.50}$$

where A_i was the amplitude value at location x_i, and f_i was the waveform frequency at location x_i, using a linear sweep from f_1 to f_2 in steps of $\Delta f = \frac{|f_2 - f_1|}{n}$.

Along with these patterns, unidirectional (UD) fibres oriented at 0° to the length direction were also required for measurement of constituent material properties. These UD beams were fabricated with and without the damping layer applied.

Weaving

Carbon fibre was selected for the fibre reinforcement as previous research indicated that increased stiffness and damping values were achieved if a fibre with high Young's modulus was used [76]. Initial attempts at shaping standard sheets of unidirectional carbon into the required patterns proved unsuccessful as lateral movement was restricted by the tight packing of the fibres and the binding cross-threads. Flexible unidirectional carbon tapes were also investigated, but buckling of the fabric and inconsistent fibre distribution made this material unsuitable for use.

A new method of fabrication which would allow the fibre strands greater flexibility was devised. The required patterns were created by twisting ribbons of unidirectional carbon tow into threads and inserting the threads into a mould of each pattern. Twining of the ribbons created a rope-like strand of carbon which provided the flexibility required for the fibre to follow the curvature of each pattern (Figure 4.11). High strength 12k carbon tow was used, with each wound thread containing approximately 12,000 carbon fibrils.

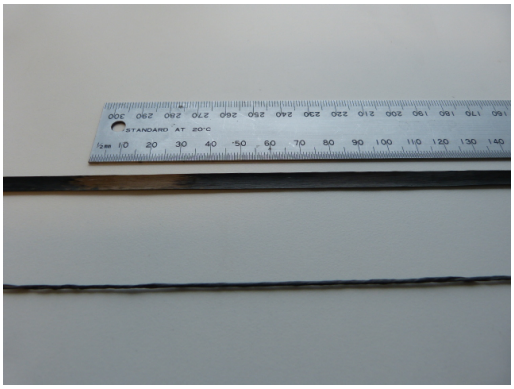

Figure 4.11: 12k carbon tow (top) and wound strand (bottom)

Moulds for each fibre pattern were created by machining a series of 1 mm wide, 1 mm deep channels into polyvinyl chloride (PVC) sheets using a CNC router, with approximately 0.2 mm separation between channels. The length of the moulds was set at 600 mm in order to achieve several full wavelengths of the longest wave in each pattern. Sufficient channels were cut to allow the finished beams to have a width of 80 mm. The mould used to create Pattern 1 is shown in Figure 4.12.

Figure 4.12: Fibre weaving mould for Pattern 1

Carbon bundles were tightly wound and inserted into each channel of the mould by hand.

Once placed, the strands were free to unwind slightly until further expansion was prevented by the channel walls. Ideally, the spacing between channels would be as small as possible to allow for greater fibre volume fraction in the laminated beams. The channel separation used was the smallest that could be achieved with the materials and machining process used.

Weaving of the fibres in this manner was practical for creating the limited number of prototype beams required for testing. It would not be suitable for large scale production due to the significant resources required to wind and lay the fibres.

The winding of the carbon strands introduced some irregularity within the beams. Some strands were wound tighter than others, or unwound to a lesser degree once placed. This resulted in a slight variation between individual strand diameters across the width of each beam, and thus a varying beam thickness. The winding process also introduced unknown effects on damping and stiffness of the beams as single carbon fibrils within each strand spiralled around one another along the length of the beam. Some pre-stress was observed as twist in several test beams. This was likely caused by the individual strands trying to unwind. When multiple strands were laid in the same direction, the rotation of each strand would act in the same direction and result in noticeable twist in the global structure. The variation in twist between different beams appeared to have little effect on the damping performance or frequency response of the pattern groups.

Addition of Damping Layer

The damping material selected for use in this analysis was tesa® 4965 (Figure 4.13), a double-sided self-adhesive tape with high shear and temperature resistance. The tape consisted of a PET core with a modified acrylic adhesive on each side and was provided in 48 mm wide rolls, with a thickness of 205 μm. The tape itself was transparent and was backed with a red polymer release liner.

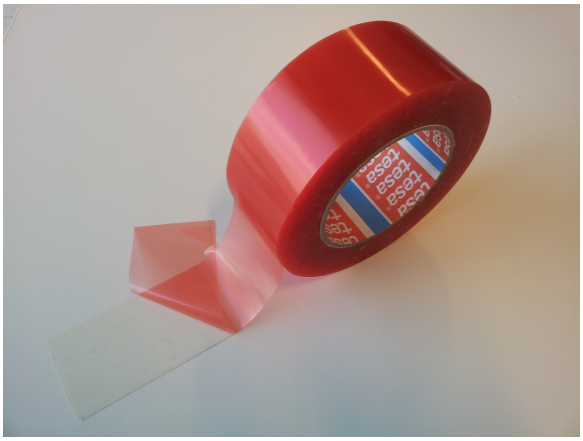

Figure 4.13: Viscoelastic damping tape, tesa® 4965

Strips of damping tape were applied directly to the first face of woven carbon fibre strands while they were still housed in the mould. Care was taken to ensure that the edges of the tape were flush and did not overlap one another. A roller was then used to press the tape firmly against the fibres and top face of the mould. Prior to rolling, fibre bundles tended to protrude from the channels of the mould. The rolling process flattened the bundles allowing for a better contact area between the tape and fibre layer.

The damping tape and first side of carbon were peeled from the mould, with the damping tape holding the fibres in the required pattern. The next set of strands were then wound and inserted into the mould. Once the second carbon face had been woven, the first fibre layer with damping tape applied was aligned and combined with the second fibre layer. Care was taken to ensure the peaks and troughs of the two carbon layers were aligned before the layers were pressed together and rolled once more. The three-layer fabric was then removed from the mould ready for infusion.

Infusion

Vacuum infusion was used for lamination of the three-layered test beams. This infusion technique involved the matrix resin being drawn into a mould and through the fabric using

a vacuum pump. The fabric and mould were enclosed in a vacuum bag to contain and control the resin flow. Once fully impregnated with resin, the composite material was heated to cure the matrix material.

In this case flat beams were required so a smooth glass table with embedded heating elements was used as the mould. Given the size of the table and strength of the vacuum pump used, up to fourteen test beams could be infused simultaneously.

The fabric beams were laid in rows on the table. Gauze material was placed between the beams and at the infusion initiation end of each beam to promote greater resin flow in these areas. Peel ply layers were also added in various configurations to increase resin flow and wick away excess resin. A vacuum bag was then laid over the moulding table and sealed around the resin inlet and outlet tubes.

Peel ply layers were used in three different configurations. Two arrangements used only a single layer of peel ply, the first against the vacuum bag face (on top of the fabric beams), and the second against the glass table face (under the beams). The third configuration used peel ply layers on both faces of the fabric beams. The major effects of the different peel ply configurations was the surface finish of the beam faces and the rate at which resin would penetrate the fabric during infusion.

As the resin was unable to penetrate through the damping layer, sufficient layer spacing and resin draw was required to allow both faces of carbon to infuse simultaneously.

Epoxy matrix material was drawn from a reservoir onto the table where it was heated to approximately 25 °C. The temperature increase was required in order to improve flow and penetration of the epoxy into the fabric. The table layout is shown in Figure 4.14.

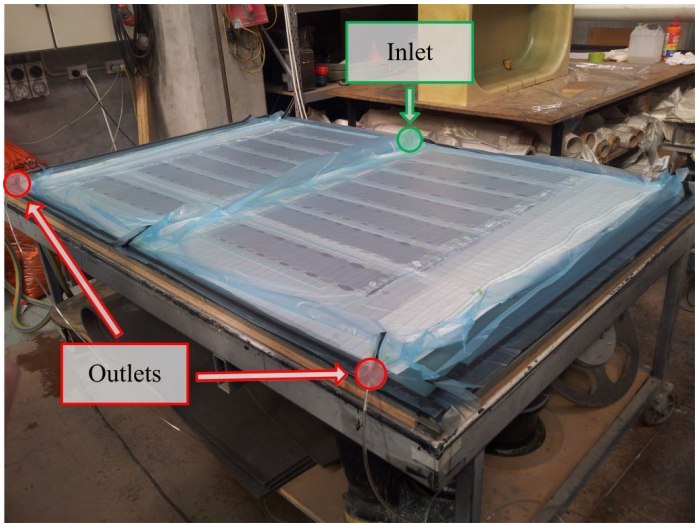

Figure 4.14: Table mould with resin inlet and outlets indicated

The matrix resin flow path for a single fabric beam is shown in Figure 4.15(a). The green gauze allowed the resin to flow more freely, facilitating penetration from one end and both edges. The resulting flow behaviour can be seen in Figure 4.15(b), the impregnated sections of fibre appear black.

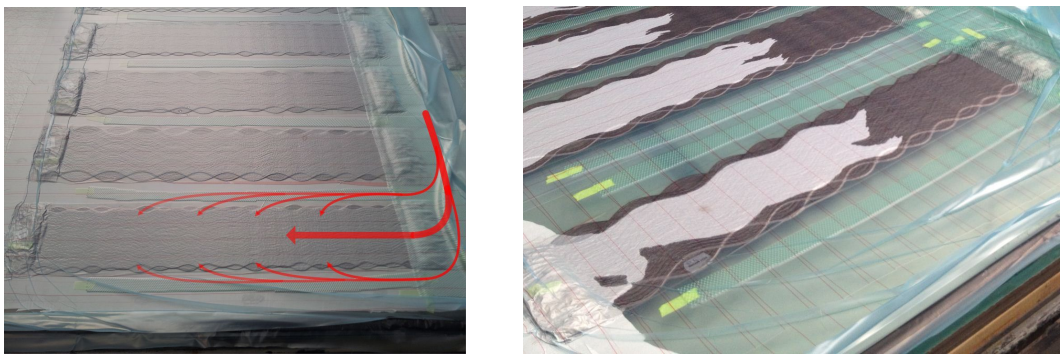

(a) Resin flow path

(b) Resin infusion

Figure 4.15: Resin infusion of three-layer beams

Once the resin had fully penetrated the beams, the supply was cut off and the table temperature was increased to approximately 70 °C for about 12 hours to cure the epoxy matrix.

Cutting the Beams to Shape

The beams needed to be uniform in width and length in order to fairly compare the differing modal properties of the four patterns. Beams within the same pattern group also needed to start and end at the same point of the fibre pattern to produce comparable samples. A water jet cutter was used to achieve the required beam dimensions and produced a clean cut with no fraying of the fibres at the edges. Each beam was cut to a width of 80 mm and a length of 480 mm. The deviation from the original 600 mm length occurred due to imperfections near the ends of some beams, requiring the shortening of all beams to meet the equal length requirement.

The geometry of the original fibre patterns and the final beam sizes can be seen in Figure 4.16. The final beams are surrounded by red lines. Ten test samples were produced for each pattern, giving a total of 40 beams.

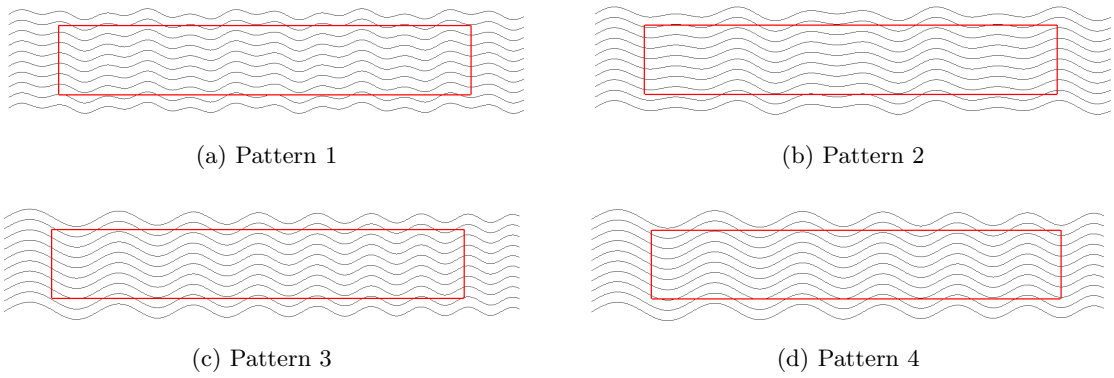

(a) Pattern 1 (b) Pattern 2

(c) Pattern 3 (d) Pattern 4

Figure 4.16: Final beams cut from their original patterns

Microscopy Evaluation

A microscopic investigation was performed to assess the fibre volume fraction present in the infused composite beams. This was of interest as the twining of the strands and strand separation due to the mould channel spacing produced an unknown packing arrangement within

the woven fibre layers. Fibre samples were cut from the excess material at a peak/trough location to obtain a cross-section with the strands normal to the cut surface. Once set in a housing epoxy, the specimen was ground and polished.

The sample was investigated using a Leica DM IRM optical microscope. Images were taken at a range of magnifications and the contrast between fibres and the surrounding matrix was used to determine the fibre volume fraction of the sample area investigated. An image using 5× magnification is shown in Figure 4.17.

Figure 4.17: Cross-section of a 3-layer beam at 5× magnification

The fibre fraction within the bundles was approximately 63%, however given the spacing between bundles, the fibre volume fraction for a single layer of woven fibre was approximately 34%. This is far lower than would normally be required for a working laminate but was acceptable for investigation at this stage of material development.

It can be seen in Figure 4.17 that the fibre bundles are partially unwound as indicated by the varying bundle diameters, fibril separation and gaps within the bundles. The damping layer is also shown to follow a curved path due to the apparent irregularities in bundle spacing. Consequently, the matrix thickness also varies along the width of the sample.

These issues would likely be reduced if an alternative weaving process were used. Fibre fraction and material consistency would benefit from weaving of the required patterns into fibre sheets. This would result in more uniform fibre distribution and fewer irregularities in the damping layer profile and matrix thickness.

4.3.3 Material Property Investigation

Validation of the finite element model required accurate material property data for the constituent materials. Within the model two material property sets were present: carbon fibre reinforced polymer (CFRP) and the viscoelastic damping material (VEM).

The CFRP was modelled as a transversely isotropic material and consequently directional values for its properties were required (as defined by the constitutive equations in Section 4.2.2). The VEM was assumed to be isotropic. As dynamic behaviour was being modelled, and both materials were likely to display frequency dependence, dynamic material properties were required. Table 4.2 lists the required values for each of the material sets. Properties that are functions of frequency are indicated by (ω).

CFRP	VEM
$E'_1(\omega)$, $\eta_1(\omega)$	$G'_v(\omega)$, $\eta_v(\omega)$
$E'_2(\omega)$, $\eta_2(\omega)$	ν_v
$G'_{12}(\omega)$, $\eta_{12}(\omega)$	ρ_v
$G'_{23}(\omega)$, $\eta_{23}(\omega)$	
ν_{12}	
ν_{23}	
ρ_c	

Table 4.2: Material properties required for the model

The frequency range that material properties were required for was determined by the frequency range present in the finite element model. Only low order modes would be able to be measured experimentally so a measurement frequency range of 10 Hz ($\log(\omega) \approx 1.8$) to 1000 Hz ($\log(\omega) \approx 3.8$) was deemed adequate for the constituent material properties. Various methods were used to obtain the required values. The techniques used and results measured for each property are detailed in the following sections.

CFPR Properties

Two tensile moduli measurements were required for the CFRP, one aligned with the fibre direction and one transverse to the fibre direction. The loss factors associated with these values were also required. The transverse tensile modulus ($E_2'(\omega)$) and associated loss factor ($\eta_2(\omega)$) were measured with a TA Q800 Dynamic Mechanical Analyser (DMA) using a tension clamp configuration. Figure 4.18 shows the general arrangement of the DMA tension clamp.

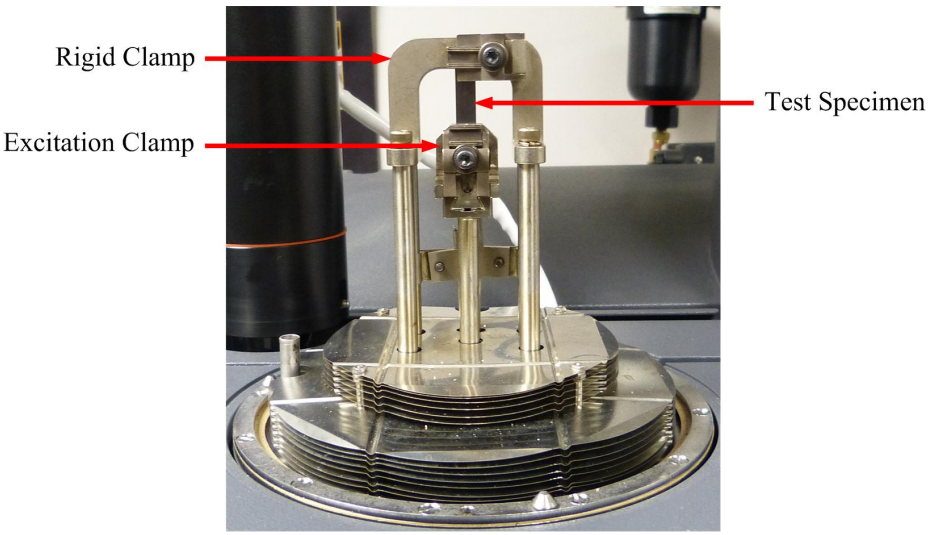

Figure 4.18: TA Q800 DMA tension clamp arrangement

A 30 mm × 10 mm test specimen was cut from a single layer of CFRP, with the fibres oriented transverse to the load direction. The DMA was limited to excitation frequencies

between 0.1 Hz – 140 Hz. Material data over a wider frequency range was required for accurate modelling so measurements were made over a range of temperatures to facilitate use of the Time-Temperature Superposition Principle (TTSP). This technique allowed calculation of a master curve for both $E_2'(\omega)$ and $\eta_2(\omega)$, providing results over the required frequency range (see Section 2.4.2).

Measurements at sub-ambient temperatures were needed to determine material property values at high frequencies and this was achieved using liquid nitrogen cooling. The test sample was lowered to the minimum required temperature and held at this point for ten minutes to ensure the sample temperature had equilibrated with the test chamber temperature. A series of discrete excitation frequencies were then applied to the test specimen. The strain applied during excitation was restricted to approximately 0.03% to meet the assumption of linear viscoelastic behaviour. After the range of excitation frequencies had been applied, the sample was raised in temperature by 1 °C and held for another ten minutes before repeating the process until the final temperature point was reached. The temperature step and isothermal duration were selected to produce reliable data at a high resolution. The DMA measurement conditions used for evaluation of $E_2'(\omega)$ and $\eta_2(\omega)$ are summarised in Table 4.3.

Thickness varied slightly along the length of the test specimen. Several values were taken and the average thickness was used in the DMA software. The results produced by the DMA for $E_2'(\omega)$ and $\eta_2(\omega)$ are shown in Figure 4.19 and Figure 4.20 respectively. The models used to approximate these results are also shown.

Parameter	Measurement setting
Clamp arrangement	Tension
Excitation frequencies (Hz)	5, 10, 20, 30, 50, 60, 70, 90
Temperature range (°C)	-5 $\rightarrow$ 30
Temperature step	+1°C
Isothermal duration	10 minutes
Strain	0.036%
Specimen length (mm)	12.84
Specimen width (mm)	10.14
Specimen thickness (mm)	0.87

Table 4.3: DMA settings for measurement of $E_2'(\omega)$ and $\eta_2(\omega)$

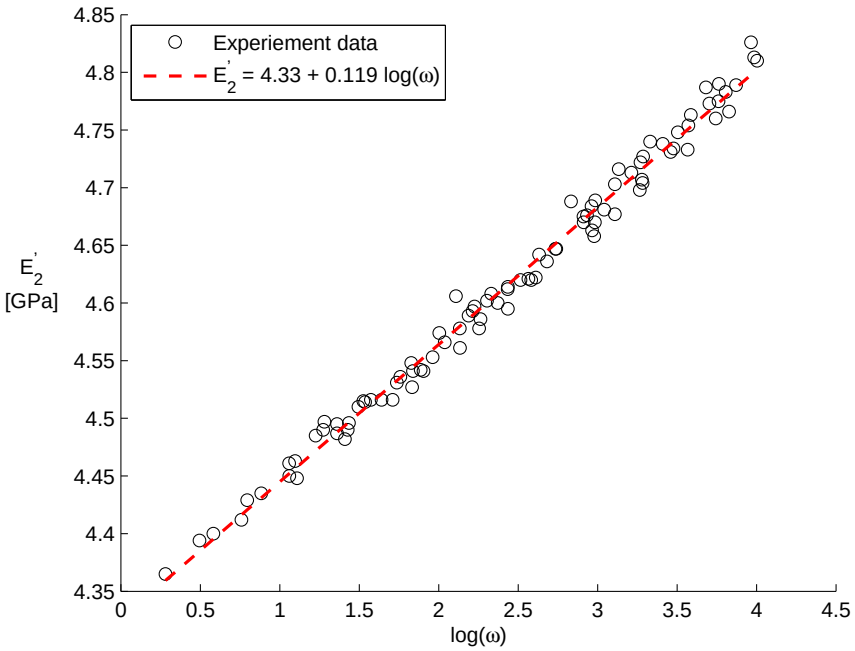

Figure 4.19: E_2' master curve from DMA testing

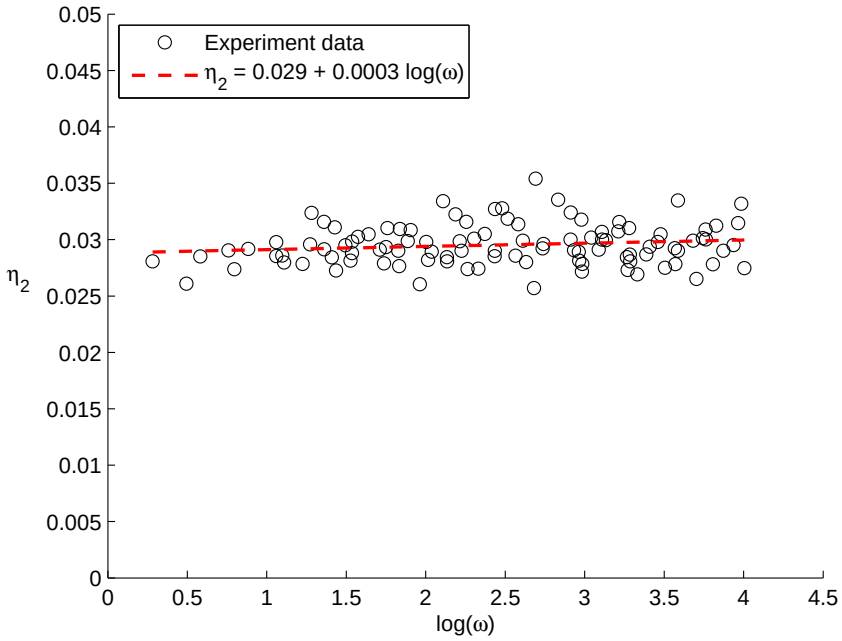

Figure 4.20: η_2 master curve from DMA testing

It can be seen in Figure 4.19 that the transverse tensile modulus increases linearly with the log of frequency and the associated loss factor is approximately constant across the frequency range. Fitting a Least Squares approximation to the data for $E_2'(\omega)$ provides the relationship to frequency required for the FEM:

$$E_2' = 4.33 + 0.119 \log(\omega) \; . \tag{4.51}$$

As the value of η_2 changes very little across the frequency range of interest ($\log(\omega)$ in the range of 1.8 to 3.8), it was assumed constant for the FEM model:

$$\eta_2 = 0.029 \; . \tag{4.52}$$

The relationship between longitudinal tensile modulus and frequency was obtained by combining measurements from an MTS tensile tester with those from the DMA. Unlike the transverse tensile modulus, $E_1'(\omega)$ could not be measured directly with the DMA. This was due to the significant stiffness of the test specimen. Instead, E_1' measurements were per-

formed using an MTS tensile tester and the frequency dependent term was approximated using DMA measurements. The general arrangement of the MTS tensile tester is shown in Figure 4.21.

Figure 4.21: MTS tensile tester arrangement

Force applied to the sample was measured with the load cell and the strains parallel and transverse to the load direction were measured with a video extensometer using the reference points on the sample. Only longitudinal strains were needed to determine the value of E'_1 but simultaneous measurement of the transverse strains allowed calculation of the longitudinal Poisson's ratio ν_{12}. Measurements of Poisson's ratio are discussed later in this section.

The test conditions set for the tensile tester are summarised in Table 4.4. The measured response from the MTS is shown in Figure 4.22. The longitudinal tensile modulus could be calculated from the gradient of this line. Two slopes were recorded from different test specimens and the average of these two gradients was used. The resulting value for E'_1 was 50.1 GPa.

Parameter	Measurement setting
Clamp arrangement	Tension
Load cell	2.5 kN
Extension rate	2 mm/minute
Specimen length (mm)	42.08
Specimen width (mm)	15.25
Specimen thickness (mm)	0.94

Table 4.4: MTS settings for measurement of E_1'

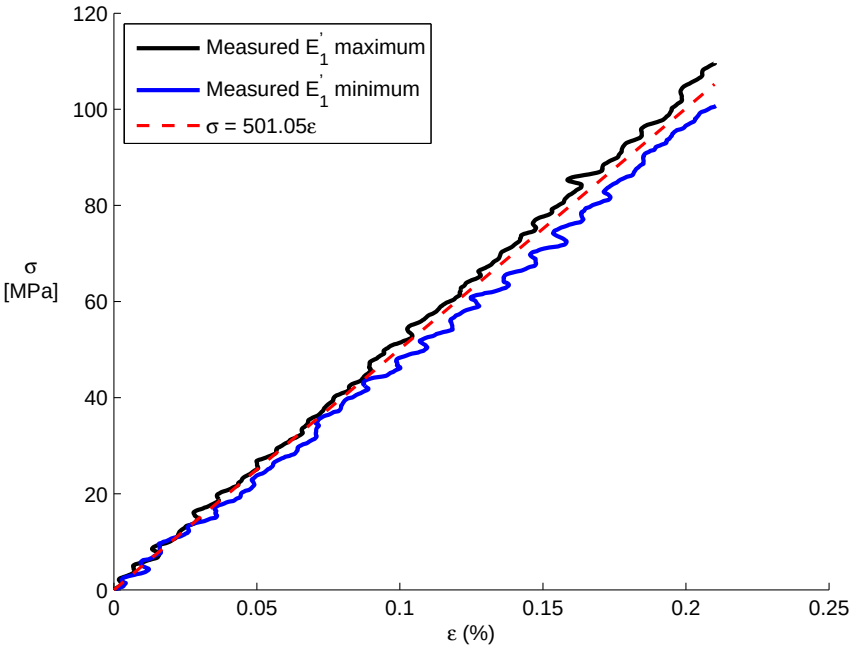

Figure 4.22: Tensile testing results for E_1'

The tensile tester was able to accurately resolve the longitudinal tensile modulus of the CFRP, but was unable to determine any changes in stiffness with frequency, nor was it able to measure the associated loss factor (η_1). These values were instead approximated using measurements from the DMA.

The frequency dependence of the longitudinal tensile modulus was assumed to be dominated by the viscoelastic nature of the matrix. Consequently a modified version of the frequency dependent term measured from the transverse tensile modulus was applied. The modification factor followed the general rule of mixtures for composite materials. It was assumed that the total frequency dependent term for E_1' would be a combination of the frequency dependence of the carbon fibres and the frequency dependence of the matrix material:

$$E'_{Total}(\omega) = E'_f(\omega)v_f + E'_m(\omega)v_m \ . \tag{4.53}$$

The frequency dependent term for the matrix was assumed to be approximately the same as the frequency dependent term measured for E_2' as the transverse material properties were dominated by the matrix. The frequency dependent term for the fibre was assumed to be negligible in comparison. Hence, the required frequency dependent term for E_1' was approximated as the frequency dependent term of E_2' ($0.119\log(\omega)$) multiplied by the matrix volume fraction of the sample (66%). This provided the relationship between frequency and longitudinal tensile modulus:

$$E_1' = 50.105 + 0.66(0.119\log(\omega)) \ . \tag{4.54}$$

Values for η_1 were obtained using the dual cantilever arrangement with the fibres aligned along the length of the sample. The general dual cantilever arrangement is shown in Figure 4.23.

Figure 4.23: TA Q800 DMA dual cantilever clamp arrangement

The test conditions for measurement of the longitudinal loss factor are summarised in Table 4.5.

Parameter	Measurement setting
Clamp arrangement	Dual cantilever
Excitation frequencies (Hz)	5, 10, 20, 30, 40, 50, 60, 70, 80
Temperature range (°C)	-10 $\rightarrow$ 50
Temperature ramp	+1 °C/minute
Strain	0.013%
Specimen length (mm)	35.00
Specimen width (mm)	12.07
Specimen thickness (mm)	0.93

Table 4.5: DMA settings for measurement of $\eta_1(\omega)$

The measured values of η_1 using these conditions are shown in Figure 4.24. It can be seen that the value of η_1 is approximately linear. Equation 4.55 shows the value used for the FEM:

$$\eta_1 = 0.0036\ . \tag{4.55}$$

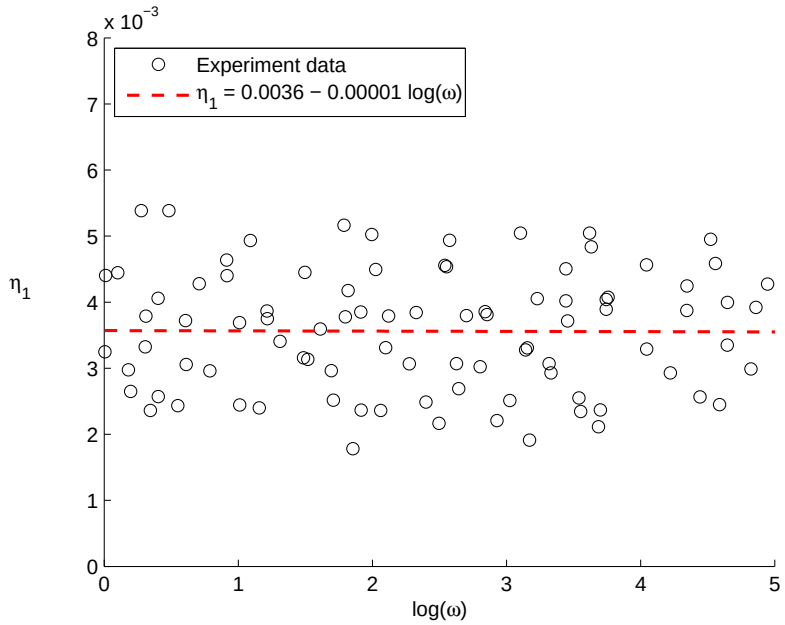

Figure 4.24: η_1 master curve from DMA testing

These approximations were based on the assumption that the carbon fibres within the composite layer were likely to display much lower damping and frequency dependent stiffness values compared to the matrix material they were embedded in. The frequency dependence for both η_1 and η_2 is very low which is expected as the glass transition point of the matrix epoxy was found to occur at approximately 115 °C.

The two shear moduli required for the CFRP were measured using the torsional pendulum method detailed in the international standard ISO 6721-2 ([97]). Using this technique, a long thin sample was excited in torsion at one end by tapping an attached disc of known inertia. The other end of the sample was fixed in place and the decaying torsional oscillations of the specimen were measured from the angular response of the inertial ring. The frequency of oscillation and the rate at which the oscillations decayed were used to calculate the torsional modulus and associated damping loss factor of the test specimen. The general configuration of the torsional pendulum is shown in Figures 4.25 an 4.26.

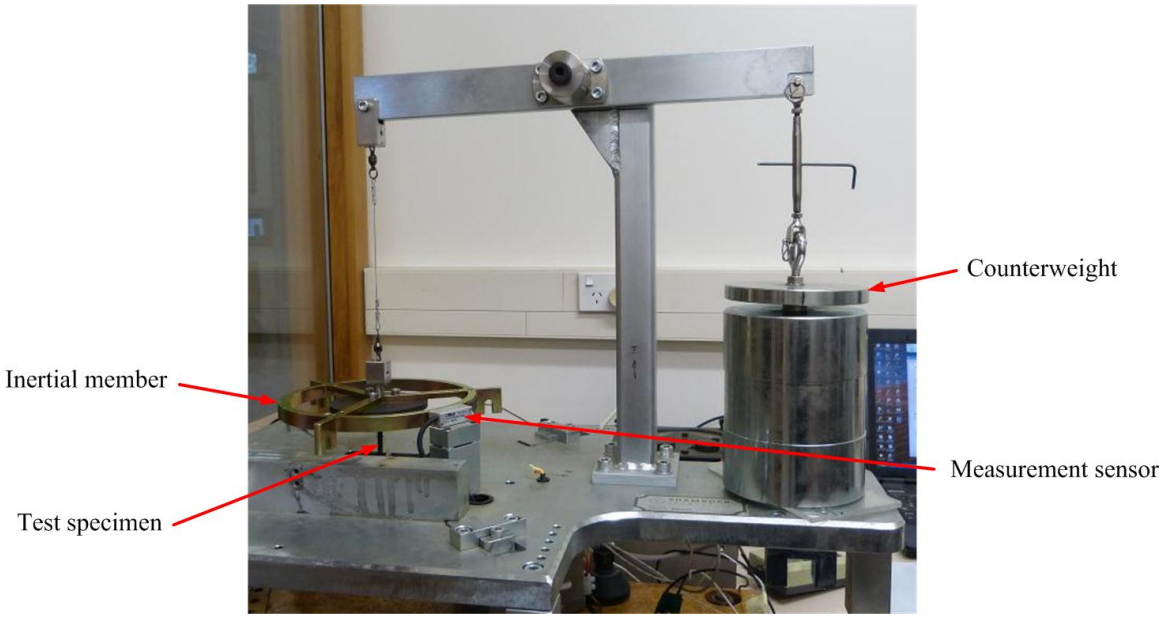

Figure 4.25: Torsional pendulum configuration (ISO 6721-2 method B)

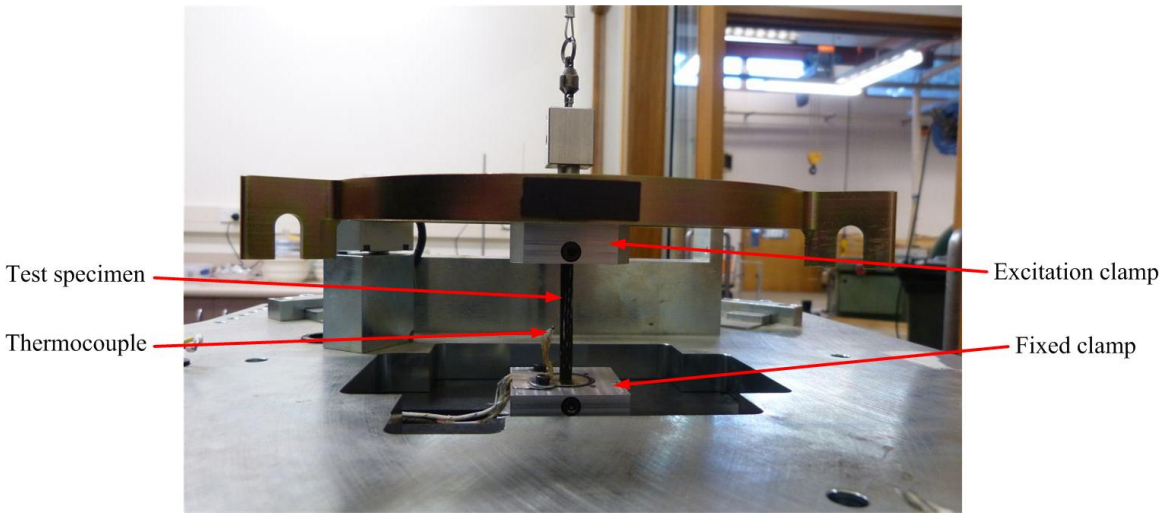

Figure 4.26: Torsional pendulum detail

Temperature control was achieved by surrounding the test specimen with a thin-walled capsule and encasing the capsule within a heating chamber. The capsule and heating chamber can be seen in Figure 4.27.

Heat was provided by elements within the heating chamber and a fan was used to distribute the heated air. The capsule surrounding the test specimen provided the means to achieve an even temperature distribution across the length of the sample.

The capsule was attached to the fixed clamp (bottom) and extended to approximately 1 mm below the excitation clamp (top). Thermocouples were located on the surface of the capsule and within the capsule to control the heating element and measure the temperature of the test specimen.

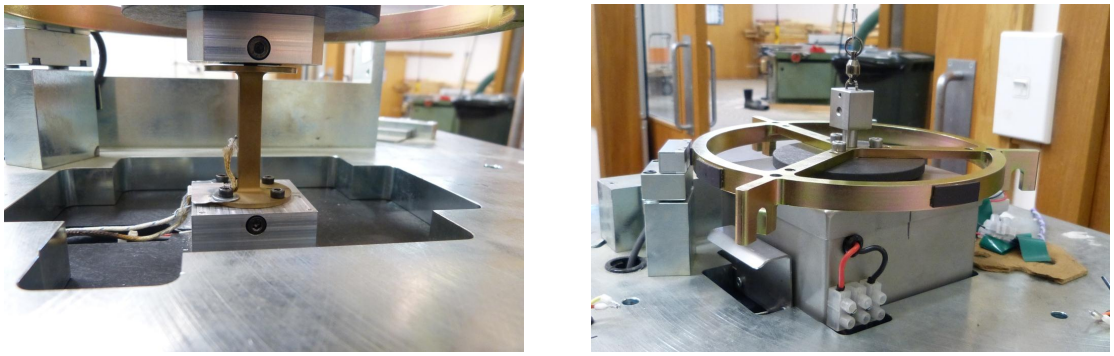

(a) Specimen capsule

(b) Heating chamber

Figure 4.27: Torsional pendulum temperature chamber

The G'_{12} and G'_{23} values for the CFRP were measured using samples with fibres at 90° and 0° to the length of the test specimen respectively. The associated loss factors η_{12} and η_{23} were also determined using these test configurations. Figure 4.28 shows how the specimen orientation corresponded to the required shear properties.

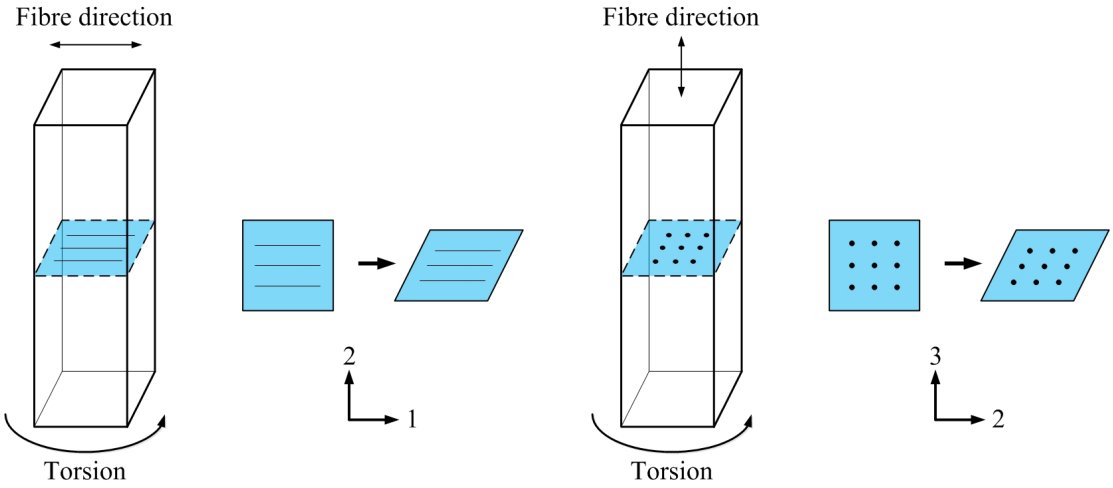

(a) G'_{12} (b) G'_{23}

Figure 4.28: Torsion specimen deformations

Rotations of approximately 0.25 ° to 1 ° were applied to the inertial ring to initiate oscillations. The amplitude and frequency of oscillation were measured using a non-contact magnetic sensor located at the rim of the inertial ring. Custom software created for the test rig was used to set the temperature, record the response of the test specimen and calculate the oscillation frequency and loss factor of the test sample. These values were determined using multiple peaks and troughs from the response curve. The software interface is shown in Figure 4.29.

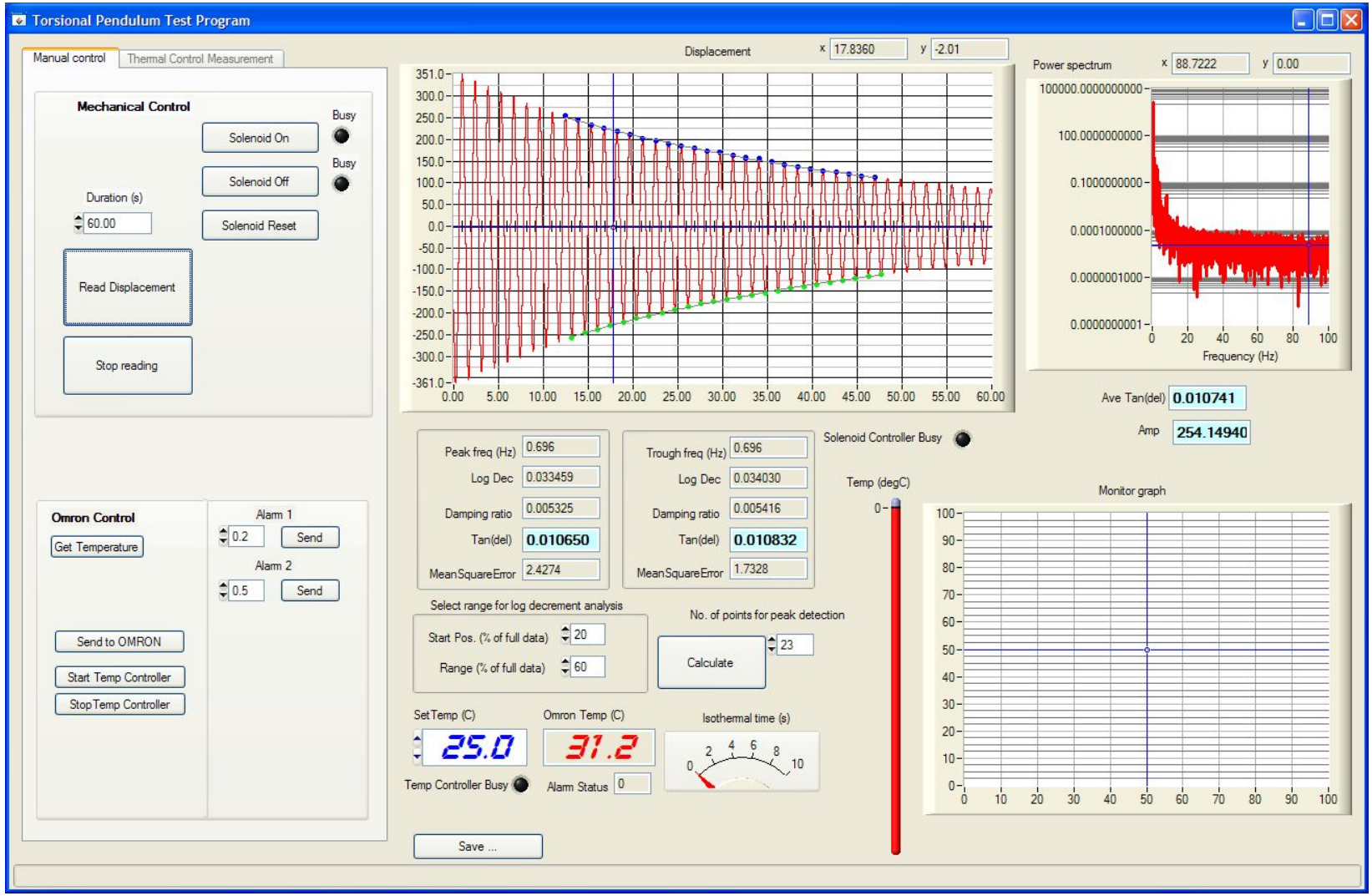

Figure 4.29: Torsional pendulum software interface

The shear modulus values were calculated using the dimensions of the test specimens, the inertia of the ring, the measured oscillation frequency and the logarithmic decrement of the test specimen [97]:

$$G'_{to} = 12\pi^2 I f_d^2 \left[1 - \left(\frac{\Lambda}{2\pi}\right)^2 - \left(\frac{f_0}{f_d}\right)^2\right] \times \frac{L}{bh^3 F_c} \,, \tag{4.56}$$

where

I = moment of inertia of the ring [kg.m^2] ,

f_0 = frequency of the pendulum without the specimen [Hz] ,

f_d = frequency of the damped oscillating system [Hz] ,

Λ = logarithmic decrement of the damped system ,

L = free length of the specimen [m] ,

b = specimen width [m] ,

h = specimen thickness [m] ,

F_c = 1 - 0.63h/b, dimensional correction factor .

Torsional loss factor, η_{to}, could be calculated from the relationship between logarithmic decrement and loss factor [98] using

$$\eta_{to} = \frac{\Lambda}{\pi} \,. \tag{4.57}$$

Several oscillation decays were measured for the 0° and 90° fibre angle test specimens. Table 4.6 shows a summary of the test conditions and average experiment results.

The frequency dependence of the two torsional moduli and associated loss factors were unable to be measured using the torsional pendulum as only one inertial ring size was available. Measurements were able to be performed at temperatures above room temperature but sub-ambient temperatures were not possible. Consequently behaviour at higher frequencies was not measurable. The frequency dependent terms of the shear moduli were approximated using values measured with the DMA in a dual cantilever arrangement. It was assumed that the two shear moduli were dominated by the matrix material behaviour, so the fibres

Parameter	0° specimen	90° specimen
I [kg.m^2]	0.0041	0.0041
f_0 [Hz]	0	0
f_d [Hz]	0.695	0.505
Λ	0.0365	0.0393
L [mm]	50.6	51.0
b [mm]	5.23	5.26
h [mm]	1.101	0.828
T [°C]	25	25
η_{to}	0.0116	0.0125
G'_{to} [GPa]	1.97	2.35

Table 4.6: Torsional pendulum conditions and results

of the test specimen were aligned transverse to the length direction. This assumption was based, in part, on the similarity of measured shear modulus values of G'_{12} and G'_{23}. The conditions used for the shear moduli frequency dependence test are shown in Table 4.7. The corresponding master curve is shown in Figure 4.30. Combining these measured values with those found from the torsional pendulum experiments, the shear moduli used in the FEM were

$$G'_{12} = 2.35 + 0.230 \log \omega \,, \tag{4.58}$$

$$G'_{23} = 1.97 + 0.230 \log \omega \,. \tag{4.59}$$

The associated damping loss factor values measured from the torsional pendulum experiments were assumed to be constant across the frequency range of interest, following the frequency dependence behaviour of η_1 and η_2. Hence, the loss factor values associated with the shear moduli used in the FEM were

$$\eta_{12} = 0.0125 \,, \tag{4.60}$$

Parameter	Measurement setting
Clamp arrangement	Dual Cantilever
Excitation frequencies (Hz)	5, 10, 20, 30, 40, 50, 60, 70, 80, 90, 100, 110
Temperature range (°C)	$24 \rightarrow 60$
Temperature step	+1°C
Isothermal duration	10 minutes
Strain	0.013%
Specimen length (mm)	35.00
Specimen width (mm)	12.14
Specimen thickness (mm)	0.96

Table 4.7: DMA settings for measurement of the G'_{23} and G'_{23} frequency dependence terms

$$\eta_{23} = 0.0116 \, . \tag{4.61}$$

Of the two required Poisson's ratios for the CFRP, only ν_{12} was able to be measured experimentally. This value was determined using the MTS tensile tester and a video extensometer. Axial and transverse strains induced by extensional loading of a test specimen with fibres aligned with the loading direction were measured by tracking the displacement of four markers in a cross configuration (Figure 4.31). The ratio between these strains was used to determine the required Poisson's ratio. The conditions for this test are detailed in Table 4.8 and the measured response is shown in Figure 4.32.

In order to measure ν_{23}, a test specimen with fibres orthogonal to both the axial and transverse strains would be required. This could be achieved by measuring the thickness change of a specimen with fibres at 90° to the loading direction. However, due to the limited thickness of the test specimens available, and the variation in thickness of the specimens along the length, accurate measurement of ν_{23} was not feasible. This value was instead approximated as the Poisson's ratio for epoxy [53, p. 13], based on the assumption that the

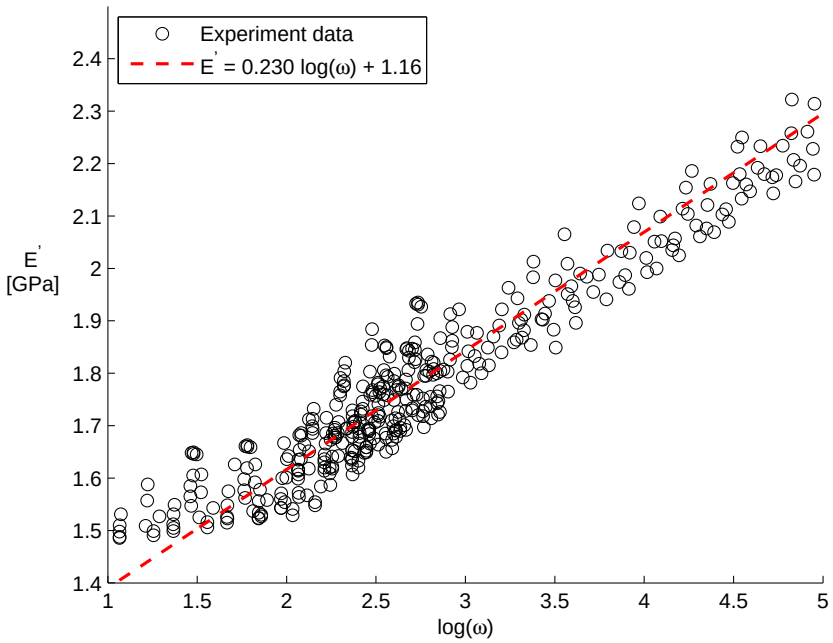

Figure 4.30: DMA master curve for determining G'_{23} and G'_{23} frequency dependence

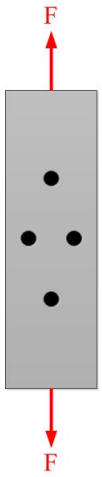

Figure 4.31: Strain tracking marker configuration

deformation would be dominated by straining of the matrix and the 2-3 plane being a plane of symmetry.

Parameter	Measurement setting
	ν_{12}
Clamp arrangement	Tension
Load cell (kN)	2.5
Extension rate (mm/minute)	2
Specimen length (mm)	42.08
Specimen width (mm)	15.25
Specimen thickness (mm)	0.94

Table 4.8: MTS settings for measurement of ν_{12}

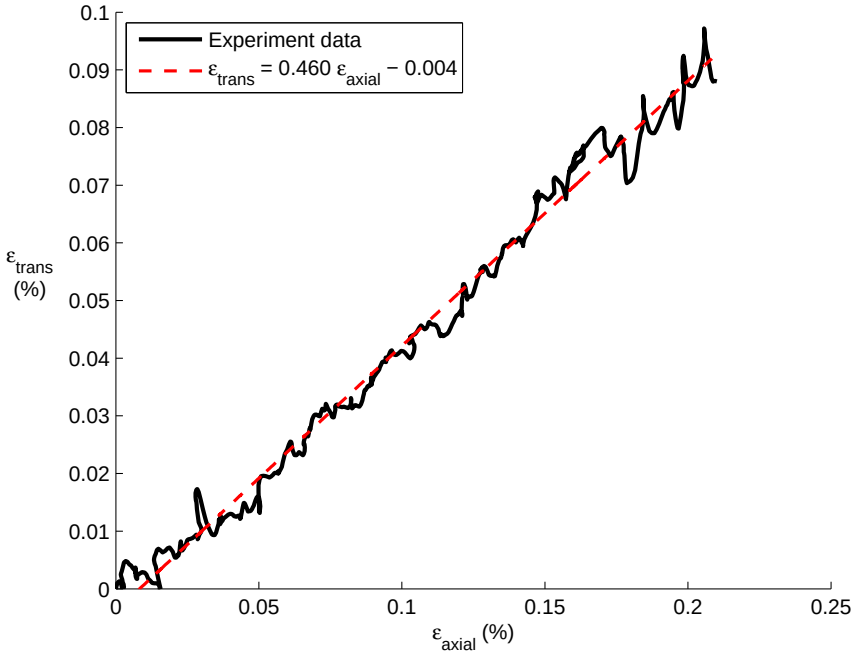

Figure 4.32: MTS strain data for determining ν_{12}

The resulting Poisson's ratios for the CFRP were

$$\nu_{12} = 0.46 \,, \tag{4.62}$$

$$\nu_{23} = 0.4 \,. \tag{4.63}$$

Density measurements of the CFRP were dependent on the relative proportions of fibre and matrix within each composite layer. In order to account for any variation in fibre/matrix volume fraction, each of the forty test beams were weighed and their length and width dimensions were measured. An accurate measure of beam thickness was determined from microscopic evaluation of a beam sample cross-section. Accounting for the density of the VEM and assuming the VEM thickness to be 0.2 mm, the average density of the CFRP could be calculated. The average dimensions, weight, and resulting CFRP density are shown in Table 4.9.

Parameter	Average value
Length (mm)	480.15
Width (mm)	80.00
Thickness (mm)	1.57
Weight (g)	81.0
ρ_c (kg.m^{-3})	1385

Table 4.9: Average beam geometry, weight and resulting CFRP density

VEM Properties

A TA Q800 Dynamic Mechanical Analyser (DMA) was used to measure the shear modulus and associated loss factor for the damping tape. The DMA lacked the clamp needed to measure shear directly so the tension-film clamp was used in a modified configuration to achieve the required properties. Figure 4.18 shows the standard configuration for the tension clamp.

Shear measurements for the damping tape were achieved by cutting a 30 mm × 10 mm sample from a three-layer beam with unidirectional carbon fibre strands oriented at 0° to the length of the beam. Each CFRP layer was reduced by 6 mm on opposite faces at the ends to produce the final test sample seen in Figure 4.33. The tension-film clamps were able to be shifted to correctly align with the extended CFRP layers, ensuring that no out of plane forces were exerted on the VEM layer.

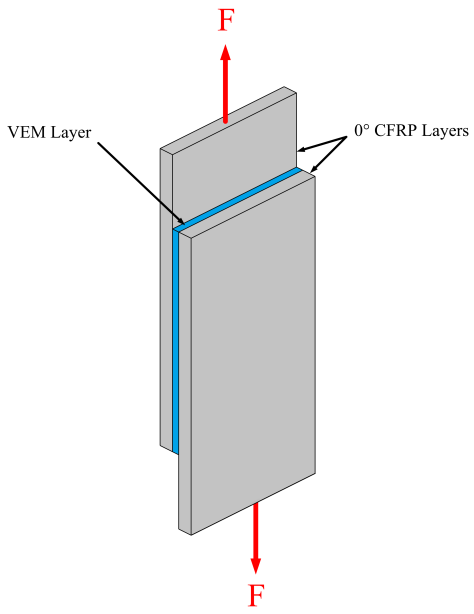

Figure 4.33: Test specimen for measuring damping tape shear modulus and loss factor

Extensional modulus values obtained from the DMA were scaled by t^2/L^2 to obtain the true shear modulus values, where t was the thickness of the damping layer and L was the length of the damping layer. This conversion factor was calculated by comparing the definitions of Young's and shear moduli and applying them to the geometry and clamp configuration used for testing.

In the configuration used $E' = \frac{FL}{\Delta x W t}$ and $G' = \frac{Ft}{\Delta x L W}$. As the force ($F$) and displacement ($\Delta x$) measured by the DMA were the same for both of these equations, a geometric

conversion (C) could be applied to convert from extensional modulus (E') to shear modulus (G') using the relationship $G' = CE'$:

$$\frac{Ft}{\Delta xLW} = C(\frac{FL}{\Delta xWt}) \, . \tag{4.64}$$

Rearranging for C resulted in

$$C = \frac{t^2}{L^2} \, . \tag{4.65}$$

Use of steel shim rather than CFRP around the damping tape was considered as the matrix material in the carbon layers may have added some additional damping to the system. However, it was important to properly account for the bonding between the matrix material and the damping tape. The alignment of the carbon bundles in the direction of the load was assumed to reduce any damping effect from the CFRP layers as the response would be dominated by the load bearing fibres rather than the matrix material. The shear modulus and associated damping loss factor of the VEM were measured using the test conditions in Table 4.10.

Parameter	Measurement setting
Clamp arrangement	Tension
Excitation frequencies (Hz)	10, 20, 30, 50, 60, 70, 80, 90, 100
Temperature range (°C)	-5 $\rightarrow$ 30
Temperature step	+1°C
Isothermal duration	10 minutes
Strain	0.08%
Specimen length (mm)	17.97
Specimen width (mm)	10.10
Specimen thickness (mm)	0.2

Table 4.10: DMA settings for measurement of $G'_v(\omega)$ and $\eta_v(\omega)$

The values of G'_v showed noticeable variation between experiments while values of η_v remained more consistent. The maximum and minimum measured values of G'_v are shown in Figure 4.34.

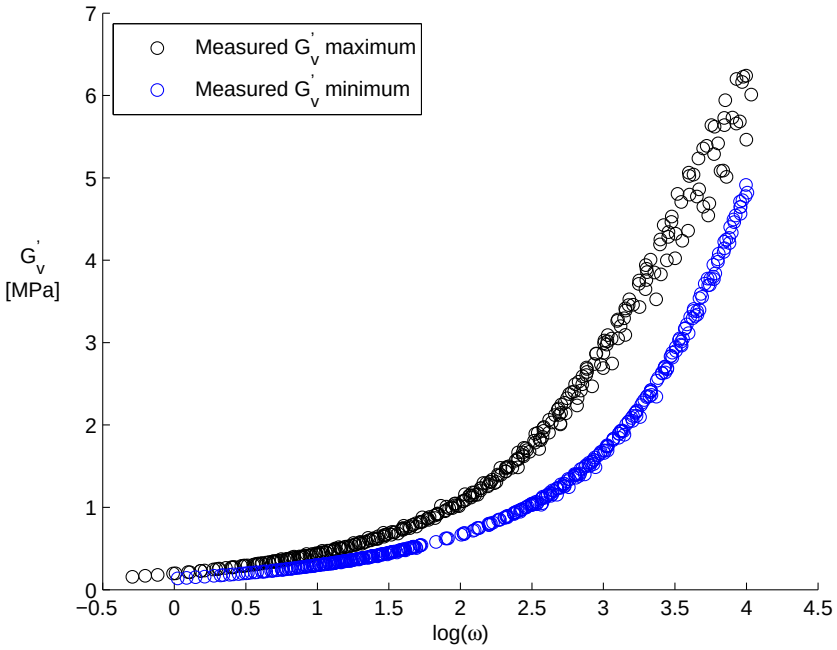

Figure 4.34: DMA master curve range for G'_v

An analytical model for each of these curves was created using the MATLAB function *polyfit* and employed to determine the average response of G'_v with frequency (Figure 4.35). The average model of G'_v was used in the FEM.

The measured values for $\eta_v(\omega)$ are shown in Figure 4.36, along with the line of best fit used to describe this value in the FEM.

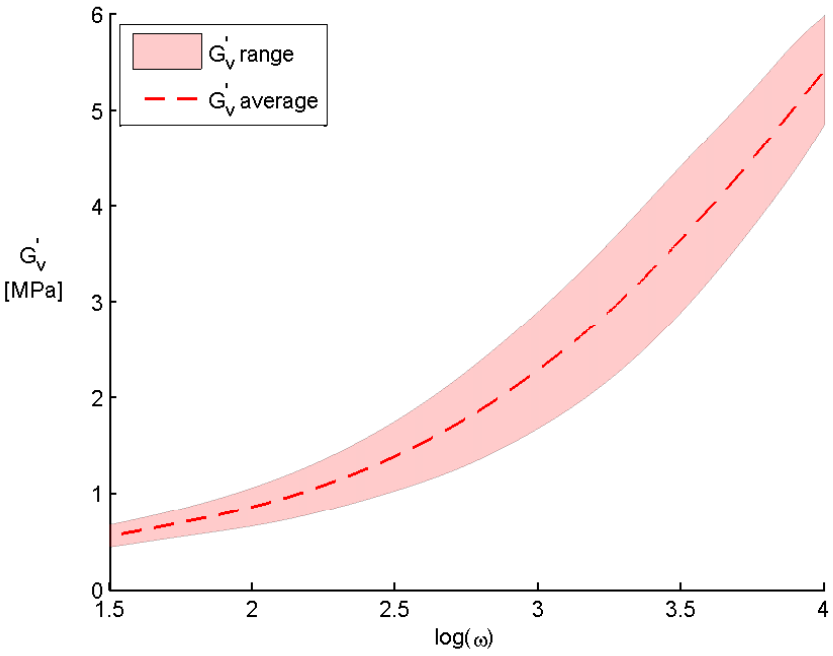

Figure 4.35: Average modelled response of G'_v

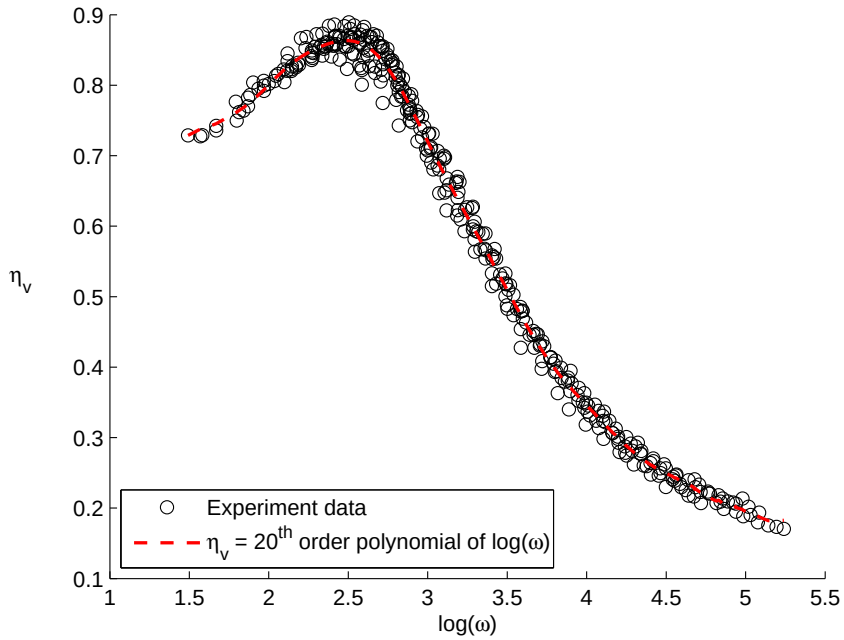

Figure 4.36: η_v master curve from DMA testing

The Poisson's ratio for the VEM was measured using the same technique as for ν_{12} and ν_{23}. The same test conditions as shown in Table 4.8 were used with a VEM specimen 70 mm long, 20.25 mm wide and 0.2 mm thick. The resulting strain curve is shown in Figure 4.37.

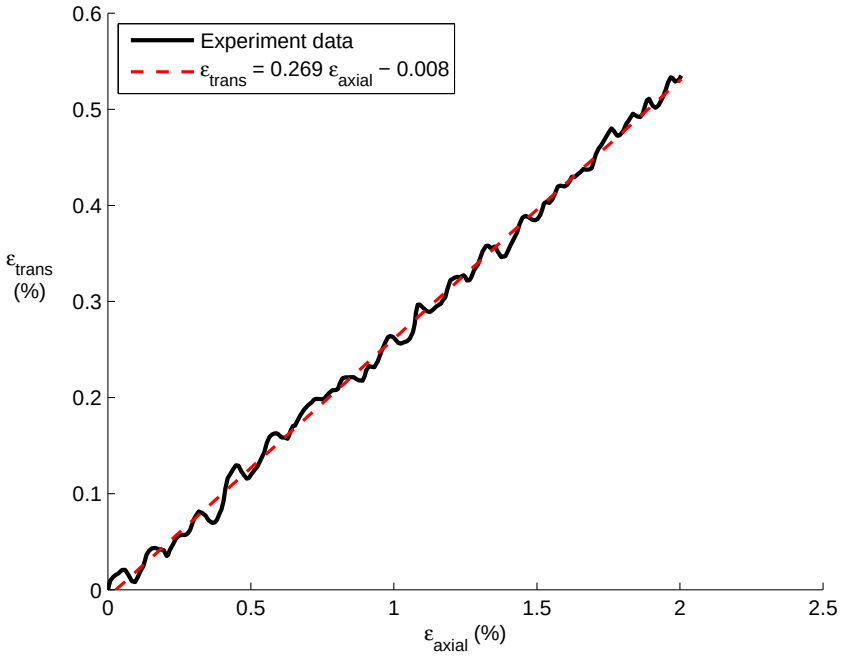

Figure 4.37: MTS strain data for determining ν_v

The gradient of this data produced a Poisson's ratio of

$$\nu_v = 0.269\ . \tag{4.66}$$

The density of the VEM was calculated by measuring the weight of a sample of the damping tape with known dimensions. The release liner remained attached for the weight measurement to prevent adhesion to the scales. The release liner was then removed from the tape sample and its weight measured to determine the weight of the damping tape alone. Table 4.11 summarises the sample dimensions, weight and resulting VEM density.

Parameter	Value
Length (mm)	74.4
Width (mm)	16.41
Thickness (mm)	0.2
Weight (g)	0.2599
ρ_c (kg.m^{-3})	1064

Table 4.11: VEM density

Summary of Properties

The summary of material properties for the VEM and CFRP are shown in Tables 4.12 and 4.13 respectively.

Property	Value used in FEM
$G'_v(\omega)$ [GPa]	20^{th} order polynomial of log(ω)
$\eta_v(\omega)$	20^{th} order polynomial of log(ω)
ν_v	0.269
L [mm]	480
W [mm]	80
t [mm]	0.2
ρ_v [kg.m^{-3}]	1064

Table 4.12: Summary of VEM properties input to FEM

Property	Value used in FEM
$E_1'(\omega)$ [GPa]	50.105 + 0.07854 log(ω)
$\eta_1(\omega)$	0.0036
$E_2'(\omega)$ [GPa]	4.33 + 0.119 log(ω)
$\eta_2(\omega)$	0.029
$G_{12}'(\omega)$ [GPa]	2.35 + 0.170 log(ω)
$\eta_{12}(\omega)$	0.0116
$G_{23}'(\omega)$ [GPa]	1.97 + 0.230 log(ω)
$\eta_{23}'(\omega)$	0.0125
ν_{12}	0.46
ν_{23}	0.4
L [mm]	480
W [mm]	80
t [mm]	0.685
ρ_c [kg.m^{-3}]	1385

Table 4.13: Summary of CFRP properties input to FEM

4.3.4 Comparison of Model and Experiment Results

The FEM was validated by comparing modelled damping results to experimental data.

Measurement Technique

The measurable properties required from the test beams were the modal frequencies and associated damping loss factors. These values were determined using the half-power bandwidth method from the frequency response of each beam (see Section 2.3.1). Loss factors for each mode were calculated using

$$\eta = \frac{f_2 - f_1}{f_r} \,, \tag{4.67}$$

where f_r is the resonant frequency of the mode, f_1 is the lower frequency which occurs 3 dB lower than the peak at f_r, and f_2 is the upper frequency which also occurs 3 dB lower than the peak at f_r.

In order to measure the frequency response curves, appropriate end conditions and excitation signals were required. Unconstrained end conditions were selected for the mounting of the samples. Cantilevering the beams was initially considered as it would more closely simulate the ISO [78] and ASTM [79] test methods. This end condition was ruled out as it would reduce the length of the fibre patterns exposed to excitation. The variation in thickness of the test samples also made an effective clamping arrangement infeasible.

Unconstrained end conditions were approximated by suspending each beam vertically by a string running through a hole 30 mm from one end. Horizontal suspension, like that used in the ISO method [78], was not used as the suspension fibres would require relocation for each mode of interest. There were also concerns that the horizontal suspension would have a noticeable effect on the measured response due to the large width and low weight of the beams.

Excitation was provided using an impact hammer and the response measured using a single axis accelerometer.

Each beam had a 1 mm hole punched on the centreline and 30 mm from one end to facilitate vertical suspension. Care was taken while punching each hole to ensure that damage to the sample, particularly fracture between fibre strands, was minimised. Test specimens were suspended 300 mm below a section of rod by inelastic thread.

A PCB 352C42 accelerometer was attached to each test specimen using wax. The accelerometer was placed on the midline of the test specimen, approximately 10 mm from the bottom edge. This location was selected to capture as many bending modes as possible without altering the natural response significantly due to the point mass of the accelerometer or the stiffness provided by the accelerometer cable. Torsional modes were not captured using this location as the accelerometer was lying on a nodal line. The weight of the accelerometer was approximately 2% of the beam weight; this was considered small enough to have minimal effect on the response.

The accelerations were recorded and passed through a Fast Fourier Transform (FFT) function using a Brüel & Kjær PULSE multi-analysis platform. A measurement frequency range of 0 - 500 Hz was sufficient to capture the first four bending modes. Modes 5 and above often had either indistinct peaks or a peak height less than 3 dB, rendering them unusable for calculation and comparison purposes. The maximum resolution for the FFT was used to accurately capture the first bending mode.

Three impact locations were used for each specimen. These were located on the lower half of the beams and on the centreline to minimise rotation about the longitudinal axis. The three impact points were selected to excite both odd and even bending mode shapes.

Each impact point was struck a total of five times to give fifteen impacts per frequency response curve measured. Ten frequency responses were recorded for each test specimen to gain an acceptable measurement sample population. Impacts were produced using a PCB 086C03 impact hammer with a medium hardness tip. Care was taken when impacting the beams to ensure clean single strikes were achieved. Double hits were often audible and could be seen in the frequency response as it was being reported in real time. A time domain signal was also used to verify impact occurrence and quality. Measurement data was discarded if a double hit was detected. The test apparatus configuration can be seen in Figure 4.38.

Figure 4.38: Testing apparatus configuration

As the test specimens were suspended from a single point with inelastic thread, the beams were prone to swinging after each impact. Rotation about the longitudinal centreline was minimised due to both impact locations and the stiffness provided by the accelerometer cable. The lack of rotation was considered not to have a large effect on the measured response as the single axis accelerometer measured only accelerations transverse to the face of the beams. Swinging of the beams after each strike was observed in the measured frequency

response. The frequency of this movement was much lower than the first bending mode, and was consequently considered to have negligible effect on the beam modal frequencies and damping loss factors.

Tests were performed at two environmental conditions, ambient temperature and sub-ambient temperature. Ambient temperature measurements were made at temperatures ranging from 23 °C - 27 °C, with a target measurement temperature of 25 °C. This represented a temperature range that could be reasonably expected in common applications. Sub-ambient temperature measurements were also performed in an attempt to better capture the temperature and frequency dependence of the damping properties. A cool store facility located at the University of Canterbury was used for the sub-ambient testing. This room was refrigerated to 4 °C but cycled between 3 °C and 7 °C during testing. In both ambient and sub-ambient conditions, the temperature was recorded using a hot-wire anemometer.

Particular care had to be taken with the impact excitation during the sub-ambient testing as air was circulated within the cool store by a fan. The forced air movement often caused the test specimens to swing, making clean strikes of the beams difficult.

Sub-ambient test results were not able to be compared to modelled results due to insufficient material property data at the low temperature condition. However, they were useful for evaluating the low temperature modal damping performance of the CPF-CLD material. The results produced by testing in sub-ambient conditions are presented in Appendix A.5.

Results

The experiment results produced at ambient temperature are shown in Figure 4.39 and tabulated in Appendix A.4. Error bars indicate one standard deviation from each data point.

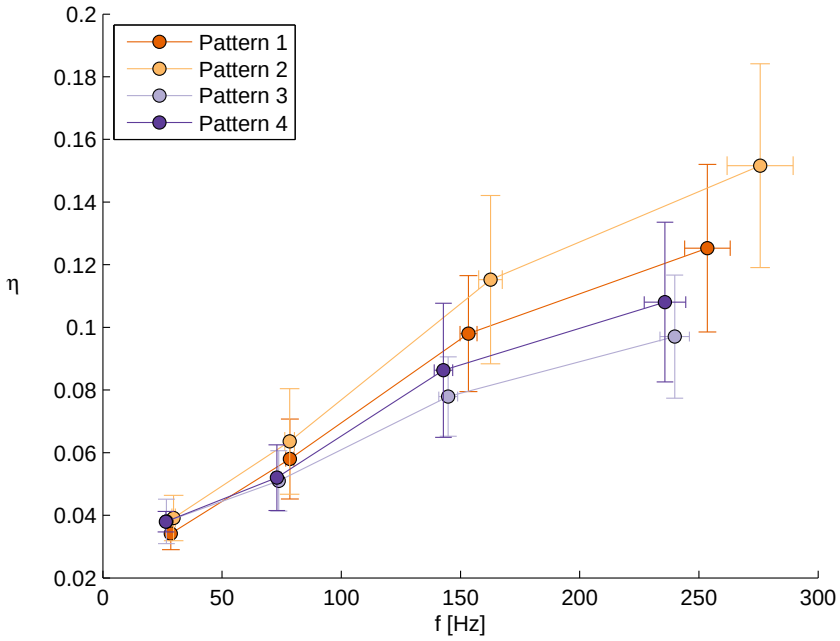

Figure 4.39: Experimental results at ambient temperature

From these results there appears to be a measurable difference between pattern damping performance, particularly at the higher measured modes. However, there is significant spread in the measured data, particularly the measured loss factor values, as shown by the error bars. As a consequence the experimental results should only be considered to indicate general trends rather than exact differences in damping performance between patterns.

Using the measured material properties, test specimen beam geometries, and accounting for the section of fibre pattern present in the test specimens, the FE model prediction of each fibre pattern was conducted. The results produced by the model for each pattern are shown in Figures 4.40 - 4.43. The boxed areas surrounding each modal data point indicate one standard deviation.

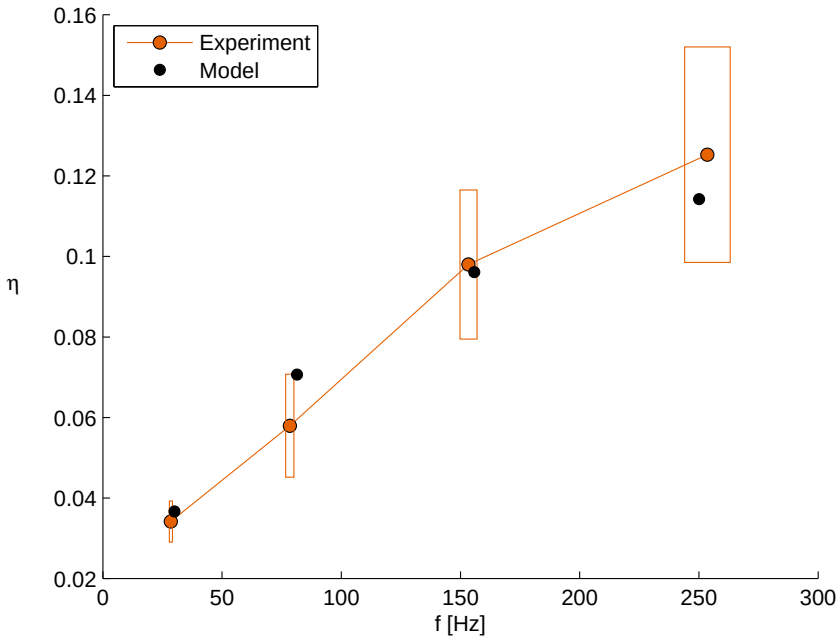

Figure 4.40: Pattern 1 model comparison

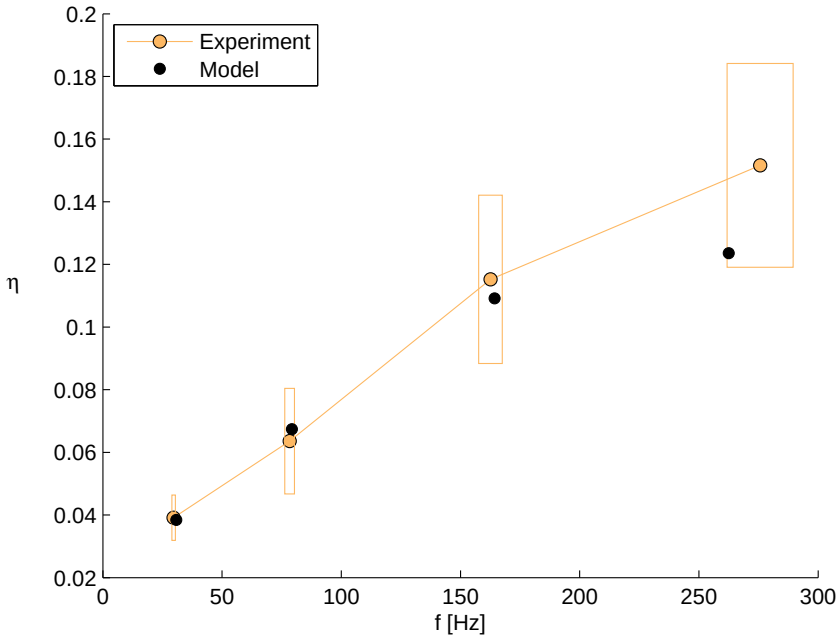

Figure 4.41: Pattern 2 model comparison

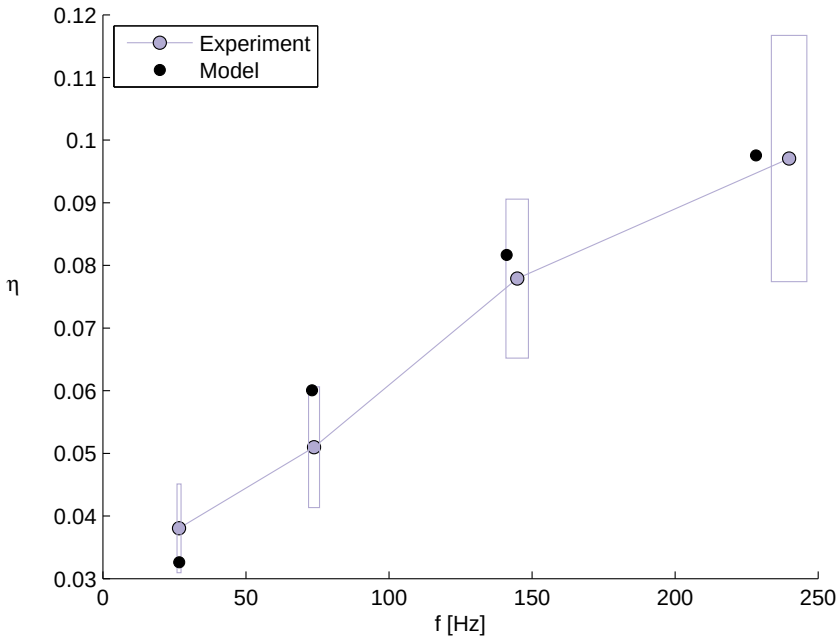

Figure 4.42: Pattern 3 model comparison

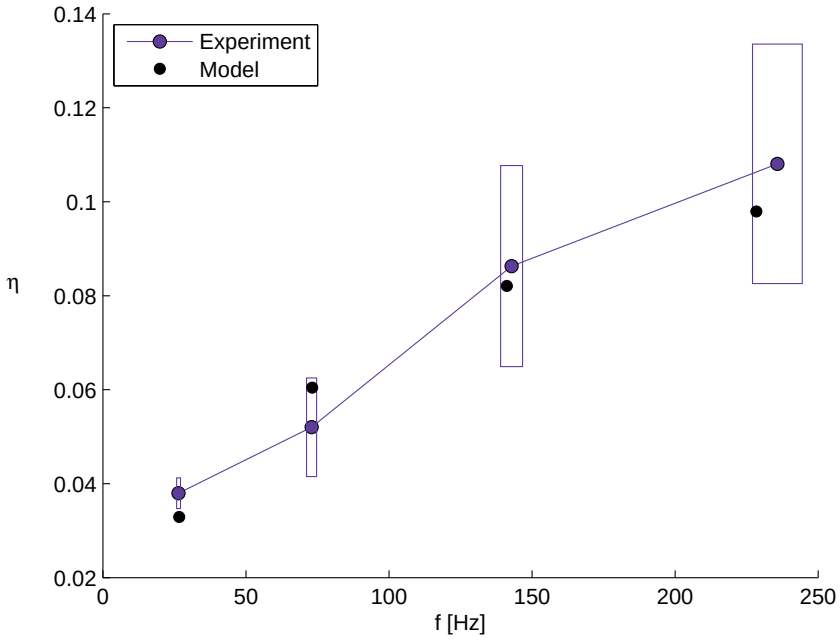

Figure 4.43: Pattern 4 model comparison

It can be seen that the majority of the modelled results fall within one standard deviation of the experiment data. Deviations from the experiment averages were likely due to the material properties used in the FE model.

Looking at each of the modes individually gives a better representation of the relative variation in data between the patterns. The modal frequencies are shown in Figures 4.44 - 4.47. Modal loss factors are shown in Figures 4.48 - 4.51.

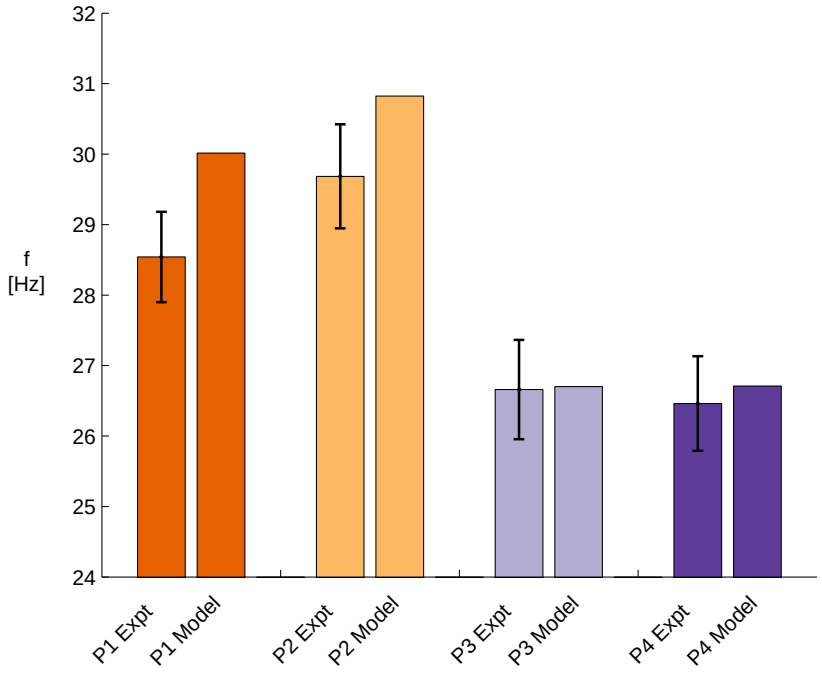

Figure 4.44: Mode 1 frequencies

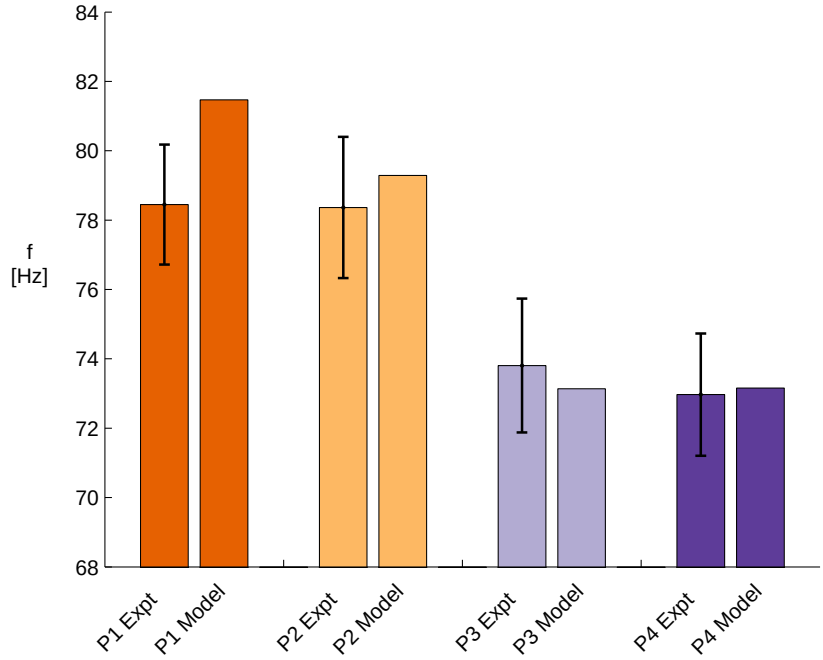

Figure 4.45: Mode 2 frequencies

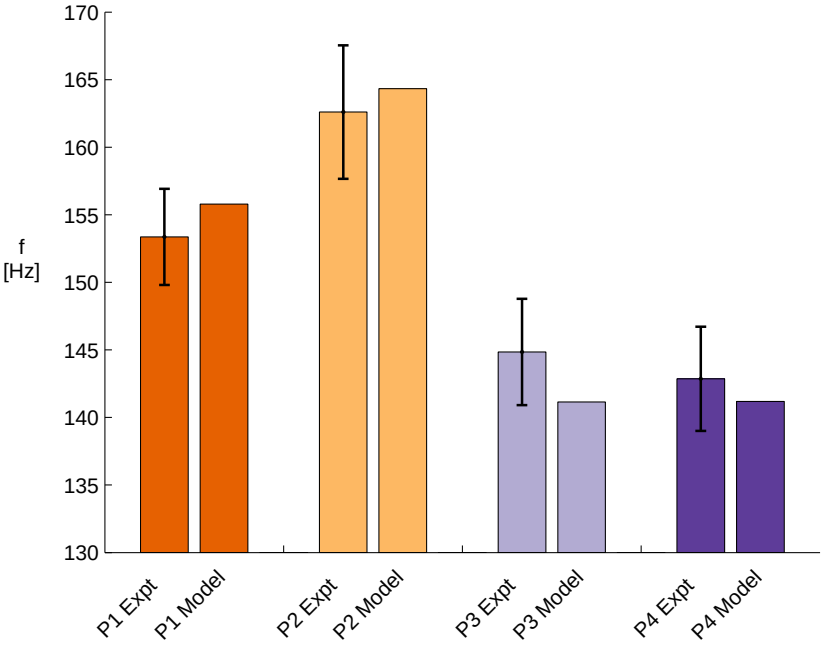

Figure 4.46: Mode 3 frequencies

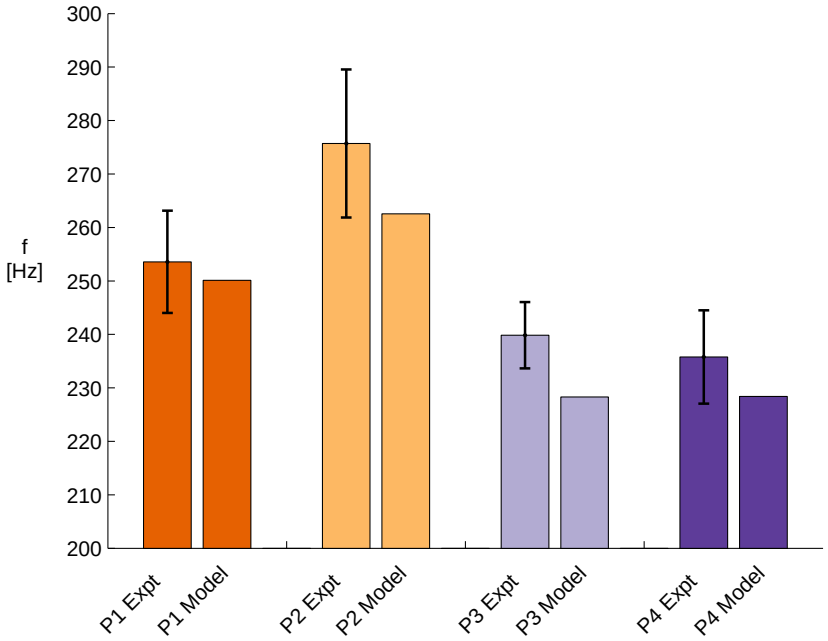

Figure 4.47: Mode 4 frequencies

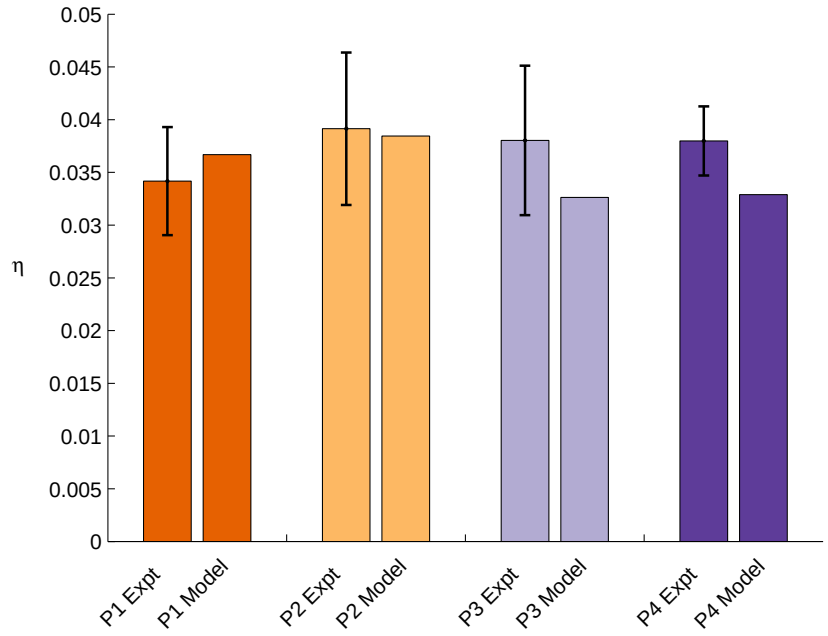

Figure 4.48: Mode 1 loss factors

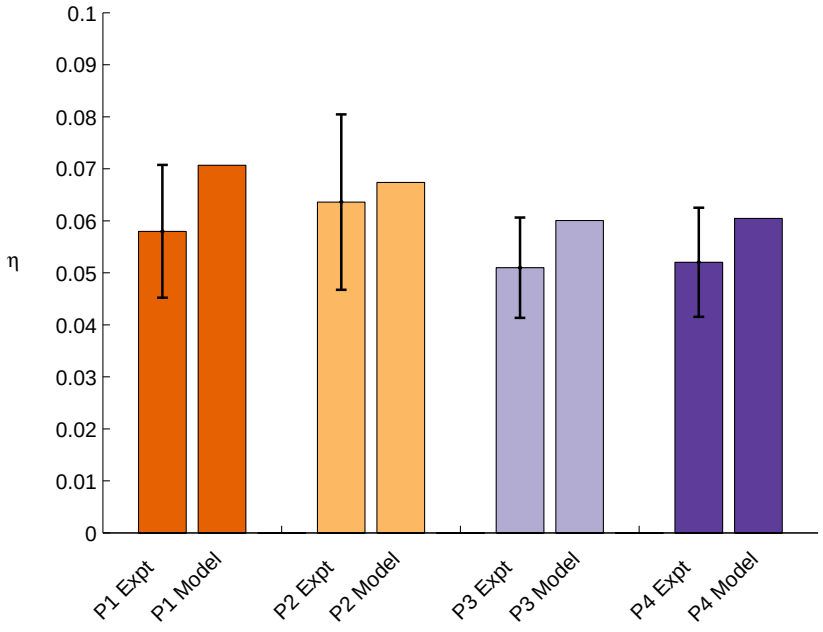

Figure 4.49: Mode 2 loss factors

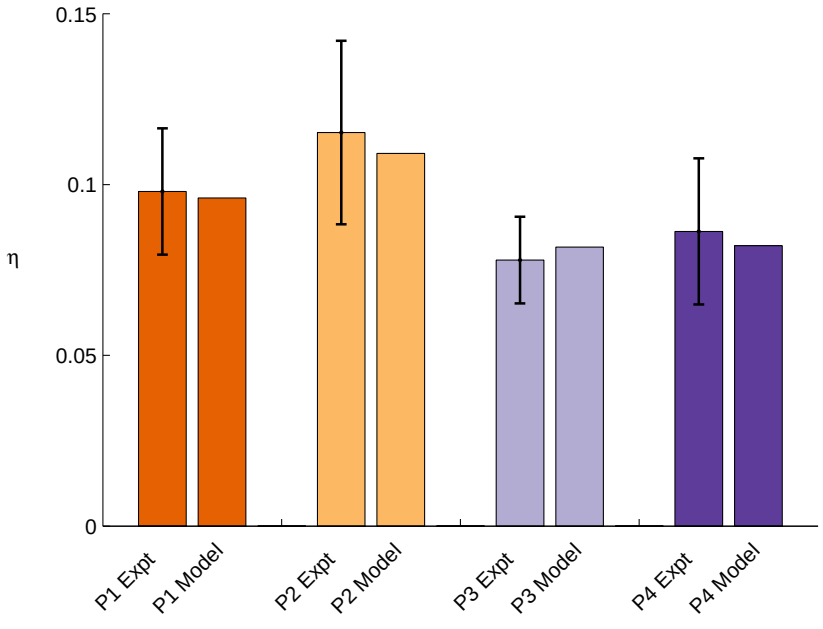

Figure 4.50: Mode 3 loss factors

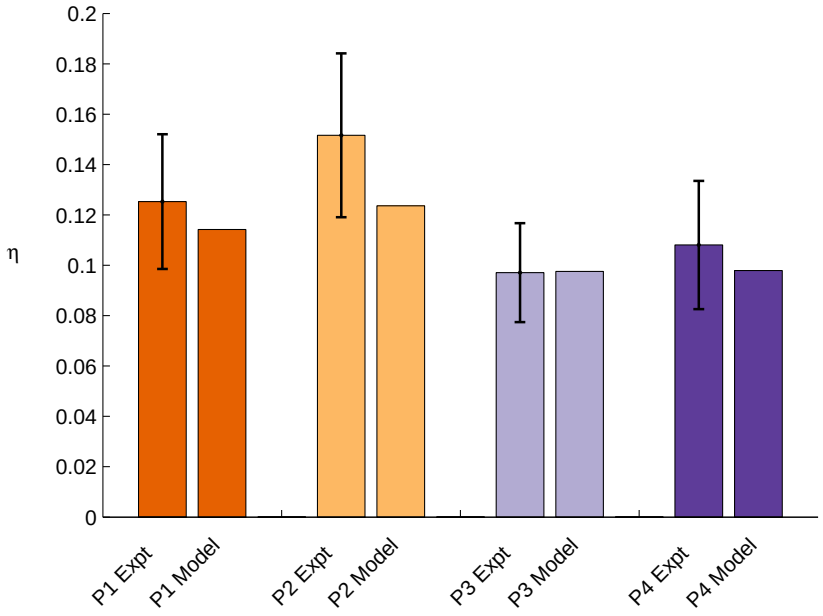

Figure 4.51: Mode 4 loss factors

From these figures it is observed that the model is capable of determining the order in which pattern modal frequencies and loss factors fall, with the exception of damping in mode 2. The relative difference between the modal behaviour of each pattern is also captured with reasonable accuracy. This is best shown by normalising the experiment and model results by the largest values produced by each for each of the four modes. Figures 4.52 - 4.55 show the normalised modal frequencies of the model and experiment results. The normalised loss factor results are shown in Figures 4.56 - 4.59. Error bars indicate one standard deviation of the normalised data.

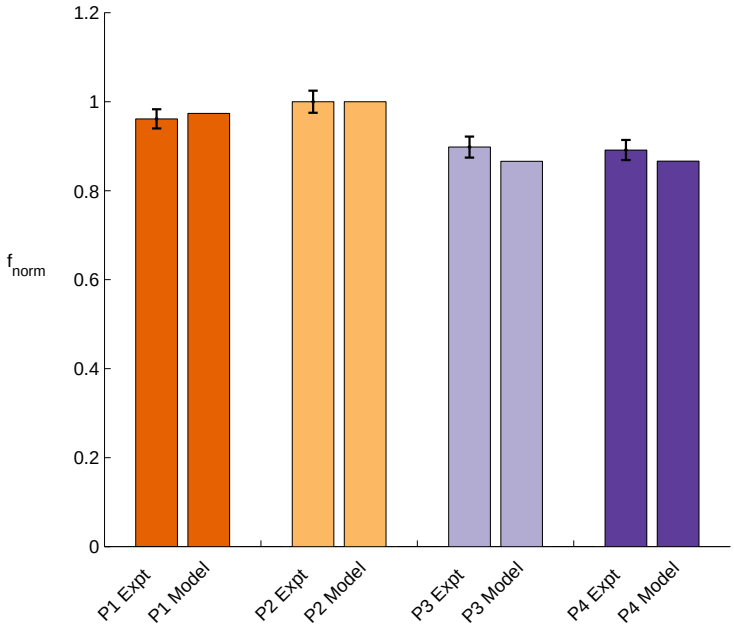

Figure 4.52: Normalised mode 1 frequencies

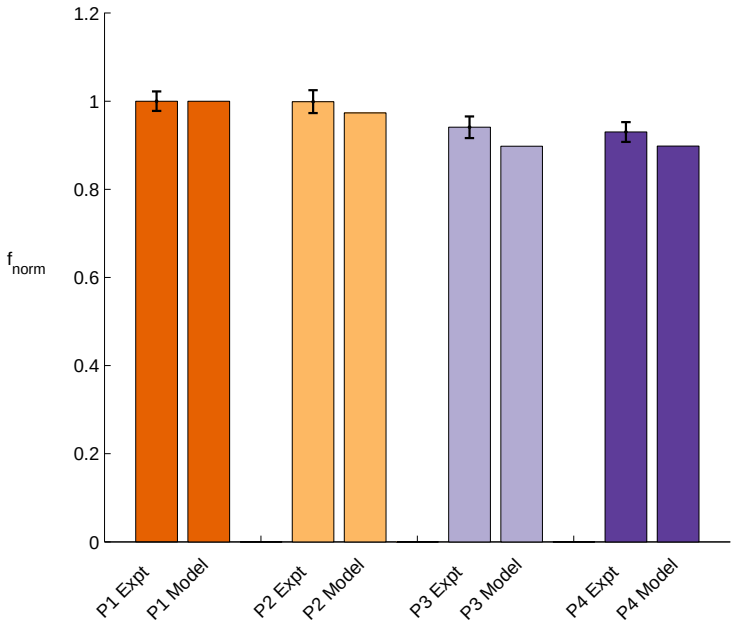

Figure 4.53: Normalised mode 2 frequencies

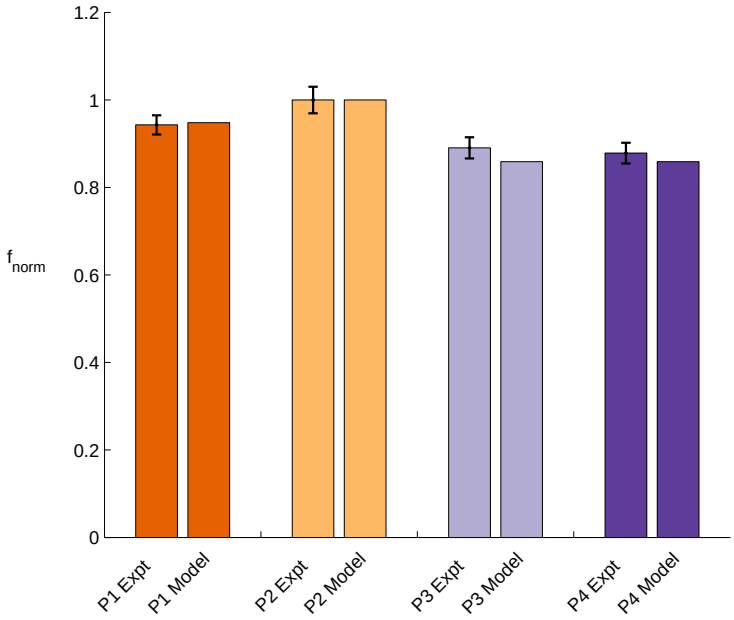

Figure 4.54: Normalised mode 3 frequencies

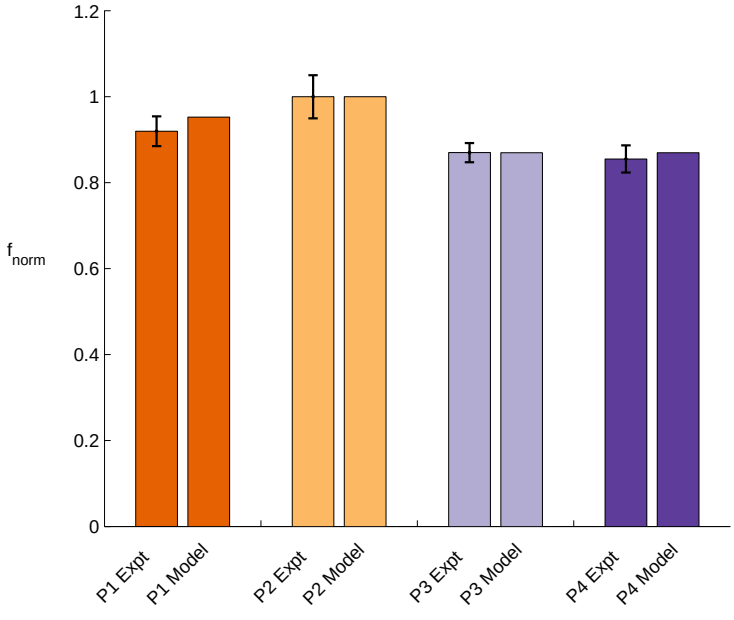

Figure 4.55: Normalised mode 4 frequencies

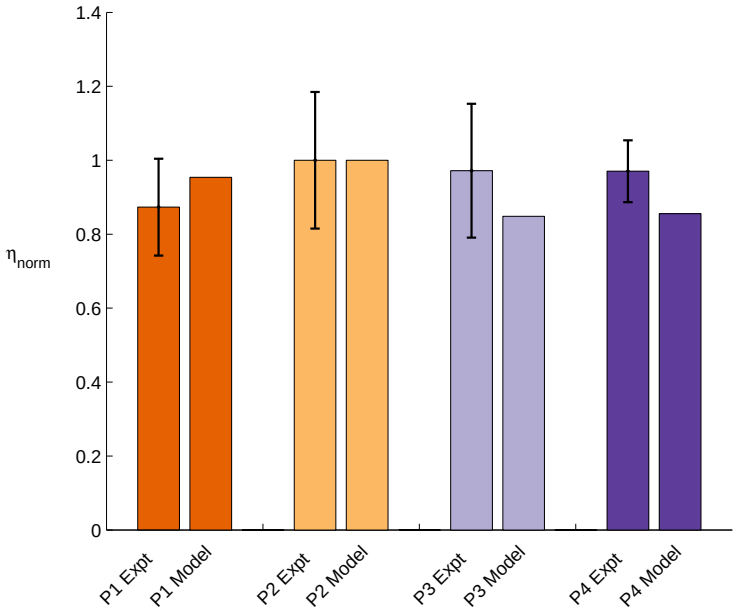

Figure 4.56: Normalised mode 1 loss factors

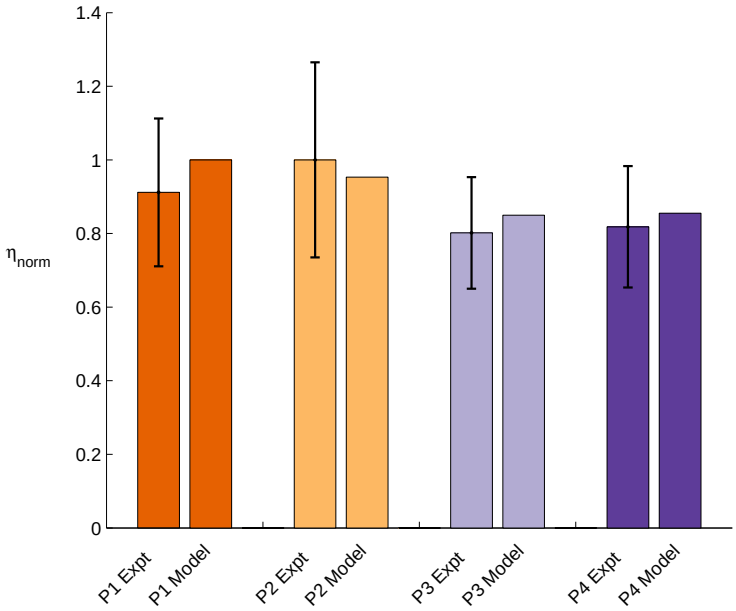

Figure 4.57: Normalised mode 2 loss factors

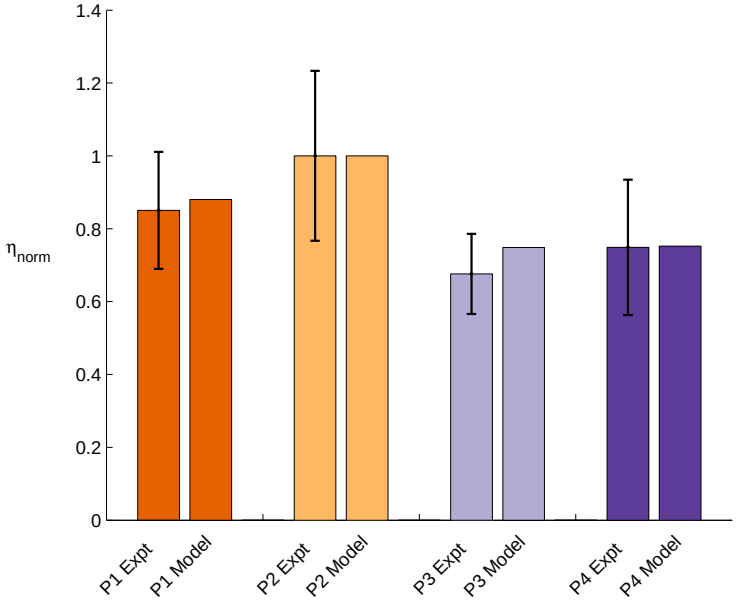

Figure 4.58: Normalised mode 3 loss factors

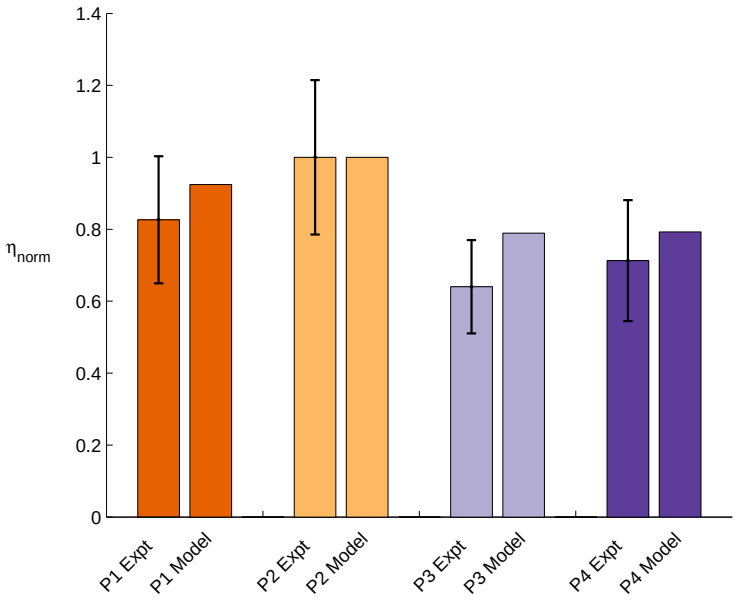

Figure 4.59: Normalised mode 4 loss factors

The relative performance difference between each of the four patterns is captured by the model with reasonable accuracy. The relative difference between the measured modal frequencies and the differences predicted by the model appear to match reasonably well. The relative loss factor performance predicted by the model shows greater deviations from the measured differences. This may be due to the large scatter present in the measured loss factor values.

It can be concluded that the FE model developed produces reasonable modal frequency and loss factor results when compared to the trends found in experimental data, given the assumptions made and the material property data provided. It is capable of determining the relative performance of fibre patterns at the first four flexural modes with a good degree of confidence.

4.4 Exploration of Patterns

The FE model was used to explore the damping behaviour produced by the various fibre patterns.

A trend was apparent from the results produced by the model. At each measured bending mode the pattern which produced the greatest modal frequency also produced the greatest associated loss factor. It was also apparent that patterns 3 and 4 produced very similar results.

Differences between the modal frequencies of each pattern would be predominantly due to the differing flexural rigidities of the patterns, as the beam geometries and densities were identical. The parameter which would influence the flexural rigidity of each pattern was the material stiffness in the direction of the propagating bending wave.

A metric useful for simplifying each fibre pattern was average absolute fibre angle ($\overline{\theta}_{abs}$). Each waveform was comprised of a finite number of fibre angles which ultimately determined the directional stiffnesses of the fibre pattern. If an axial load was applied in the length direction of each pattern, the pattern with the lowest $\overline{\theta}_{abs}$ in the length direction would exhibit greater extensional stiffness as more of the load would be taken by the fibres. It follows that patterns with a lower average absolute fibre angle in the direction of bending wave propagation would exhibit greater flexural rigidity, and would consequently produce higher modal frequencies.

Determining the average absolute fibre angles in the length (x) direction for the four patterns, using the fibre angle at each Gauss point, produced the following results.

Pattern	$\overline{\theta}_{abs}$ [$^\circ$]
Pattern 1	15.1
Pattern 2	13.0
Pattern 3	19.9
Pattern 4	19.5

Table 4.14: Pattern average absolute fibre angles

These values were consistent with the modal frequency and damping trends predicted by the model. Smaller values of $\overline{\theta}_{abs}$ produced greater bending mode frequencies and associated loss factors.

This trend indicated that for bending modes in the length direction, the greatest damping performance would be achieved by a fibre pattern with an average absolute fibre angle of 0° relative to the x axis. The modal response of a unidirectional (UD) fibre pattern with fibres aligned in the length direction of the beam, termed UD0, was compared to the responses of the four patterns using the FEM. The length of the beams studied was set at 600 mm to

capture the full waveform of each of the patterns. As a consequence, the modal frequencies and associated damping loss factors of the patterned fibre beams was lower than the values produced in the validation comparisons. The results produced by the first four bending and torsion modes of each beam in a free-free configuration are displayed in Figures 4.60 and 4.61 respectively.

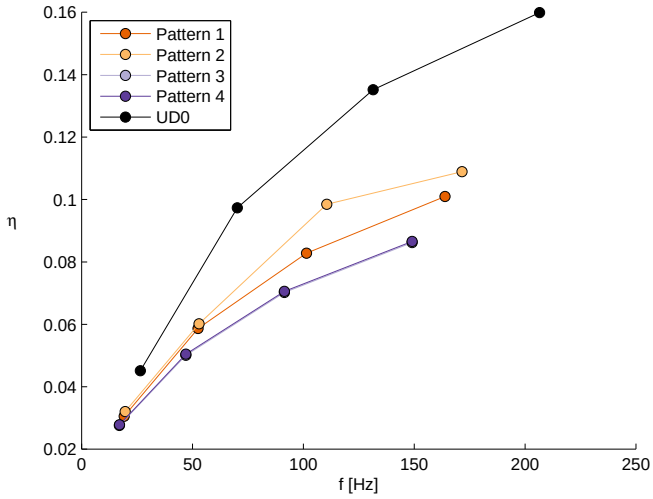

Figure 4.60: Damping comparison for the first 4 bending modes

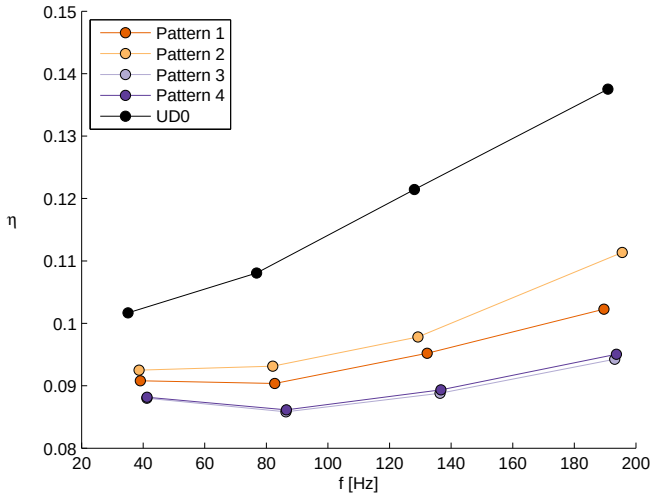

Figure 4.61: Damping comparison for the first 4 torsion modes

Bending and torsion modal responses were distinguished by comparing the mode shapes produced by the real part of the eigenvectors associated with each modal frequency (eigenvalue). In Figures 4.60 and 4.61 the response of pattern 3 and 4 was approximately equivalent, resulting in partially obscured data for pattern 3.

It is clear from these results that the unidirectional 0° (UD0) fibre pattern produced greater values of η across all of the first four bending and torsion modes. Modal frequencies between the patterns fell in a predictable order. The patterns with lower $\overline{\theta}_{abs}$ values in the length direction produced higher bending mode frequencies and lower torsional mode frequencies, although the pattern order for the torsional modes became less clear at modes 3 and above. Interestingly, reduced torsional stiffness did not result in lower values of η, which indicated that the damping response of the torsional modes was dominated by the shear strains acting in the length direction rather than the width direction.

Examination of the shear strains within the VEM layer produced a clearer picture of this. Strain behaviour was produced for the first bending and torsion mode of each pattern.
As the eigenvectors were used to calculate the strain behaviour, the values produced were arbitrary but proportional to one another. The three shear strain fields produced by each mode shape were normalised by the largest of the shear strain components to gain a clearer representation of the behaviour.

The normalised shear strain fields present within the VEM layer, along with exaggerated fibre pattern and mode shape, are displayed for patterns $1-4$ and UD0 in Figures 4.62 to 4.71.

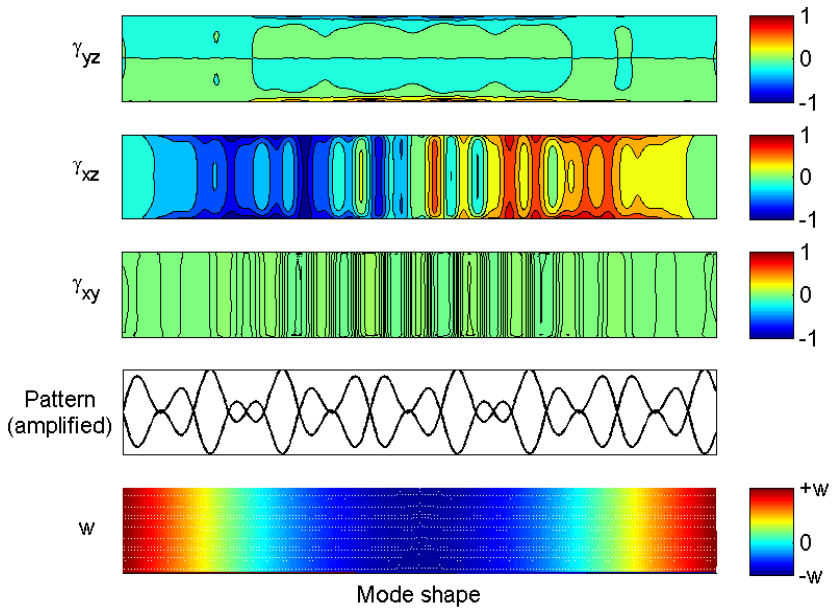

Figure 4.62: Shear strains within the VEM for Pattern 1 in bending mode 1

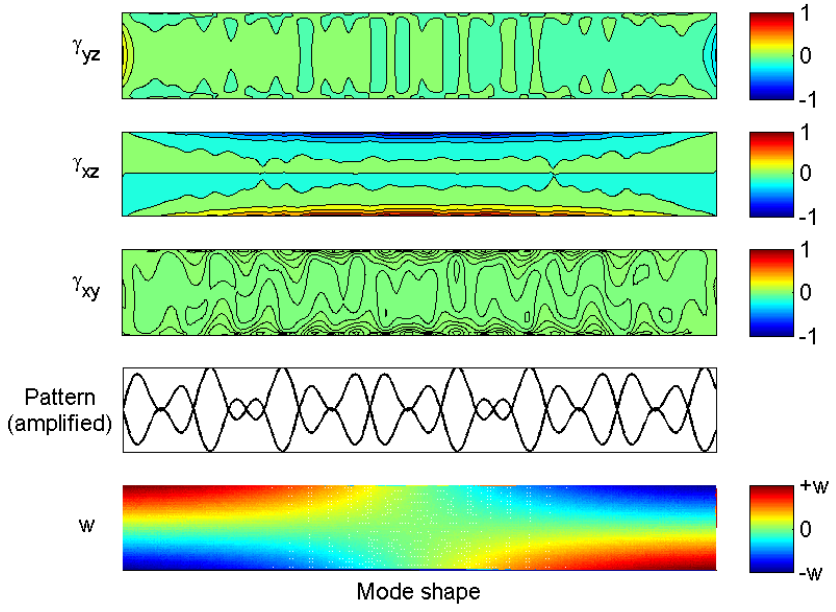

Figure 4.63: Shear strains within the VEM for Pattern 1 in torsion mode 1

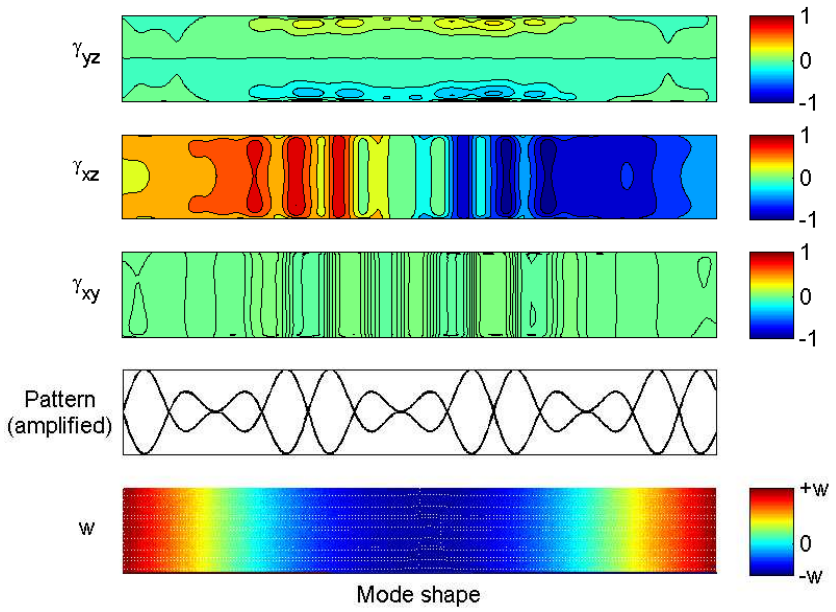

Figure 4.64: Shear strains within the VEM for Pattern 2 in bending mode 1

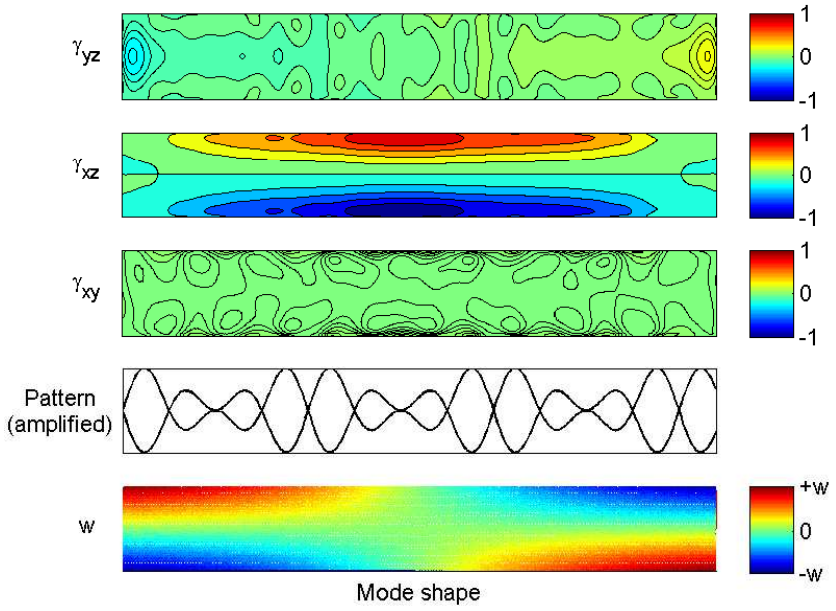

Figure 4.65: Shear strains within the VEM for Pattern 2 in torsion mode 1

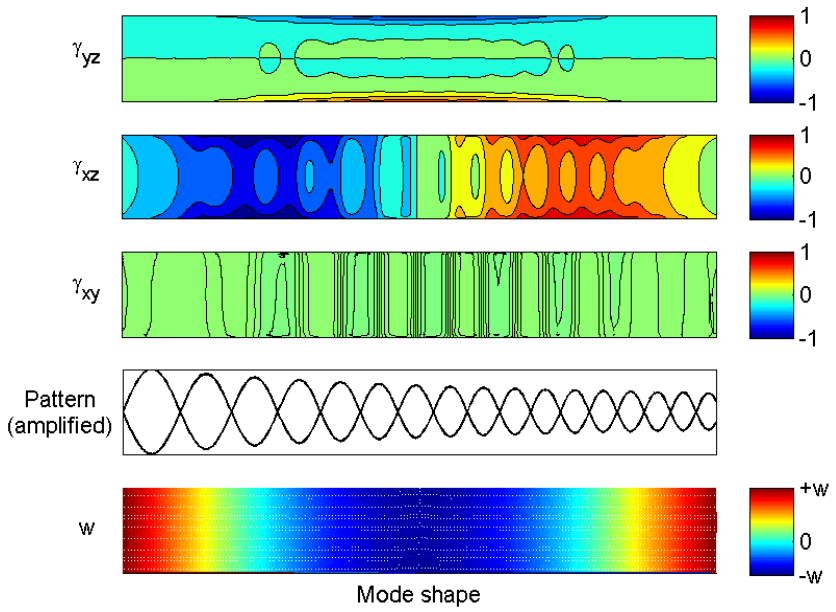

Figure 4.66: Shear strains within the VEM for Pattern 3 in bending mode 1

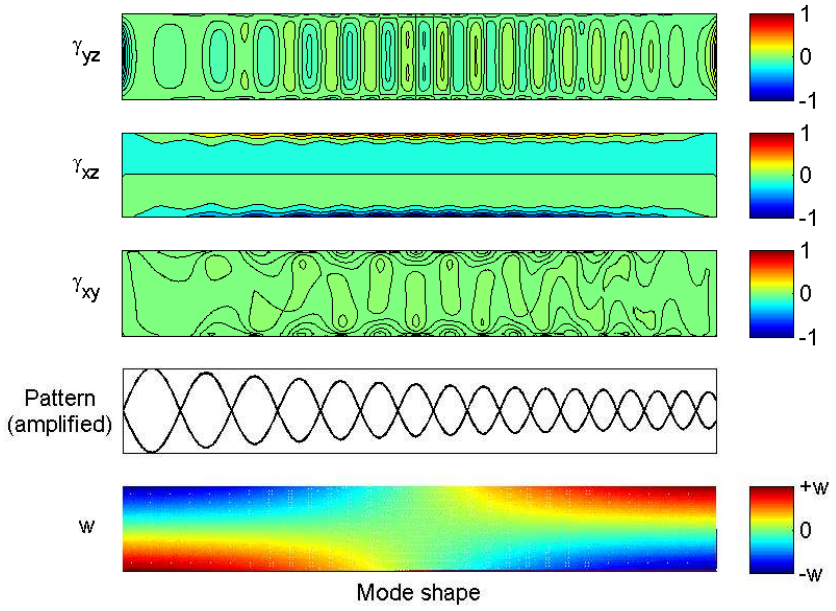

Figure 4.67: Shear strains within the VEM for Pattern 3 in torsion mode 1

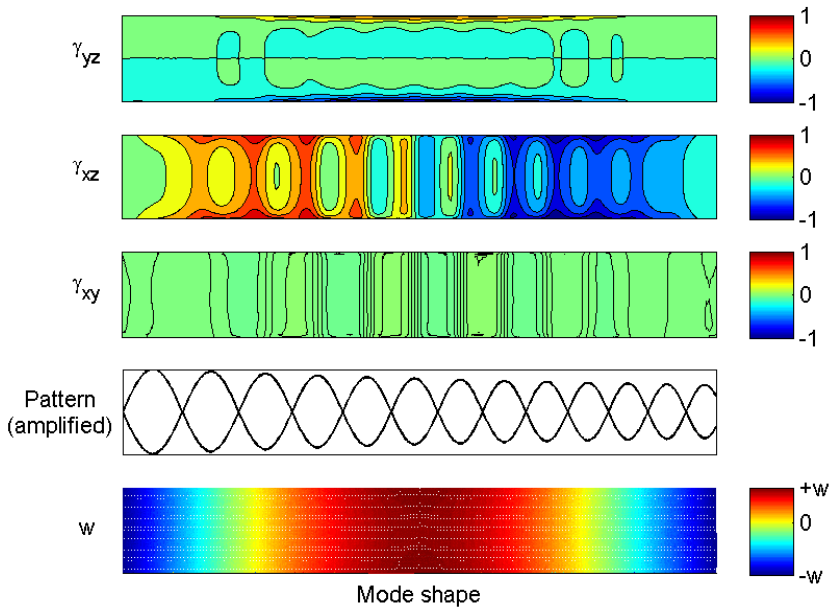

Figure 4.68: Shear strains within the VEM for Pattern 4 in bending mode 1

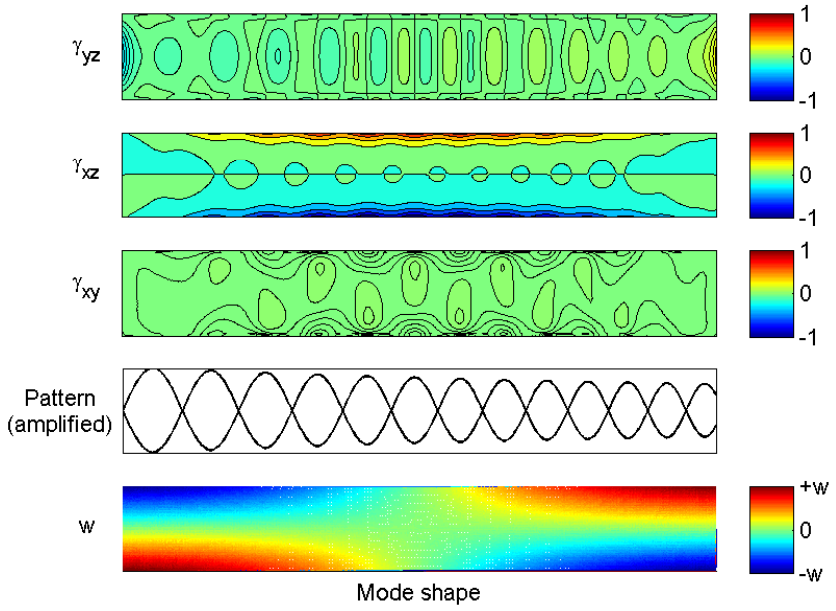

Figure 4.69: Shear strains within the VEM for Pattern 4 in torsion mode 1

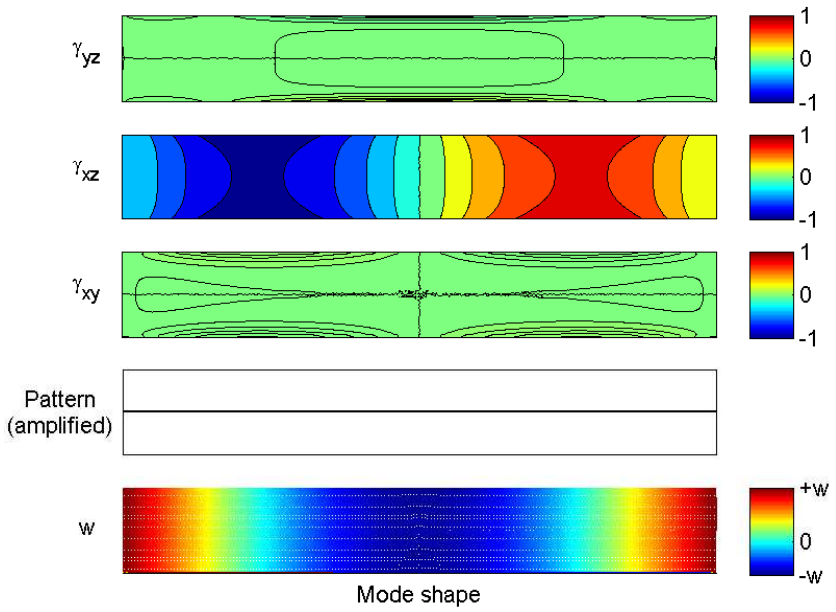

Figure 4.70: Shear strains within the VEM for UD0 in bending mode 1

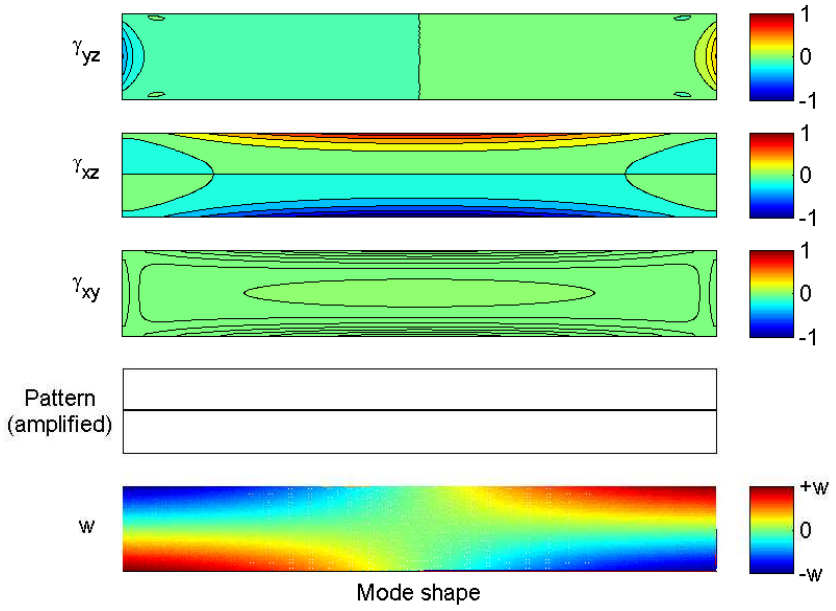

Figure 4.71: Shear strains within the VEM for UD0 in torsion mode 1

Summing the absolute values of each normalised shear strain field within the VEM layer produced a metric useful for determining which shear strain component was most dominant for each mode shape. These values were designated Γ_{xz}, Γ_{yz}, and Γ_{xy}, corresponding to each of the strain fields. Table 4.15 shows the percentage proportions of each Γ value for the first bending and torsion mode for patterns $1-4$ and UD0.

Pattern	Mode	Γ_{yz}	Γ_{xz}	Γ_{xy}
1	Bending 1	10.4%	86.3%	3.3%
	Torsion 1	21.8%	77.4%	0.8%
2	Bending 1	8.9%	88.7%	2.4%
	Torsion 1	15.0%	84.6%	0.4%
3	Bending 1	13.6%	85.1%	1.3%
	Torsion 1	28.4%	70.4%	1.2%
4	Bending 1	14.5%	82.6%	2.9%
	Torsion 1	25.6%	75.8%	0.6%
UD0	Bending 1	1.5%	98.5%	0.0%
	Torsion 1	15.1%	84.6%	0.3%

Table 4.15: Shear strain component proportions

It can be seen that for both the first bending and torsion mode that the γ_{xz} shear strains dominated within the VEM layer for each pattern. Consequently the η values for the torsion mode were more dependent on the stiffness in the length direction than in the width direction.

Observing the bending modes for each pattern, it was clear that the patterns with larger $\overline{\theta}_{abs}$ in the length direction exhibited greater proportions of γ_{yz}. However, the reduced proportion of γ_{xz} resulting from the diminished stiffness in the length direction resulted in reduced η values. This indicated that while patterns with greater $\overline{\theta}_{abs}$ values produced

additional γ_{yz} shear strains, the damping associated with these strains was not sufficient to account for the reduced damping associated with the reduced γ_{xz} shear strains, and modal damping performance reduced as a consequence.

Further exploration of $\overline{\theta}_{abs}$ was performed by comparing a number of patterns which had the same value of $\overline{\theta}_{abs}$ as patterns $1-4$. This examination was performed to establish whether patterns with the same average directional stiffness properties produced equivalent modal damping results.

Three new patterns were compared to each of the four original patterns, two constant sine waves and a UD pattern. The wavelength of each of the simple sine waves was defined by λ_1 and λ_2 of the pattern they were being compared to. The θ_{max} values of the constant sine waves were selected to produce an identical $\overline{\theta}_{abs}$ value. The angle of the UD pattern was set to the $\overline{\theta}_{abs}$ value of the pattern under comparison. Table 4.16 shows and example of the pattern specifications for comparison of the three new patterns to pattern 1.

Pattern	Type	λ [mm]	θ_{max} [$^\circ$]	$\overline{\theta}_{abs}$ [$^\circ$]
1	Sine superposition	125 & 50	30.0	15.0
Sine 1	Constant sine	125	23.3	15.0
Sine 2	Constant sine	50	23.1	15.0
UD	Unidirectional	–	15.0	15.0

Table 4.16: Comparison pattern specifications and average absolute fibre angles

Damping behaviour of the first four bending and torsional modes produced by the new and original patterns are shown in Figures 4.72 to 4.79.

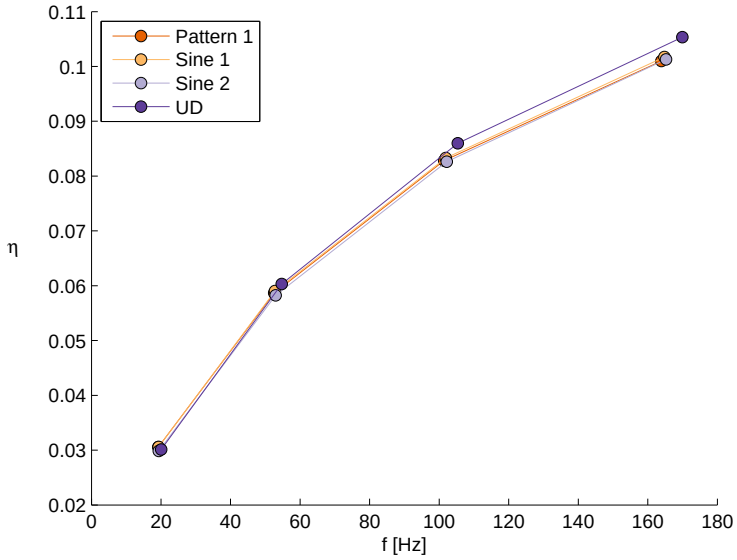

Figure 4.72: Damping comparison for the first 4 bending modes of patterns with equivalent $\overline{\theta}_{abs}$ to pattern 1

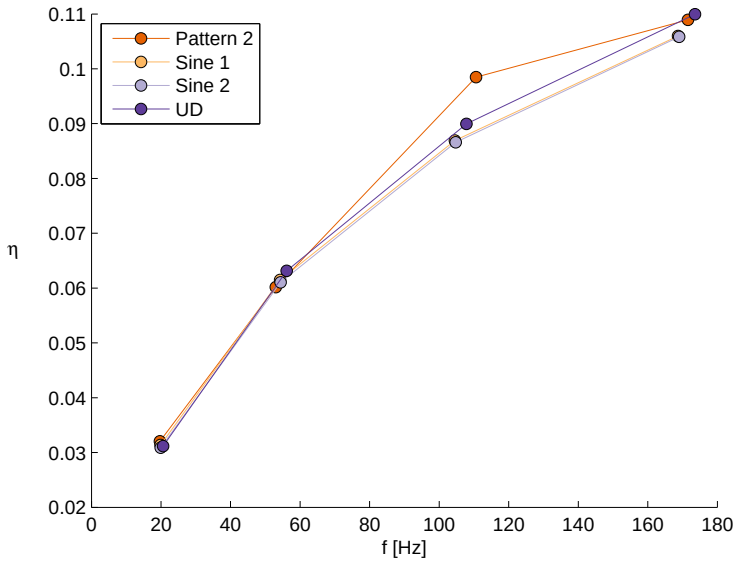

Figure 4.73: Damping comparison for the first 4 bending modes of patterns with equivalent $\overline{\theta}_{abs}$ to pattern 2

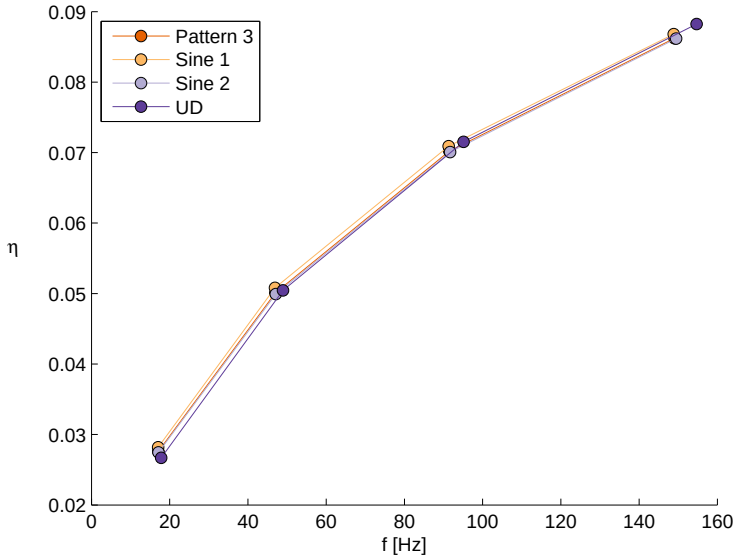

Figure 4.74: Damping comparison for the first 4 bending modes of patterns with equivalent $\overline{\theta}_{abs}$ to pattern 3

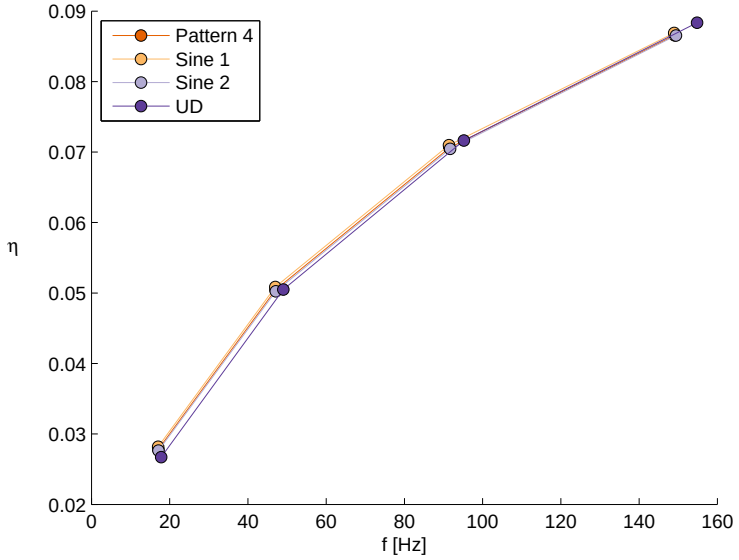

Figure 4.75: Damping comparison for the first 4 bending modes of patterns with equivalent $\overline{\theta}_{abs}$ to pattern 4

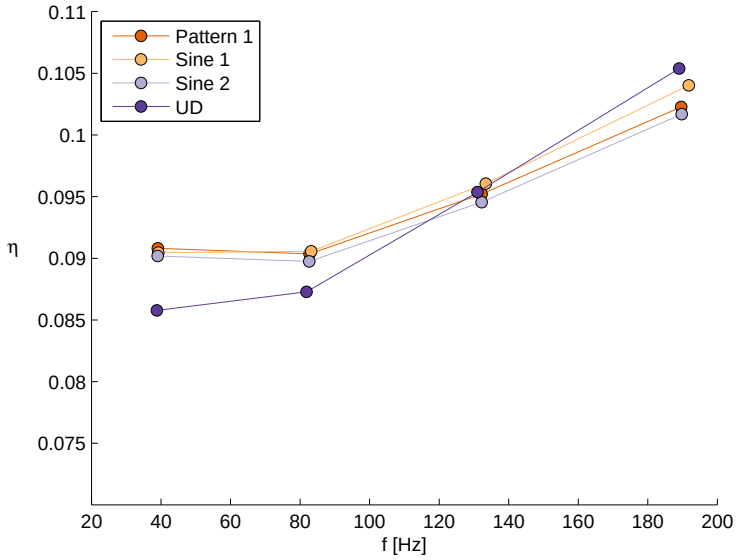

Figure 4.76: Damping comparison for the first 4 torsion modes of patterns with equivalent $\overline{\theta}_{abs}$ to pattern 1

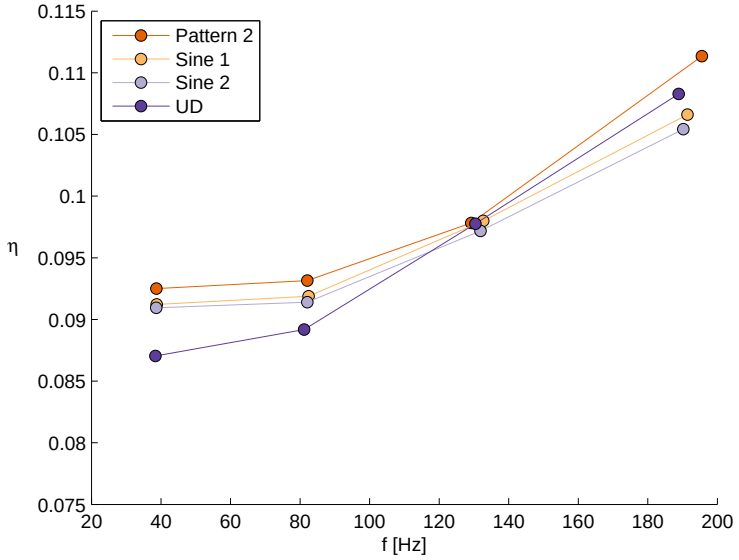

Figure 4.77: Damping comparison for the first 4 torsion modes of patterns with equivalent $\overline{\theta}_{abs}$ to pattern 2

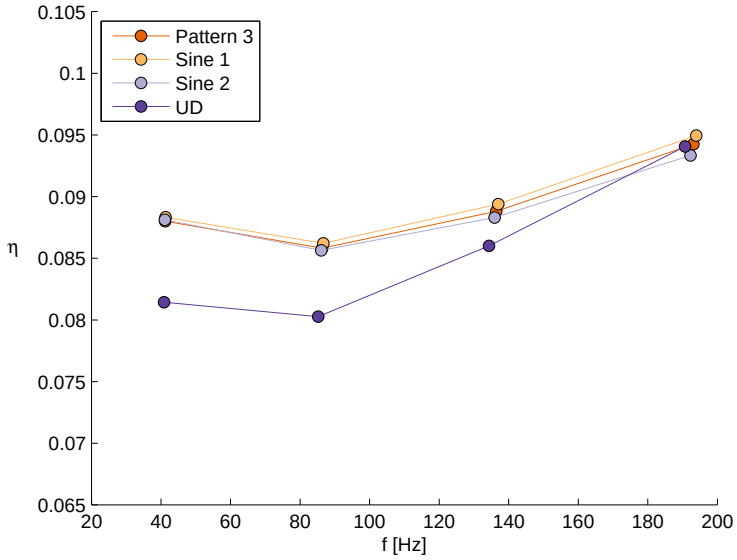

Figure 4.78: Damping comparison for the first 4 torsion modes of patterns with equivalent $\overline{\theta}_{abs}$ to pattern 3

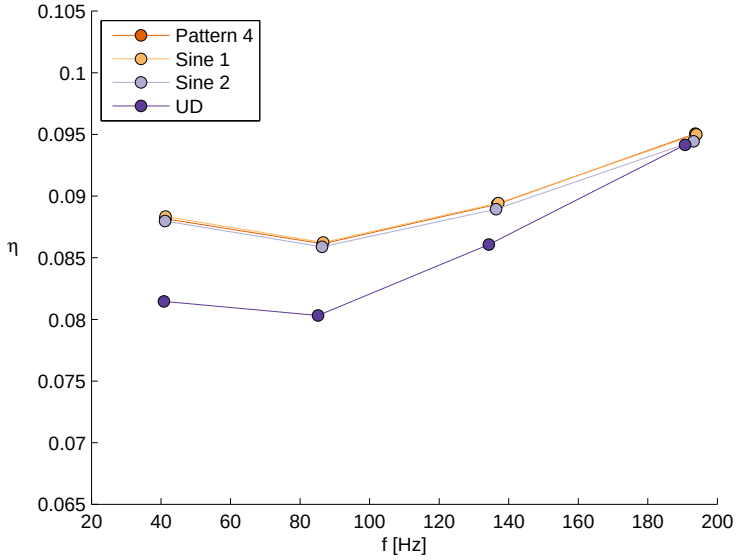

Figure 4.79: Damping comparison for the first 4 torsion modes of patterns with equivalent $\overline{\theta}_{abs}$ to pattern 4

It was clear from these results that fibre patterns with equivalent values of $\overline{\theta}_{abs}$ did not produce identical modal damping responses. This indicated that localised material properties influenced the modal behaviour sufficiently to produce different values of η.

This was clearly demonstrated by comparing two simple patterns: a half-sine wave and a half-cosine wave, each with an identical wavelength (1200 mm), θ_{max} value (23.0°), and $\overline{\theta}_{abs}$ value (14.92°). A UD pattern with the same $\overline{\theta}_{abs}$ value was used as reference. The first four bending and torsion modal damping values for these three patterns are shown in Figures 4.80 and 4.81 respectively.

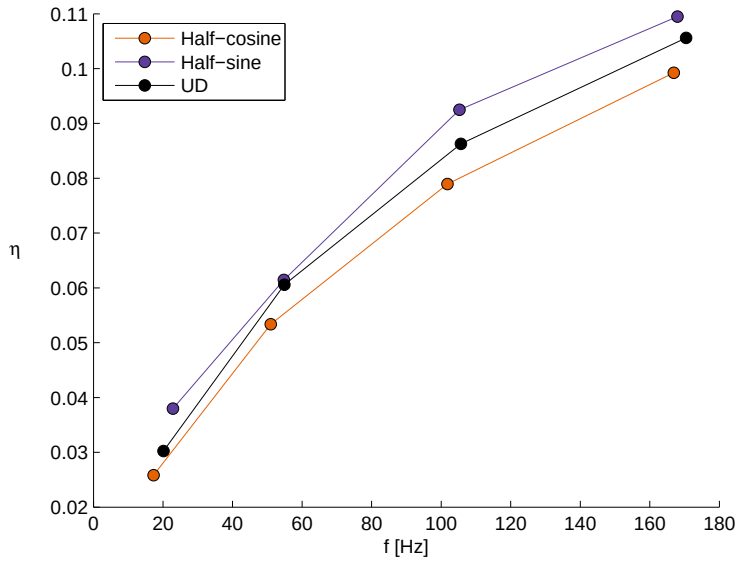

Figure 4.80: Effect of localised stiffness variation on the first four bending modes

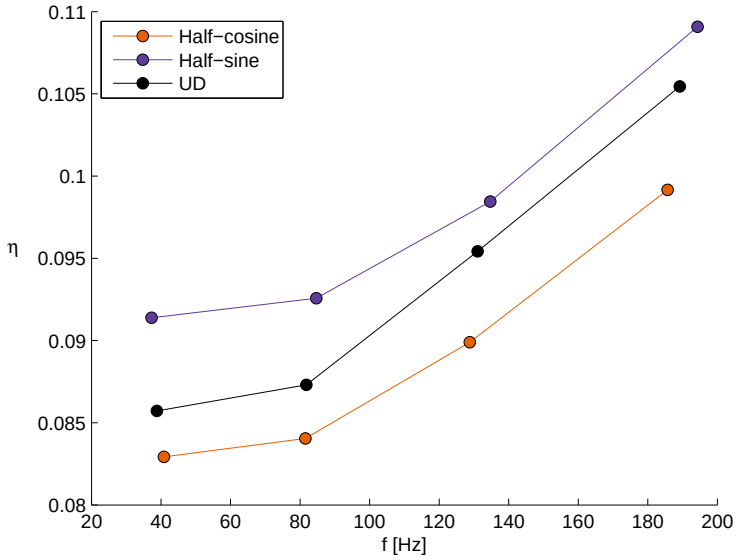

Figure 4.81: Effect of localised stiffness variation on the first four torsion modes

It can be seen that the half-sine wave pattern had greater bending modal frequencies than the other two patterns and also produced the greatest η values in each of the first four bending and torsion modes. Aside from showing that the stiffness distribution present within the half-sine pattern was more beneficial for damping purposes than the corresponding half-cosine pattern's stiffness distribution, it also showed that greater damping performance was possible from more complex fibre patterns over UD patterns with the same $\overline{\theta}_{abs}$ value. The same result was also apparent in Figures 4.73, 4.76, 4.77, 4.78, and 4.79.

This may allow design of CPF-CLD patterns which would be suitable for replacing conventional laminate pairs, such as [±45], to increase damping performance whilst maintaining the required directional stiffness properties.

The results from these pattern comparisons were consistent with findings from [54] and [58], which found that the greatest loss factor values produced by sandwich plates with a $[+\theta/\text{VEM}/-\theta]$ stacking sequence were achieved with $\theta = 0°$. However, the presented re-

sults contradicted conclusions drawn in previous research performed on constant sinusoidal fibres [75, 76]. The previous work determined that constant sinusoidal fibre patterns with $\theta_{max} \approx 30^{\circ}$ values produced greater loss factors than patterns with lower θ_{max} values. The current investigation did not produce the same behaviour, as patterns with a lower θ_{max} value would also have a lower $\overline{\theta}_{abs}$ value and consequently produce greater damping performance.

The model presented provides a method for evaluating the modal damping performance, deformation, stress and strain behaviour of patterned fibre layers surrounding a viscoelastic core. It is a useful tool for comparison and design of complex fibre pattens.

While beam geometries were the primary focus of this investigation, plate behaviour is equally able to be simulated, albeit at greater computational cost due to the increased degrees of freedom.

4.5 Summary

The modal damping performance of a novel three-layer composite constrained layer damping (CLD) arrangement was investigated using finite element analysis and experiment. The composite CLD material consisted of two carbon fibre reinforced polymer (CFRP) layers surrounding a viscoelastic core. The CFPR layers were woven with opposing complex fibre patterns to induce transverse shear strains within the viscoelastic core by way of orthotropic anisotropy. This complex patterned fibre constrained layer damping (CPF-CLD) material was an evolution of materials which had previously utilised 'zig-zag' or constant sinusoidal fibre patterns.

The finite element model (FEM) was developed in MATLAB and was used to predict modal damping, deformation, stress, and strain behaviour of various CPF-CLD materials.

Damping within the system was modelled using a complex stiffness matrix and accounted for damping in both the CFRP and viscoelastic material (VEM) layers.

Stiffness and damping properties of the constituent materials were modelled as functions of frequency to properly capture their dynamic behaviour. Modal damping behaviour was calculated by solving the complex eigen-problem resulting from the complex stiffness and real mass matrices. Modal frequencies and associated damping loss factors were determined from the complex eigenvalues. An iterative method was used to ensure that material properties used in the computation of the stiffness matrix were matched with the modal frequency being determined.

Ten test specimens were produced for each of four CPF-CLD designs. The modal damping performance of these specimens was evaluated experimentally for the first four bending modes using the half-power bandwidth technique and compared to results from the FEM. Material properties required for the FEM were measured using material samples fabricated in the same manner as the CPF-CLD test specimens.

The values produced by the FEM for the first four bending modes generally fell within one standard deviation of the experimentally measured modal results with few exceptions. Deviations from the experimental results may have been due to assumptions made for material properties which were not able to measured directly.

The model correctly predicted the relative damping performance of each of the patterns, making it suitable for comparison of pattern performance.

An investigation into CPF-CLD modal behaviour was performed. Of the four patterns initially studied, it was found that the order of the patterns from lowest to highest $\overline{\theta}_{abs}$

value matched the order of η values from highest to lowest for both bending and torsion modes. Comparison of these patterns to a unidirectional (UD) fibre pattern with a $\overline{\theta}_{abs} = 0°$ value showed that the UD pattern produced the greater damping values.

Observation of the shear strain fields within the viscoelastic core resulting from bending modes, and comparison with the corresponding modal damping behaviour provided an interesting result. This comparison indicated that while CPF-CLD patterns with larger $\overline{\theta}_{abs}$ values produced additional γ_{yz} shear strains, the damping associated with these strains was insufficient to account for the diminished damping associated with the reduced γ_{xz} shear strains.

Comparison of the four CPF-CLD patterns with simpler patterns with equivalent $\overline{\theta}_{abs}$ values showed that the 'equivalent' patterns did not produce the same damping performance. This result indicated that localised stiffness distributions within the modelled beams influenced the modal damping behaviour. The same behaviour was also demonstrated by comparison of two sinusoidal patterns with identical wavelengths, amplitudes and $\overline{\theta}_{abs}$ values, but differing phase angles. These patterns were also compared to a unidirectional pattern with an equivalent $\overline{\theta}_{abs}$ value. The results produced by these three patterns and the previous CPF-CLD study showed that greater damping performance was possible from more complex fibre patterns over UD patterns with the same $\overline{\theta}_{abs}$ value.

The results from the pattern comparisons were consistent with findings from [54] and [58], which found that the greatest loss factor values produced by sandwich plates with a $[+\theta/\text{VEM}/-\theta]$ stacking sequence were achieved with a $\theta = 0°$ value. However, the modelled results contradicted conclusions drawn in previous research performed on constant sinusoidal fibres [75, 76]. The previous work determined that constant sinusoidal fibre patterns with $\theta_{max} \approx 30°$ values produced greater loss factor values than patterns with lower

θ_{max} values. The current investigation did not produce the same behaviour, as patterns with a lower θ_{max} value also had a lower $\overline{\theta}_{abs}$ value and consequently produced greater damping performance.

While beam geometries with free edge conditions were the primary focus of these investigations, plate behaviour and various edge conditions are equally able to be simulated using the presented FEM.

Chapter 5

Implementation of Patterned Fibre Constrained Layer Damping

5.1 Introduction

With any new damping treatment it is useful to know how it should be applied in order to obtain the greatest increase in system damping performance. The Design of Experiments (DOE) methodology described in Section 3.2 is particularly useful to this end. In order to investigate the application of complex patterned fibre damping treatments to composite structural configurations commonly found in the marine industry, a DOE schedule was created and carried out on physical test specimens.

Composite geometries commonly found in large marine craft are sandwich panels. Sandwich panels are comprised of a lightweight core material, usually a foamed polymer, faced with fibre reinforced polymer composite layers. These configurations are typically used in the construction of a vessel's hull and bulkheads (structural elements which require the high stiffness provided by separating the fibre reinforced face sheets). Such structural components are prone to vibration transmission due to their continuity throughout a vessel's

structure, their low density, and their high stiffness. The foam core and face sheet thicknesses vary between hull and bulkhead arrangements. For large composite marine craft the foam core thickness for hull and bulkhead geometries is typically 50 mm and 25 mm respectively [86]. Face sheets tend to be glass fibre reinforced polymer with thickness of approximately 1-2 mm for bulkheads and 2-4 mm for hull constructions [86]. Sandwich beam specimens treated with CPF-CLD layers were fabricated to investigate the changes to structural damping performance.

5.2 Experiment Design

The CPF-CLD treatments were costly to manufacture so a limited number of test specimens were available for this part of the experimental work. A total of eight specimens was determined to be the maximum allowable. Implementation variables available for exploration were:

- Damping treatment fibre pattern type
- Sandwich beam core material
- Core thickness
- Face sheet material
- Face sheet thickness
- Number of damping layers
- Lay-up configuration

From this list, four variables were selected for further study. The effect of foam core thickness was of interest as this would provide some comparison between use of the damping treatment on hull or bulkhead geometries. The effect of fibre pattern type was also clearly of interest and was broken into two variables, pattern type and fibre wavelengths used. The

final variable of the study was lay-up configuration, specifically placement of the damping treatment adjacent to the core material or as an external treatment. The results of which would provide some indication to the effectiveness of using CPF-CLD materials as surface treatments for composite structures.

The foam core material was kept constant between specimens, as was the fibre reinforced face sheet material and thickness. Damping treatments were added to both sides of each test specimen to preserve symmetry about each test beam's central axis. The length and width of each test specimen were fixed at 480 mm × 80 mm respectively to ensure that the damping treatments were present across the entirety of each specimen and were aligned correctly.

The design matrix for this experimental study was formulated with the values detailed in Table 5.1.

Variable	Designation	Low level (-1)	High level (+1)
Fibre pattern type	A	Swept sine	Sine superposition
Minimum fibre wavelength	B	50	75
Foam core thickness (mm)	C	25	50
Damping treatment location	D	Core adjacent	Surface

Table 5.1: Sandwich beam DOE variable values

The maximum fibre wavelength value required to complete the swept and superposed sine waves was set as 125 mm to facilitate the use of patterns produced for validation of the FE model.

A 2^{4-1} fractional factorial design was used to achieve the 8 test specimen limitation. This resulted in single factors being confounded with three factor interactions, and two factor

interactions confounded with other two factor interactions. The confounding structure for the experiment is shown in Table 5.2 and the resulting experiment design matrix is shown in Table 5.3.

Effect	Alias
A	BCD
B	ACD
C	ABD
D	ABC
AB	CD
AC	BD
BC	AD

Table 5.2: Sandwich beam DOE variable values

Specimen configuration	Fibre pattern (A&B)	Core thickness (mm) (C)	Damping treatment location (D)
1	Pattern 1	25	Surface
2	Pattern 3	25	Core adjacent
3	Pattern 2	25	Core adjacent
4	Pattern 4	25	Surface
5	Pattern 1	50	Core adjacent
6	Pattern 3	50	Surface
7	Pattern 2	50	Surface
8	Pattern 4	50	Core adjacent

Table 5.3: Sandwich beam experiment design matrix

5.3 Fabrication

The eight test specimens were constructed from materials commonly used in the fabrication of composite marine constructions. The core material used for the DOE test beams was a cross-linked polyvinyl chloride (PVC) foam with density of $80\,\mathrm{kg.m^{-3}}$. The reinforcing fibre layers were fabricated from pre-laminated CPF-CLD sheets and E-glass fibre sheets, with a surface density of $300\,\mathrm{g.m^{-2}}$ infused with epoxy. The stacked and infused layers of E-glass are referred to as glass reinforced polymer, or GRP for brevity. The GRP layer thickness was set to 2 mm to simulate values found in both hull and bulkhead constructions. As the CPF-CLD materials were already infused, the vacuum infusion method used previously was not suitable for the sandwich beam fabrication and a wet lay-up method was employed.

Two different lay-up procedures were used for fabrication of the sandwich beams, dependant on the CPF-CLD location. For the beams with the CPF-CLD adjacent to the core, epoxy was applied to each side of the foam core and the CPF-CLD layers were added. Several layers of E-glass cloth were layered on either side to achieve the 2 mm thickness required, epoxy was applied with a roller as each layer was added. Aluminium plates were then used to compress and fix the sandwich beam to allow partial curing over several hours at room temperature. Each beam was then baked at 50 °C for eight hours to complete the curing cycle of the epoxy.

For the beams with CPF-CLD applied to the surface, each side of the sandwich beam had to be laminated separately to facilitate stable clamping during curing. The E-glass layers were applied to one side of the foam core and infused with epoxy using a roller. The CPF-CLD layer was then added to the wet surface before the partially constructed beam was clamped between aluminium plates and left to dry at room temperature. The process was repeated for the opposite face before fully curing the beam at 50 °C for eight hours.

Two trial specimens were produced to ensure that the fabrication method produced specimens of adequate quality. These beams were of the configuration [GRP/Foam/GRP] and [CPF-CLD/GRP/Foam/GRP/CPF-CLD]. Pattern 3 CPF-CLD was used for the damping layers and a 25 mm foam core was used for both beams. The resulting sandwich beams were found to meet the required quality and enabled the general comparison of damped and undamped sandwich beam responses.

5.4 Test Method

The test method used to measure the modal damping performance of the CPF-CLD specimens was employed again for this study. Two suspension methods were tested on the damped and undamped trial specimens. Both suspension configurations were an approximation of free end conditions. Using the first method beams were suspended with a single attachment point provided by an eyelet which was screwed into one end of the beam. This produced a rotation point on the plane of the beam central axis but external to the beam.

Using the second method, beams were suspended by two attachment points provided by two nails driven into the exposed foam edges, 30 mm from one end of the beam. This produced a rotation axis on the plane of the beam central axis. The two suspension configurations can be seen in Figure 5.1. Noticeable differences in the results produced by each suspension method were observed for the second and third bending modes. The eyelet suspension method produced greater damping values across these modes for both damped and undamped beams. The increased damping performance may have been due to the friction at the eyelet-foam interface resulting from the end displacements of the beams. The results from this study can be found in Section A.6. The pinned configuration was ultimately selected for the DOE experimental investigation as this suspension technique was deemed to provide the more natural bending response in the beams about their central axis.

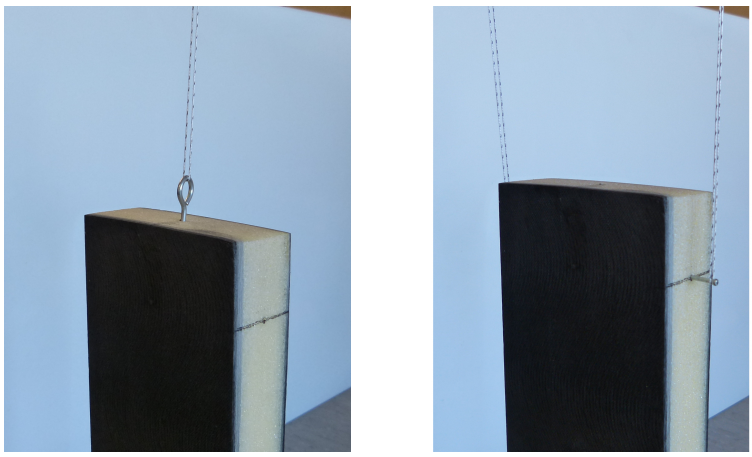

(a) Eyelet suspension (b) Pinned suspension

Figure 5.1: Suspension methods

The excitation signal and measured response of each sandwich beam was performed using the same method as detailed in Appendix 4.3.4. As the sandwich beams were significantly stiffer than the CPF-CLD specimens, a wider frequency range was required for the FFT response. A frequency range of 0 Hz - 2500 Hz was used to capture the first five bending modes.

Test specimens were struck in several locations during the measurement of each frequency response curve in order to excite as many modes as possible. If a double hit was detected during one of the strikes, that frequency response curve was discarded. A total of ten frequency response curves were measured for each of the sandwich beam specimens.

As with the CPF-CLD specimens, the response produced by swinging of the beam was apparent in the frequency response curve but could be ignored as it occurred at frequencies much lower than the first bending mode.

Measurements were performed at temperatures between 22 °C and 24 °C.

5.5 Results and Discussion

The first five bending mode loss factors for each of the eight test beams are shown in Figure 5.2. Error bars indicate one standard deviation in the measured modal values.

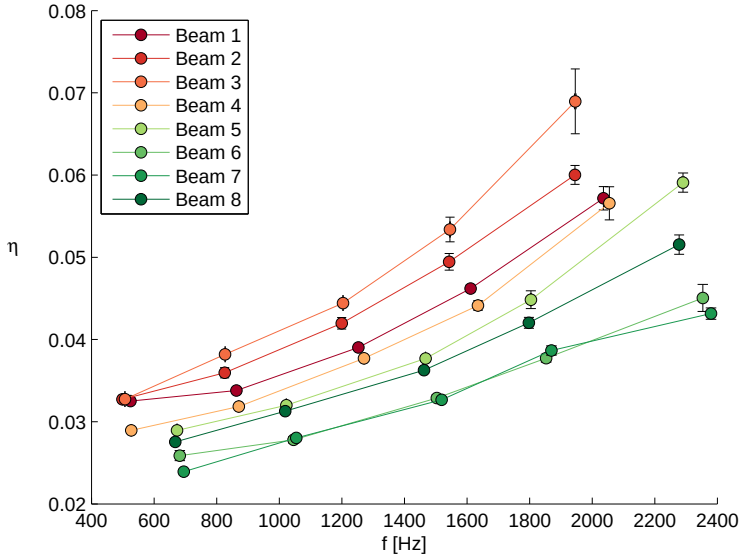

Figure 5.2: Test schedule modal damping results

The influence of each of the four variables could be determined at each mode from these results. Calculations for the influence of each variable followed the pattern outlined in Section 3.4.2. The modal loss factor was used as the performance metric for this experiment. Consequently, the influence of each variable was dependent on the mode under consideration. The influence of variable X on the damping loss factor of mode r is calculated using

$$I_X = \overline{\eta^r}_{high} - \overline{\eta^r}_{low} \ , \tag{5.1}$$

where

$\overline{\eta^r}_{high}$ = the average loss factor at mode r for beams with a high value of X,

$\overline{\eta^r}_{low}$ = the average loss factor at mode r for beams with a low value of X.

As an example, the influence of variable A on the damping of mode r is

$$I_A = \frac{\eta_r^{(1)} + \eta_r^{(3)} + \eta_r^{(5)} + \eta_r^{(7)}}{4} - \frac{\eta_r^{(2)} + \eta_r^{(4)} + \eta_r^{(6)} + \eta_r^{(8)}}{4} \,. \tag{5.2}$$

The relative influence of each of the four variables and the two factor interactions are shown in Figure 5.3. As the relative influence of each variable was of interest, the absolute value of each influence result was normalised by the most influential variable. The error bars indicate one standard deviation of the calculated values. For reference, the variables are

A = Fibre pattern type,

B = Minimum fibre wavelength,

C = Foam core thickness,

D = Damping treatment location.

The two factor interactions of AB, AC, and BC were confounded with CD, BD, and AD respectively. This meant that it was not possible to determine which of the confounded variable interactions produced the recorded influence value. A full factorial experiment design would be required to separate these interactions.

From the results presented in Figure 5.3 it can be seen that of the four initial variables, the foam core thickness had the most pronounced effect on modal damping values, followed by the location of the damping layers and fibre pattern type. Minimum fibre wavelength had a significant effect in the first mode but a negligible effect in all other modes.

In order to determine which level of each variable produced the greatest damping performance, the gradient of the variable influence was considered. If the gradient was positive, the high variable level produced the greater damping performance, and vice versa if the gradient was negative. Figure 5.4 shows the gradients produced by the four variables and two factor interactions for the damping of the first mode.

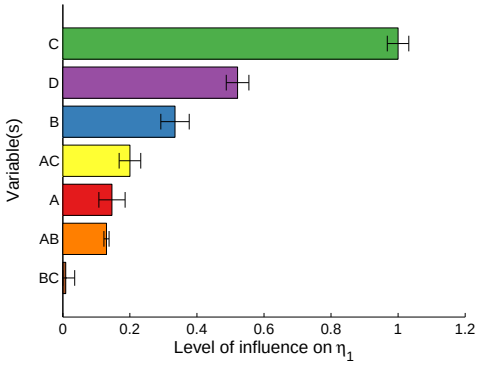

(a) Mode 1

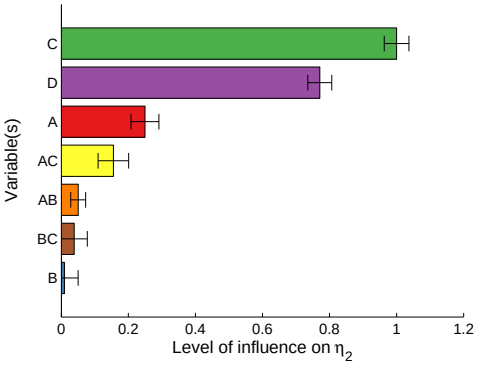

(b) Mode 2

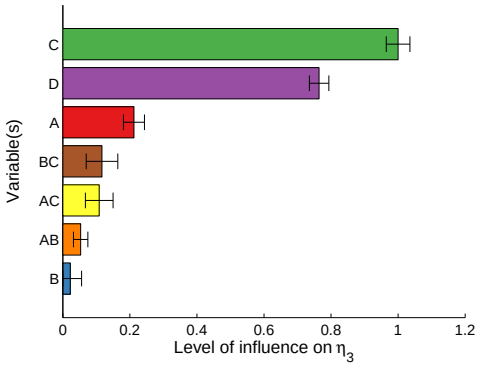

(c) Mode 3

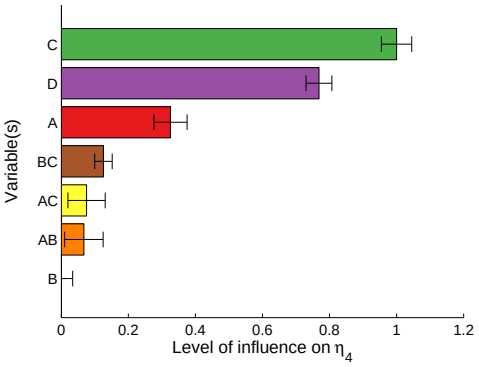

(d) Mode 4

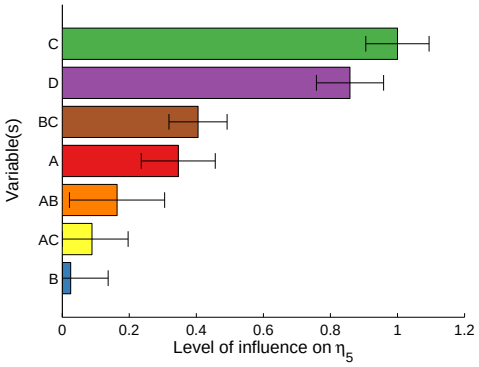

(e) Mode 5

Figure 5.3: Relative influence of variables on modal damping

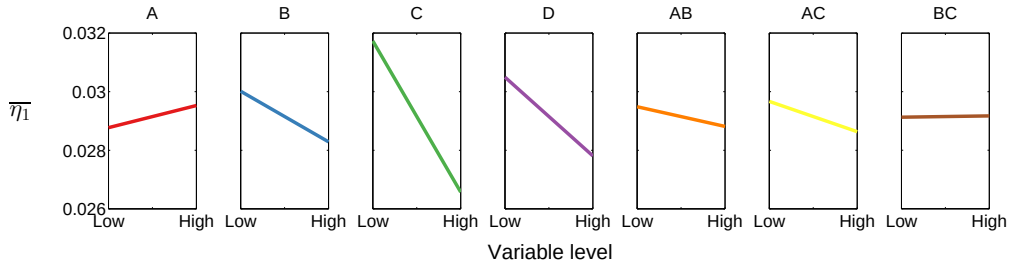

Figure 5.4: Influence gradients for mode 1 damping

The influence gradient directions for each variable across the five modes is shown in Table 5.4. Positive gradients are labelled as +, negative gradients as −, and no change as 0.

Mode	Variable(s)						
	A	B	C	D	AB	AC	BC
1	+	−	−	−	−	−	+
2	+	−	−	−	+	−	−
3	+	−	−	−	+	−	−
4	+	0	−	−	+	−	−
5	+	−	−	−	−	−	−

Table 5.4: Influence gradients for each mode

From these values it is clear that the greatest damping values were found using:

- Superposition fibre patterns
- Minimum fibre wavelength of 50 mm
- 25 mm foam core thickness
- Core adjacent CPF-CLD layers

The increase in damping performance resulting from changing the levels of each variable are shown in Table 5.5.

Variable	Increase factor				
	$\Delta\eta_1$	$\Delta\eta_2$	$\Delta\eta_3$	$\Delta\eta_4$	$\Delta\eta_5$
A	2.6	4.1	3.4	5.6	7.1
B	6.1	0.2	0.4	0	0.5
C	19.4	17.4	17.0	18.3	22.1
D	9.7	13.1	12.7	13.8	18.7

Table 5.5: Damping increases from lowest performance to highest performance of each variable

Increasing the foam core size from 25 mm to 50 mm does several things. Firstly it increases the bending stiffness of the sandwich beam by increasing the area moment of inertia through greater separation of the stiff facing layers. This results in greater modal frequencies, which may in turn affect the damping performance of the VEM layers within the beam. The distance between the constrained damping layers and the central axis of the beam is also increased. Normally, additional distance between a surface CLD treatment and the central axis of a beam would benefit the damping properties of the system as the shear strains within the CLD layer would be greater leading to increased energy removal [7, 99]. However, this behaviour assumes that the deflection of the core material is constant between specimens of varying thickness. In the presented experiment, the increased bending stiffness of the thicker sandwich beams would likely have resulted in reduced curvature of the specimen, producing smaller shear strains within the CPF-CLD layers and hence lower damping.

Use of the thinner core material also increases the ratio of VEM thickness to substrate thickness, or in other words, increases the proportion of damping material within the structure. Inclusion of a greater proportion of damping material within the damping layers of a structure would generally lead to increased energy removal and hence an improved damping performance. Ideally, scaling the proportions of damping material with the thickness of the

substrate would have produced a more precise comparison, however this was not possible due to resource constraints of the CPF-CLD materials.

The increased damping performance observed by positioning the CPF-CLD materials adjacent to the core was likely due to the additional stiffness provided by the GRP to the outer constraining face. Increased bending stiffness of this face would induce greater shear strains within the VEM core of the CPF-CLD producing improved damping performance.

Changing the fibre pattern type within the CPF-CLD treatment resulted in differing average extensional moduli within the CFRP layers of the treatment. As discussed in the previous chapter, when operating in flexure the extensional modulus of the constraining layer in the direction of bending wave propagation dominates the shear strain behaviour within the VEM core of the CPF-CLD treatment. As the superposition patterns exhibit higher extensional stiffness in this direction when compared to the swept sine patterns, it would be expected that they produce greater damping performance. This conclusion seems to be contradicted by the influence of the minimum wavelength of the fibre pattern as the 50 mm minimum wavelength resulted in marginally lower apparent extensional moduli in the bending direction (see Table 4.14). However, this variable produced negligible influence in the system damping response in all but the first mode.

Exploring the exact mechanisms of each variable was not possible without further test specimens and experiment designs. While these mechanisms are not investigated further in this thesis, they are worthy of future consideration.

In terms of application to marine constructions, these results show that greater damping performance will be achieved if bulkheads are preferentially treated over hulls, and inclusion of the damping treatment is provided adjacent to the core as this produces larger damping

values than using the damping material as a surface treatment.

The efficacy of applying the damping treatments can be observed by comparing the modal damping results obtained from the two trial beam specimens mentioned in Section 5.3. One beam was treated with pattern 3 CPF-CLD on the outer faces while the other was a standard undamped sandwich configuration. While both specimens had a foam core thickness of 25 mm, DOE specimens with this core thickness could not be directly compared as different core foams and binding epoxies were used in the fabrication of the trial beams resulting in higher modal frequencies. The damped trial beam was also of a configuration not replicated in the DOE schedule. The results of the damped and undamped beams are shown in Figure 5.5.

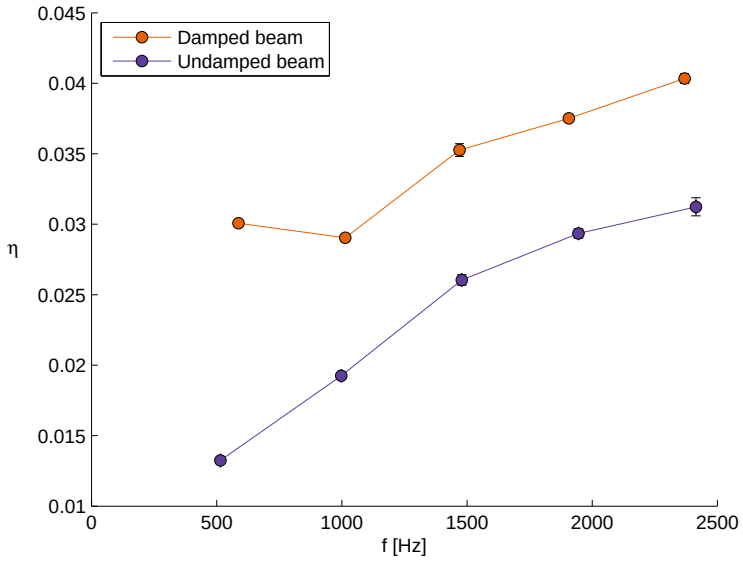

Figure 5.5: Comparison of sandwich beams with and without CPF-CLD treatment

The increase in damping produced by the surface CPF-CLD treatment for each mode is shown in Table 5.6. Even in the lower performing surface location, inclusion of CPF-CLD layers increases the damping performance of typical composite sandwich panel configurations across all of the first five bending modes. The damping performance of the first

Mode	η		
	Undamped Beam	Damped Beam	Increase factor
1	0.0132	0.0300	2.3
2	0.0193	0.0290	1.5
3	0.0260	0.0353	1.4
4	0.0293	0.0375	1.3
5	0.0312	0.0403	1.3

Table 5.6: Damped vs. undamped sandwich beam

bending mode shows the greatest improvement with more than double the measured loss factor of the undamped specimen. Higher order bending modes appear to reach a more consistent damping increase of approximately 1.3 times that of the undamped beam. Observation of the damping trends beyond the fifth bending mode were not possible as loss factor values of the damped beam were unable to be measured due to low peak amplitudes.

5.6 Summary

Implementation of CPF-CLD treatments to composite sandwich beams was analysed using Design of Experiments methodology. Test specimens were fabricated using materials and geometries commonly found in marine hull and bulkhead constructions.

A fractional factorial design was used to study the effects of CPF-CLD pattern type, beam core thickness and location of the CPF-CLD layers within the structure on system damping performance. These variables were selected to determine how to efficiently utilise CPF-CLD materials in composite marine structural elements. The relative influence of each variable on system damping performance was also determined.

Damping values of the first five bending modes were measured using the half-power bandwidth method, with sandwich beams in a freely suspended configuration.

Foam core thickness and placement of the CPF-CLD treatments were found to have the greatest influence over the system damping performance of the sandwich beams.

Beams with the smaller core thickness produced greater damping values, as did beams with the CPF-CLD layers adjacent to the core. CPF-CLD layers with the sine superposition fibre patterns also produced greater damping values over those with swept sine patterns. Fibre patterns with a lower minimum fibre wavelength produced greater damping values in the first bending mode, but had negligible effect at higher modes.

The mechanisms resulting in each variable's behaviour were not able to be examined in greater detail due to resource constraints surrounding fabrication of further test specimens. While these behaviours were not examined further in this work, they are considered worthy of further investigation.

The results produced by the experiment presented indicate that the greatest increases in system damping performance would be gained by treating bulkhead constructions preferentially over hull constructions, and by embedding CPF-CLD treatments adjacent to the core of sandwich constructions rather than adding them as surface treatments.

Comparison of an undamped sandwich beam to a sandwich beam with surface CPF-CLD treatment produced damping increases of 230% in the first bending mode, and increases of 130% at higher modes.

Chapter 6

Conclusions and Future Work

Unwanted vibrations in metal and composite marine structures can be mitigated through use of layered viscoelastic damping treatments. To this end, investigations were made into:

- measurement of damping material properties
- damping of metal plates with unconstrained layer damping treatments
- modal damping behaviour of a novel fibre reinforced composite constrained layer damping arrangement
- application of the composite damping arrangement to composite sandwich constructions commonly found in large marine vessels

An overview of these investigations, resulting conclusions, and recommendations for areas of future consideration are detailed in the following sections.

6.1 Measurement of Viscoelastic Damping Performance

The dynamic behaviour of unconstrained layer viscoelastic materials was studied using two measurement techniques:

1. Resonant frequency response half-power bandwidth

2. Dynamic mechanical analysis

Test fixtures were designed and constructed to facilitate measurement of the damping loss factor to international standards ISO 6721-3 and ASTM E756. Both of these standards evaluated damping performance using half-power bandwidth measurements from the frequency response of beam specimens undergoing harmonic excitation. Test specimens were comprised of a metal beam coated on one side with the viscoelastic material being investigated.

Using the ISO standard, test beams could have free edge conditions or be cantilevered. The ISO standard produced the damping loss factor (η) for the metal-viscoelastic system. The ASTM standard used a cantilever test beam arrangement and the η values of the viscoelastic material alone were able to be calculated from the response of the metal-viscoelastic system.

Measurements of the material loss factor were made according to the ASTM standard and were compared to measurements made with a Dynamic Mechanical Analyser (DMA). Values of η produced by the DMA were calculated by measuring the phase shift between cyclical stress and strain responses of a sample of the viscoelastic material under investigation. Excitation frequencies produced by the DMA were limited to a range of approximately 0.1 Hz to 140 Hz but measurement of η values over a wider frequency range were possible by performing measurements over a large temperature range and applying the Time-Temperature Superposition Principle. Measurement of η over a range of temperatures also allowed the peak damping performance, which occurred at the glass transition temperature, to be measured.

Comparison of the ASTM and DMA methods over a range of temperatures found that the DMA produced similar peak damping values and glass transition temperatures to the ASTM results, but material loss factors varied significantly at temperatures higher than the

glass transition temperature.

The DMA was found to be well suited to measurements of material loss factor over a wide range of temperatures, requiring significantly less time and user input to achieve measurement data compared to the ISO and ASTM tests. It was concluded that the DMA would be excellent for testing relative performance between materials, making it a useful method in the prototype stages of damping material design.

It would be of interest to quantify differences in results produced by different heating rates using the DMA as temperatures recorded by the method may not have accurately reflected the temperature present within the sample material, particularly at higher heating rates. Such an investigation would provide useful information on test conditions appropriate for accurate testing.

6.2 Unconstrained Layer System Damping Performance

The relative influence of five variables on the system damping performance of metal plates treated with unconstrained viscoelastic material was investigated using Design of Experiments methodology. Damping layer thickness, ambient temperature, boundary conditions, plate size and substrate material were each studied at two levels. A fractional factorial design was employed to reduce the number of test configurations required to gain useful data and meet time and resource constraints. The fractional design resulted in eight test configurations.

Clamping arrangements used in the experiments were evaluated by comparing the measured resonant vibration response of the various undamped plate and clamp configurations to several analytical models for plate natural frequencies. Some responses were well matched

to the modelled results, while others deviated from the predicted responses. Large deviations between measured and modelled responses were attributed to non-uniform clamping and the material properties used in the models.

Values of system loss factor (η_{sys}) were obtained using an impulse decay method similar to that outlined in ISO 10848-1 [87]. The test plates were excited with an impulse force and the structural reverberation time was measured using accelerometers. Forty eight vibration decay measurements were recorded for each of the eight test configurations.

Of the five variables studied, substrate material was found to have the greatest influence on both one-third octave band average damping and the maximum damping performance of the plate systems. Aluminium plates produced a 1.39 fold increase in average damping and 1.51 fold increase in maximum damping over the steel plate configurations.

Damping layer thickness was found to be the second most influential variable, with a 2:1 damping layer to substrate layer thickness ratio producing a 1.37 fold increase in average damping and a 1.45 fold increase in maximum damping over a 1:1 thickness ratio.

When tracking variable influence over each one-third octave band, it was found that the influence of plate dimension overtook the substrate material variable for frequencies 500 Hz and above. This result is perhaps less significant than it first appears as the two plate dimension levels selected were constrained by the testing facilities at hand and consequently were not dimensions that would likely be found in practice.

An interesting result from the study was that boundary conditions had little influence on the measured system loss factor. Simply-supported edge conditions yielded an increase in damping performance by a factor of 1.04 for average damping and 1.03 for maximum

damping over fully clamped edge conditions. However, the simply-supported clamping arrangements used during testing may have added measurable dissipative effects through interfacial friction making this result inconclusive.

Further studies on the effect of clamping would be useful in determining the relevance of the boundary condition result found in the presented investigation. It would also be beneficial to explore the behaviour of the different substrate materials in greater detail. One such method would be to keep the material properties constant and vary the substrate thickness to produce a greater bending stiffness. Using this method with more than one material would allow comparison of the influences of mass and stiffness to the resulting system damping performance.

The DOE methodology provided a useful technique for determining the relative influence of multiple variables on the system damping performance. Previous research had determined that a varying unconstrained layer damping material (ULD) thickness distribution could be used to optimise the system loss factor. Further investigation comparing the influence of optimal damping layer distribution to the likes of ambient environmental conditions, curved plate geometries and substrate material properties would provide useful insight into effective application of optimised UDL treatments to marine structures among others.

6.3 Patterned Fibre Constrained Layer Damping

A finite element model (FEM) was created using MATLAB to determine the modal damping, deformation, stress, and strain behaviour of a novel three-layer fibre reinforced constrained layer damping material. The composite damping material consisted of two carbon fibre reinforced polymer (CFRP) layers with complex fibre patterns surrounding a viscoelastic core. The waveforms used for the two patterned fibre layers were the inverse

of one another to produce stress-coupling within the viscoelastic core through anisotropic orthotropic mechanisms. The presented patterns were an evolution of previously studied materials which had 'zig-zag' or constant sinusoidal fibre patterns [59, 61, 64]. Fibre patterns considered in the investigation included swept-sine and sine superposition waveforms. The new materials were termed complex fibre pattern constrained layer damping (CPF-CLD) materials.

The FEM accounted for the damping contributions from the CFRP face sheets and the viscoelastic core, and the frequency dependence of the CFRP and viscoelastic material (VEM) stiffness and damping properties. Damping within the FEM was modelled using a complex stiffness matrix, resulting from complex elastic and shear moduli values used for both the CFRP and VEM constituent materials. Modal damping performance of the CPF-CLD materials was calculated by solution of the complex eigen-problem. An iterative method was used to account for the variation of constituent material properties with modal frequency.

The FEM was validated through comparison with experimental results. Ten three-layer beam test specimens were produced for each of four different CPF-CLD designs. The modal damping performance of the test specimens was evaluated experimentally for the first four bending modes of the beams with free edge conditions. Modal damping loss factor values (η) were obtained using the half-power bandwidth technique.

Values of η and modal frequency produced by the FEM for the first four bending modes generally fell within one standard deviation of the values measured experimentally, with few exceptions. Deviations from the experimental results may have been due to assumptions made in the FEM for constituent material properties which could not be measured directly.

The model correctly predicted the relative damping performance of each of the four patterns studied for each mode. Consequently, the FEM was suitable for comparison of pattern performance.

CPF-CLD modal behaviour was investigated. Of the four patterns initially studied, it was found that a pattern property $\overline{\theta}_{abs}$, the average absolute fibre angle of the pattern in the length direction of the beam, was related to the values of η produced by each pattern in both bending and torsion modes. Pattern with lower values of $\overline{\theta}_{abs}$ produced greater values of η.

Comparison of the four CPF-CLD designs to a pattern with unidirectional (UD) fibres oriented at 0° to the length direction ($\overline{\theta}_{abs}$=0), showed that the UD pattern (UD0) produced the largest values of η for all of the bending and torsion modes studied.

Observation of the shear strain fields within the VEM layer of each of the patterns showed that the longitudinal shear strains γ_{xz} dominated in both the bending and torsion modal behaviours, although this was clearest in the bending modes. The patterns with larger $\overline{\theta}_{abs}$ values were found to produce greater proportions of the transverse in-plane shear strain γ_{yz} for bending modes. It was proposed that while these patterns induced greater γ_{yz} values, the diminished damping associated with lower γ_{xz} values, resulting from lower stiffness in the length direction, ultimately produced lower values of η.

Further exploration into the effect of $\overline{\theta}_{abs}$ was performed by comparison of the four CPF-CLD patterns with simpler patterns which had equivalent $\overline{\theta}_{abs}$ values. The simpler patterns considered were constant sinusoids and asymmetric UD arrangements. It was found that the 'equivalent' patterns did not produce the same damping performance as the associated CPF-CLD patterns. This result indicated that localised stiffness distributions within the

modelled beams influenced the modal damping behaviour.

The same behaviour was demonstrated by comparison of two constant sinusoidal patterns with identical wavelengths, amplitudes and $\overline{\theta}_{abs}$ values, but different pattern initiation points. These two patterns were also compared to a unidirectional pattern with an equivalent $\overline{\theta}_{abs}$ value. The results produced by the three patterns and the previous CPF-CLD study showed that greater damping performance was possible from more complex fibre patterns over UD patterns with the same $\overline{\theta}_{abs}$ value.

The results from the pattern comparisons were consistent with findings from [54] and [58], which found that the greatest loss factor values produced by sandwich plates with a $[+\theta/\text{VEM}/-\theta]$ stacking sequence were achieved with a $\theta = 0°$ value. However, the modelled results contradicted conclusions drawn in previous research performed on constant sinusoidal fibres [75, 76]. This earlier work determined that constant sinusoidal fibre patterns with $\theta_{max} \approx 30°$ values produced greater loss factor values than patterns with lower θ_{max} values. The current investigation did not produce the same behaviour, as patterns with a lower θ_{max} value also had a lower $\overline{\theta}_{abs}$ value and consequently produced greater damping performance.

While beam geometries with free edge conditions were the primary focus of these investigations, plate behaviour and various edge conditions are equally able to be simulated using the developed FEM. Modal behaviour of plate geometries and design of CPF-CLD patterns that utilise high shear strains induced by constrained edge conditions would be a logical pathway continuing this work.

The presented finite element model and CPF-CLD material investigation findings also provide scope for further analysis. It was found that the localised stiffness within asymmetric

fibre layers surrounding a viscoelastic core influenced the modal damping performance of the three-layer composite system. It was also demonstrated that if the stiffness within such a composite beam was distributed favourably, greater damping performance over asymmetric unidirectional arrangements with the same $\overline{\theta}_{abs}$ value were possible. It would therefore be useful to explore designs of CPF-CLD patterns with the same $\overline{\theta}_{abs}$ values as commonly used asymmetric laminate pairs, such as ± 45 or ± 30, with the aim of producing greater damping performance. Evaluation of the strength and stiffness properties of the resulting patterns relative to these standard fibre arrangements may provide justification into replacement of these arrangements with CPF-CLD treatments to enhance damping properties of a laminate while retaining the directional stiffness properties.

The investigations into CPF-CLD designs were also limited to cases of flexural vibration. Exploration of CPF-CLD damping performance produced by harmonic axial loads may reveal other effective areas of application for these materials.

6.4 Implementation of Patterned Fibre Constrained Layer Damping

Design of Experiments (DOE) methodology was used to analyse the implementation of CPF-CLD treatments to laminated composite sandwich beams. Test specimens were fabricated using materials and geometries commonly found in hull and bulkhead constructions of large composite marine vessels.

A fractional factorial experiment design was used to study the effects of CPF-CLD pattern type, beam core thickness and location of the CPF-CLD layers within the structure on system damping performance. These variables were selected to determine how to efficiently

utilise CPF-CLD materials in composite marine structural elements. The relative influence of each variable on system damping performance was also determined.

Damping values of the first five bending modes were measured using the half-power bandwidth method, with the sandwich beams in a freely suspended configuration.

Foam core thickness and placement of the CPF-CLD treatments were found to have the greatest influence over the system damping performance of the sandwich beams.

The specimens with thinner foam cores produced greater damping values, as did beams with the CPF-CLD treatments located adjacent to the core. CPF-CLD materials with the sine superposition fibre patterns were found to produce greater damping values over those with swept sine patterns. Fibre patterns with a lower minimum fibre wavelength produced greater damping values in the first bending mode, but had negligible effect at higher modes.

The results produced by the experiment indicated that the greatest increases in system damping performance would be gained by treating bulkhead constructions preferentially over hull constructions, and by embedding CPF-CLD treatments adjacent to the core of sandwich constructions rather than adding them as surface treatments.

Comparison of an undamped sandwich beam to a sandwich beam with surface CPF-CLD treatment showed that the treated beam produced damping increases of 230% in the first bending mode, and increases of 130% at higher modes.

The mechanisms resulting in the behaviour of each DOE variable were not able to be examined in greater detail due to resource constraints surrounding fabrication of further test specimens. While these behaviours were not examined further in this work, they are

considered worthy of further investigation.

Modification of the presented finite element model to incorporate greater numbers of layers would provide a useful tool in further evaluation of applying CPF-CLD treatments to multi-layer composite constructions.

Appendix A

Appendix

A.1 Simply-Supported and Clamped Plate Modal Frequency Analytical Models

A.1.1 Simply-Supported Plate Models

Analytical models for modal frequencies of isotropic elastic plates with all edges simply-supported are presented below. The models included are sourced from Leissa [89] and Pilkey [90].

Warburton model:

$$\omega_{mn}^2 = \frac{\pi^4 D}{a^4 \rho_s} \left(m^4 + n^4 \beta^4 + 2\beta^2 \left(\nu m^2 n^2 + (1-\nu) m^2 n^2 \right) \right) . \tag{A.1}$$

Leissa model:

$$\omega_{mn} = \left(\left(\frac{m\pi}{a} \right)^2 + \left(\frac{n\pi}{b} \right)^2 \right) \sqrt{\frac{D}{\rho_s}} . \tag{A.2}$$

Pilkey model:

$$\omega_{mn} = \frac{\lambda_{mn}}{a^2} \sqrt{\frac{D}{\rho_s}} , \tag{A.3}$$

where

$\lambda_{mn} = \pi^2(m^2 + \beta^2 n^2)$.

Janich model: (mode m=n=1 only)

$$\omega_{11}^2 = \frac{\pi^4 DA}{a^4 \rho_s B} , \tag{A.4}$$

where

$A = 0.25 + 0.50\beta^2 + 0.25\beta^4$,

$B = 0.25$.

A.1.2 Clamped Plate Models

Analytical models for modal frequencies of isotropic plates clamped on all edges are presented below. The models included are sourced from Leissa [89] and Pilkey [90].

Warburton model:

$$\omega_{mn}^2 = \frac{\pi^4 D}{a^4 \rho_s} \left(A_x^4 + A_y^4 \beta^4 + 2\beta^2 \left(\nu B_x B_y + (1-\nu) B_x B_y \right) \right) , \tag{A.5}$$

where

for $m = 1$,	$A_x = 1.506$	$B_x = 1.248$
for $n = 1$,	$A_y = 1.506$	$B_y = 1.248$
for $m > 1$,	$A_x = m + 1$	$B_x = (m+1)^2 \left(1 - \frac{2}{\pi(m+0.5)}\right)$
for $n > 1$,	$A_y = n + 1$	$B_y = (n+1)^2 \left(1 - \frac{2}{\pi(n+0.5)}\right)$.

Pilkey model: (modes m=n only)

$$\omega_{mn} = \frac{\lambda_{mn}}{a^2} \sqrt{\frac{D}{\rho_s}} , \tag{A.6}$$

where

$\lambda_{11} = \beta^2(89.3 - 84.73\beta + 36.7\beta^2 - 5.27\beta^3)$,

$\lambda_{22} = \beta^2(107.2 - 51.9\beta + 21.5\beta^2 - 3\beta^3)$,

$\lambda_{33} = \beta^2(262.7 - 241.3\beta + 102.1\beta^2 - 14.47\beta^3)$,

$1.0 \leq \beta \leq 3.0$.

Janich model: (mode m=n=1 only)

$$\omega_{11}^2 = \frac{\pi^4 DA}{a^4 \rho_s B} , \tag{A.7}$$

where

$A = 12 + 8\beta^2 + 12\beta^4$,

$B = 2.25$.

Gailin model: (mode m=n=1 only)

$$\omega_{11} = 12\sqrt{\frac{7}{2}\left(\frac{1}{a^4} + \frac{4}{7a^2b^2} + \frac{1}{b^4}\right)}\sqrt{\frac{D}{\rho_s}} . \tag{A.8}$$

Bolotin's approximated results for clamped square plates:

$$\omega_{mn} a^2 \sqrt{\frac{\rho_s}{D}} = \begin{bmatrix} 35.10 & 72.90 & 131.63 & 210.35 \\ & 107.47 & 164.39 & 242.20 \\ & & 219.32 & 295.69 \\ & & & 370.66 \end{bmatrix} , \tag{A.9}$$

where matrix entry $(m, n) = (n, m)$.

A.2 Uniformly Distributed Loading Equations

In general, a known uniformly distributed load can be applied to nodes on an element using the interpolation functions from those nodes and the element's area or length. For example, for a uniformly distributed load applied to an edge of a single element, the external force can be considered as:

$$f^{ext} = \int_{\Gamma} \{N\}\ p(\xi)\ l\ d\xi\ , \tag{A.10}$$

where f^{ext} is the applied external load, Γ is the surface that the force load distribution $p(\xi)$ is acting over, N are the interpolation functions of the nodes on this surface, and l is the length of the element edge the force is acting on.

A similar procedure can be used for UDLs acting on an area. If the loading $p(\xi, \eta)$ is uniform and the area of the surface is known, the proportion of load applied to each node is defined from the integral of the interpolation functions alone.

When considering a 'brick-16' element, a surface loading at $\xi = 1$, the loaded nodes will be nodes 2, 3, 6, 10, 11, and 14 (see Figure 4.3). The proportion of applied load for each of these nodes was calculated using integration in the isoparametric domain, with all ξ values in the interpolation functions set as $+1$. For a single element under load

$$f^{ext} = p\ A\ \int_{-1}^{1}\int_{-1}^{1} \{N\}\ d\eta d\zeta\ , \tag{A.11}$$

where p is the uniformly distributed load [N.m^{-2}], A is the element end face area [m^2], and $\{N\}$ is a 6×1 vector of the interpolation functions for nodes 2, 3, 6, 10, 11 and 14. This results in nodes 2, 3, 10 and 11 (corner nodes) having point loads of $\frac{p\ A}{3}$, and nodes 6 and 14 (mid nodes) having point loads of $\frac{4p\ A}{3}$. These fractions sum to $4(p\ A)$ due to the integral limits imposed by the isoparametric domain, thus each node load fraction must be divided by 4 to correctly match the total applied load. This produces a final proportion of $\frac{p\ A}{12}$ for nodes 2, 3, 10 and 11, and $\frac{p\ A}{3}$ for nodes 6 and 14. As a beam end is typically comprised

of multiple elements, some nodes are shared by more than one 'brick-16' element. At these points, nodal load proportions were summed and all applied forces are scaled by the total number of element faces under load to correctly match the total applied surface load. This results in four point load values which can be seen in the 3×3 element example in Figure A.1.

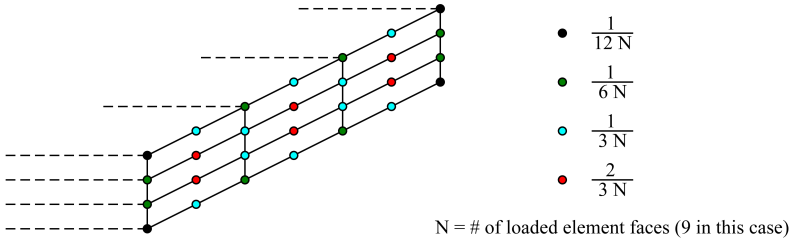

Figure A.1: Point load proportions for a uniformly distributed face loading

For a UDL applied to the $\xi = 1$, $\zeta = 1$ edge of and element, the force proportion integral is in the η direction only yielding

$$f^{ext} = p\ A\ \int_{-1}^{1} \{N\}\ d\eta\ , \tag{A.12}$$

where $\{N\}$ is a 3×1 vector of the interpolation functions for nodes 10, 11 and 14. Values of ξ and ζ are set to $+1$ for the interpolation functions of these nodes. The loading proportions are again summed for all shared nodes and scaled to match the edge load distribution. The three resulting loading proportions can be seen in Figure A.2.

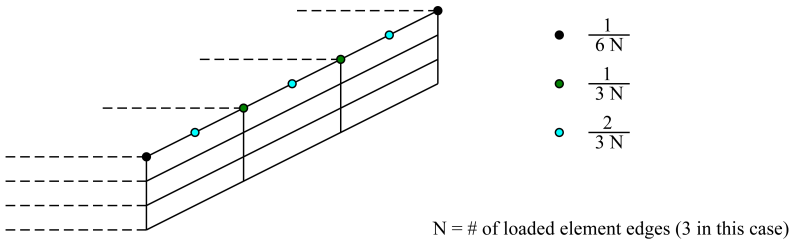

Figure A.2: Point load proportions for a uniformly distributed edge loading

A.3 Mesh Refinement

The changes in modal frequency and loss factor results produced by the model are shown in Figures A.3 - A.10.

In order to ensure equal element aspect ratio in the laminate plane the number of elements in the length direction was maintained at 6 times the number of elements in the width direction.

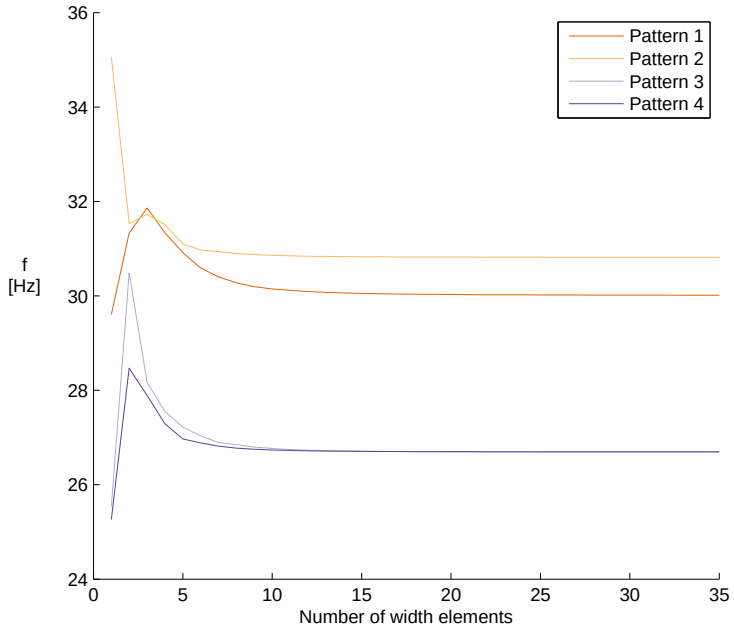

Figure A.3: Mode 1 frequency results with increasing element numbers

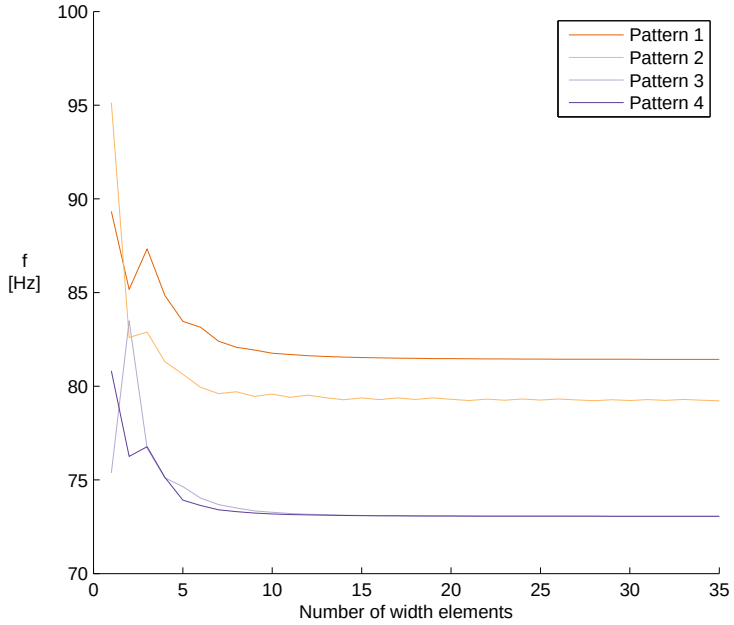

Figure A.4: Mode 2 frequency results with increasing element numbers

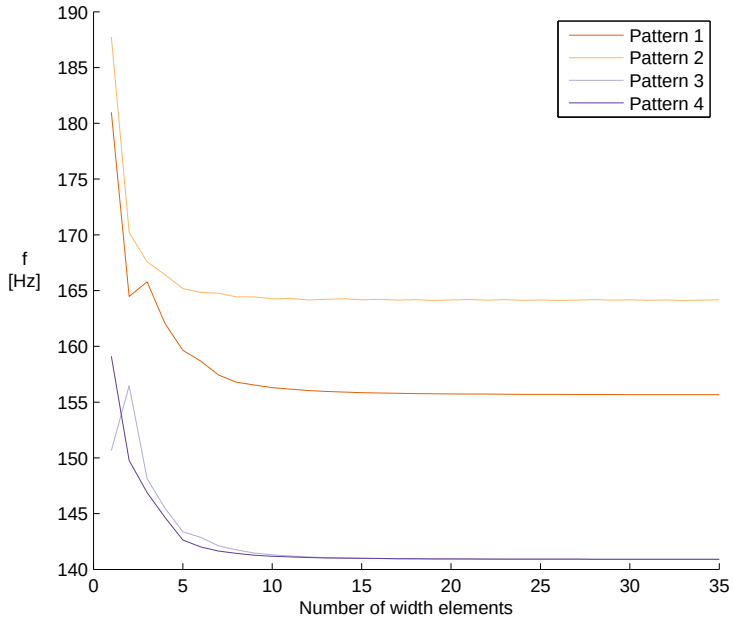

Figure A.5: Mode 3 frequency results with increasing element numbers

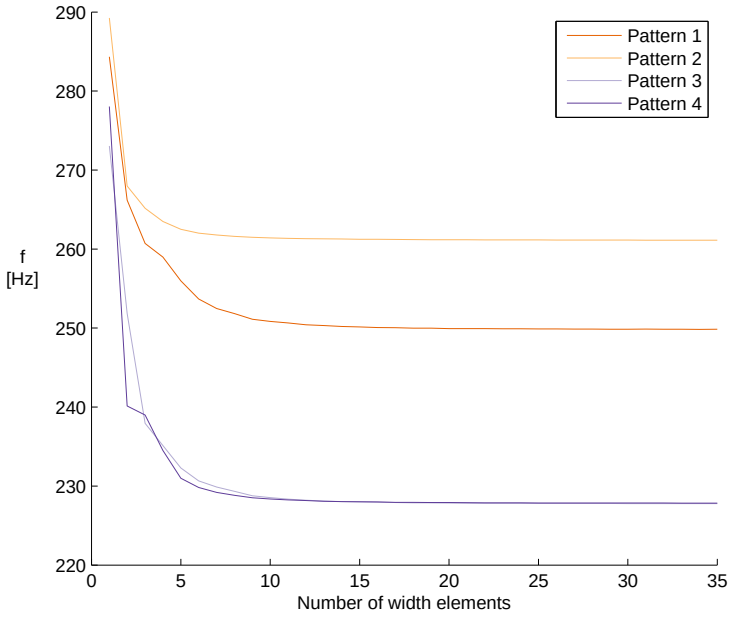

Figure A.6: Mode 4 frequency results with increasing element numbers

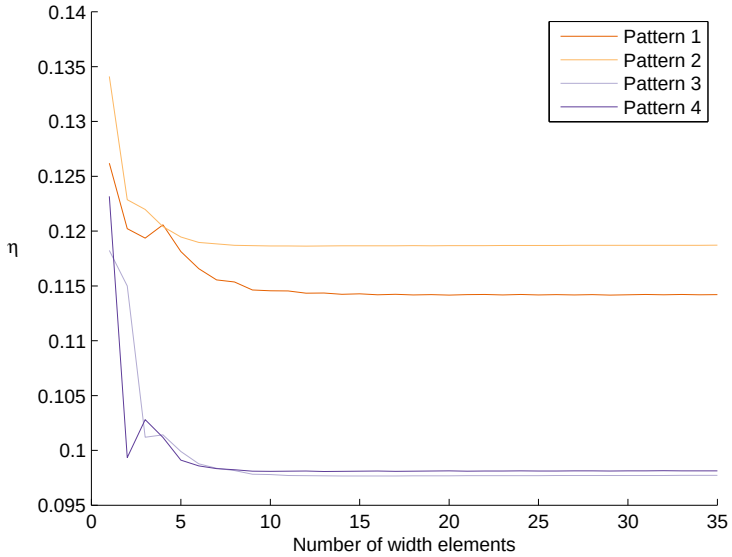

Figure A.7: Mode 1 damping results with increasing element numbers

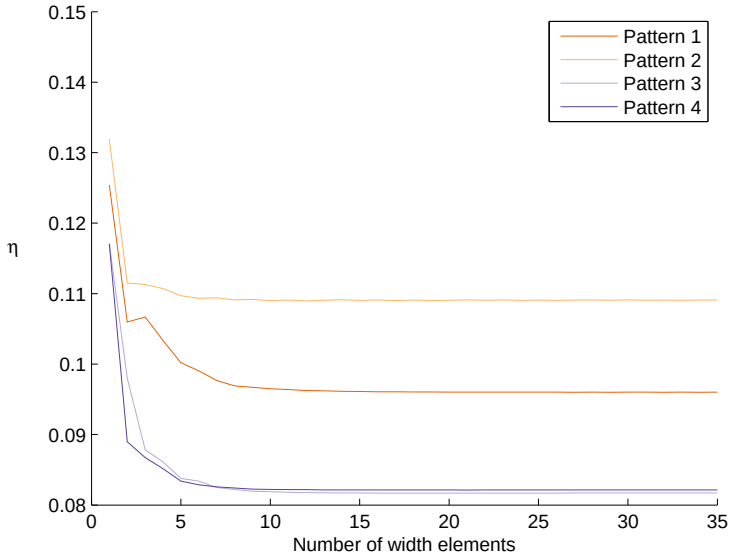

Figure A.8: Mode 2 damping results with increasing element numbers

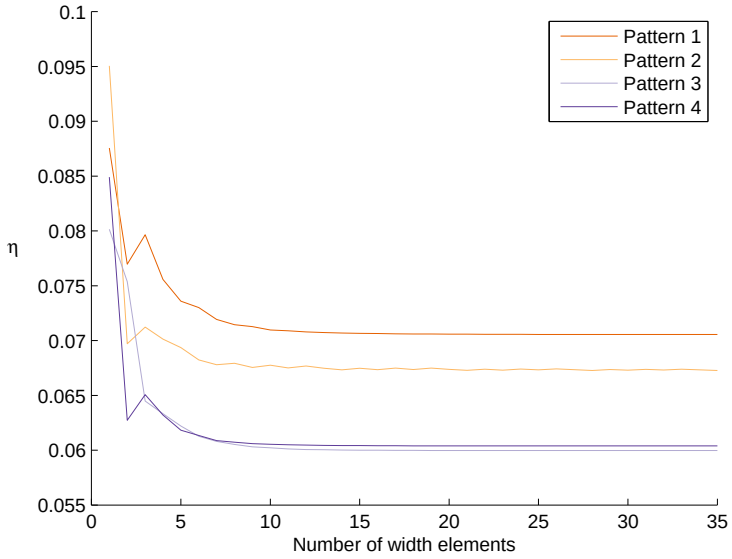

Figure A.9: Mode 3 damping results with increasing element numbers

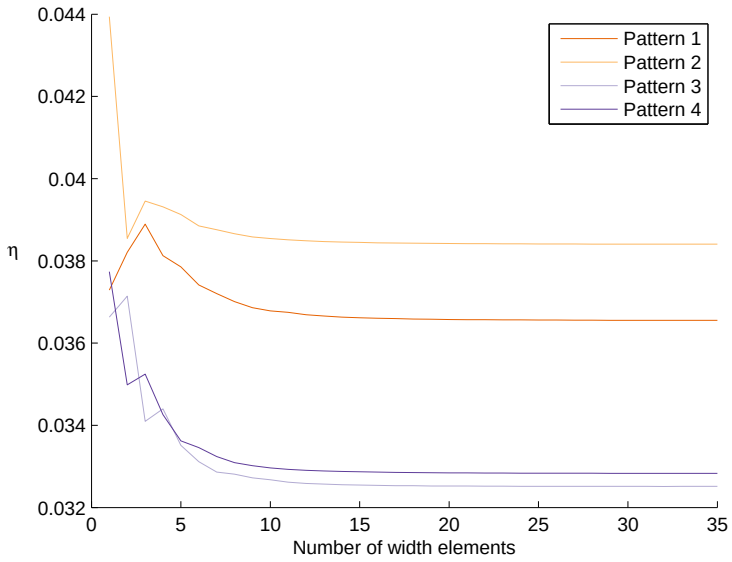

Figure A.10: Mode 4 damping results with increasing element numbers

A.4 Modal Damping Test Results of CPF-CLD Materials at Ambient Temperature

The experimental modal frequency and associated damping loss factor data measured for the first four bending modes of the ten tests specimens of each pattern are shown in Tables A.1 to A.4. The values presented are the average results produced by each specimen from the ten frequency response measurements.

Specimen number	Mode 1		Mode 2		Mode 3		Mode 4	
	f_1 [Hz]	η_1	f_2 [Hz]	η_2	f_3 [Hz]	η_3	f_4 [Hz]	η_4
P1-1	27.0	0.036	74.8	0.052	144.8	0.089	249.5	0.128
P1-2	28.9	0.032	79.2	0.053	152.7	0.084	260.3	0.137
P1-3	28.0	0.042	77.0	0.069	148.2	0.121	253.1	0.159
P1-4	27.6	0.047	75.8	0.098	146.6	0.152	251.3	0.125
P1-5	29.6	0.041	81.0	0.071	157.5	0.109	270.6	0.170
P1-6	28.2	0.040	77.1	0.071	148.7	0.119	253.6	0.195
P1-7	27.9	0.029	76.9	0.052	153.4	0.094	241.9	0.105
P1-8	29.4	0.032	80.9	0.051	159.6	0.094	258.2	0.112
P1-9	27.8	0.031	76.6	0.051	151.9	0.091	239.7	0.107
P1-10	28.5	0.033	78.3	0.050	154.3	0.091	248.0	0.111

Table A.1: Average modal damping results of pattern 1 test specimens

Specimen number	Mode 1		Mode 2		Mode 3		Mode 4	
	f_1 [Hz]	η_1	f_2 [Hz]	η_2	f_3 [Hz]	η_3	f_4 [Hz]	η_4
P2-1	30.5	0.043	80.5	0.077	165.6	0.130	293.2	0.187
P2-2	30.0	0.033	79.0	0.049	162.5	0.096	284.3	0.145
P2-3	29.6	0.051	78.3	0.076	161.4	0.133	286.2	0.167
P2-4	28.4	0.042	74.4	0.090	152.8	0.155	272.3	0.199
P2-5	28.9	0.030	76.5	0.045	161.6	0.092	251.2	0.122
P2-6	28.5	0.055	74.8	0.092	152.0	0.182	269.1	0.152
P2-7	30.1	0.045	79.7	0.073	160.5	0.182	286.8	0.188
P2-8	30.2	0.037	79.1	0.072	164.7	0.118	287.2	0.159
P2-9	30.5	0.036	81.0	0.049	170.7	0.096	270.9	0.128
P2-10	29.2	0.036	77.4	0.046	163.8	0.091	259.9	0.113

Table A.2: Average modal damping results of pattern 2 test specimens

Specimen number	Mode 1		Mode 2		Mode 3		Mode 4	
	f_1 [Hz]	η_1	f_2 [Hz]	η_2	f_3 [Hz]	η_3	f_4 [Hz]	η_4
P3-1	26.2	0.050	72.0	0.070	140.4	0.102	232.7	0.135
P3-2	26.7	0.049	73.9	0.063	144.2	0.095	239.3	0.120
P3-3	26.6	0.039	73.6	0.048	143.9	0.080	238.1	0.109
P3-4	26.3	0.032	72.6	0.046	142.1	0.086	235.4	0.108
P3-5	28.3	0.044	77.5	0.049	152.5	0.073	251.5	0.090
P3-6	27.5	0.035	76.8	0.060	151.2	0.075	249.8	0.090
P3-7	25.7	0.034	71.4	0.046	140.9	0.067	233.9	0.080
P3-8	26.1	0.033	72.1	0.039	142.3	0.060	235.0	0.073
P3-9	26.9	0.036	74.6	0.044	146.4	0.069	242.6	0.087
P3-10	26.5	0.030	73.6	0.045	144.7	0.072	240.3	0.083

Table A.3: Average modal damping results of pattern 3 test specimens

Specimen number	Mode 1		Mode 2		Mode 3		Mode 4	
	f_1 [Hz]	η_1	f_2 [Hz]	η_2	f_3 [Hz]	η_3	f_4 [Hz]	η_4
P4-1	26.1	0.038	72.1	0.059	140.5	0.094	227.7	0.125
P4-2	25.8	0.041	71.1	0.061	138.5	0.119	225.9	0.143
P4-3	25.6	0.043	70.5	0.069	137.4	0.132	223.2	0.145
P4-4	26.0	0.043	72.0	0.067	140.2	0.104	229.2	0.128
P4-5	26.4	0.043	73.0	0.071	142.2	0.118	232.3	0.132
P4-6	27.0	0.033	73.7	0.049	142.6	0.084	230.9	0.131
P4-7	26.8	0.036	74.0	0.048	145.1	0.076	242.6	0.093
P4-8	25.8	0.038	71.1	0.038	140.3	0.066	235.7	0.080
P4-9	26.4	0.038	72.9	0.046	143.8	0.066	240.8	0.081
P4-10	27.8	0.036	76.6	0.042	151.2	0.069	252.5	0.086

Table A.4: Average modal damping results of the pattern 4 test specimens

Examination of each pattern's entire data set produced the average modal frequencies, damping loss factors and associated standard deviations (SD) shown in Table A.5.

Pattern		Mode 1		Mode 2		Mode 3		Mode 4	
		f_1 [Hz]	η_1	f_2 [Hz]	η_2	f_3 [Hz]	η_3	f_4 [Hz]	η_4
1	Value	28.5	0.034	78.4	0.058	153.4	0.098	253.6	0.125
	SD	0.6	0.005	1.7	0.013	3.6	0.018	9.6	0.027
2	Value	29.7	0.039	78.4	0.064	162.6	0.115	275.7	0.152
	SD	0.7	0.007	2.0	0.017	4.9	0.027	13.9	0.033
3	Value	26.7	0.038	73.8	0.051	144.8	0.078	239.8	0.097
	SD	0.7	0.007	1.9	0.010	3.9	0.013	6.2	0.020
4	Value	26.5	0.038	73.0	0.052	142.9	0.086	235.8	0.108
	SD	0.7	0.003	1.8	0.010	3.9	0.021	8.7	0.025

Table A.5: Summary of average modal damping values for patterns 1 to 4 with associated standard deviation values

A.5 Modal Damping Test Results of CPF-CLD Materials at Sub-Ambient Temperature

Average modal damping values produced by measurement of the four CPF-CLD patterns under sub-ambient conditions are shown in Table A.6. The displayed results were obtained from multiple frequency response functions of three test specimens of each pattern. Temperatures during testing were centred on 4 °C but varied by up to ±2°C.

Pattern		Mode 1		Mode 2		Mode 3		Mode 4	
		f_1 [Hz]	η_1	f_2 [Hz]	η_2	f_3 [Hz]	η_3	f_4 [Hz]	η_4
1	Value	29.7	0.055	81.7	0.032	158.6	0.042	279.9	0.050
	SD	0.4	0.006	0.7	0.002	1.2	0.006	2.2	0.004
2	Value	31.4	0.045	83.1	0.029	173.7	0.053	307.9	0.042
	SD	0.2	0.003	0.6	0.003	1.5	0.003	1.9	0.006
3	Value	27.4	0.041	76.6	0.034	150.5	0.049	253.9	0.049
	SD	0.3	0.005	0.6	0.004	1.2	0.011	1.3	0.003
4	Value	27.7	0.043	77.4	0.031	151.2	0.033	251.3	0.050
	SD	0.3	0.004	0.5	0.006	1.0	0.004	5.2	0.004

Table A.6: Summary of average modal damping values for patterns 1 to 4 with associated standard deviation values from sub-ambient temperature measurements

A.6 Sandwich Beam Suspension Comparison

The damping results produced from the first five bending modes of vibration of damped and undamped sandwich beams with eyelet suspension and pinned suspension is shown in Figure A.11.

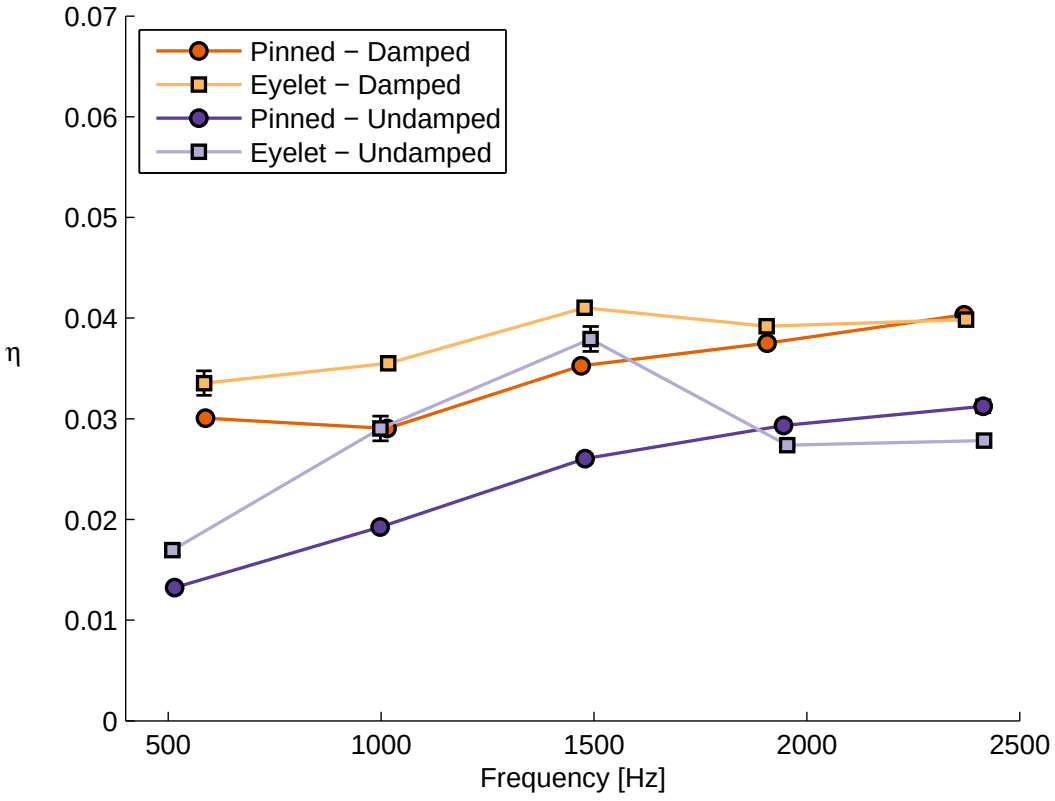

Figure A.11: Suspension method results for damped and undamped sandwich beams

A.7 ISO and ASTM Test Rig Drawings

The engineering drawings used in the fabrication of the ISO and ASTM test rigs are shown in Figures A.12 to A.18 on the following pages.

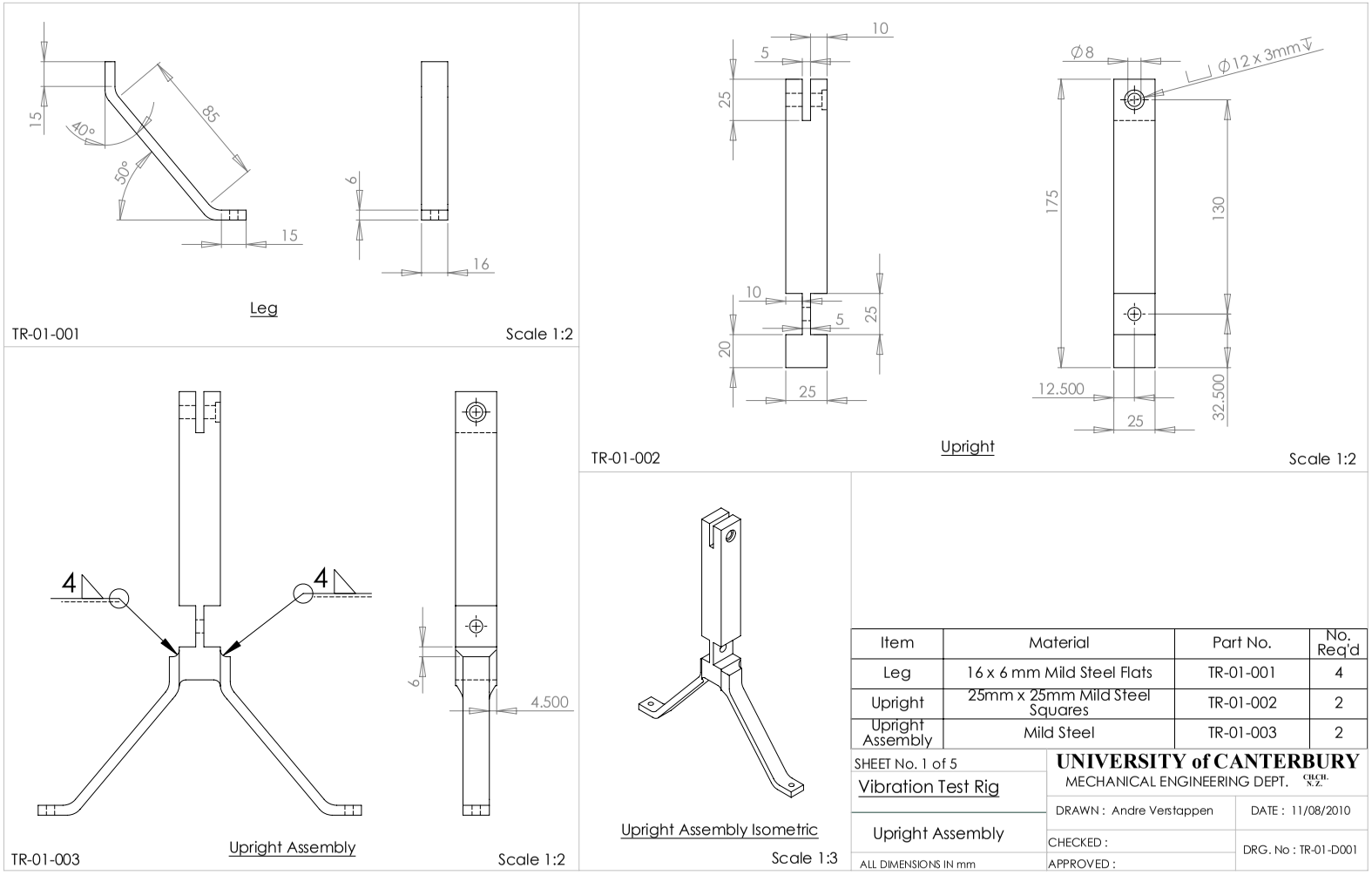

Figure A.12: ISO test rig - 1 of 4

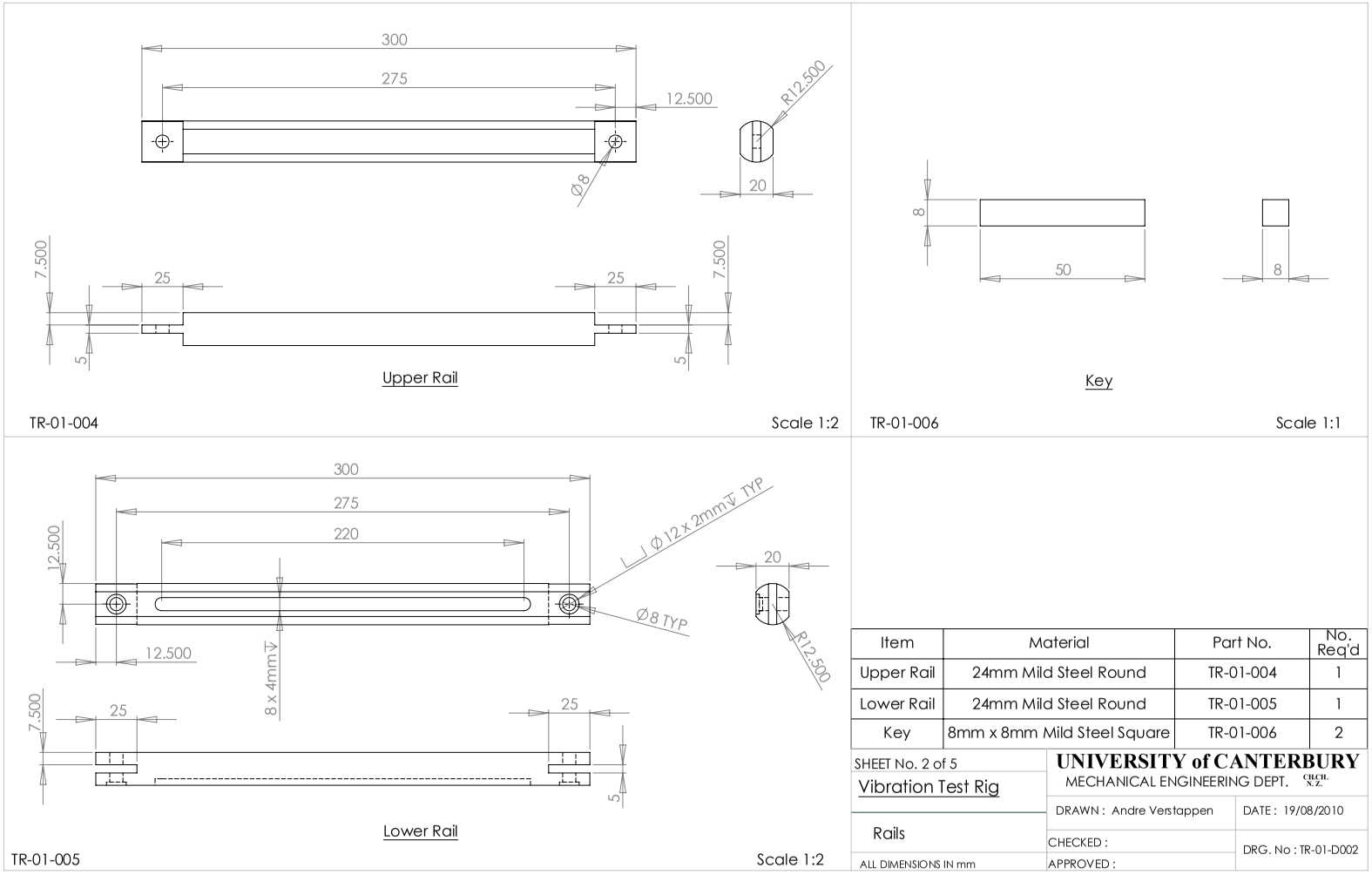

Figure A.13: ISO test rig - 2 of 4

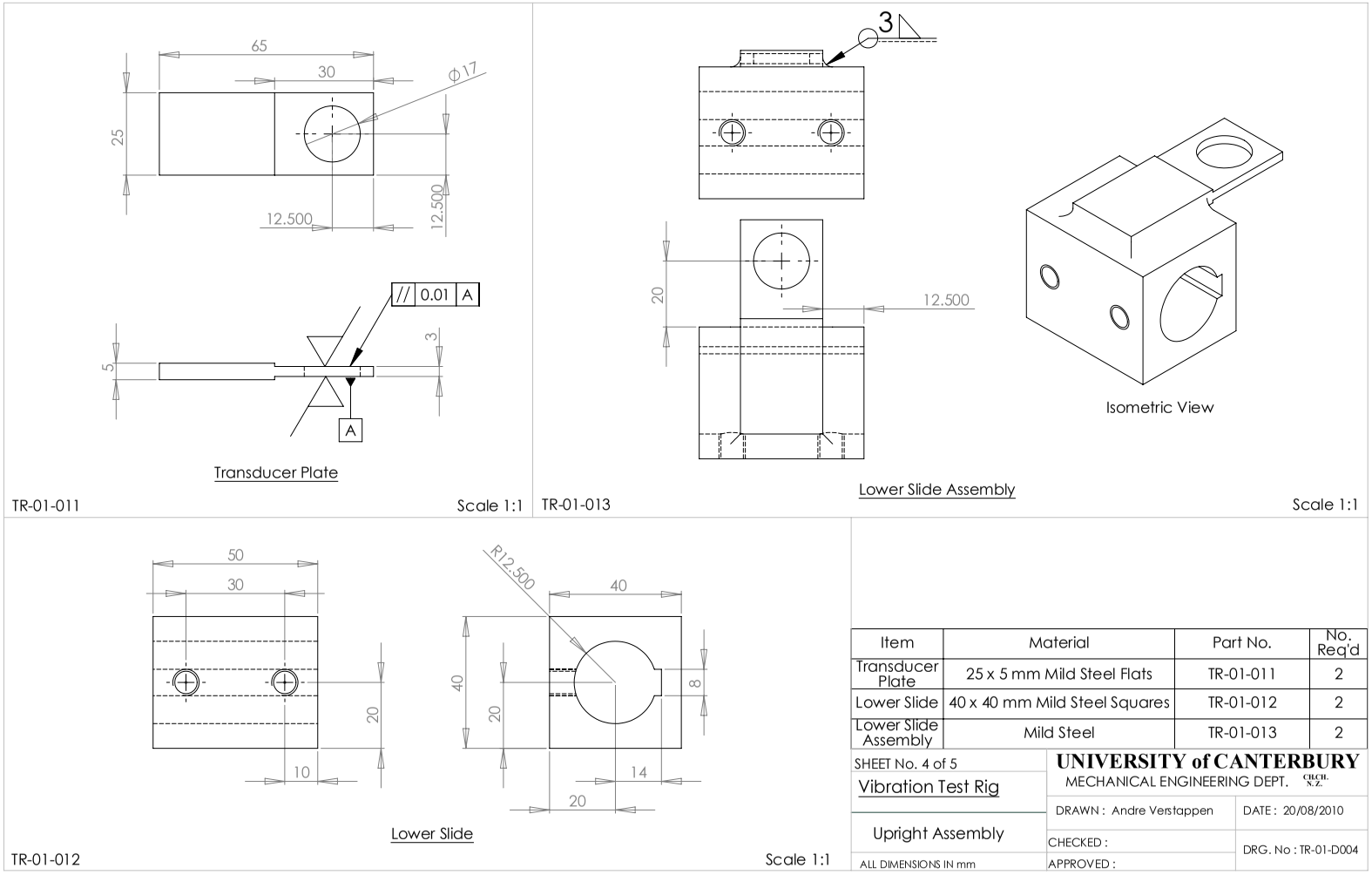

Item	Material	Part No.	No. Req'd
Transducer Plate	25 x 5 mm Mild Steel Flats	TR-01-011	2
Lower Slide	40 x 40 mm Mild Steel Squares	TR-01-012	2
Lower Slide Assembly	Mild Steel	TR-01-013	2

SHEET No. 4 of 5	**UNIVERSITY of CANTERBURY** MECHANICAL ENGINEERING DEPT. CHCH. N.Z.	
Vibration Test Rig	DRAWN : Andre Verstappen	DATE : 20/08/2010
Upright Assembly	CHECKED :	DRG. No : TR-01-D004
ALL DIMENSIONS IN mm	APPROVED :	

Figure A.14: ISO test rig - 3 of 4

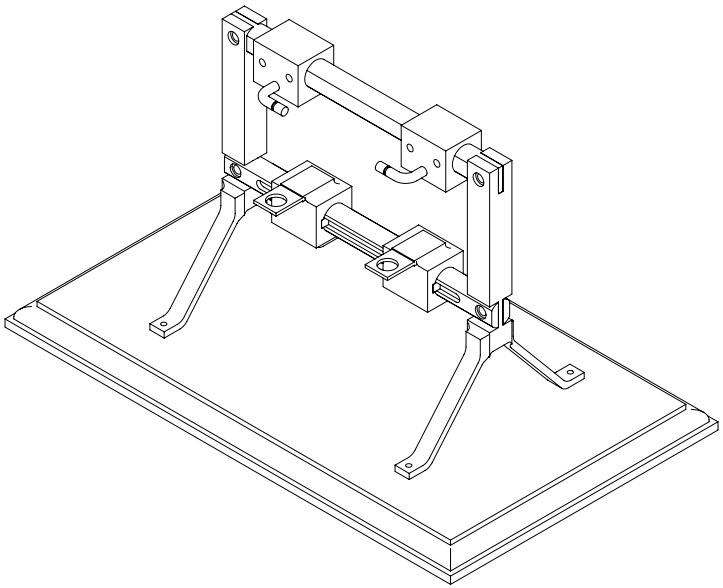

Test Rig

Scale 1:3

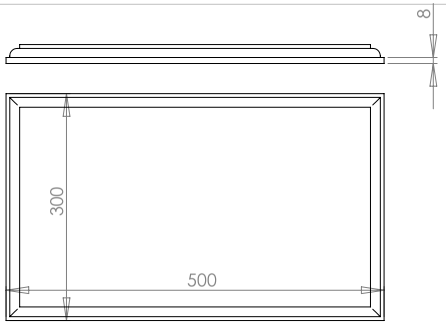

Base Plate

TR-01-014

Scale 1:5

Item	Material	Part No.	No. Req'd
Base Plate	6mm Mild Steel Plate	TR-01-014	1
Leg	16 x 6 mm Mild Steel Flat	TR-01-001	4
Upright	25 x 25 mm Mild Steel Square	TR-01-002	2
Lower Rail	24mm Mild Steel Round	TR-01-005	1
Lower Slide	40mm x 40mm Mild Steel Square	TR-01-012	2
Transducer Plate	25mm x 5mm Mild Steel Flat	TR-01-011	2
Key	8mm x 8mm Mild Steel Square	TR-01-006	2
Upper Rail	24mm Mild Steel Round	TR-01-004	1
Upper Slide	40mm x 40mm Mild Steel Square	TR-01-008	2
Hook	8mm Mild Steel Round	TR-01-007	2
Cap Screw	M8 x 30	-	16
Nut	M8	-	4

SHEET No. 5 of 5

Vibration Test Rig

Test Rig Assembly

ALL DIMENSIONS IN mm

UNIVERSITY of CANTERBURY
MECHANICAL ENGINEERING DEPT. CHCH. N.Z.

DRAWN : Andre Verstappen

DATE : 20/08/2010

CHECKED :

APPROVED :

DRG. No : TR-01-D005

Figure A.15: ISO test rig - 4 of 4

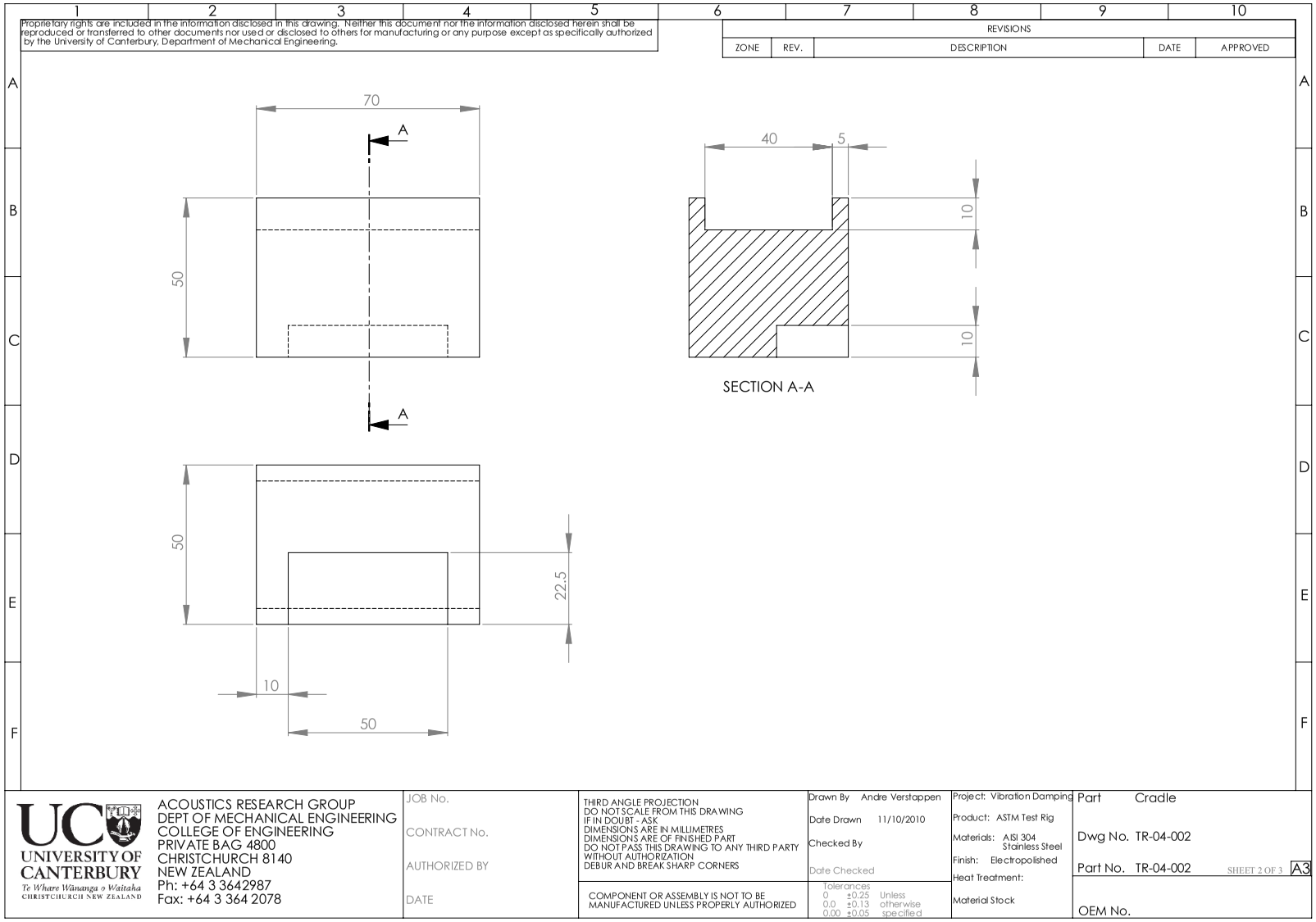

Figure A.16: ASTM test rig - 1 of 3

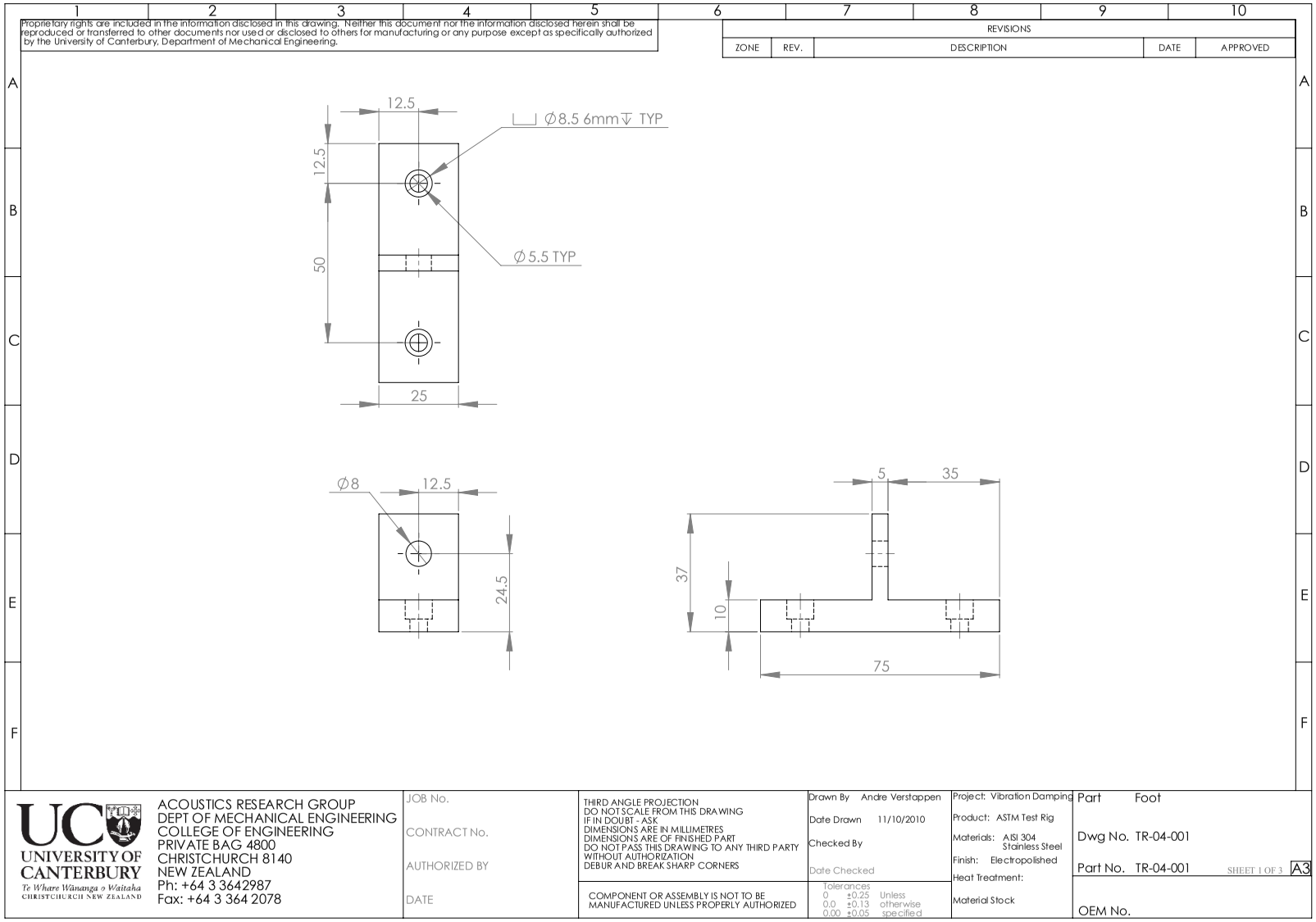

Figure A.17: ASTM test rig - 2 of 3

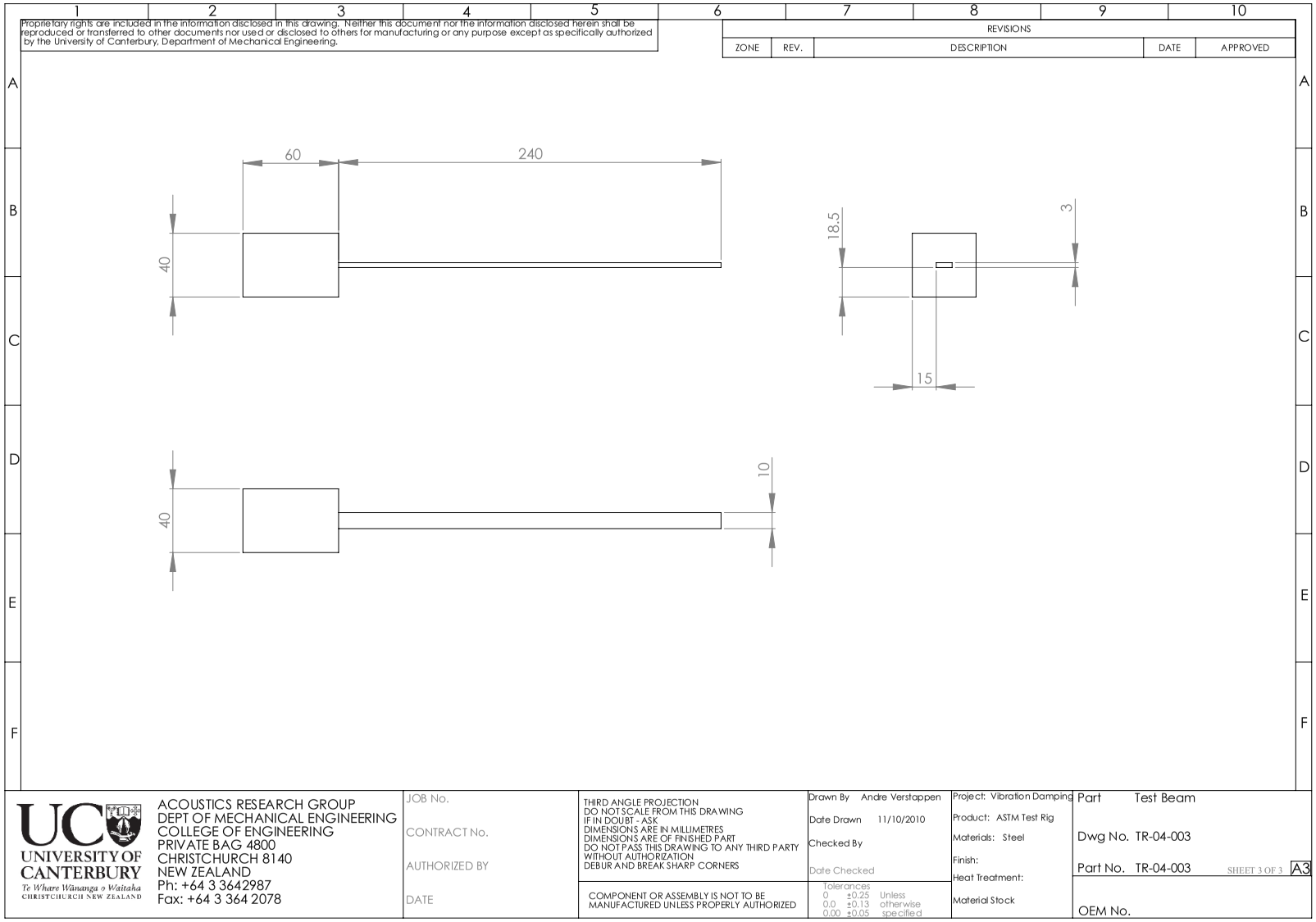

Figure A.18: ASTM test rig - 3 of 3

A.8 Plate Clamping Frame Drawings

The engineering drawing used in the fabrication of metal frames to provide edge clamping to the plate test specimens are shown in Figures A.19 to A.27 on the following pages.

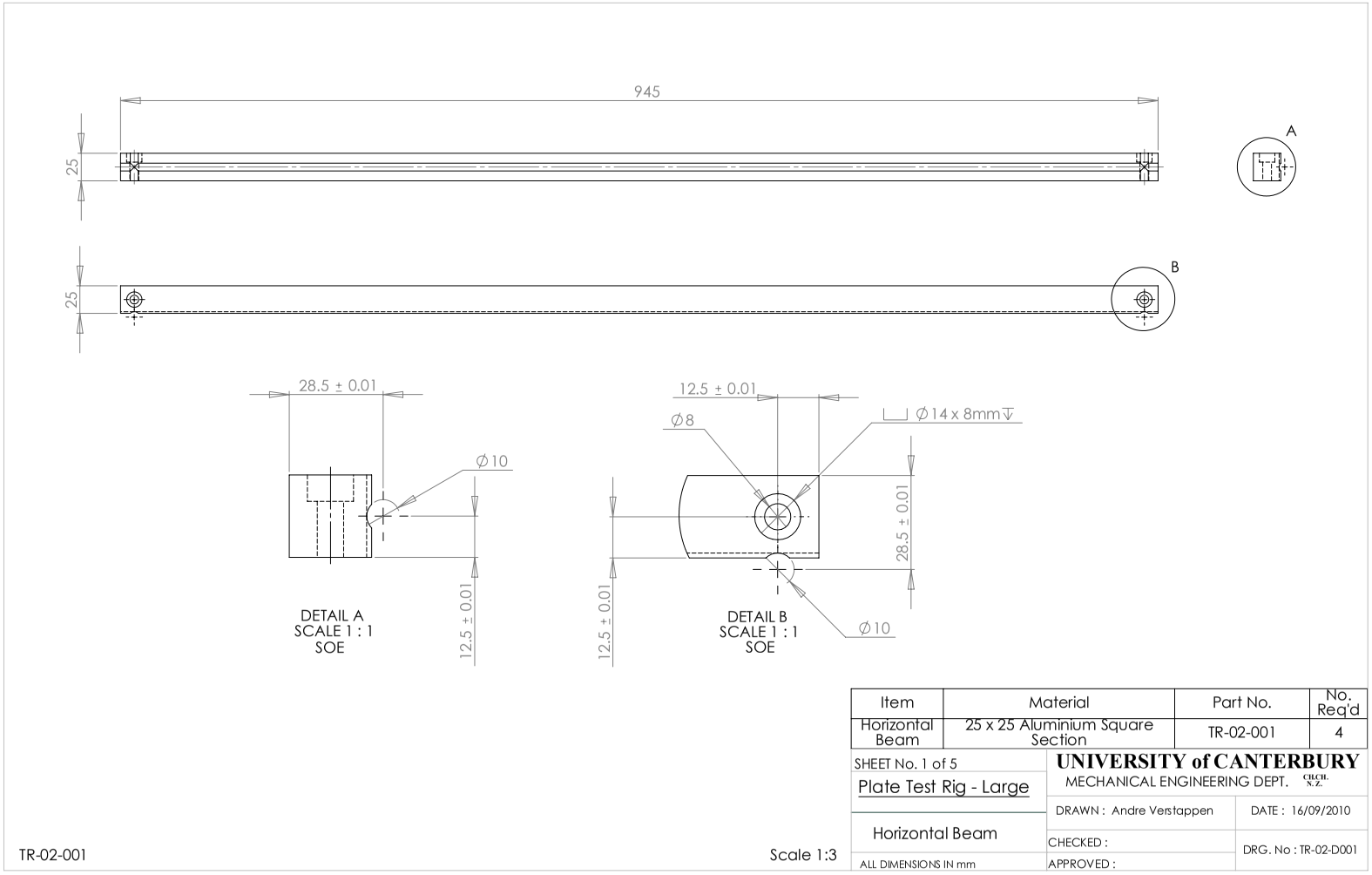

Item	Material	Part No.	No. Req'd
Horizontal Beam	25 x 25 Aluminium Square Section	TR-02-001	4

SHEET No. 1 of 5	**UNIVERSITY of CANTERBURY** MECHANICAL ENGINEERING DEPT. CHCH. N.Z.	
Plate Test Rig - Large	DRAWN : Andre Verstappen	DATE : 16/09/2010
Horizontal Beam	CHECKED :	DRG. No : TR-02-D001
ALL DIMENSIONS IN mm	APPROVED :	

Figure A.19: Large plate clamping frame - 1 of 5

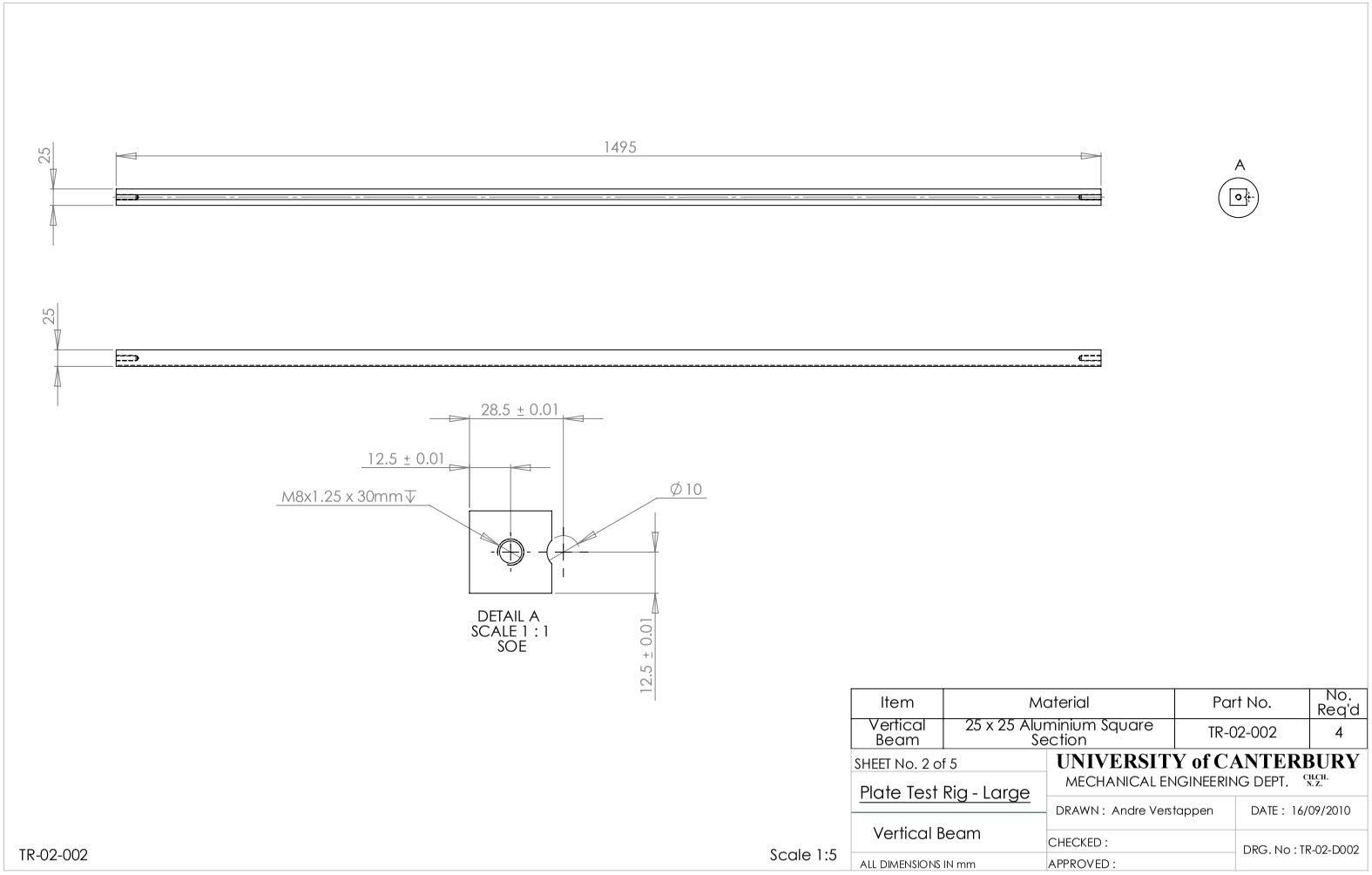

Figure A.20: Large plate clamping frame - 2 of 5

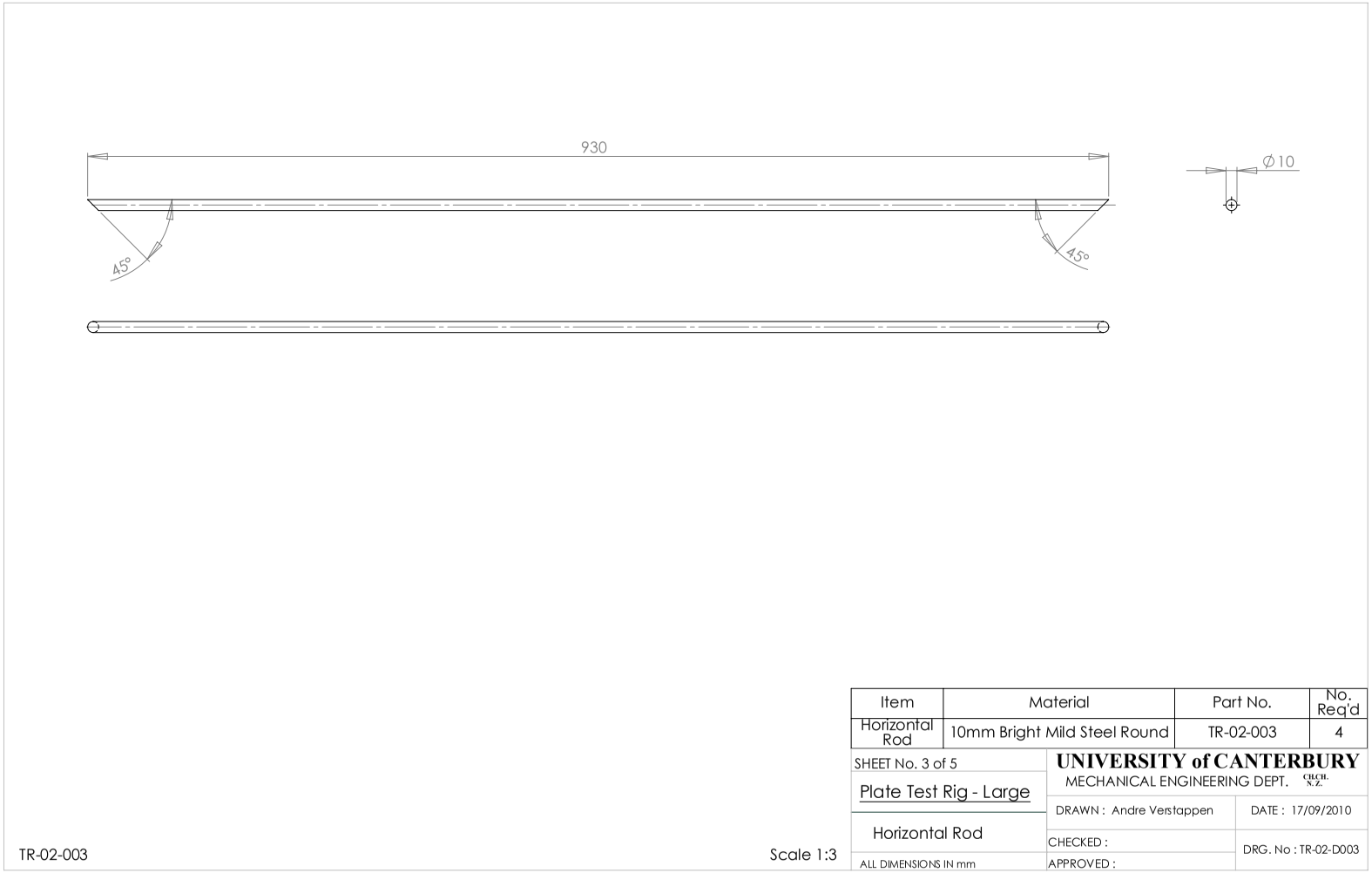

Figure A.21: Large plate clamping frame - 3 of 5

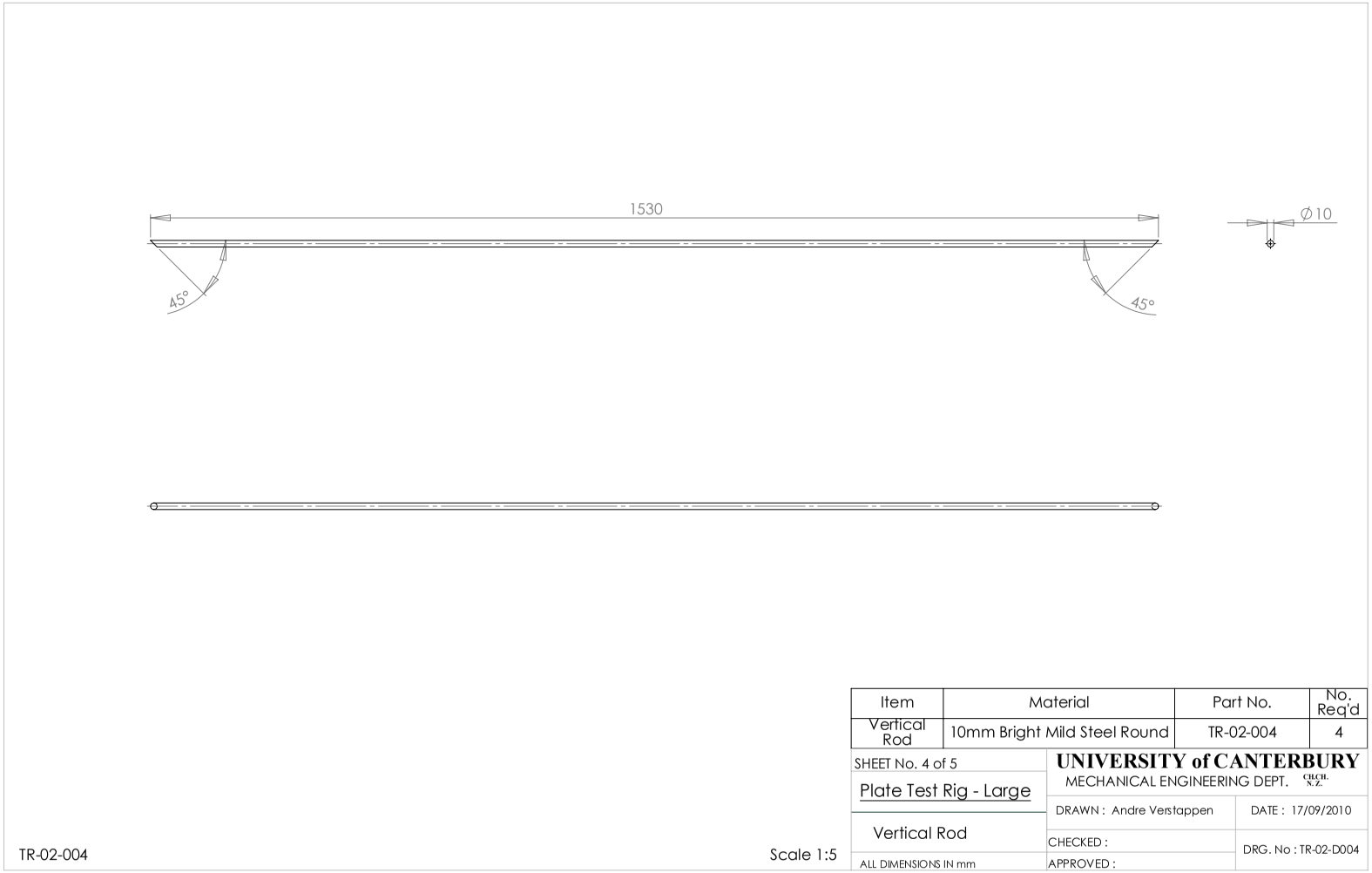

Figure A.22: Large plate clamping frame - 4 of 5

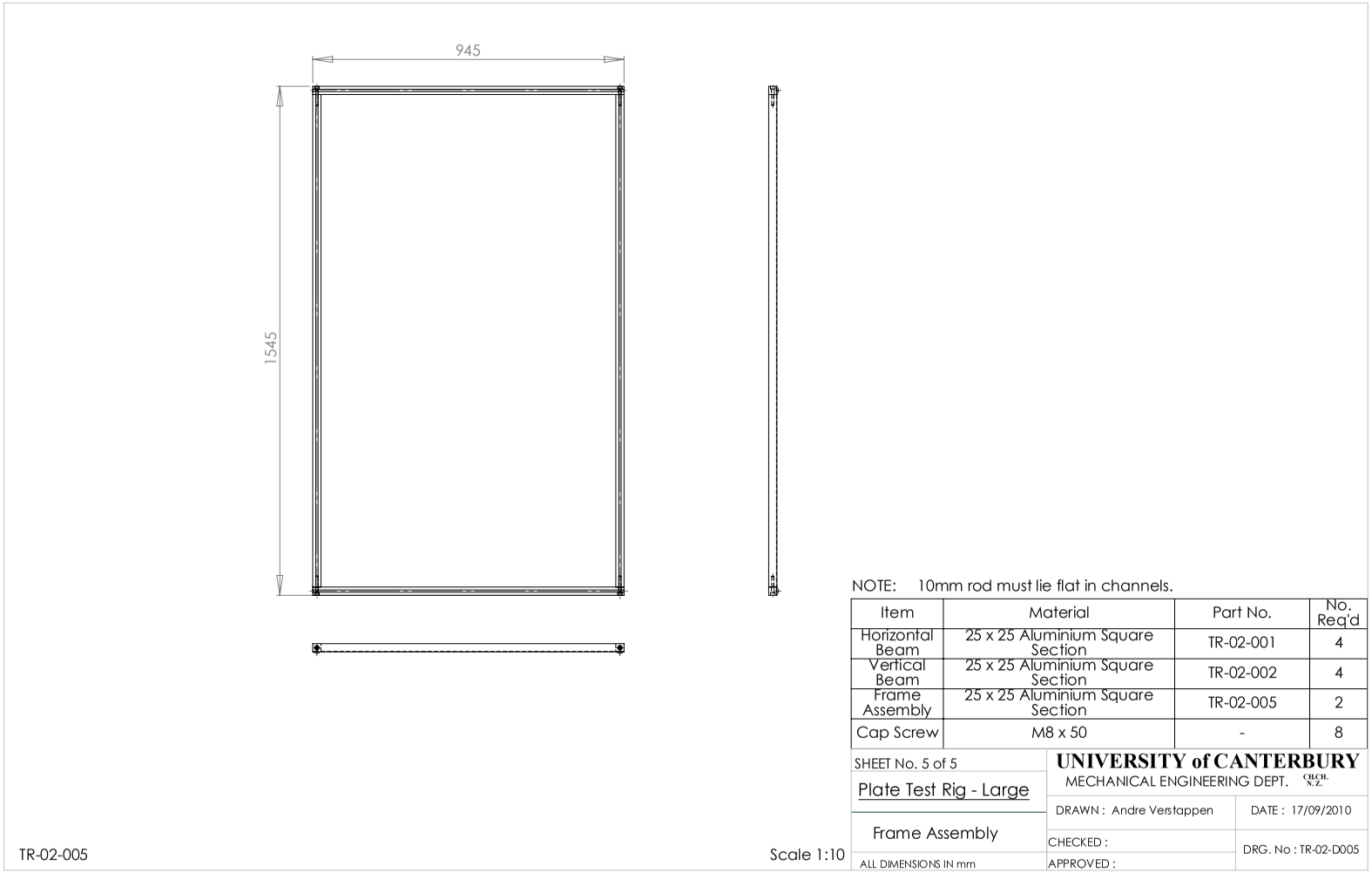

Figure A.23: Large plate clamping frame - 5 of 5

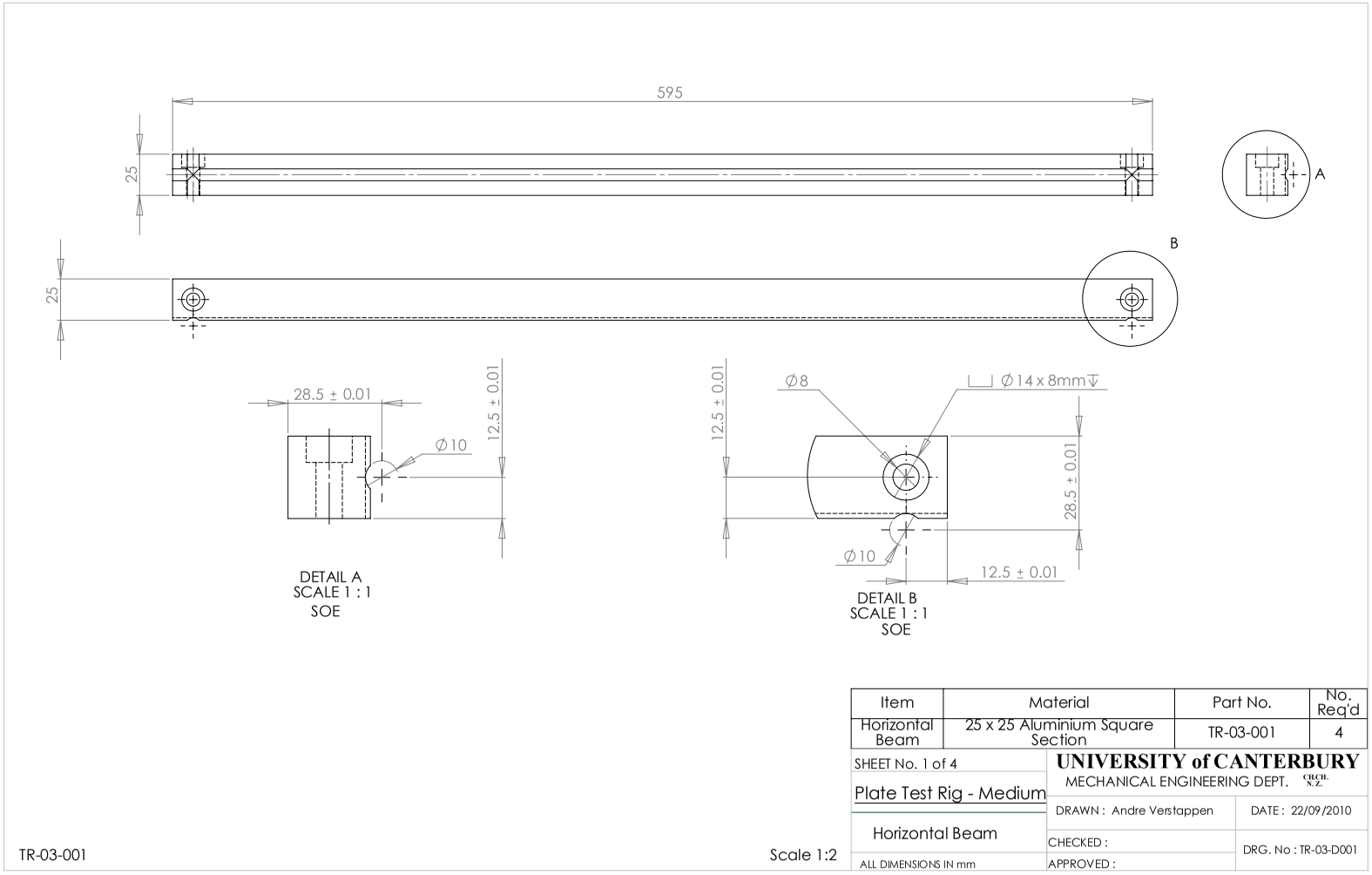

Item	Material	Part No.	No. Req'd
Horizontal Beam	25 x 25 Aluminium Square Section	TR-03-001	4

SHEET No. 1 of 4	UNIVERSITY of CANTERBURY MECHANICAL ENGINEERING DEPT. CHCH. N.Z.	
Plate Test Rig - Medium	DRAWN : Andre Verstappen	DATE : 22/09/2010
Horizontal Beam	CHECKED :	DRG. No : TR-03-D001
ALL DIMENSIONS IN mm	APPROVED :	

Figure A.24: Small plate clamping frame - 1 of 4

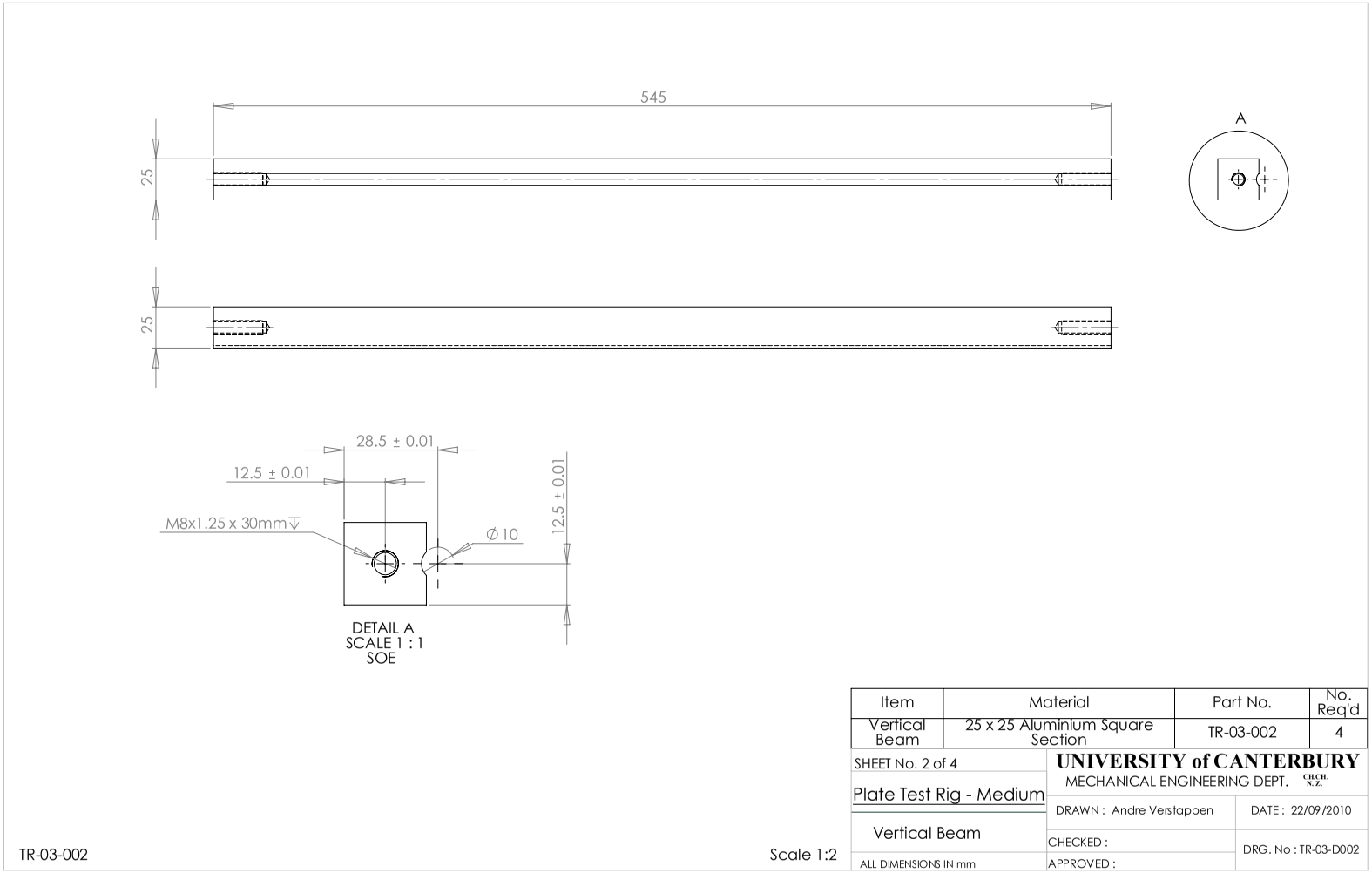

Item	Material	Part No.	No. Req'd
Vertical Beam	25 x 25 Aluminium Square Section	TR-03-002	4

SHEET No. 2 of 4	UNIVERSITY of CANTERBURY MECHANICAL ENGINEERING DEPT. CHCH. N.Z.	
Plate Test Rig - Medium	DRAWN : Andre Verstappen	DATE : 22/09/2010
Vertical Beam	CHECKED :	DRG. No : TR-03-D002
ALL DIMENSIONS IN mm	APPROVED :	

Figure A.25: Small plate clamping frame - 2 of 4

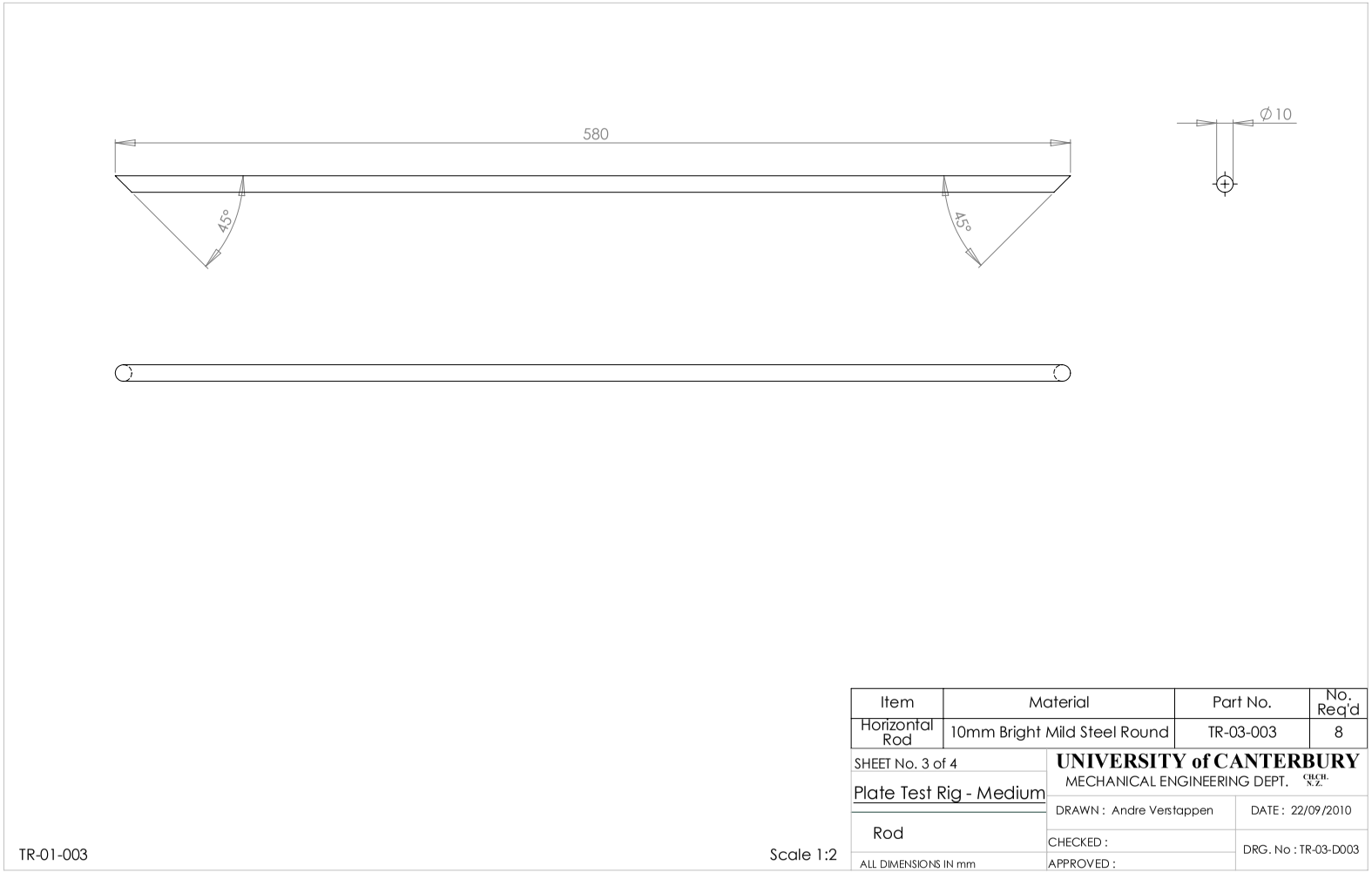

Figure A.26: Small plate clamping frame - 3 of 4

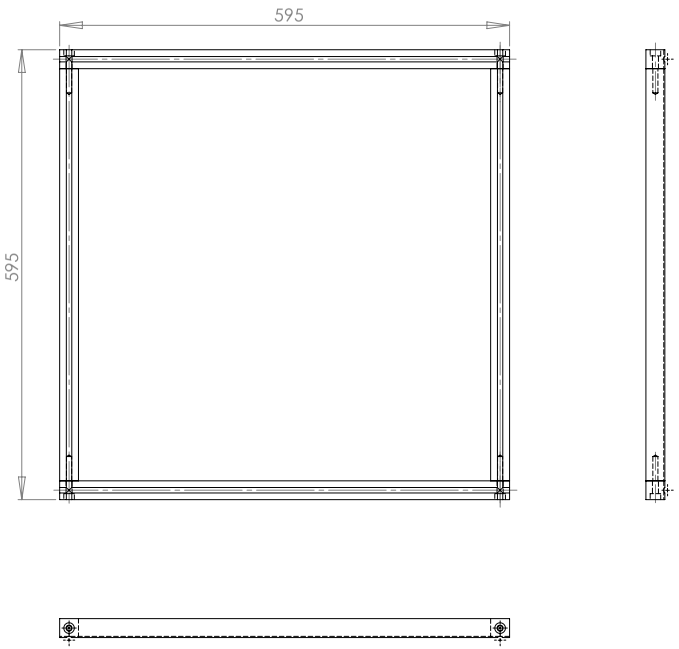

NOTE: 10mm rod must lie flat in channels.

Item	Material	Part No.	No. Req'd
Horizontal Beam	25 x 25 Aluminium Square Section	TR-03-001	4
Vertical Beam	25 x 25 Aluminium Square Section	TR-03-002	4
Frame Assembly	25 x 25 Aluminium Square Section	TR-03-004	2
Cap Screw	M8 x 50	-	8

SHEET No. 4 of 4

UNIVERSITY of CANTERBURY
MECHANICAL ENGINEERING DEPT. CHCH. N.Z.

Plate Test Rig - Medium

DRAWN : Andre Verstappen

DATE : 22/09/2010

Frame Assembly

CHECKED :

DRG. No : TR-03-D004

ALL DIMENSIONS IN mm

APPROVED :

TR-03-004

Scale 1:5

Figure A.27: Small plate clamping frame - 4 of 4

Bibliography

[1] J. D. Ferry. *Viscoelastic Properties of Polymers.* John Wiley & Sons, New York, 3rd edition, 1980.

[2] Jones D. I. G. Henderson J. P. Nashif, A. D. *Vibration Damping.* John Wiley & Sons, New York, 1985.

[3] H. Oberst and K. Frankenfeld. On the damping of bending vibrations of thin plates using attached layers. *Acustica*, 4:181–194, 1952. (In German).

[4] E. Kerwin. Damping of flexural waves by a constrained viscoelastic layer. *J. Acoust. Soc. Am.*, 31(7):952, 1959.

[5] T. E. Alberts and Xia Houchun. Design and analysis of fiber enhanced viscoelastic damping polymers. *Transactions of the ASME. Journal of Vibration and Acoustics*, 117(4):398–404, 1995.

[6] Woo-Young Jung and Amjad J. Aref. A combined honeycomb and solid viscoelastic material for structural damping applications. *Mechanics of Materials*, 35(8):831–844, 2003.

[7] Ungar E.E. Kerwin E.M. Ross, D. Damping of plate flexural vibrations by means of viscoelastic laminae. In *Structural Damping: Papers Presented at a Colloquium on Structural Damping Held at the the ASME Annual Meeting*, New York, 1959. ASME.

[8] T. Tarnoczy. Vibration of metal plates covered with vibration damping layers. *Journal of Sound and Vibration*, 11(3):299–307, 1970.

[9] Joseph R. Baumgarten and Britt K. Pearce. The damping effects of viscoelastic materials: Part 1—transverse vibrations of beams with viscoelastic coatings. *Journal of Engineering for Industry*, 93(2):645–650, 1971.

[10] Britt K. Pearce and Joseph R. Baumgarten. The damping effects of viscoelastic materials: Part 2—transverse vibrations of plates with viscoelastic coatings. *Journal of Engineering for Industry*, 93(2):651–655, 1971.

[11] D. K. Rao. Vibration damping of tapered unconstrained beams. *Acustica*, 39(4):264–9, 1978.

[12] R. Lunden. Optimum distribution of additive damping for vibrating beams. *Journal of Sound and Vibration*, 66(1):25–37, 1979.

[13] R. Lunden. Optimum distribution of additive damping for vibrating frames. *Journal of Sound and Vibration*, 72(3):391–402, 1980.

[14] K. K. Stevens, C. H. Kung, and S. E. Dunn. Damping of plates by partial viscoelastic coatings - 1. analysis. In *Proceedings - National Conference on Noise Control Engineering*, pages 445–448, Raleigh, NC, USA, 1981. Noise Control Found.

[15] S. E. Dunn, C. H. Kung, V. Jaising, and K. K. Stevens. Damping of plates by partial viscoelastic coatings - 2. experimental evaluation. In *Proceedings - National Conference on Noise Control Engineering*, pages 449–452, Raleigh, NC, USA, 1981. Noise Control Found.

[16] K. K. Stevens, C. H. Kung, and S. E. Dunn. Partial damping layer treatments for plates. In *Proceedings - International Conference on Noise Control Engineering*, pages 363–366, Amsterdam, Netherlands, 1981. Netherlands Acoustical Society.

[17] A. Yildiz and K. Stevens. Optimum thickness distribution of unconstrained viscoelastic damping layer treatments for plates. *Journal of Sound and Vibration*, 103:183–99, 1985.

[18] G. Parthasarathy, C. V. R. Reddy, and N. Ganesan. Partial coverage of rectangular plates by unconstrained layer damping treatments. *Journal of Sound and Vibration*, 102:203–16, 1985.

[19] P. K. Roy and N. Ganesan. Dynamic studies on beams with unconstrained layer damping treatment. *Journal of Sound and Vibration*, 195:417–27, 1996.

[20] A. Lumsdaine and R. A. Scott. Shape optimization of unconstrained viscoelastic layers using continuum finite elements. *Journal of Sound and Vibration*, 216:29–52, 1998.

[21] E. Bespalova and A. Kitaigorodskii. Damping of the vibrations of plates by the coating method. *International Applied Mechanics*, 35(11):1167–1172, 1999.

[22] Mohan D. Rao. Recent applications of viscoelastic damping for noise control in automobiles and commercial airplanes. *Journal of Sound and Vibration*, 262(3):457–474, 2003.

[23] Bayraktar F. Sanliturk K. Y. Serabatir, D. A. Structural damping optimization using viscoelastic materials. Inter-Noise 2007: Istanbul, Turkey, 2007.

[24] D. J. Mead. The measurement of the loss factors of beams and plates with constrained and unconstrained damping layers: A critical assessment. *Journal of Sound and Vibration*, 300:744–62, 2007.

[25] F. Cortes and M. J. Elejabarrieta. Structural vibration of flexural beams with thick unconstrained layer damping. *International Journal of Solids and Structures*, 45:5805–13, 2008.

[26] M. Rak, M. Ichchou, and J. Holnicki-Szulc. Identification of structural loss factor from

spatially distributed measurements on beams with viscoelastic layer. *Journal of Sound and Vibration*, 310(4-5):801–11, 2008.

[27] J. Berthaut, M. N. Ichchou, and L. Jezequel. K-space identification of apparent structural behaviour. *Journal of Sound and Vibration*, 280(3-5):1125–1131, 2005.

[28] J. G. McDaniel, P. Dupont, and L. Salvino. A wave approach to estimating frequency-dependent damping under transient loading. *Journal of Sound and Vibration*, 231(2): 433–449, 2000.

[29] J. Gregory McDaniel and Jr W. Steve Shepard. Estimation of structural wave numbers from spatially sparse response measurements. *Journal of the Acoustical Society of America*, 108(4):1674–1682, 2000.

[30] Xiao He-ye and Sheng Mei-ping. Dynamic analysis of a steel beam with various cross-section unconstrained layer by differential transformation method. In *Proceedings - 2nd International Conference on Information Engineering and Computer Science (ICIECS)*, Piscataway, NJ, USA, 2010. IEEE.

[31] E.E. Ungar, D. Ross, and E.M. Kerwin. Damping of flexural vibrations by alternate visco-elastic and elastic layers. In *Fourth Conference on Solid Mechanics*, 1959.

[32] R. DiTaranto. Effect of end constraints on the damping of laminated beams. *J. Acoust. Soc. Am.*, 39(2):405, 1966.

[33] R. A. DiTaranto. Theory of vibratory bending for elastic and viscoelastic layered finite-length beams. *American Society of Mechanical Engineers – Transactions – Journal of Applied Mechanics*, 32(4):881–886, 1965.

[34] D. J. Mead and S. Markus. The forced vibration of a three-layer, damped sandwich beam with arbitrary boundary conditions. *Journal of Sound and Vibration*, 10(2): 163–75, 1969.

[35] R. Plunkett and C. T. Lee. Length optimization for constrained viscoelastic layer damping. *Journal of the Acoustical Society of America*, 48(1):150–61, 1970.

[36] D. J. Mead and S. Markus. Loss factors and resonant frequencies of encastre damped sandwich beams. *Journal of Sound and Vibration*, 12(1):99–112, 1970.

[37] P. Grootenhuis. Control of vibrations with viscoelastic materials. *Journal of Sound and Vibration*, 11(4):412–433, 1970.

[38] D. I. G. Jones, A. D. Nashif, and M. L. Parin. Parametric study of multiple-layer damping treatments on beams. *Journal of Sound and Vibration*, 29(4):423–434, 1973.

[39] D. K. Rao. Frequency and loss factors of sandwich beams under various boundary conditions. *Journal of Mechanical Engineering Science*, 20(5):271–282, 1978.

[40] D. J. Mead. A comparison of some equations for the flexural vibration of damped sandwich beams. *Journal of Sound and Vibration*, 83(3):363–77, 1982.

[41] M.J. Yan and E.H. Dowell. Governing equations for vibrating constrained-layer damping sandwich plates and beams. *Journal of Applied Mechanics, Transactions ASME*, 39 Ser E(4):1041 – 1046, 1972. ISSN 00218936.

[42] Conor D. Johnson and David A. Klenholz. Finite element prediction of damping in structures with constrained viscoelastic layers. *Collection of Technical Papers - AIAA/ASME/ASCE/AHS/ASC Structures, Structural Dynamics and Materials Conference*, pages 17–24, 1981.

[43] E. Ungar. Loss factors of viscoelastic systems in terms of energy concepts. *J. Acoust. Soc. Am.*, 34(7):954, 1962.

[44] C. T. Sun, B. V. Sankar, and V. S. Rao. Damping and vibration control of unidirectional composite laminates using add-on viscoelastic materials. *Journal of Sound and Vibration*, 139(2):277–287, 1990.

[45] T. C. Ramesh and N. Ganesan. Vibration and damping analysis of cylindrical shells with constrained damping treatment-a comparison of three theories. *Transactions of the ASME. Journal of Vibration and Acoustics*, 117(2):213–19, 1995.

[46] Ahmed K. Noor, W.Scott Burton, and Jeanne M. Peters. Assessment of computational models for multilayered composite cylinders. *International Journal of Solids and Structures*, 27(10):1269 – 1286, 1991.

[47] D.J. Wilkins Jr, C.W. Bert, and D.M. Egle. Free vibrations of orthotropic sandwich conical shells with various boundary conditions. *Journal of Sound and Vibration*, 13 (2):211 – 228, 1970.

[48] T.P. Khatua and Y.K. Cheung. Bending and vibration of multilayer sandwich beams and plates. *International Journal for Numerical Methods in Engineering*, 6(1):11 – 24, 1973.

[49] Liming Yu, Yue Ma, Chungen Zhou, and Huibin Xu. Damping efficiency of the coating structure. *International Journal of Solids and Structures*, 42(11-12):3045–3058, 2005.

[50] A. Reuss. Elastic deformation according to theory of plasticity. *Zeitschrift fuer Angewandte Mathematik und Mechanik*, 10(3):266 – 274, 1930.

[51] Z. Hashin and S. Shtrikman. A variational approach to the theory of the elastic behaviour of multiphase materials. *Journal of Mechanics and Physics of Solids*, 11(2): 127 – 140, 1963.

[52] R. T. Natarajan and A. F. Lewis. Advanced composite constrained layer laminates. *Journal of Composite Materials*, 10:220–30, 1976.

[53] Daniel Gay, Suong V. Hoa, and Stephen W. Tsai. *Composite materials: design and applications*. CRC press, London, 2002.

[54] A.K. Mukhopadhyay and H.B. Kingsbury. On the dynamics of a rectangular sandwich plate with viscoelastic core and generally orthotropic facings. *Journal of Sound and Vibration*, 47(3):347 – 358, 1976.

[55] Yu S. Lipatov, L. M. Sergeeva, L. V. Karabanova, V. F. Rosovitskii, L. A. Gorbach, and N. V. Babkina. Viscoelastic properties of gradient interpenetrating polymer networks. *Mechanics of Composite Materials*, 24(6):765–770, 1989.

[56] Yu S. Lipatov and L. V. Karabanova. Gradient interpenetrating polymer networks. *Journal of Materials Science*, 30(10):2475–2484, 1995.

[57] D.J. Barrett. A design for improving the structural damping properties of axial members. In *Proceedings of Damping '89*, pages HCB 1–18, 1989.

[58] D.J. Barrett. An anisotropic laminated damped plate theory. *Journal of Sound and Vibration*, 154(3):453–465, 1992.

[59] Dennis D. Olcott. *Improved damping in composite structures through stress coupling, co-cured damping layers, and segmented stiffness layers.* PhD thesis, Brigham Young University, 1992.

[60] Dennis D. Olcott, Christopher A. Rotz, and Paul F. Eastman. Improved vibration damping in composite structures using 'zig-zag' fibers and embedded viscoelastic damping layers. In *Proceedings - 38th International SAMPE Symposium and Exhibition*, pages 1357 – 1370, Anaheim, CA, USA, 1993. SAMPE.

[61] Angela Trego, Dennis D. Olcott, and Paul F. Eastman. Improved axial damping of mechanical elements through the use of multiple layered, stress coupled, co-cured damped fiber reinforced composites. *Journal of Advanced Materials*, 28(2):28 – 34, 1997.

[62] Angela Trego and Paul F. Eastman. Flexural damping predictions of mechanical elements designed using stress coupled, co-cured damped fiber reinforced composites. *Journal of Advanced Materials*, 31:7–17, 1999.

[63] T. E. Alberts. Fibre enhancement of viscoelastic damping polymers. U.S. Patent 5,256,223, Oct. 26, 1993.

[64] William F. Pratt, Christopher A. Rotz, and C.Greg Jensen. Improved damping and stiffness in composite structures using geometric fiber wave patterns. In *Proceedings - ASME International Mechanical Engineering Congress and Exposition*, volume 23, pages 37 – 43, Atlanta, GA, USA, 1996. ASME.

[65] J.D. Marshall and D.W. Jensen. Enhanced damping of hat-stiffened panels using continuous wave fiber composites. In *Proceedings - Smart Structures and Materials 2000: Damping and Isolation*, volume 3989, pages 344 – 53, USA, 2000. SPIE-Int. Soc. Opt. Eng.

[66] Keith A. Steurer and David W. Jensen. Enhanced damping of continuous wave fiber composite sandwich panels. In *Collection of Technical Papers - AIAA/ASME/ASCE/AHS/ASC Structures, Structural Dynamics and Materials Conference*, volume 1, pages 1039 – 1046, Atlanta, GA, USA, 2000. AIAA.

[67] Angela Trego, Christopher Davis, and Paul F. Eastman. Axial passive damping testing of mass-produced stress coupled, cocured damped composites. *AIAA Journal*, 41(3): 512 – 516, 2003.

[68] J. P. Talbot and J. Woodhouse. The vibration damping of laminated plates. *Composites Part A (Applied Science and Manufacturing)*, 28A(12):1007–12, 1997.

[69] Yeong-Moo Yi, Sang-Hoon Park, and Sung-Kie Youn. Design of microstructures of viscoelastic composites for optimal damping characteristics. *International Journal of Solids and Structures*, 37(35):4791–4810, 2000.

[70] Li Zhuang and M. J. Crocker. A review on vibration damping in sandwich composite structures. *International Journal of Acoustics and Vibration*, 10(4):159–69, 2005.

[71] Shao Hui Zhang and Hua Ling Chen. A study on the damping characteristics of laminated composites with integral viscoelastic layers. *Composite Structures*, 74(1):63 – 69, 2006.

[72] Rabindra Kumar Patel, Bishakh Bhattacharya, and Sumit Basu. A finite element based investigation on obtaining high material damping over a large frequency range in viscoelastic composites. *Journal of Sound and Vibration*, 303(3-5):753–766, 2007.

[73] J. Park and D. L. Palumbo. Damping of structural vibration using lightweight granular materials. *Experimental Mechanics*, 49:697–705, 2009.

[74] Marc Rebillat and Xavier Boutillon. Measurement of relevant elastic and damping material properties in sandwich thick plates. *Journal of Sound and Vibration*, 330(25): 6098–6121, 2011.

[75] W.F Pratt, M.S Allen, and C.G Jensen. Designing with wavy composites. In *International SAMPE Symposium and Exhibition (Proceedings)*, 2001.

[76] W. F. Pratt, M. S. Allen, and T. J. Skousen. Highly damped lightweight wavy composite. Technical report, Air Force Research Laboratory, Kirtland, NM, USA, July 2001 2001.

[77] Roderic Lakes. *Viscoelastic Materials*. Cambridge University Press, 2009.

[78] Iso 6721-3, plastics – determination of dynamic mechanical properties – part 3: Flexural vibration – resonance-curve method, 1994.

[79] Astm e756, standard test method for measuring vibration-damping properties of materials, 2005.

[80] D. I. G. Jones. Temperature-frequency dependence of dynamic properties of damping materials. *Journal of Sound and Vibration*, 33(4):451–470, 1974.

[81] Malcolm L. Williams, Robert F. Landel, and John D. Ferry. The temperature dependence of relaxation mechanisms in amorphous polymers and other glass-forming liquids. *Journal of the American Chemical Society*, 77(14):3701–3707, 1955.

[82] M. van Gurp and J. Palmen. Time-temperature superposition for plolymeric blends. *Rheology Bulletin*, 67(2), 1998.

[83] J. Dealy and P Plazek. Time-temperature superposition - a users guide. *Rheology Bulletin*, 78(2):16–31, 2009.

[84] M. Kluppel. Evaluation of viscoelastic master curves of filled elastomers and applications to fracture mechanics. *Journal of Physics: Condensed Matter*, 21(Copyright 2009, The Institution of Engineering and Technology):035104 (10 pp.), 2009.

[85] Jiju Antony. *Design of Experiments for Engineers and Scientists*. Elsevier, Amsterdam, 2003.

[86] Richard Bootten. Typical geometries in composite superyachts, October 17th 2012.

[87] Iso 10848-1, acoustics – laboratory measurement of the flanking transmission of airborne and impact sound between adjoining rooms – part 1: Frame document, 2006.

[88] A. P. Verstappen and J. R. Pearse. Evaluation of viscoelastic vibration damping properties with a dynamic mechanical analyzer. In *Proceedings - 18th International Congress on Sound and Vibration*, pages 1984–1991, Rio de Janeiro, Brazil, 2011. IIAV.

[89] Arthur W. Leissa. *Vibration of Plates*. NASA, Washington, D.C., 1969.

[90] Walter D. Pilkey. *Formulas for Stress, Strain, and Structural Matrices*. John Wiley & Sons, New York, 1994.

[91] William D. Callister. *Materials science and engineering: an introduction*. John Wiley & Sons, New York, 2007.

[92] Vladimir V. Bolotin. Dynamic edge effect in the elastic vibrations of plates. *Inshen. Sbornik.*, 31:3–14, 1961. (In Russian).

[93] O. C. Zienkiewicz and Robert L. Taylor. *The finite element method.* Butterworth-Heinemann, Oxford, 2000.

[94] Robert D. Cook, Davis S. Malkus, Michael E. Plesha, and Robert J. Witt. *Concepts and Applications of Finite Element Analysis.* John Wiley & Sons, New York, 2002.

[95] William F. Pratt. Finite element analysis of wavy composites. In *Proceedings of the ASME International Design Engineering Technical Conferences and Computers and Information in Engineering Conference*, volume 1 C, pages 2375 – 2381, 2005.

[96] C. M. A. Vasques, R. A. S. Moreira, and J. D. Rodrigues. Viscoelastic damping technologies - part 1: Modelling and finite element implementation. *Journal of Advanced Research in Mechanical Engineering*, 1:76–95, 2010.

[97] Iso 6721-2, plastics – determination of dynamic mechanical properties – part 2: Torsion-pendulum method, 2008.

[98] D. J. Mead. *Passive Vibration Control.* John Wiley & Sons, New York, 1998.

[99] A.W. Van Vuure, I. Verpoest, and F.K. Ko. Sandwich-fabric panels as spacers in a constrained layer structural damping application. *Composites Part B: Engineering*, 32 (1):11 – 19, 2001.